Dissecting nociceptin opioid peptide function at the intersection of stress and reward circuitry

Carrie Stine

A dissertation

submitted in partial fulfillment of the

requirements for the degree of

Doctor of Philosophy

University of Washington

2025

Reading Committee:

Michael R. Bruchas, Chair

Larry Zweifel

Susan Ferguson

Program Authorized to Offer Degree:

Molecular and Cellular Biology

University of Washington

Abstract

Dissecting nociceptin opioid peptide function at the intersection of stress and reward circuitry

Carrie Stine

Chair of the Supervisory Committee:

Michael R. Bruchas

Department of Pharmacology

Nociceptin/orphanin FQ (N/OFQ), an endogenous opioid neuropeptide, and its G-protein coupled receptor NOPR are implicated in diverse behavioral states including the stress response, motivation, aversion, and reward-seeking. Stress-induced dysfunction in these behaviors is central to the development of both mood and substance use disorders, driving wide interest in NOPR as a therapeutic target. Despite promising evidence of NOPR's therapeutic potential, a critical gap remains in our understanding of how stress reshapes N/OFQ function within mesolimbic pathways that mediate motivated behavior. In particular, the discrete circuitry and specific mechanisms by which the N/OFQ-NOPR system influences and possibly links stress and reward responses remain largely unknown.

Seeking to address this gap, my dissertation work investigates the expression, connectivity, and function of N/OFQ neurons within key mesolimbic reward circuitry during both stress and reward-related behaviors. **Chapter 1** reviews N/OFQ's known roles in stress and motivation and introduces the mesolimbic pathway, a central reward circuit from the ventral tegmental area (VTA) to the striatum where we focused our investigations of N/OFQ's function.

Chapter 2 identifies the spatial, molecular, and developmental expression of *Pnoc*, the N/OFQ precursor gene, across different striatal compartments. **Chapter 3** presents NOPLight, a novel genetically encoded sensor we developed for real-time monitoring of N/OFQ release, and its use in detecting N/OFQ dynamics within the VTA during stress and reward. **Chapter 4** characterizes VTA N/OFQ neuron activity in response to various stressors and identifies functional afferent connectivity to this population from the lateral hypothalamus. Finally, **Chapter 5** discusses these findings in the context of existing literature surrounding N/OFQ's roles in stress and motivation, outlining future research directions. Overall, my research advances our understanding of N/OFQ's influence on stress and motivation by identifying N/OFQ circuitry that may integrate these two states, creating a foundation for further exploration of the N/OFQ-NOPR system's therapeutic potential and its role in the development and progression of reward-related disorders.

TABLE OF CONTENTS

DEDICATION

To my dad – all of my accomplishments are shared with you.

Six years of grad school,
Now a new chapter awaits.
Look Dad, I did it!

ACKNOWLEDGEMENTS

Emily Hueske and Tomoko Yoshida were primary contributors to the content of Chapter 2. Together, we are co-first authors on the associated publication in the *Journal of Comparative Neurology* (Hueske, Stine, Yoshida et al., 2024). Similarly, Xuehan Zhou was a primary contributor to the content of Chapter 3, and we are co-first authors on the associated publication in *Nature Communications* (Zhou and Stine et al., 2024). All individual author contributions are summarized at the end of each chapter. None of this research would have been possible without the leadership and guidance first and foremost from my graduate advisor, Dr. Michael R. Bruchas, but also from my collaborators Drs. Tommaso Patriarchi, Ann Graybiel, and Diego Pizzagalli.

I am so lucky to have been mentored over the past 10 years by some of the most hard-working, caring, and dedicated scientists I've known. Thank you to my mentor and dissertation advisor, Michael Bruchas, for granting me the opportunity to learn from you and the incredibly talented members of our lab over the past five years. Your enthusiasm for science is contagious and energizing; thank you for the countless times you brought life back into my projects and inspired me to keep going after I felt like I'd hit a dead end. Your support and patience, especially during this past year, meant more than I can express.

Thank you to my undergraduate research mentor John Streicher for trusting me with an independent research project at such an early stage of my research career. The skills and confidence I gained from my time in your lab encouraged me to pursue graduate school and have helped immensely in my PhD.

I would also like to thank the members of my thesis committee, Drs. Larry Zweifel, Susan Ferguson, Ajay Dhaka, and Smita Yadav, for providing years of feedback, guidance, and new perspectives that strengthened my graduate research.

I am extremely grateful to the many postdocs who have patiently provided me with guidance and advice on a daily basis, thank you especially to Drs. Raaj Gowrishankar and Wei Lei for your personal mentorship. I also highly appreciate all members of the Bruchas Lab past and present that created such a supportive, collaborative, and fun community. I truly enjoyed working with each of you! Special thanks to Avi Matarasso and Anthony English, I couldn't have asked for a better cohort to start with in this lab. Finally, thank you to my lab mentees: Ananya Achanta, Joey Johnson, Amanda Pasqualini, and Sanjana Jadhav. It was a joy mentoring each

of you and I am so grateful for all of the hard work you contributed to my research; I could not have done this without you.

Thank you to all of the friends I made in my graduate program's cohort, especially Frances, Ellen, Violet, Cera, Maggie, and Mark (but also many more!) for making Seattle feel like home from the start. Beyond the friends I've made through the science community, I'm so grateful for my larger support system of friends in Seattle. Thank you Kat, Kristin, Zach, Tyler, Christina, Angelo, Jake, Morgan, my Spikedelics volleyball team, and honorary Seattleite Darcie (and again, many more!) for all of the board games, beach days, ski trips, and trivia nights. All of you make living here so much fun.

To my partner, Evan, I am forever grateful for you and the life we share. Graduate school often felt like a maze of uncertainties that I wasn't sure how to find my way out of, but through it all you were my constant source of stability and sanity. Your love and support carried me through those ups and downs across the finish line and reminded me to enjoy the ride along the way – thank you, for everything. And of course, thank you to our cat Winry, who I may owe authorship to for the countless times she walked across my keyboard to grace my dissertation with her insights.

I am extremely grateful to my entire family for cheering me on throughout my PhD and being the biggest supporters of my education. My parents' passion for their careers has been a lifelong source of inspiration for me. Seeing how much they cared about and enjoyed their jobs has always motivated me to find that same spark in my own work. My mom especially has always been such a hard worker, so thank you mom for instilling those values in me. You are one tough lady and I am lucky to be your daughter!

Lastly, I would like to thank my dad for motivating me to pursue a PhD and being my biggest supporter along the way. My dad was kind, patient, funny, and growing up I always wanted to be just like him. It is bittersweet to stand here at the end of my academic journey without getting to share this moment with him, but to echo his favorite misquote from The Princess Bride (and a mantra that was heard many times in our household to settle sibling disputes), "Life isn't fair, princess. Anyone who says differently is trying to sell you something." My dad had an impressive ability to lighten any mood by drawing from what seemed like an endless supply of these pearls of wisdom embedded in humor. So with that, I'll simply say: thank you, Dad, for everything. I couldn't have done this without you.

LIST OF FIGURES AND TABLES

Supplementary Figures

CHAPTER 1: Introduction

1.1 The consequences of stress exposure on mood and motivated behavior

1.1.1 The stress response and psychiatric disorders

Perceiving, evaluating, and appropriately responding to environmental threats are fundamental processes essential for survival. When an animal detects a stressor that threatens its safety or well-being, the body activates an internal stress response consisting of a cascade of neurobiological and physiological processes within the central nervous system that shape the animal's behavioral reaction (e.g., fight-or-flight) to the stressor (Bernard, 1957; Schneiderman et al., 2005; Selye, 1978). These essential adaptive responses dynamically change throughout an animal's lifetime, continually updating based on individual, learned experiences with different stressors.

Despite its evolutionary roots in promoting survival, repeated or prolonged activation of the stress response can also lead to drastic health consequences. Stress exposure is a major risk factor in the development of addiction, relapse susceptibility, anxiety, and mood disorders, all of which collectively impose a staggering global health burden (Brown et al., 1995; Kosten et al., 1986; MÉNARD et al., 2016; Pittenger and Duman, 2008). While the disorders affected by stress are vastly diverse, a recurring theme common among them is the emergence of anhedonia and atypical motivation (Der-Avakian and Markou, 2012).

1.1.2 Clinical evidence linking stress and anhedonic behaviors

Anhedonia is a symptom of dysfunctional reward processing characterized by an inability to feel pleasure, a lack of motivation, or a loss of interest in stimuli that were previously perceived as rewarding (Gorwood, 2008). Clinical studies have shown that patients with major depressive disorder (MDD) display reduced sensitivity to reward, blunted detection of positive facial expressions, and are less willing than healthy controls to exert effort to receive higher value monetary rewards (Kunisato et al., 2012; Persad and Polivy, 1993; Pizzagalli et al., 2008; Suslow

et al., 2004). In turn, anhedonic symptoms have also been shown to predict future diagnosis with depression and have been associated with worsened disease outcomes (McMakin et al., 2012; Spijker et al., 2001; Wardenaar et al., 2012).

Several humans studies have linked stress exposure to the development of anhedonia. Observational studies have found a higher occurrence of stress events prior to the onset of major depressive episodes, with one study discovering that 80% of the depressive episodes reported during their study were preceded by a major, stressful life event (Brown and Harris, 1978; Mazure, 1998). In parallel to these large cohort findings, experimental evidence demonstrates that under the threat of a stressful shock, individuals will have a lower response bias to rewarding outcomes and reduced sensitivity to reward (Bogdan and Pizzagalli, 2006). Although chronic or severe stressors are typically considered more likely to alter behavior, even acute stressors such as academic exams have also been shown to reduce reward responsiveness (Nikolova et al., 2011). Together, these findings indicate that stress can alter reward processing in humans, resulting in anhedonic-like behaviors.

1.1.3 Preclinical evidence linking stress and anhedonic behaviors

In addition to the clinical findings that link stress exposure to anhedonia, converging evidence from animal studies further suggests that stress may underlie some of the deficits in motivation and reward-responding observed in psychiatric disorders. It is important to note that there is no single, comprehensive animal model capable of fully recapitulating depression or any other mood disorder. This is in large part due to the vast heterogeneity found in these disorders which present with wide-ranging symptoms, etiologies, and severities, creating a level of complexity that cannot be compressed into a single model. But beyond this limitation, there is an inherent challenge in ascertaining the subjective emotional states and cognitive decision-making processes underlying behavior in animals lacking the capacity for verbal self-report. Despite our absence of a shared

linguistic framework, there are still many depression-like behaviors that we can reasonably evaluate using animal models for stress exposure.

In rodents, maternal separation models of early life stress produce behavioral changes that last into adulthood, including increased vulnerability to substance abuse (Moffett et al., 2007). Animal models of stress exposure have consistently recapitulated many of the depression-like symptoms and behaviors associated with stress-induced psychiatric disorders in humans, including devaluation of and reduced sensitivity to reward, diminished social interaction, and behavioral despair (Berghorst et al., 2013; Henn and Vollmayr, 2005; Soares et al., 2012). Notably, the effects of stress on motivated behavior can vary widely depending on the form and duration of stress exposure (Patchev and Patchev, 2006), suggesting there are multiple mechanisms underlying behavioral outcomes induced by stress.

Overall, anhedonia plays a key role in the onset and progression of psychiatric disorders, indicating that the biology underlying functional reward-related behaviors is highly vulnerable to disruption in these disease states. Converging human and animal studies have pointed to stress as a major factor in the emergence of anhedonia. In addition to the anhedonic behavioral outcomes observed as a consequence of stress, stress exposure has a marked effect on the neurocircuitry that underlies motivated behavior. Understanding the circuitry and neurobiological substrates central to reward processing that become altered by stress is a critical first step toward identifying viable therapeutic targets with improved outcomes in psychiatric disorders.

1.2 Neural circuitry underlying stress and reward

1.2.1 Reward and stress responses in the mesolimbic dopamine system

Dopamine is a catecholamine neurotransmitter in the brain with major roles in reward anticipation, reinforcement learning, and the initiation of goal-directed motor action, all of which are central features of motivated behavior (Berridge, 2007; Russo and Nestler, 2013; Schultz, 2016, 1997). The mesolimbic dopamine system is part of the most well-characterized reward circuitry,

consisting of midbrain dopaminergic neurons that originate in the ventral tegmental area (VTA) and project to the nucleus accumbens (NAc). The NAc is a major reward structure primarily made up of GABAergic medium spiny neurons (MSNs) that express either 1) D1-type G_s-coupled dopamine receptors, which increase cAMP production, or 2) D2-type G_i-coupled dopamine receptors, which inhibit cAMP production. These two dopamine receptor types have different apparent affinities for dopamine, with D2-type receptors displaying a 10 to 100-fold greater affinity than D1-type (Baik, 2013; Beaulieu and Gainetdinov, 2011; Tritsch and Sabatini, 2012). Dopamine neurons are found to fire in distinct patterns, either 'tonically' at a low-frequency or 'phasically' where they exhibit burst-firing at a higher frequency (Grace et al., 2007). Given these two firing patterns and the higher affinity for dopamine by D2-type receptors, it is generally thought that dopamine released into the NAc by tonic, low-frequency firing preferentially activates the higher affinity D2-type receptors, which are associated with avoidance behaviors, while phasic burst-firing of dopamine will activate D1-type receptors, which promote goal-directed and reward-related behaviors (Goto et al., 2007; Goto and Grace, 2005; Grace et al., 2007; Verharen et al., 2019). However, isolating the actual contributions of these two receptor types *in vivo* during behavior is more difficult to evaluate, and the true behavioral implications of dopamine receptor signaling in the NAc remain to be determined.

As a major source of dopamine to limbic and forebrain regions, the VTA plays an important part in neural circuits regulating motivation and reward-based learning (Schultz, 2016; Wise, 2004). It is well established that VTA dopaminergic projections to the NAc are essential for encoding adaptive motivated behavior toward both beneficial and aversive stimuli (Mccutcheon et al., 2012). Recordings of single unit dopamine neuron activity in primates performing an operant reward task established the idea that dopamine activity encodes reward prediction error, reporting the difference between an expected reward and the actual rewarded outcome (Schultz, 1997). Furthermore, suppressing dopamine transmission can reduce reward-seeking behaviors and

disrupt the ability of a reward-paired cue to motivate reward-seeking (Fouriezos and Wise, 1976; Halbout et al., 2019; Iglesias et al., 2023).

Mesolimbic circuitry has also been implicated in stress. In particular, multiple human studies using functional MRI recordings have demonstrated changes in striatal activity following stress. A higher exposure to stressful events early in life was connected to blunted neural response during reward receipt in multiple basal ganglia structures including the NAc and ventral striatum (Vidal-Ribas et al., 2019). In another study, patients with blunted NAc activity during reward presentation following exposure to an acute stressor had stronger associations between reported life stress and the severity of anhedonia (Kirshenbaum et al., 2024). Similarly, acute stress exposure has been shown to blunt neural activity in the striatum during reward delivery in a human monetary guessing task (Lincoln et al., 2019). Adolescents exposed to emotional neglect are also found to have lower activity in the ventral striatum (Hanson et al., 2015). Animal models have supported these findings, with one study demonstrating that early life stress exposure in rats decreases dopamine transporter levels in the NAc (Brake et al., 2004), and others showing that prolonged exposure to inescapable stressors decreases dopamine release in the NAc (Cabib and Puglisi-Allegra, 2012) and reduces the number of spontaneously active VTA dopamine neurons by 64% (Moore et al., 2001).

1.2.2 Afferent connectivity of the mesolimbic pathway

Upstream inputs to the VTA are also implicated in regulating VTA dopamine neuron activity, contributing to the expression of dopamine-regulated reward behaviors. One critical afferent input to the VTA is the lateral hypothalamus (LH), also referred to interchangeably as the lateral hypothalamic area (LHA). The LH provides dense inhibitory and excitatory input into the VTA, and these inputs have been implicated in both reward and avoidance behavior.

GABAergic projections from the LH to the VTA enhance dopamine release and are important for encoding appetitive behaviors, positive reinforcement, and social interaction

(Jennings et al., 2015; Nieh et al., 2016, 2015; Schiffino et al., 2019). In contrast, LH glutamatergic projections to the VTA are shown to suppress dopamine release and have been linked to social avoidance behaviors (Nieh et al., 2016). Conflicting evidence suggests that LH glutamatergic activity provides excitatory drive onto VTA dopamine neurons (Kempadoo et al., 2013). However, Nieh and colleagues propose an alternate interpretation of these findings, suggesting that the approach used in the Kempadoo study may have inadvertently blocked both LH glutamatergic action and the phasic burst-firing of dopamine neurons, making it difficult to isolate the specific effect of LH glutamatergic activity in the VTA. Furthermore, multiple groups have reported that VTA dopamine transmission is largely regulated via disinhibition (Henny et al., 2012; Paladini and Roeper, 2014; Watabe-Uchida et al., 2017; Yang et al., 2018). Specifically, it is thought that GABAergic inputs from afferent projections inhibit local VTA GABAergic neurons, which normally drive tonic suppression of VTA dopamine neurons. This model of disinhibition supports the idea that LH GABAergic input to the VTA would enhance dopamine release by suppressing local tonic inhibition.

Ultimately, the LH provides key modulatory input to the VTA, regulates motivation during approach and avoidance behaviors, and separately has been implicated in the stress response (Gomes-de-Souza et al., 2019; Li et al., 2020; Wang et al., 2021). Together these factors pinpoint the LH as a region of strong interest within the framework of this dissertation.

1.2.3 Neuropeptides as emerging modulators of mesolimbic circuitry

Although inhibitory GABAergic and excitatory glutamatergic neurotransmission are traditionally considered the primary regulators of neural circuit activity, neuropeptides have recently emerged as crucial modulators within these reward pathways and structures. Neuropeptides are small proteins synthesized and released by neurons as a form of chemical communication to regulate diverse physiological functions, and collectively neuropeptides make up the largest class of signaling molecules in the brain (Burbach, 2011). Specifically, recent studies have expanded on

the signaling complexity within the mesolimbic pathway by identifying diverse neuropeptides that have significant influence over this critical reward circuitry.

The LH, for example, has multiple neuropeptidergic projections that influence VTA-NAc neurotransmission (Nestler and Carlezon, 2006). Melanin-concentrating hormone (MCH), a pro-appetite peptide that promotes feeding behavior, is expressed on a subpopulation of LH inputs to the NAc, and is shown to help mediate reward by stimulating feeding behaviors (Hsu et al., 2005; Saito et al., 1999). Similarly, the LH releases orexin, another pro-feeding peptide that promotes alertness, into the VTA where it stimulates dopamine neuron activity (Korotkova et al., 2003; Nakamura et al., 2000). More recently, one study reported on an LH projection to the VTA that co-releases both the neuropeptide neurotensin (Nts) and the inhibitory neurotransmitter GABA which initiate separate but complementary mechanisms that together drive a coordinated increase in VTA dopamine neuron activity, demonstrating the importance of neuropeptide transmission in regulating reward circuitry (Soden et al., 2023).

Within the VTA itself, endogenous opioid neuropeptides and their respective receptors are differentially expressed on VTA subpopulations (Phillips et al., 2022). The VTA is a critical site for opioid-induced changes in dopamine neurotransmission via activation of mu opioid receptors (MOPR) within the VTA, as MOPR agonists infused into the VTA drive strong positive reinforcement effects (see (Fields and Margolis, 2015; Koob and Nestler, 1997) for review). Further, brief stress exposure induces prolonged activation of kappa opioid receptors (KOPR) within the VTA (Polter et al., 2017), suggesting that neuropeptide activity within the VTA has roles in both stress and reward responses.

In summary, the mesolimbic dopamine pathway provides critical regulation of reward-seeking and motivated behaviors. The profound effects of stress on dopamine transmission within this circuitry indicate that stress-induced changes within this system could underlie the clinically observed relationship between stress exposure and anhedonia. Recent work further highlights the role of neuropeptides in the stress response and the fine-tuning of mesolimbic circuitry during

reward-related behaviors. Notably, studies of neuropeptide systems have historically been limited by the lack of tools available to measure and detect neuropeptide signaling in real time in behaving animals, making it difficult to ascertain when and in which circuitry neuropeptides are released (Girven et al., 2022). Given that neuropeptide receptors are highly targetable for therapeutic intervention, neuropeptidergic systems are a strong candidate for further exploration in the context of stress and reward.

1.3 N/OFQ: an endogenous opioid peptide at the interface of stress and reward

1.3.1 N/OFQ and its cognate receptor NOPR

One such neuropeptide with relevance in stress and reward is nociceptin/orphanin-FQ (N/OFQ). N/OFQ is an endogenous opioid neuropeptide that along with its cognate receptor (NOPR) represents the most recently discovered opioid peptide/receptor system (Meunier et al., 1995; Reinscheid et al., 1995). The N/OFQ-NOPR system is the first example of reverse pharmacology, with the discovery of NOPR, originally named ‘opioid receptor-like 1’ (ORL1), predating the identification of its endogenous ligand. Shortly after, N/OFQ was discovered simultaneously by two different research groups, with one naming it ‘nociceptin’ due to its apparent induction of hyperalgesia (Meunier et al., 1995), and the other naming it ‘orphanin FQ’ for its status as the endogenous ligand for the now ‘deorphanized’ receptor ORL1 (Reinscheid et al., 1995). N/OFQ is derived from a precursor peptide, prepronociceptin (preproN/OFQ or PNOC), which is encoded by the *Pnoc* gene. Since its discovery, N/OFQ’s functions have been shown to extend beyond pain modulation to influence motivation, stress, hormone regulation, learning and memory, mood regulation, feeding, and substance use disorder (D’Oliveira da Silva et al., 2023; Jenck et al., 1997; Kash et al., 2015; Koob, 2008; Mogil et al., 1996; Parker et al., 2019).

NOPR is a G protein-coupled receptor (GPCR) that shares 60% sequence similarity with the other receptors in the opioid family (Wang et al., 2023), yet retains a unique pharmacological profile (Thompson et al., 2012). Upon occupancy by its endogenous peptide ligand N/OFQ, the

receptor activates downstream G_i/G_o proteins and induces intracellular signaling that includes the inhibition of cAMP formation, and ultimately reduces neurotransmission via the inhibition of voltage-gated calcium channels and the activation of inwardly-rectifying potassium channels (Toll et al., 2016).

NOPR is abundantly expressed within the central nervous system (Berthele et al., 2003; Mollereau and Mouledous, 2000; Neal et al., 1999), in line with the broad range of neural and cognitive functions regulated by this endogenous opioid system (Andero, 2015; Moulédous, 2019). In contrast to its receptor's broad expression, N/OFQ ligand expression is more restricted and primarily localized in regions related to stress, feeding, and dopamine regulation (Neal et al., 1999; Norton et al., 2002; Ubaldi et al., 2021). Both NOPR and N/OFQ-expressing neurons are highly enriched in several key reward structures including the arcuate nucleus of the hypothalamus (ARC), dorsal striatum, nucleus accumbens (NAc), medial prefrontal cortex (mPFC) and the ventral tegmental area (VTA) (Neal et al., 1999). In the VTA in particular, a population of N/OFQ-expressing paranigral ventral tegmental area (VTA) neurons that locally modulate VTA dopamine neurons have also been shown to mediate motivated behaviors, which is discussed further in section **1.3.3** (Parker et al., 2019).

1.3.2 Antidepressant effects of N/OFQ-NOPR blockade

Notably, N/OFQ has also recently been identified as a potential treatment candidate for major depressive disorder (Der-Avakian et al., 2017; D'Oliveira da Silva et al., 2023; Gavioli and Calo', 2013; Post et al., 2016; Ubaldi et al., 2021; Witkin et al., 2019). Preclinical studies with NOPR antagonists have consistently shown antidepressant-like effects such as restoration of normal sucrose intake following chronic stress and decreased immobility time, which is indicative of reduced 'despair' behavior, during the forced swim and tail suspension tests, (Gavioli et al., 2004, 2003; Gavioli and Calo', 2013; Goeldner et al., 2010; Vitale et al., 2009). Genetically altered mice that lack the NOPR gene (NOPR-/-) also spend less time immobilized during forced swim and tail

suspension (Gavioli et al., 2004, 2003), corroborating the pharmacological evidence that N/OFQ-NOPR function is important for despair-like behavior.

While investigations of roles for N/OFQ in humans are limited, clinical research has further highlighted the relevance of N/OFQ-NOPR signaling in anhedonia. One NOPR antagonist was evaluated in a clinical trial where it did improve depression scores, although not to a level that satisfied the predefined efficacy criteria (required >88% efficacy relative to placebo; achieved 82.9%) (Post et al., 2016). N/OFQ plasma levels are also elevated in patients with major depressive disorder (MDD), post-partum depression, and bipolar depression, all of which are commonly associated with anhedonic behaviors and reduced motivation (Gu et al., 2003; Wang et al., 2009). Lastly, a neuroanatomical investigation of NOPR mRNA expression in post-mortem tissue of patients with bipolar disorder showed an upregulation of NOPR mRNA in the orbitofrontal cortex (Ryan et al., 2006).

1.3.3 Roles of N/OFQ-NOPR in stress and reward

At the behavioral level, N/OFQ inhibits conditioned place preference to morphine, amphetamine and cocaine (Chiou et al., 2007; Ciccocioppo et al., 2000), and disruption of the N/OFQ system is associated with motivated responding disorder (Civelli, 2008). ICV administration of N/OFQ was reported to potently block reward-associated cues but showed no effect on aversion associated cues (Sakoori and Murphy, 2008).

In a recent study, we identified a subgroup of PNOC-enriched neurons located in the paranigral VTA (pnVTA^{PNOC} neurons) which, when activated, caused avoidance behavior and decreased motivation for reward (Parker et al., 2019). Using a progressive ratio task for reward, where the number of nose pokes a mouse needs to make to earn a reward increases exponentially with each subsequent trial, we found that activation of pnVTA^{PNOC} activity would constrain effort-based reward-seeking behavior and mice would earn fewer rewards than normal. Conversely, we found that inhibiting these same neurons drove an increase in motivation, with

animals achieving more rewards during the progressive ratio task. We also observed increased avoidance behaviors when activating these pnVTA^{PNOC} neurons during both real-time and conditioned-place preference tests, indicating that activity of this population drives real-time and learned aversion.

An additional population of PNOC neurons located in the ARC has emerged as an important neuronal population involved in regulating feeding behavior. These GABA-expressing neurons are activated after three days of a high-palatable, energy-dense diet and have been found to play a crucial role in feeding control. In particular, optogenetic stimulation of PNOC-expressing neurons in the ARC induces feeding, while selective ablation of these neurons decreases food intake and prevents obesity (Jais et al., 2020). Apart from its roles in the VTA-NAc and ARC circuits, N/OFQ can also inhibit mPFC-projecting VTA neurons (Driscoll et al., 2019) and a reduction in mPFC N/OFQ level was reported in rodents that underwent conditioned opioid withdrawal (Walker et al., 2002).

Beyond reward-related responses, the N/OFQ-NOPR system has also been linked to stress. N/OFQ signaling influences the HPA axis, a central component of the stress response that initiates neuroendocrine responses to restore homeostasis following a stressful event. Specifically, administration of N/OFQ can activate and sustain neuroendocrine activity within the HPA axis, elevating corticosterone levels and prolonging the physiological effects of the stress response (Devine et al., 2001; Green et al., 2007). N/OFQ signaling can also enhance stress vulnerability, with one study demonstrating that NOPR activation increased the percentage of rats developing learned helplessness after an acute stress exposure (Holanda et al., 2019). There are also several studies demonstrating that stress alters ppN/OFQ mRNA expression across the brain, although the magnitude and direction of these changes vary across several dimensions including brain region, sex, and the form and/or duration of the stress manipulation (see (Gavioli et al., 2021) for a summary of effects).

Of note, past studies on N/OFQ signaling have generated some contradictory results (Ciccocioppo et al., 2019). Activation of NOPR with a selective agonist was reported to reduce alcohol drinking and seeking behavior (Ciccocioppo et al., 2014; Kuzmin et al., 2007), while a selective NOPR antagonist, LY2940094, was reported to have the same effect (Rorick-Kehn et al., 2016). In anxiety-related behaviors, it has been reported that central injection of a NOPR agonist induces anxiogenic effect, but anxiolytic effects of NOPR agonists had also been reported (Gavioli et al., 2002; Jenck et al., 1997; Varty et al., 2008). These observations can be interpreted in different ways. The dynamics of NOPR desensitization after application of agonists or antagonists, for example, could contribute to these contradictory results. Another possible explanation could be the competition of different local neural circuits simultaneously recruited by the N/OFQ system, as most of the studies mentioned before do not have fine spatial control over the application of drugs nor the resolution to isolate endogenous release dynamics of the peptide. These conflicting findings underscore that although N/OFQ signaling is clearly implicated in the stress response, the specific mechanisms, circuitry, and roles of N/OFQ in mediating stress-related behaviors are far from fully understood.

1.3.4 Evidence of N/OFQ function within mesolimbic circuitry

Several studies have shown that the N/OFQ system exerts an important modulatory effect on mesolimbic dopaminergic circuits. For example, intracerebroventricular (ICV) injection of N/OFQ produces a decrease in extracellular dopamine in the NAc (Murphy et al., 1996) and exerts an inhibitory constraint on dopamine transmission by either inhibiting tyrosine hydroxylase phosphorylation or dopamine D1 receptor signaling (Olianas et al., 2008). In the context of drug use, N/OFQ has been shown to prevent morphine- and cocaine-induced dopamine increase in the NAc (Di Giannuario and Pieretti, 2000; Lutfy et al., 2001). In the VTA, NOPR is largely expressed on dopamine neurons (Norton et al., 2002), and its activation has been shown to

negatively regulate dopamine activity (Zheng et al., 2002), paralleling many of the reported effects of stress (Bouarab et al., 2019; Lowes and Harris, 2022).

There is a strong precedent for opioid signaling in the striatum, with extensive literature pointing to numerous striatal functions of other endogenous opioid systems, most notably mu and kappa, in the coordination of key reward and feeding behaviors (Al-Hasani et al., 2015; Bodnar et al., 1995; Castro et al., 2021; Castro and Berridge, 2014; Castro and Bruchas, 2019; Ragnauth et al., 2000). In addition, dysregulated striatal opioid signaling can contribute to a wide range of neurological disorders, including mood disorders, substance use disorder, Huntington's disease, Parkinson's disease, and schizophrenia, among others (Banghart et al., 2015; Canales and Graybiel, 2000; Clark and Abi-Dargham, 2019; Cui et al., 2014; Kennedy et al., 2006; Margolis et al., 2023; Morigaki et al., 2020; Sgroi and Tonini, 2018). This is due in part to the distinct patterns of expression exhibited by different opioid receptors and peptides throughout the striatum, including differential expression in striosome and matrix compartments (Brimblecombe and Cragg, 2017; Crittenden and Graybiel, 2011; Graybiel, 1990; Tajima and Fukuda, 2013).

Although *Pnoc*-expressing neurons can be found throughout the striatum, their organization within striatal neuronal types and their anatomical intersection with dopamine circuitry across striatal subregions have remained largely unknown, especially in comparison to the other striatal opioid systems. Despite this, several studies have implied functional significance for the N/OFQ system in both the dorsal striatum and nucleus accumbens. Studies of dorsal striatal dopamine release following activation or blockade of NOP receptors in SNc highlighted bidirectional modulation of dopamine (Marti et al., 2004; Murphy and Maidment, 1999; Olianas et al., 2008). In the nucleus accumbens, N/OFQ infusion has been shown to reduce dopamine release (Koizumi et al., 2004; Murphy and Maidment, 1999) and inhibit dopamine synthesis at DA nerve terminals in the NAc by reducing tyrosine hydroxylase phosphorylation (Olianas et al., 2008). With regard to behavioral function, NOP receptor activation in the nucleus accumbens has been implicated in the modulation of reward-related behaviors and the reinforcing properties of

drug use in several studies (Bebawy et al., 2010; Caputi et al., 2014; Lutfy et al., 2002; Marquez et al., 2008; Murphy and Maidment, 1999; Romualdi et al., 2007; Sakoori and Murphy, 2004; Vazquez-DeRose et al., 2013). Overall, the exact mechanisms of the NOPR-N/OFQ system and its impact on critical mesolimbic reward circuitry are, at best, only partially understood.

1.3.5 Identifying the circuit-level function of N/OFQ in stress and reward

In this dissertation, I will describe my work on complementary studies that collectively seek to better define N/OFQ's roles within mesolimbic circuitry, particularly during stress, reward, and motivated behavior. In **Chapter 2**, we investigated the expression patterns of ppN/OFQ (PNOC) mRNA across different compartments of the dorsal and ventral striatum, discovering variable expression between early developmental stages and adulthood. We also characterize the prominence of PNOC expression on the primary molecular subpopulations that exist within the striatum (D1 medium spiny neurons, D2 medium spiny neurons, and a selection of interneuron subtypes). In **Chapter 3**, we developed a novel, genetically encoded sensor for the detection of endogenous N/OFQ release called NOPLight. We characterized NOPLight extensively *in vivo* and then used it to record N/OFQ release in the VTA during operant reward-seeking behavior. Finally, in **Chapter 4** we characterized the effects of different types of stress exposure on N/OFQ neuron activity within the VTA. We also probed the synaptic connectivity of GABAergic and glutamatergic projections from the LH onto VTA N/OFQ neurons. Collectively, these studies advance our understanding of the circuitry and mechanisms engaging N/OFQ signaling at the intersection of stress and reward.

CHAPTER 2: Developmental and adult striatal patterning of nociceptin ligand marks striosomal population with direct dopamine projections.

This chapter includes results and figures adapted from the following manuscript:

> Hueske E[#], **Stine C*,#**, Yoshida T[#], Crittenden JR, Gupta A, Johnson JC, Achanta AS, Bhagavatula S, Loftus J, Mahar A, Hu D, Azocar J, Gray RJ, Bruchas MR, Graybiel AM. Developmental and adult striatal patterning of nociceptin ligand marks striosomal population with direct dopamine projections. ***Journal of Comparative Neurology.*** December 10, 2024. doi.org/10.1002/cne.70003.
> [#]*These authors contributed equally*

2.1 Introduction

The midbrain neurons of the substantia nigra influence motor and cognitive behaviors related to reinforcement learning, motivation, behavioral choice, and movement initiation (da Silva et al., 2018; Hikosaka et al., 2014; Howe and Dombeck, 2016; Schultz, 2016). The circuits that innervate these dopamine neurons can bias, enhance, or diminish these modulatory functions. A labyrinthine striosomal compartment of the striatum that winds through the surrounding matrix contains neurons unique among striatal projection neurons (SPNs) in their direct innervation of midbrain dopamine-containing neurons, forming a striosome-dendron bouquet capable of shutting down dopamine neuron activity (Crittenden et al., 2016; Evans et al., 2020; Matsushima and Graybiel, 2020; Watabe-Uchida et al., 2012). Here, we report that among these bouquet-innervating striosomal neurons there is a population selectively defined by the developmental expression of prepronociceptin (*Pnoc*), a gene encoding the opioid-like ligand nociceptin/orphanin FQ (N/OFQ) associated with pain, stress, and reinforcement-related processing by way of its dampening effect on dopamine (Flau et al., 2002; Norton et al., 2002; Parker et al., 2019; Zheng et al., 2002).

While there is evidence of N/OFQ's modulatory effects on striatal dopamine as discussed in **Chapter 1**, little is known about the organization of striatal circuits subserving N/OFQ signaling and how they intersect with the midbrain dopamine system. This organization may be critical to

N/OFQ's influence on approach-avoidance and reward behaviors since several studies have demonstrated diversity in function of opioid peptide/receptor systems specific to their location within different striatal subregions (Al-Hasani et al., 2015; Castro et al., 2021; Castro and Berridge, 2014; Cui et al., 2014; Resendez et al., 2013; Tejeda et al., 2017). In the current study, we investigated the spatial and molecular expression pattern of the N/OFQ ligand prepronociceptin (*Pnoc*) across the dorsal and ventral striatum. To visualize *Pnoc*$^{+}$ neurons, we crossed mice with prepronociceptin-driven expression of Cre recombinase (PNOC-Cre) with the Cre-dependent Ai14 (tdTomato) reporter line to induce a lasting tdTomato fluorescent label in *Pnoc*$^{+}$ neurons (Pnoc^{tdTomato}). Using this mouse line, we visualized the spatial distribution of *Pnoc*$^{+}$ neurons across the dorsal striatum and the nucleus accumbens and co-stained for various SPN and interneuron molecular markers to identify the neuronal subtypes labeled by Pnoc^{tdTomato} reporter expression. We also evaluated differences in neonatal and adult striatal *Pnoc* expression, which suggest that N/OFQ function in the striatum may vary from development into adulthood.

2.2 Results

2.2.1 Pnoc^{tdTomato} cells cluster within striosomes in the dorsal striatum

To visualize *Pnoc*-expressing neurons, we bred mice harboring prepronociceptin-driven expression of Cre recombinase (PNOC-Cre) with a Cre-dependent "reporter line", *loxP-Stop-loxP-tdTomato* (Ai14; *LSL-tdTomato*), such that offspring enduringly "report" red fluorescent protein, tdTomato, in cells that have shown expression of *Pnoc* (Pnoc^{tdTomato}), whether current or previously. Examination of these Pnoc^{tdTomato} cells in the striatum demonstrated distinct spatial distribution patterns across both dorsal and ventral regions (**Figure 2.1**). In the dorsal striatum, Pnoc^{tdTomato} cells were largely confined to striosomes, as identified by overlap with the known striosomal marker mu opioid receptor, MOR1 (**Figure 2.1a–d**). Discrete patterning was also evident in the ventral striatum, with Pnoc^{tdTomato} neurons found predominantly in the dorsomedial

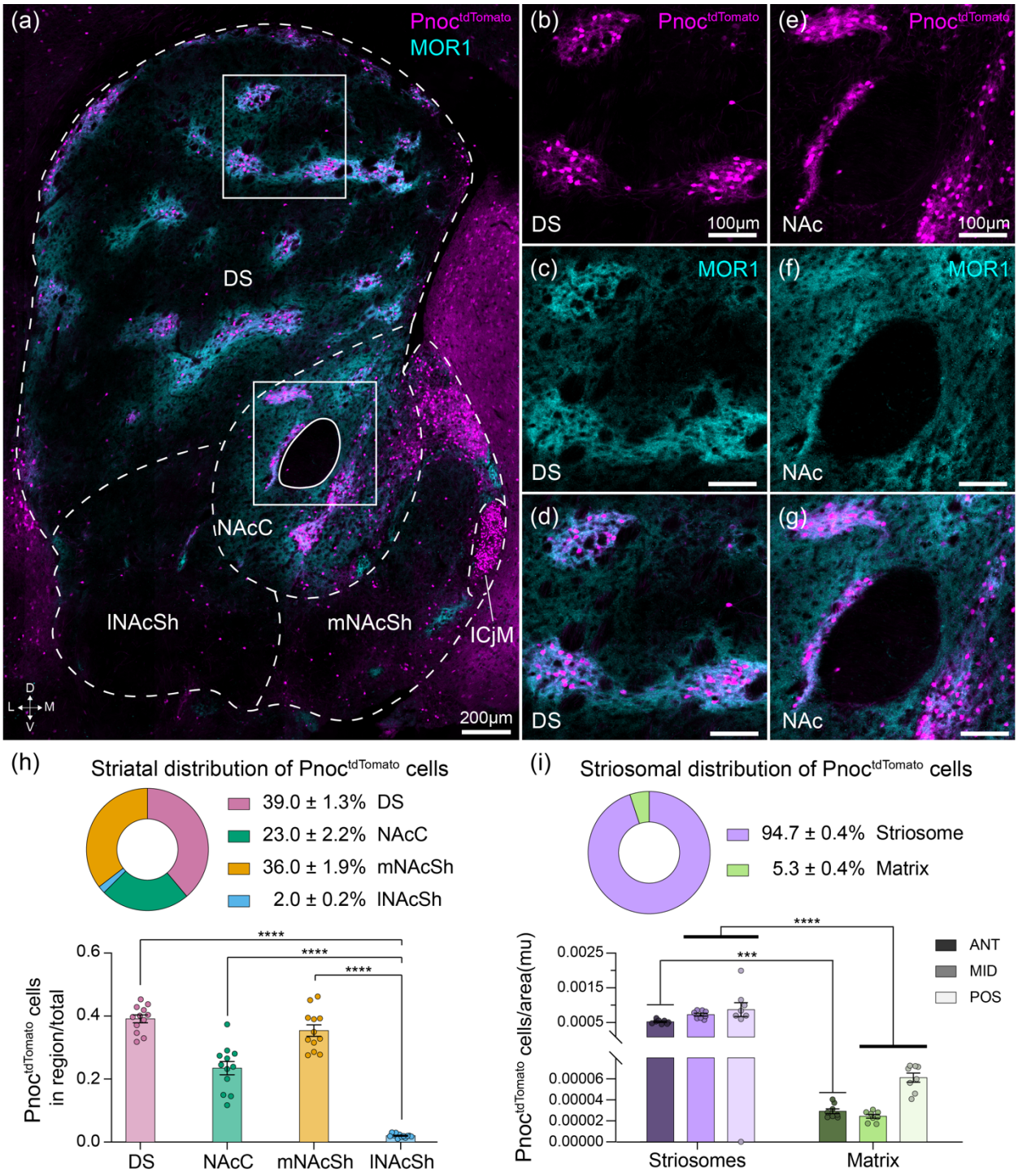

Figure 2.1: Pnoc^{tdTomato} reporter expression shows compartmental distribution across the striatum and corresponds with striosomes in the dorsal striatum.

(a) Composite image showing Pnoc^{tdTomato} (magenta) and striosomal marker MOR1 (cyan) in the striatum. **(b–d)** Higher magnification images of the top boxed region from panel (a) with Pnoc^{tdTomato} (b, magenta) and MOR1 (c, cyan) shown separately. Merged image (d) shows strong overlap between Pnoc^{tdTomato} neurons and MOR1 expression. **(e–g)** same as (b–d) but for the lower boxed region in the ventral striatum from panel (a). **(h)** Quantification of PnoctdTomato spatial distribution across the dorsal and ventral (nucleus accumbens core, medial shell, and lateral shell) striatum (bar graph, one-way

ANOVA with Bonferroni's multiple comparisons test, ****p < 0.0001, N = 12 mice, N = 19 sections, 1–2 sections/mouse. **(i)** Quantification of Pnoc^{tdTomato} spatial localization in striosomes vs. the matrix across the anterior to posterior axis in the dorsal striatum (two-way ANOVA shows main effect of striatal compartment ***p < 0.001, no significant effect of anterior-posterior axis p = 0.0851bar graph, two-way ANOVA with Bonferroni's multiple comparisons test, ***p < 0.001, ****p < 0.0001, N = 8 mice, 3 sections/mouse). All data represented as mean ± SEM across mice. ANT = anterior; DS = dorsal striatum; lNAcSh = lateral accumbens shell; MID = medial; mNAcSh = medial accumbens shell; NAc = nucleus accumbens; NAcC = nucleus accumbens core; POS = posterior.

portion of the medial shell, in high-density clusters in the nucleus accumbens core, and scattered sparsely and more homogeneously throughout the lateral shell (**Figure 2.1a, e–g**). Across the entire striatum, Pnoc^{tdTomato} neurons were distributed in similar proportions between the dorsal striatum, NAc core, and medial NAc shell, with a much smaller proportion found in the lateral NAc shell (**Figure 2.1h**). Pnoc^{tdTomato} neurons were consistently found in clusters that localized with striosomes along the dorsal striatum's anterior to posterior axis at a ~20-fold higher density than found in the surrounding matrix (0.0007 ± 0.0001 cells/μm in striosomes; $3.8x10^{-5}$ ± $1.2x10^{-5}$ cells/μm in matrix; **Figures 2.1i and S2.1**). These findings demonstrate that *Pnoc* expressing neurons in the dorsal striatum are highly selective to the striosomal compartment and show clustered patterning in the ventral striatum.

2.2.2 Striatal Pnoc^{tdTomato} neurons predominantly overlap with D1 SPNs

To further molecularly classify striatal *Pnoc*$^{+}$ neurons, we evaluated Pnoc^{tdTomato} co-expression with markers for different SPN subtypes. We crossed our *PNOC-Cre*;*LSL-tdTomato* reporter line with *Drd1-GFP* (D1^{GFP}) or *Drd2-GFP* (D2^{GFP}) reporter mice to simultaneously visualize Pnoc^{tdTomato} neurons colocalized with either D1+ or D2+ neurons labeled by GFP (**Figure 2.2**). We found a significant colocalization of Pnoc^{tdTomato} with D1^{GFP}-type SPNs in both dorsal (87.9% ± 0.7%) and ventral (63.7% ± 10.8%) striatum (**Figure 2.2a–i**), to the near exclusion of D2^{GFP} SPNs (dorsal 1.3% ± 0.2%; ventral 4.3% ± 1.1%, **Figure 2.2j–r**). Due to a lack of full genetic penetrance that is characteristic of GFP reporter lines, we also quantified the SPN cell types by *in situ* hybridization

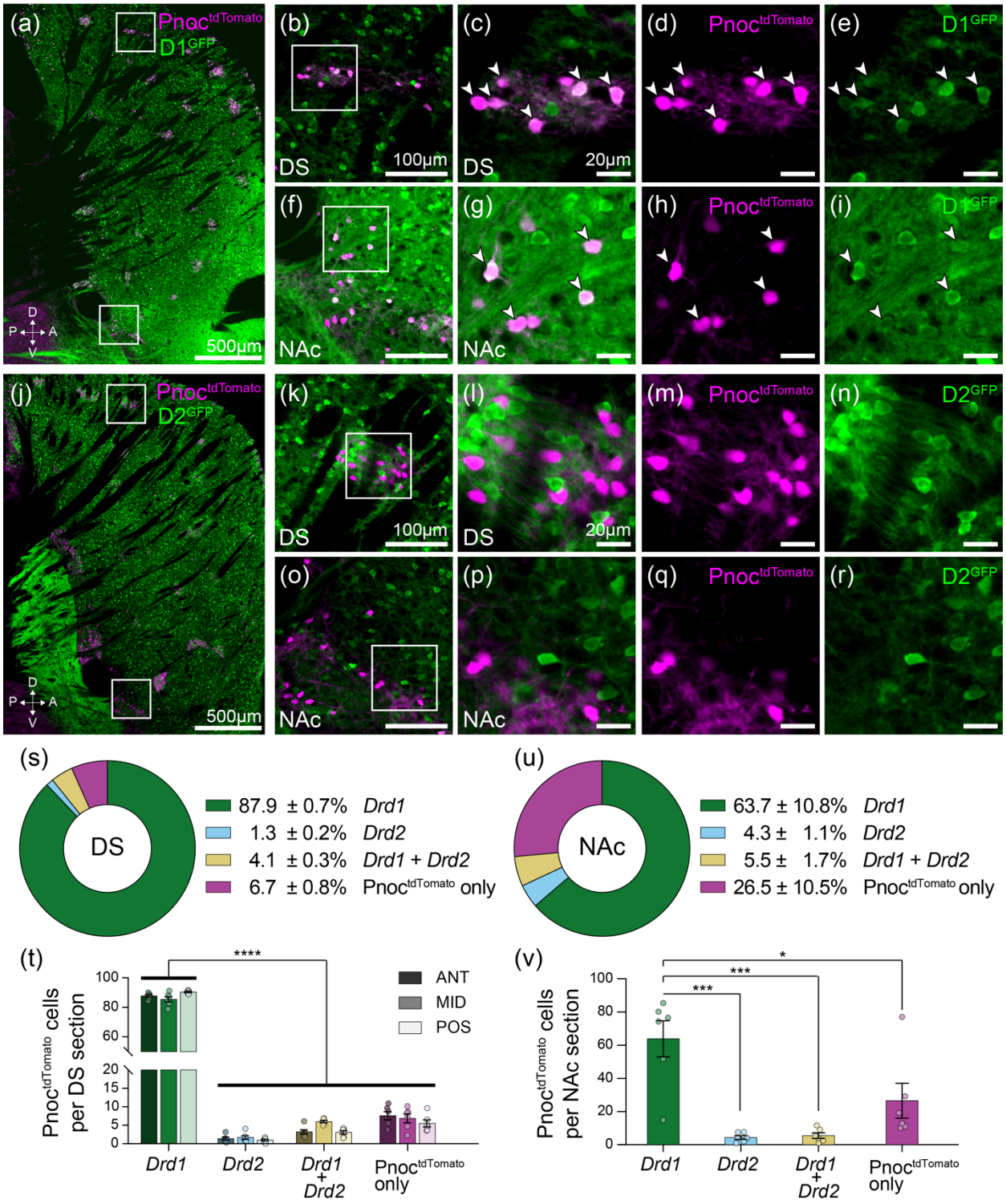

Figure 2.2: Pnoc^{tdTomato} striatal neurons cluster with *Drd1* SPNs to near exclusion of *Drd2*.

(a) Sagittal image of Pnoc^{tdTomato} cells (magenta) colocalizing with D1-GFP-expressing SPNs (green) in dorsal (b–e) and ventral (f–i) striatum. **(b)** Higher magnification image of top boxed region from panel (a) in the dorsal striatum. **(c–e)** Higher magnification images from inset in (b) of dorsal striatum. Arrowheads point to cells expressing markers for both Pnoc^{tdTomato} and D1-GFP. **(f)** Higher magnification image of the bottom boxed region from panel (a) in the ventral striatum (nucleus accumbens).

(g–i) Higher magnification images from inset in (f) of the ventral striatum. **(j)** Sagittal image of minimal overlap between Pnoc^{tdTomato} cells (magenta) and D2-GFP expression (green) in dorsal (k–n) and ventral (o–r) striatum (same as [b–e] and [f–i] but for D2-GFP expression). **(s)** Summary of IHC-stained Pnoc^{tdTomato} reporter cell colocalization with *in situ* hybridization-labeled *Drd1* and *Drd2* SPNs in dorsal striatum. **(t)** Quantification of Pnoc^{tdTomato} cells on *Drd1* and *Drd2* labeled SPNs across the anterior to posterior axis in the dorsal striatum (main effect of neuron type, two-way ANOVA, ****$p < 0.0001$; bar graph, two-way ANOVA with Bonferroni's multiple comparisons test, ****$p < 0.0001$, N = 6 mice, 3 brain sections/mouse). **(u)** Same as (s) for the nucleus accumbens. **(v)** Quantification in nucleus accumbens of Pnoc^{tdTomato} labeling in *Drd1* and *Drd2* SPNs (bar graph, one-way ANOVA with Bonferroni's multiple comparisons test, ***$p < 0.001$, *$p < 0.05$, N = 6 mice, N = 8 sections, 1–2 sections/mouse). All data represented as mean ± SEM across mice. ANT = anterior; DS = dorsal striatum; MID = medial; NAc = nucleus accumbens; POS = posterior.

(ISH) of *Drd1* and *Drd2*, which were consistent with our initial findings (**Figure 2.2s–u**). The distribution of Pnoc^{tdTomato} neurons that co-localized with *Drd1, Drd2,* both, or neither, remained consistent across the dorsolateral, ventrolateral, and medial dorsal striatum (**Figure S2.2**). By contrast, Pnoc^{tdTomato} SPN subpopulations in the ventral striatum appeared more heterogeneous, with just under half of Pnoc^{tdTomato} neurons in the lateral NAc shell (48.0% ± 12.5%) and almost a third in the medial shell (29.8% ± 10.5%) not co-localized with either *Drd1* or *Drd2* (**Figure S2.3**). These results indicate that Pnoc^{tdTomato} labeling predominantly overlaps with *Drd1* expression across the dorsal and ventral striatum, suggesting that striatal *Pnoc* expression largely occurs within D1-type SPNs.

2.2.3 A small, interneuronal population of SST/NPY^{+} Pnoc^{tdTomato} cells

We next asked whether Pnoc^{tdTomato} cells are found within any interneuronal populations in the striatum by staining for the interneuron markers neuropeptide Y (NPY), somatostatin (SST), choline acetyltransferase (ChAT), and parvalbumin (PV) in combination with Pnoc^{tdTomato} labeling (**Figure 2.3**). The majority of striatal Pnoc^{tdTomato} neurons did not overlap with any interneuronal markers (dorsal striatum: 92.3% ± 0.5% Pnoc^{tdTomato} only; ventral striatum: 81.0% ± 5.3% Pnoc^{tdTomato} only), a small dorsal striatal population of Pnoc^{tdTomato} neurons overlapped with NPY+/SST+ interneurons (5.2% ± 0.5%), often seen near the borders of striosomal Pnoc^{tdTomato}

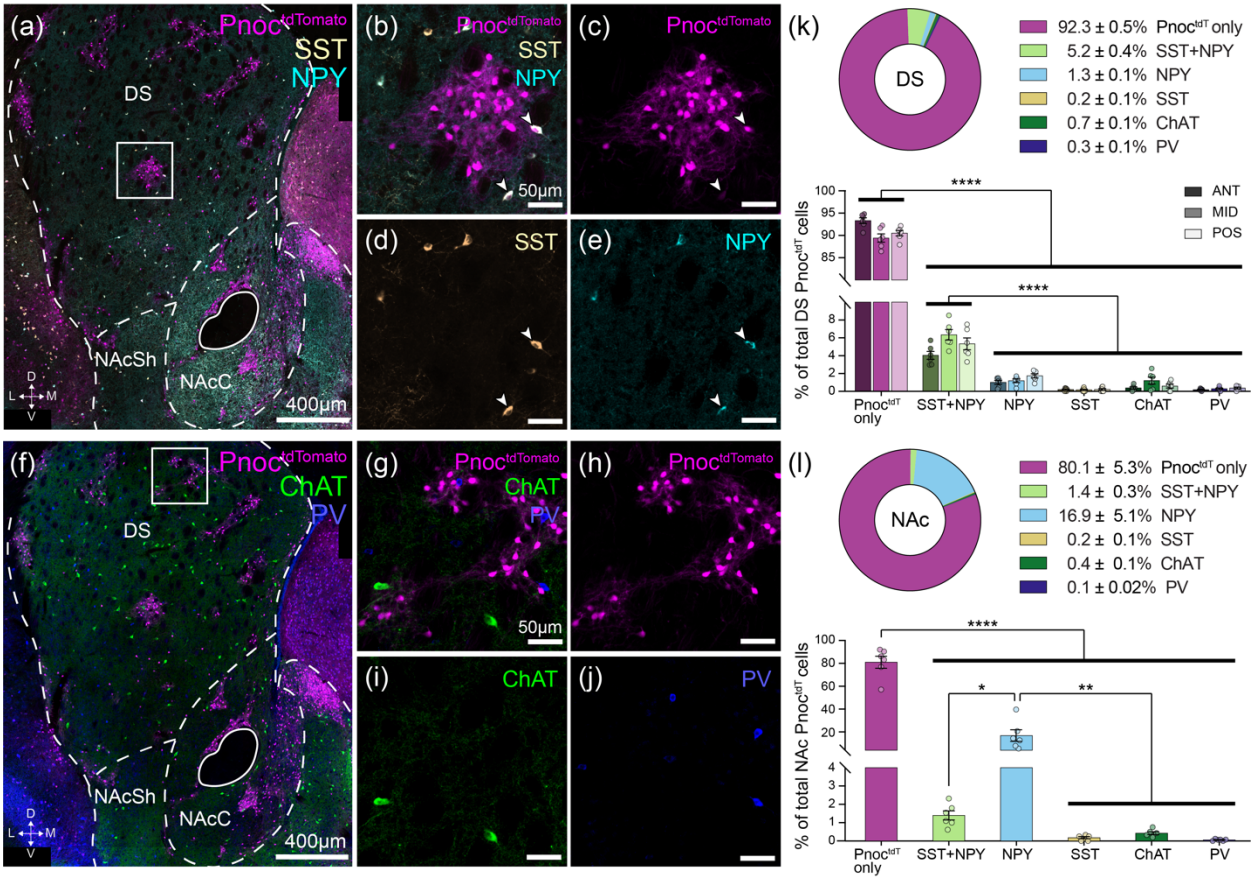

Figure 2.3: Pnoc^{tdTomato} reporter expression marks a population of NPY and SST co-expressing interneurons.

(**a**) Coronal image of Pnoc^{tdTomato} cells (magenta), somatostatin (white, SST), and neuropeptide Y (cyan, NPY) expression in the striatum. Higher magnification images of inset from panel (a) for **(b)** merged and **(c-e)** individual channels showing Pnoc^{tdTomato} (c) colocalization with a subset of striatal interneurons co-expressing SST (d) and NPY (e). **(f-j)** Same organization as (a-e) for additional interneuron markers; Pnoc^{tdTomato} cells (magenta) show little colocalization with choline acetyltransferase (green, ChAT) or parvalbumin (blue, PV) expressing striatal interneurons. **(k)** Top: Summary of quantified Pnoc^{tdTomato} cells colocalized with different interneuron markers in dorsal striatum. Bottom: Quantification of Pnoc^{tdTomato} cells colocalized with different interneuron markers across the anterior to posterior axis in the dorsal striatum (main effect of neuron type, two-way ANOVA, ****$p < 0.0001$; bar graph, two-way ANOVA with Bonferroni's multiple comparisons test, ****$p < 0.0001$, N = 6 mice, 3 sections/mouse.) **(l)** Same as (k) but for nucleus accumbens (bar graph, one-way ANOVA with Bonferroni's multiple comparisons test, ****$p < 0.0001$, **$p < 0.01$, *$p < 0.05$, N = 6 mice, N = 11 sections, 1-2 sections/mouse). All data represented as mean ± SEM across mice. NAcC = nucleus accumbens core; lNAcSh = lateral accumbens shell; mNAcSh = medial accumbens shell. ANT = anterior; MID = medial; POS = posterior.

cell clusters, and a marginally larger subset in the ventral striatum overlapped with NPY+/SST- interneurons (16.9% ± 5.1%) (**Figure 2.3a–e, k, l, Figure S2.4**). In both dorsal and ventral striatum, *Pnoc* reporter expression showed little to no overlap with PV^+ or $ChAT^+$ striatal interneurons (**Figure 2.3f–j**). These $Pnoc^{tdTomato}$ interneuronal expression patterns did not detectably vary across the anterior to posterior striatal axis (**Figure 2.3k**). These multiple findings indicate that striatal $Pnoc^{tdTomato}$ cells primarily overlap with D1-type SPNs and not with striatal interneurons.

2.2.4 Adult, striatal *Pnoc* mRNA levels do not elicit Cre-based recombination

In contrast to the abundant $Pnoc^+$ labeling found throughout the striatum using the tdTomato reporter line, when we instead probed for *Pnoc* mRNA expression using *in situ* hybridization (ISH) we detected surprisingly little *Pnoc* mRNA in adult striatal tissue with no appearance of striosomal patterning (**Figure 2.4a–p**). Indeed, although *Pnoc* levels in reporter-positive (tdT^+) neurons were elevated relative to a negative control (NC) labeled tissue, they were not different from *Pnoc* levels in reporter-negative (tdT^-) neurons (**Figure 2.4q, r**). This puzzling finding suggests that while not nonexistent, *Pnoc* mRNA expression in adult animals is not sufficient to drive *Pnoc* promoter-driven Cre expression required for Cre-dependent recombination of the LSL-tdTomato reporter.

Supporting this, we observed a lack of Cre-dependent recombination in adult tissue following injection of a viral vector encoding a Cre-dependent (DIO-) membrane GFP construct into the dorsal striatum of adult PNOC-Cre mice (**Figure S2.5**). Intriguingly, average *Pnoc* levels in both tdT^+ and tdT^- cells were statistically higher than NC-labeled tdT^+ cells assayed in adjacent brain sections labeled with an NC ISH probe in place of the *Pnoc* probe (**Figure 2.4q, r**). This indicates that there may be low, basal level expression throughout the striatum of the Pnoc gene that is subthreshold to levels required for Cre-dependent recombination. Functional studies will be required to evaluate if there is any physiological relevance of this low-level expression.

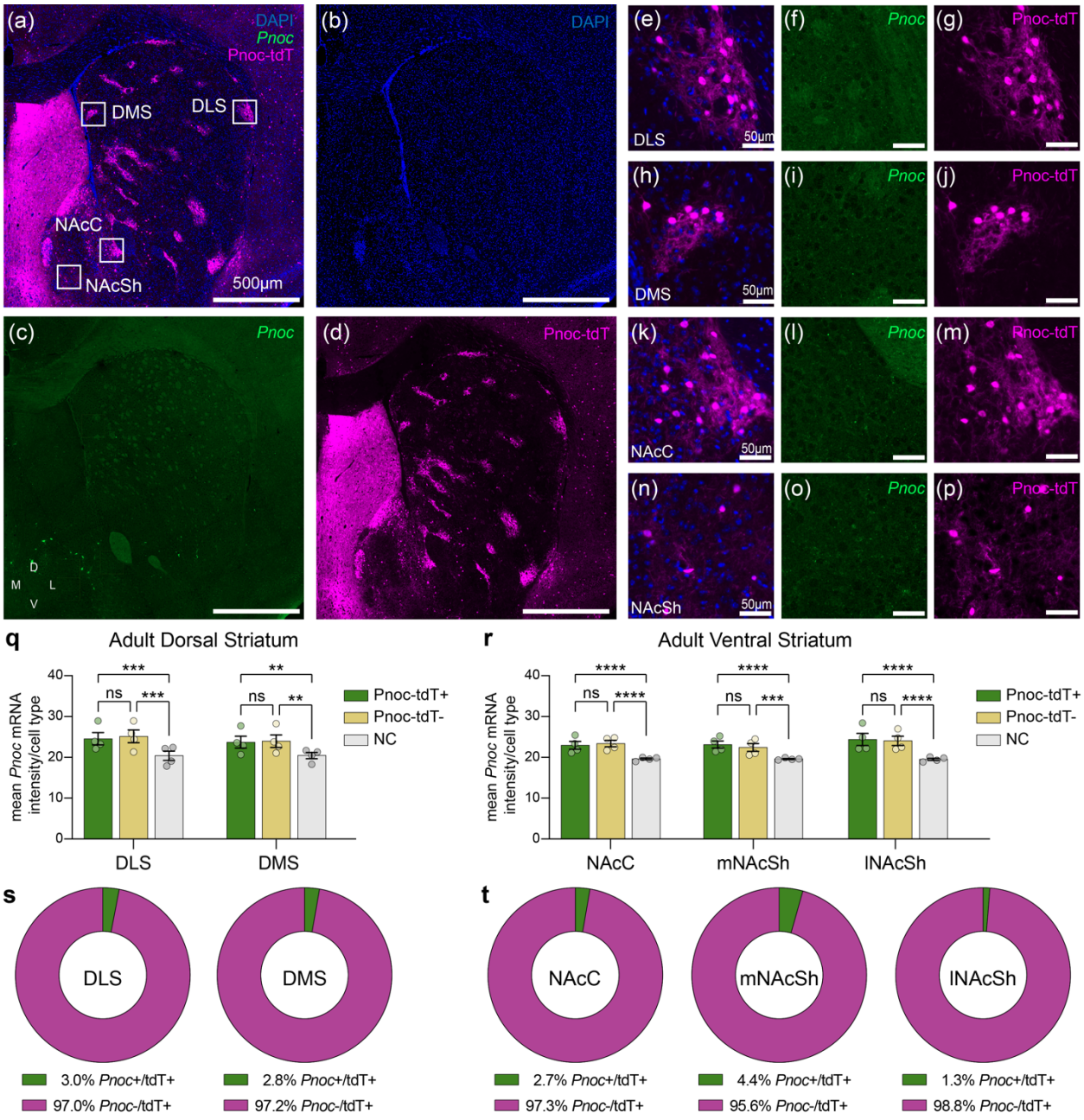

Figure 2.4: Adult expression of striatal *Pnoc* mRNA is sparse relative to reporter-labeled Pnoc^{tdTomato} cells.

(a-d) Coronal image showing composite (a) of DAPI (blue, b), *Pnoc* mRNA expression evaluated by ISH (green, c), and reporter-labeled Pnoc^{tdTomato} cells (magenta, d) in the adult striatum. Magnified insets from the dorsolateral striatum **(e-g)**, dorsomedial striatum **(h-j)**, nucleus accumbens core **(k-m)**, and nucleus accumbens shell **(n-p)** show Pnoc^{tdTomato} reporter-labeled cells that do not co-label with adult *Pnoc* mRNA expression. **(q)** Quantification of mean *Pnoc* mRNA intensity in Pnoc^{tdTomato} cells (tdT^{+}, green), nearby non-reporter labeled cells (tdT^{-}, yellow), and in Pnoc^{tdTomato} cells from adjacent control sections labeled with a negative control probe (NC, gray) in adult dorsal striatum. (two-way ANOVA with Bonferroni's multiple comparisons test, ***p < 0.001, **p < 0.01, ns = non-significant, N = 4 mice, N = 7 sections, 1-2 sections/mouse). **(r)** Same as (q) but for adult ventral striatum (two-way ANOVA with Bonferroni's multiple comparisons test, ****p < 0.0001, ***p < 0.001, ns = non-significant, N = 4 mice, N = 7 sections, 1-2 sections/mouse). **(s)** Proportion of Pnoc^{tdTomato} reporter cells identified as *Pnoc* mRNA

positive (Pnoc$^+$/tdT$^+$, green) or negative (Pnoc$^-$/tdT$^+$, magenta) in adult dorsal striatum. **(t)** same as (s) but for adult ventral striatum. All data represented as mean ± SEM across mice. DLS = dorsolateral striatum; DMS = dorsomedial striatum; NAcC = nucleus accumbens core; mNAcSh = medial accumbens shell; lNAcSh = lateral accumbens shell.

Based on these findings, we also quantified the proportion of striatal Pnoc^{tdTomato} reporter cells that were positive for *Pnoc* mRNA, classifying cells as positive based on *Pnoc* signal levels that outstrip the homogenous "background" labeling seen in tdT$^-$ cells (**Figure 2.4s, t**). Between ~1 and 5% of tdT$^+$ cells were found to be *Pnoc*$^+$ across all striatal subregions (**Figure 2.4s, t).** These results indicate that active *Pnoc* mRNA expression in adult striatal tissue is both markedly low and sparse, occurring at levels insufficient to drive the Cre recombinase expression that induces tdTomato-reporter labeling. Taken together, our findings suggest that the majority of reporter-labeled Pnoc^{tdTomato} neurons in the striatum are representative of transient *Pnoc* gene expression that occurred at an earlier time point.

2.2.5 *Pnoc* mRNA is developmentally expressed in striosomes

In *PNOC-Cre;LSL-tdTomato* reporter animals, Pnoc^{tdTomato} labeling of a given cell is triggered by the earliest sufficient expression of Cre-recombinase in that cell and will persist throughout the lifetime of the mouse. Given this, the discrepancy between the robust Pnoc^{tdTomato} reporter labeling and the dearth of adult *Pnoc* mRNA expression suggested that the *Pnoc* expression in the dorsal striatum could be developmentally regulated, with higher expression levels during embryonic and/or postnatal stages followed by a downregulation of expression as animals reach maturity.

To investigate this possibility, we used ISH to detect *Pnoc* mRNA expression in the striatum of postnatal Day 1 (P1) *PNOC-Cre;LSL-tdTomato* reporter mice (**Figure 2.5**). In contrast to our findings in adult tissue, *Pnoc* mRNA expression in neonatal tissue did recapitulate the reporter-labeled patterning of Pnoc^{tdTomato} cells (**Figure 2.5a–p**). Average *Pnoc* intensity in tdT$^+$ cells across

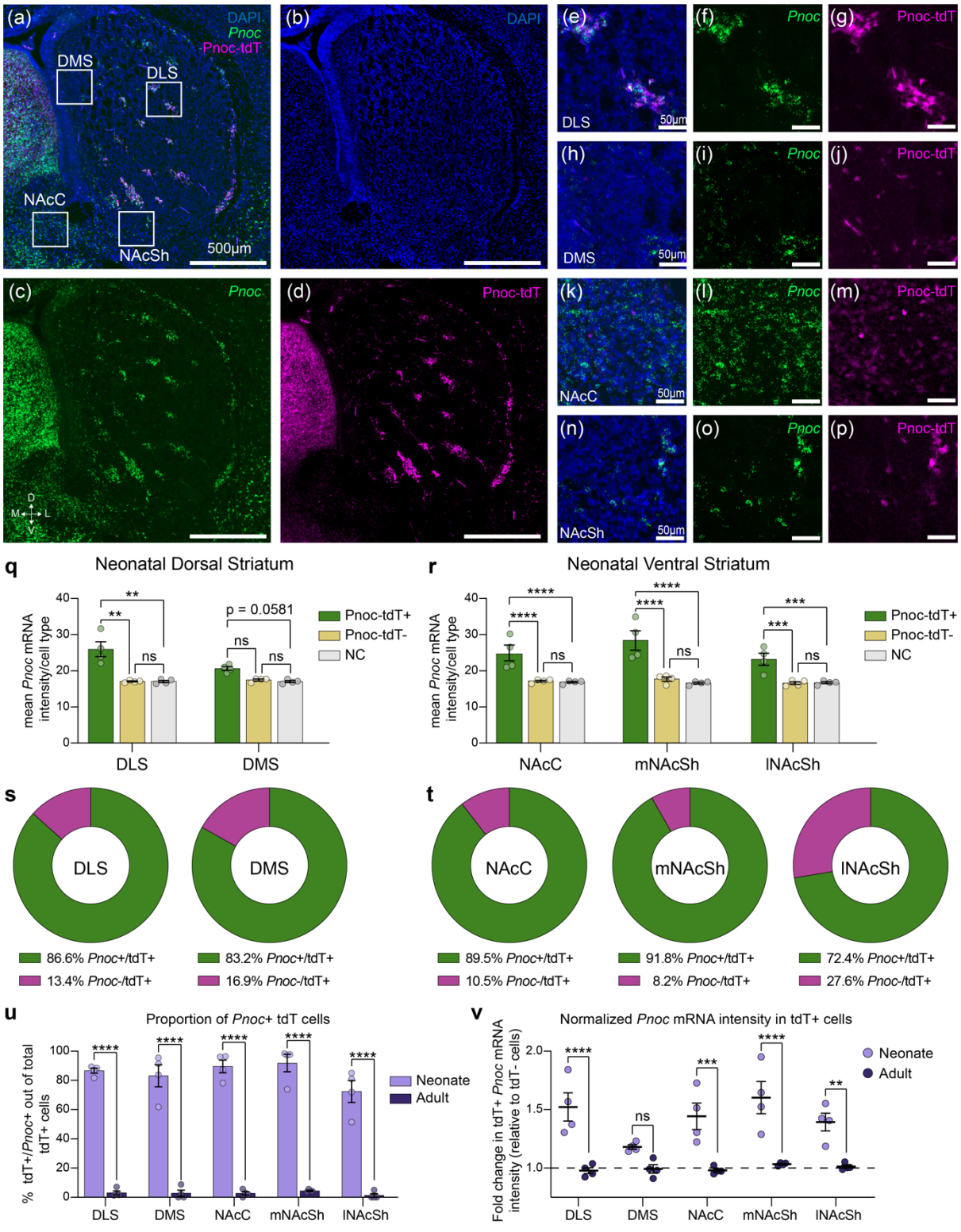

Figure 2.5: Neonatal expression of striatal *Pnoc* mRNA recapitulates reporter-labeled patterning in Pnoc^{tdTomato} cells.

(a-d) Coronal image showing composite (a) of DAPI (blue, b), *Pnoc* mRNA expression evaluated by ISH (green, c), and reporter-labeled Pnoc^{tdTomato} cells (magenta, d) in postnatal day 1 (P1) brain sections. Magnified insets from the dorsolateral striatum (**e-g**), dorsomedial striatum **(h-j),** nucleus accumbens

core **(k-m)** and nucleus accumbens shell **(n-p)** show Pnoc^{tdTomato} reporter-labeled cells co-labeled with neonatal *Pnoc* mRNA expression. **(q)** Quantification of mean *Pnoc* mRNA intensity in Pnoc^{tdTomato} cells (Pnoc-tdT^{+}, green), nearby non-reporter labeled cells (Pnoc-tdT^{-}, yellow), and in Pnoc^{tdTomato} cells from adjacent control sections labeled with a negative control probe (NC, gray) in neonatal dorsal striatum. (two-way ANOVA with Bonferroni's multiple comparisons test, **p < 0.01, ns = non-significant, N = 4 mice, N = 8 sections, 2 sections/mouse). **(r)** Same as (q) but for neonatal ventral striatum (two-way ANOVA with Bonferroni's multiple comparisons test, ****p < 0.0001, ***p < 0.001, ns = non-significant, N = 4 mice, N = 7 sections, 1-2 sections/mouse) **(s)** Proportion of Pnoc^{tdTomato} reporter cells identified as *Pnoc* mRNA positive (Pnoc^{+}/tdT^{+}, green) or negative (Pnoc^{-}/tdT^{+}, magenta) in neonatal dorsal striatum. **(t)** same as (s) but for neonatal ventral striatum. **(u)** Proportion of Pnoc^{tdTomato} reporter cells identified as *Pnoc* mRNA positive in neonate (light purple) vs adult (dark purple) tissue (two-way ANOVA with Bonferroni's multiple comparisons test, ****p < 0.0001, N = 4 mice/group, N = 7 sections, 1-2 sections/mouse). **(v)** Fold-change in mean *Pnoc* mRNA intensity in tdT^{+} cells relative to background (tdT^{-} cells) in neonate (light purple) vs adult (dark purple) tissue (two-way ANOVA with Bonferroni's multiple comparisons test, ****p < 0.0001, *** p < 0.001, ** p < 0.01, ns = non-significant, N = 4 mice/group, N = 7 sections, 1-2 sections/mouse). All data represented as mean ± SEM across mice. DLS = dorsolateral striatum; DMS = dorsomedial striatum; NAcC = nucleus accumbens core; NAcSh = nucleus accumbens shell.

the dorsolateral striatum and all ventral striatal subregions was significantly elevated compared to both nearby tdT^{-} cells and NC-labeled Pnoc^{tdTomato} cells from adjacent sections (**Figure 2.5q, r**). In the dorsomedial striatum, average *Pnoc* intensity in tdT^{+} cells relative to NC controls neared but did not reach statistical significance after averaging across mice (tdT^{+} vs NC p = 0.0581, **Figure 2.5q**). We found that the vast majority (~70–90%) of neonatal Pnoc^{tdTomato} cells were positive for *Pnoc* mRNA expression across all striatal subregions (**Figure 2.5s, t**).

When we compared the proportion of Pnoc^{tdTomato} cells expressing *Pnoc* mRNA in adult vs. neonatal tissue, we found a significantly higher proportion of *Pnoc*$^{+}$ tdTomato-labeled cells in neonates relative to adults across the striatum (neonatal vs. adult percent tdT^{+} cells positive for *Pnoc* p < 0.0001 for all striatal subregions, **Figure 2.5u**). This result is congruent with our hypothesis that striatal *Pnoc* mRNA expression is developmentally enriched. In addition, we compared the intensity of *Pnoc* mRNA expression in tdT^{+} cells relative to background levels (tdT^{-} cells) in adult vs. neonatal tissue, finding that *Pnoc* mRNA intensity in neonatal tdT^{+} cells is elevated relative to adult levels across the dorsolateral and ventral striatum (p < 0.01 for all striatal subregions except DMS, **Figure 2.5v**). In the dorsomedial striatum (DMS), the average, normalized *Pnoc* mRNA intensity did not reach significance in neonatal tissue relative to adults (p

= 0.4174, **Figure 2.5v**). However, there is still a higher proportion of *Pnoc*$^{+}$ cells among tdT^{+} cells (*Pnoc*$^{+}$/tdT^{+}) in neonatal DMS, indicating that *Pnoc* mRNA expression is more abundant in neonatal DMS than in adult DMS. Together, these findings demonstrate that *Pnoc* gene expression in the striatum is generally elevated and more abundant during earlier developmental stages, becoming subsequently downregulated by adulthood.

2.2.6 Pnoc^{tdTomato} neurons in striosomes directly project to dopamine neurons

Striosomal *Drd1* (D1) neurons are unique among striatal SPNs, or nearly so, in their direct innervation of midbrain dopamine neurons, in particular the ventral tier dopamine neurons of the SNc. However, we recently reported that Pnoc^{tdTomato} cells represent ~40% of striosomal *Drd1*$^{+}$ neurons (Lazaridis et al., 2024), and it is not known whether all striosomal D1 neurons forge such a projection. Our identification of Pnoc^{tdTomato} neurons as predominantly overlapping with *Drd1*$^{+}$ SPNs suggests that dorsal striatal Pnoc^{tdTomato} cells might correspond to this projection population. Examining midbrain sections of the Pnoc^{tdTomato} reporter mice, we observed specific innervation of the nigral striosome-dendron bouquets by the labeled axons of Pnoc^{tdTomato} cells (**Figure 2.6a**) both in the adult (**Figure 2.6b–d**) and in early P5 mouse tissue (**Figure 2.6e–g**).

We then established that axons projecting specifically from striosomes account for these bundled fibers entwining themselves with dopamine-containing dendrons, rather than from another source, by injecting a Flp-dependent membrane GFP-expressing AAV vector into dorsal striatum of *PNOC-Cre;loxP-Stop-loxP-FlpO* (Pnoc^{FlpO}) mice (**Figure 2.6h–m**). Again, the striosome-dendron bouquets were innervated by the population of striosomal neurons defined by early *Pnoc* expression. These findings demonstrate that *Pnoc*$^{+}$ striatal neurons comprise a population of dorsal striatal SPNs highly selective to the striosomal compartment, and that these *Pnoc*$^{+}$ neurons forge the specialized striatonigral circuit targeting striosome-dendron bouquets early in development.

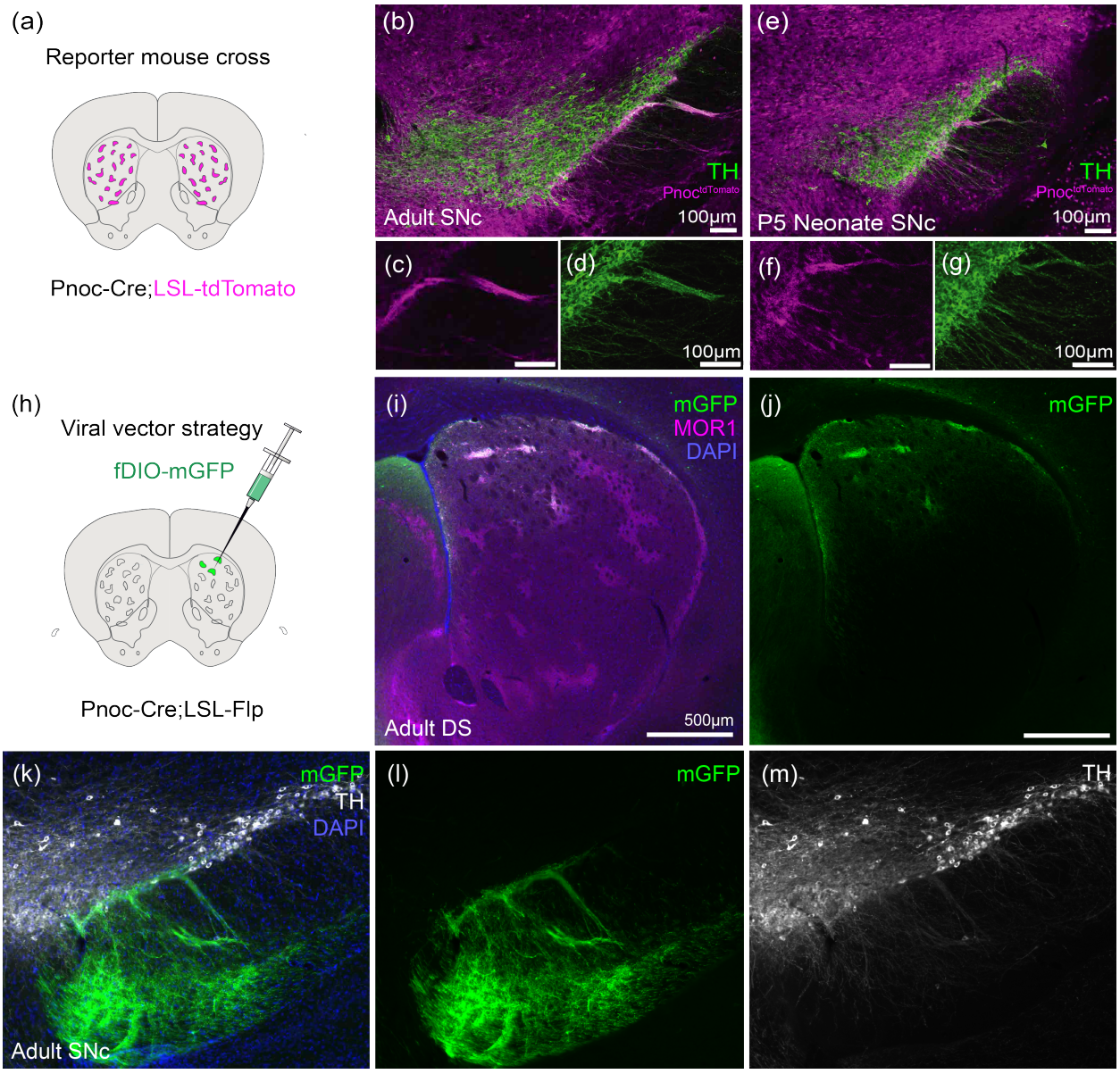

Figure 2.6: Striosomal fibers from Pnoc^{tdTomato} targeted neurons project to the striosome-dendron bouquet in SNc in both adults and neonates.

In Pnoc^{tdTomato} reporter mice **(a)**, tdTomato-labeled fibers (magenta) project to TH-labeled dopamine neurons (green) in adults **(b–d)** and neonates **(e–g)**. **(h)** Schematic of mouse genetic strategy by viral labeling of striosomal cells in *PNOC-Cre;loxP-Stop-loxP-FlpO* mice with a Flp-dependent AAV expressing membrane-GFP (mGFP, green). Virally targeted mGFP-expressing Pnoc^{Flp} neurons (green) **(i, j)** exhibit projections to dopamine (TH, white) dendrons in SNc **(k–m)**.

2.3 Discussion

The N/OFQ system has a demonstrated ability to disrupt the landscape of dopamine signaling with functional consequences relevant to stress and mood regulation, substance use disorder, and Parkinson's disease among others. The striatal circuits and cell types that N/OFQ intersects with to drive these effects have remained poorly defined. Here we lay the groundwork for investigating N/OFQ-mediated striatal contributions to these dopamine-related functions. Our findings reveal an anatomical and molecular organization of *Pnoc* expression primarily in striatal $D1^+$ neurons, indicative of the structure that underlies N/OFQ's functional interactions with striatal-nigral circuitry. We also report dynamic expression in the striatum throughout the development of this opioid neuropeptide ligand known for its modulatory effects on behavior and dopamine function.

We found that $Pnoc^{tdTomato}$ neurons exhibit highly selective striosomal patterning in the dorsal striatum, and within the ventral striatum, we found distinctly concentrated $Pnoc^{tdTomato}$ cell clusters in the core and medial shell, but not in the lateral shell. In particular, we have demonstrated that striosomal $Pnoc^{tdTomato}$ cells in the dorsal striatum largely co-express *Drd1* but not *Drd2*, thereby comprising part of the unique striosomal direct pathway neurons that make direct connections with dopamine-containing neurons via striosome-dendron bouquet structures in the ventral tier SNc (Crittenden et al., 2016; Evans et al., 2020; Matsushima and Graybiel, 2020; Watabe-Uchida et al., 2012).

In the ventral striatum, we highlight a newly identified population of molecularly heterogeneous *Pnoc* neurons with distinct spatial distribution patterns across the nucleus accumbens shell and core and adjoining ventral territories. Drd1 was similarly the leading marker found co-expressed with $Pnoc^{tdTomato}$ neurons in the ventral striatum; however, a significant proportion of $Pnoc^{tdTomato}$ neurons did not overlap with either Drd1 or Drd2 expression in the lateral NAc shell. To determine whether these ventral striatal direct pathway neurons share a circuit motif of dopamine projection with their dorsal striosomal neighbors will require careful mapping of

individual ventral striatal populations. Given the known importance of the ventral striatum for many of the functions for which N/OFQ has been implicated and in which dopamine is involved, we suggest that the afferent and efferent projections of these distinct ventral populations are an important next step in pursuit of evaluating ventral striatal N/OFQ function.

We found Pnoc^{tdTomato} to be a superlative marker of striosomes across development and into maturity, but that this reporter-based patterning is reflective of developmentally transient expression of the *Pnoc* gene that becomes downregulated by adulthood (**Figures 2.4, 2.5, and S2.5**). Such transient developmental expression is reminiscent of a number of striatal genes that exhibit striosomal patterning early in development, including *FoxP2* (Enard, 2011; Fong et al., 2018), *Asc1,* and *Dlx1* (Kelly et al., 2018). Striosomal neurons are born during embryonic days ~10.5–13.5 and lead the migration out into the striatal primordium ahead of the migration of neurons destined for the matrix compartment (Graybiel and Hickey, 1982; Kelly et al., 2018; Lança et al., 1986; Matsushima and Graybiel, 2020). In the course of development, striosomes and matrix exhibit different patterns of neurochemical and mRNA expression (Eblen and Graybiel, 1995; Gokce et al., 2016; Graybiel and Hickey, 1982; Kelly et al., 2018; Lança et al., 1986; Märtin et al., 2019; Matsushima and Graybiel, 2020; Saunders et al., 2018) and develop distinct efferent and afferent patterns of connectivity. Striosomal neurons are more connected with limbic regions than are neurons of the matrix; they receive enriched inputs from limbic regions of the cortex, the bed nucleus of the stria terminalis, and the amygdala as well as providing the main source of striatal projections to midbrain dopamine neurons (Crittenden et al., 2016; Crittenden and Graybiel, 2011; Graybiel and Matsushima, 2023; Lee et al., 2024; Ragsdale and Graybiel, 1988; Smith et al., 2016; Watabe-Uchida et al., 2012).

Due to concerns surrounding the selectivity of opioid antibodies and the widely known challenges associated in particular with labeling neuropeptides in fixed tissue (Liu et al., 1991), we instead utilized detection methods that probe for *Pnoc* gene expression. It is important to note however that mRNA transcript expression does not necessarily equate to presence of the fully

processed N/OFQ peptide. While the proteolytic processing of the precursor peptide pronociceptin is not entirely known, the enzyme prohormone convertase 2 (PC2), which is central to this process for many neuropeptides including the other opioid peptides, has been shown to metabolize pronociceptin into N/OFQ (Allen et al., 2001). PC2 is abundantly present across the dorsal striatum and nucleus accumbens in both D1 and D2 SPNs (Montalban et al., 2022), so it is certainly plausible that functional N/OFQ peptide can be generated throughout the striatum. Still, this is a limitation of the current study and an important consideration for the interpretation of our findings.

Striatonigral N/OFQ signaling could play a role in the development of the striosome-dendron bouquet circuit. Studies following the discovery of N/OFQ showed that high levels of *Pnoc* transcript in undifferentiated neural cells are accompanied by neurite outgrowth (Saito et al., 1997, 1996, 1995; Zaveri et al., 2006). N/OFQ signaling also activates the master transcriptional regulator, NFκB, important in the regulation of genes involved in synaptic plasticity, memory formation, cognition, development, and neuronal survival (Donica et al., 2011; Levenson et al., 2006). In addition, N/OFQ modulates immune factors such as TNFα and IL-6 (Fu et al., 2007), crucial to the formation and maintenance of neural circuit development and synaptic plasticity (Boulanger, 2009). Our finding of robust *Pnoc* expression selectively in striosomal direct pathway neurons slated for dopaminergic interconnection opens the door for evaluation of how these genetic and immune interactions unfold in a circuit of wide functional and pathological consequences. Still to be determined is the impact on the striatonigral circuitry of developmental perturbations of *Pnoc* expression.

The potential for the development of circuit vulnerabilities and dysfunction through the mis-wiring of striosomal neurons with the dopamine system is evident from the nature of those neurons with which striosomes form interconnections. Here, we show that the striosomal neurons that developmentally expressed *Pnoc* directly innervate vSNc dopamine neurons (**Figure 2.6**). The dopamine neurons of the vSNc, which are the recipient neurons of these striosomal-dendron

bouquet axons, carry particular susceptibility to degeneration in Parkinson's disease (Damier et al., 1999; Giguère et al., 2018; Kordower et al., 2013; Mendez et al., 2005; Pereira Luppi et al., 2021; Yamada et al., 1990). More widely, the cortico-striosome-dopamine circuit is implicated in mood regulation and dysregulation as striosomes are differentially implicated from surrounding matrix in reinforcement-related updating paradigms (Bloem et al., 2022, 2017; Yoshizawa et al., 2018), and, in particular, in influencing cost-benefit conflict decision-making in both rodents (Friedman et al., 2020, 2017, 2015) as well as non-human primates (Amemori and Graybiel, 2012; Amemori et al., 2018, 2021, 2020). These findings have also been extended to human patient populations (Ironside et al., 2020; Pedersen et al., 2021; Rolle et al., 2021). These studies suggest circuits to study for a mechanistic understanding of how the cortico-striato-nigral circuit, and the nigro-striato-nigral loop, operate in dopamine regulation in the context of such disorders. As a result of its modulation of dopamine, the N/OFQ system has attracted interest as a therapeutic target for modulating dopamine in both Parkinson's disease, substance use disorder, and mood regulation (Gavioli and Calo', 2013; Lambert, 2008; Post et al., 2016; Witkin et al., 2019; Zaveri, 2011), including in alleviation of depressive symptoms resulting from developmental inflammatory insults arising from maternal immune activation (Medeiros et al., 2015). Our findings point to the value of further work on this developmental impact.

2.4 Methods

Mouse lines and husbandry

All animal procedures were approved by the Committee on Animal Care at the Massachusetts Institute of Technology, were performed in accordance with the U.S. National Research Council Guide for the Care and Use of Laboratory Animals were maintained under conditions of constant temperature (25°C) and humidity (50%), and a 12:12 h light/dark cycle. The following mouse strains were used for behavioral, neural recording and histological experiments: PNOC-Cre (Parker et al., 2019), Ai14 (Madisen et al., 2010), and LSL-Flpo (He et al., 2016). We crossed

PNOC-Cre mice on a C57BL/6J background (Jackson Laboratory) to the Cre-dependent Ai14 (LSL-tdTomato reporter line) or Cre-dependent LSL-Flpo line on FVB background (Taconic Biosciences) corrected for behavioral optimization. Consequently, F1 hybrid mice are produced to suit behavioral characterization (Menalled and Brunner, 2014), avoiding the early hearing loss of the C57BL/6J mouse strain and poor vision of the FVB strain.

Surgical preparations of stereotactic striatal injections

All surgeries were performed on adult mice over 8 weeks of age. Animals were anesthetized briefly with 5% isoflurane and maintained at 1-2% throughout the surgery. For intrastriatal delivery of viral vectors, PNOC-Cre or *PNOC-Cre; LSL-Flp* mice were injected unilaterally with AAVs packaging Cre- or Flp-dependent membrane-GFP and synaptophysin-mRuby constructs (AAV2/8 vector packaging hSyn-DIO-mGFP-T2A-Synaptophysin-mRuby and hSyn-FDIO-mGFP-T2A-Synaptophysin-mRuby; Biohippo, Gaithersburg, MD) targeting the anterior dorsal striatum. All viruses were injected at a rate of 100 nL/min. Injection coordinates empirically optimized for F1 hybrid C57BL/6J x FVB mice were based on for ages <6 months: AP: +1.1 mm; ML: ± 1.7 mm; DV: 2.0 mm from brain surface.

Histological labeling of brain tissue

Animals were transcardially perfused with a phosphate buffered saline solution (PBS) followed by 4% paraformaldehyde in PBS. Extracted brains were soaked in the paraformaldehyde solution for 24 hours and then maintained in 30% sucrose in PBS at 4°C for cryoprotection. After 24 hours, brains were frozen in dry ice and stored at -80°C. A sliding microtome was used to cut 30-µm thick sagittal or coronal sections from the brains of the adults, and 54µm-thick coronal sections from the brains of P1 to P20 mice. Sections were stored at 4°C in 0.02% sodium azide in 0.1 M PB ahead of preparation for immunofluorescence staining. For fluorescent *in situ* hybridization (FISH), 10-µm thick coronal sections were cut from adult mouse brains and 18-µm thick coronal

sections were cut from the P1 to P20 mouse brains. Sections were mounted on slide and stored at -80°C until use.

For immunofluorescence (IF) staining, sections were rinsed 3 times for 10 min in PBS with 0.2% Triton X-100 (Tx), then blocked with tyramide signal amplification (TSA) blocking solution (Akoya Bioscience FP1012) for 20 min at room temperature, and then incubated with primary antibodies (**Table 2.1)** diluted in TSA blocking solution for 48-72 hours at 4°C. Sections were again rinsed with PBS-Tx for 3 × 10 min, and were incubated with fluorescent conjugated secondary antibodies (**Table 2.1**) for 2 hours at room temperature. Sections were rinsed with PB for 10 minutes, then counterstained with DAPI solution diluted in PB for 2 minutes. After rinsing in PB for 3 times, sections were mounted with ProLong Gold and stored at 4°C until imaging. For FISH, RNAscope Multiplex Fluorescent Reagent Kit (Cat. 320850; Advanced Cell Diagnostics (ACD), Hayward, CA) and manufacturer's protocols were used. For neonatal and adult tissue, Multiplex Fluorescent Detection Reagents kit V2 (Cat. 323110; Advanced Cell Diagnostics (ACD), Hayward, CA) was used and manufacturer's protocols were followed. Probes used in this study are shown in **Table 2.2** with the combination of channels 1 to 3. For IF-FISH co-staining, RNase-free blocking reagent and Co-detection Target Retrieval Reagents from RNA-Protein Co-detection Ancillary Kit (Cat No. 323180, ACD) were used.

Image analysis

Images were collected on a confocal TissueFAXs SL slide scanner (TissueGnostics) and were exported in tiff format. For the IF-FISH co-staining experiment, images were collected on the Epifluorescent TissueFAXs slide scanner (TissueGnostics) after IF staining (image set 1), then images were collected again following FISH (image set 2). These two image sets were exported in tiff format, then registered by the ImageJ plugin, StackRegJ (Stowers Institute for Medical Research). Registered images were then evaluated using ImageJ (FIJI), QuPath (Bankhead et al., 2017) or HALO image analysis software (IndicaLabs).

For detection and classification of cells and colocalization with cell type markers, QuPath software was used to annotate striatal subregions, and the cell detection module used to detect cells based on tdTomato signal or nuclear signals NeuN or DAPI. Detections were visually inspected and corrected for missed or false positive detections and measurements collected for mean intensity values and classification for each detection in each annotated subregion in each brain section. For classification of cell type, the QuPath classifier module was used to establish thresholds based on average intensity values of each marker for classifying cells for one or multiple probe and/or antibody labels. For adult and neonatal quantification, of *Pnoc* ISH labeling was evaluated in Pnoc-tdTomato positive and tdTomato-negative cells and in negative control section tdTomato positive cells treated identically and simultaneously but labeled with an ISH probe against soil in place of the *Pnoc* probe. Neonatal and adult tissue require different histological processing due to differences in tissue density, and mean probe intensity values cannot be directly compared between adult and neonatal sections. Negative control labeling was done to draw comparisons between the tissues by allowing for normalization and thresholding purposes.

Statistical analyses

Statistical analyses were performed as indicated using GraphPad Prism version 10.0.0 for Windows, GraphPad Software, Boston, Massachusetts USA, www.graphpad.com. All data are expressed as mean ± SEM.

2.5 Acknowledgements

We thank Sophia Robertson for assistance with histological cell counting. We thank Diego Pizzagalli for comments on the manuscript. This research was supported by NIH/NIMH P50 MH119467 (Project 3 to AMG; Project 4 to MRB), NIH/NIMH R01 MH060379 (AMG), NIH/NIMH F31 F31DA059438-01A1 (CS), Saks-Kavanaugh Foundation (AMG), Hock E. Tan and K. Lisa

Yang Center for Autism Research (AMG), Mallinckrodt Foundation (MRB), Simons Foundation grant to the Simons Center for the Social Brain at MIT (AMG).

2.6 Author Contributions

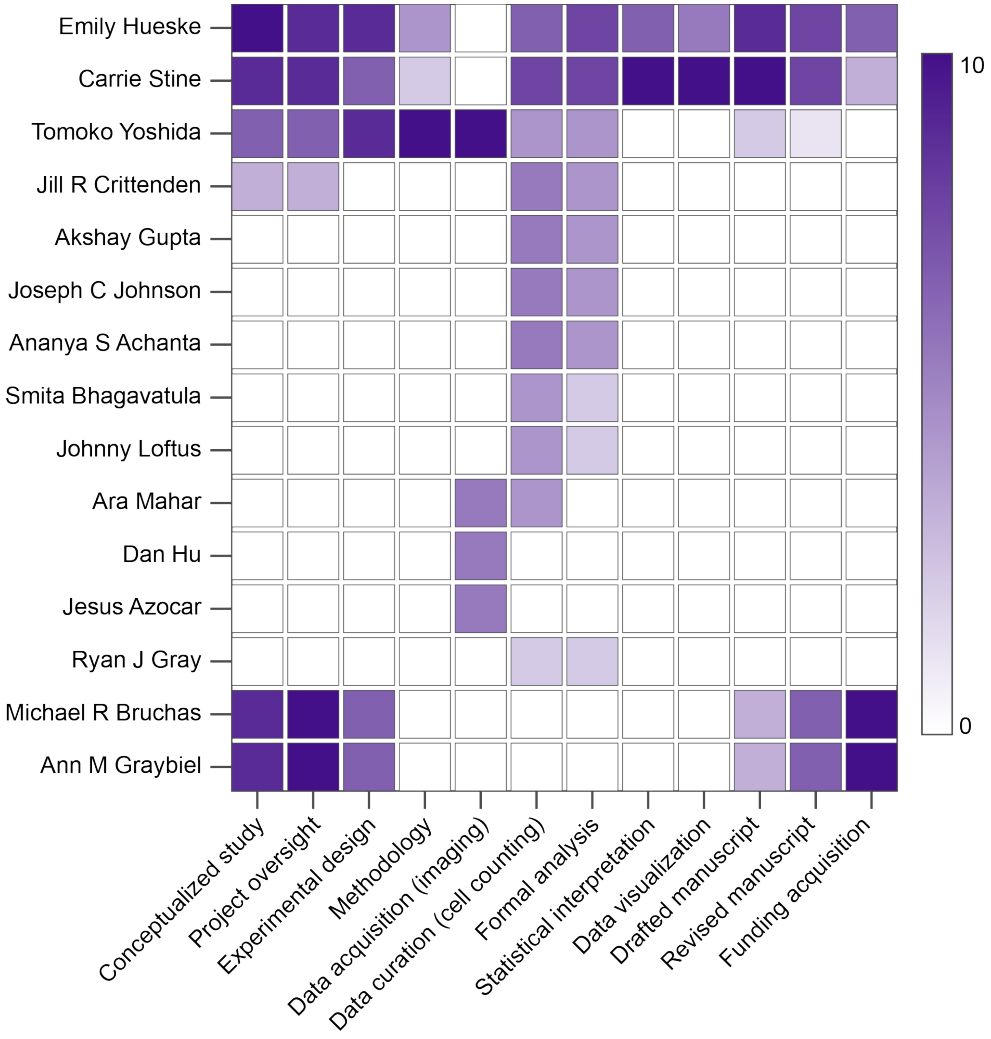

2.7 Tables

Table 2.1: Antibodies used in Chapter 2

Antibodies	Source	Catalog #	RRID
Polyclonal chicken anti-GFP	Abcam	ab13970	AB_300798
Monoclonal rat anti-mCherry	Invitrogen	M11217	AB_2536611
Monoclonal rabbit anti-MOR1	Abcam	ab134054	AB_3122135

Polyclonal rabbit anti-TH	Abcam	ab112	AB_297840
Monoclonal rat anti-somatostatin	Millipore	MAB354	AB_2255365
Polyclonal rabbit anti-neuropeptide Y	Abcam	ab221145	AB_2894872
Polyclonal guinea pig anti-PV	Synaptic Systems	195004	AB_2156476
Polyclonal goat anti-ChAT	Millipore	AB144P	AB_2079751
Goat anti-chicken IgY, Alexa Fluor 488	Invitrogen	A-11039	AB_2534096
Goat anti-rat IgG, Alexa Fluor 546	Invitrogen	A-11081	AB_2534125
Goat anti-rabbit IgG, Alexa Fluor 647	Invitrogen	A-21245	AB_2535813
Donkey anti- guinea pig IgG, DyLight 405	Jackson ImmunoResearch	706-475-148	AB_2340470
Donkey anti-goat IgG, Alexa Fluor 488	Invitrogen	A-11055	AB_2534102
Donkey anti-rat IgG, Alexa Fluor 647	Invitrogen	A78947	AB_2910635
Donkey anti-rabbit IgG, Biotin	Invitrogen	A16039	AB_2534713
Streptavidin, Alexa Fluor 750	Invitrogen	S21384	N/A

Table 2.2: *In situ* hybridization probes used in Chapter 2

Probe name	Source	Catalog # of Channel 1
Mm-Drd1a	Advanced cell diagnostics	406491
Mm-Drd2	Advanced cell diagnostics	406501
Mm-Pnoc	Advanced cell diagnostics	437881
tdTomato	Advanced cell diagnostics	317041
Mm-Oprm1	Advanced cell diagnostics	315841
Mm-Lypd1	Advanced cell diagnostics	318361
Negative control probe	Advanced cell diagnostics	320871

CHAPTER 3: Development of a genetically encoded opioid peptide sensor for *in vivo* detection of endogenous nociceptin release.

This chapter includes results and figures adapted from the following manuscript:

> Zhou X[#], **Stine C[*,#]**, Oliveira Prada P, Fusca D, Assoumou K, Dernic J, Bhat MA, Achanta AS, Johnson JC, Pasqualini AL, Jadhav S, Bauder CA, Steuernagel L, Ravotto L, Benke D, Weber B, Suko A, Palmiter RD, Stoeber M, Kloppenburg P, Brüning JC, Bruchas MR, Patriarchi T. Development of a genetically encoded sensor for probing endogenous nociceptin opioid peptide release. ***Nature Communications***. June 25, 2024. doi.org/10.1038/s41467-024-49712-0
> [#]*These authors contributed equally*

3.1 Introduction

A major factor hindering a clearer understanding of N/OFQ regulation of neural circuits is the limitations imposed by current tools and techniques used to detect the release of neuropeptides in living systems. Conventional techniques such as microdialysis and mass spectrometry-coupled high-performance liquid chromatography can successfully detect picomolar level of neuropeptides in extracellular fluid (Al-Hasani et al., 2018), yet the spatial and temporal resolution of these techniques is limited to single point measurements and long timescales on the order of minutes (Jaquins-Gerstl and Michael, 2015). This temporal and spatial resolution is low for decoding the neuronal mechanisms of dynamic peptide action *in vivo*, particularly alongside other neurophysiological methods. New approaches to probe the nervous system using fluorescent sensors have started to gain traction across the field (Labouesse and Patriarchi, 2021; Ravotto et al., 2020; Sabatini and Tian, 2020; Wu et al., 2023, 2022). Combined with rapidly developing fluorescent recording and imaging techniques, these sensor-based approaches are uniquely suited for *in vivo* observations with finer spatiotemporal resolution than was previously possible (Patriarchi et al., 2018; Sun et al., 2018; Wu et al., 2022).

Here we report the development and characterization of NOPLight, a genetically encoded opioid peptide sensor that provides a selective and sensitive fluorescent readout of endogenous

N/OFQ dynamics with high temporal resolution both *ex vivo* and *in vivo*. Using the sensor, we could detect ligand binding by systemically administered NOPR agonists and antagonists within the central nervous system. We also measured both chemogenetically-evoked and behaviorally induced dynamics of endogenous N/OFQ in freely moving mice. Thus, NOPLight extends the neuropeptide molecular toolbox necessary to investigate the physiology of neuropeptides and in particular this important endogenous opioid system with high resolution.

3.2 Results

3.2.1 Development of a genetically encoded N/OFQ opioid peptide sensor

To develop a fluorescent sensor for N/OFQ, we started by designing a prototype sensor based on the human NOPR, which has 93-94% sequence identity to the mouse and rat receptors. We replaced the third intracellular loop (ICL3) of human NOPR with a circularly-permuted green fluorescent protein (cpGFP) module that was previously optimized during the development of the dLight1 family of dopamine sensors (Patriarchi et al., 2018) (**Figures 3.1a and S3.1a**). This initial construct exhibited poor membrane expression and no fluorescent response to N/OFQ (**Figure S3.1b**). Given the pivotal role of the GPCR C-terminus in trafficking (Bockaert et al., 2003), we reasoned that replacement of the NOPR C-terminus with that of another opioid receptor may facilitate membrane targeting of the sensor. Based on our prior experience (Patriarchi et al., 2018), we chose to use the C-terminus from the kappa-type opioid receptor. The resulting chimeric receptor showed improved expression at cell surface but still exhibited only a small response to N/OFQ (**Figure S3.1b**).

We then aimed to improve the dynamic range of the sensor through mutagenesis efforts. First, we elongated the N-terminal cpGFP linker with additional amino acids originating from dLight1 (Patriarchi et al., 2018). This led to the identification of a variant with a fluorescent response ($\Delta F/F_0$) of approximately 100% (**Figure S3.1c, d**). Prior work demonstrated that sequence variations in the second intracellular loop (ICL2) of the sensor can effectively be used

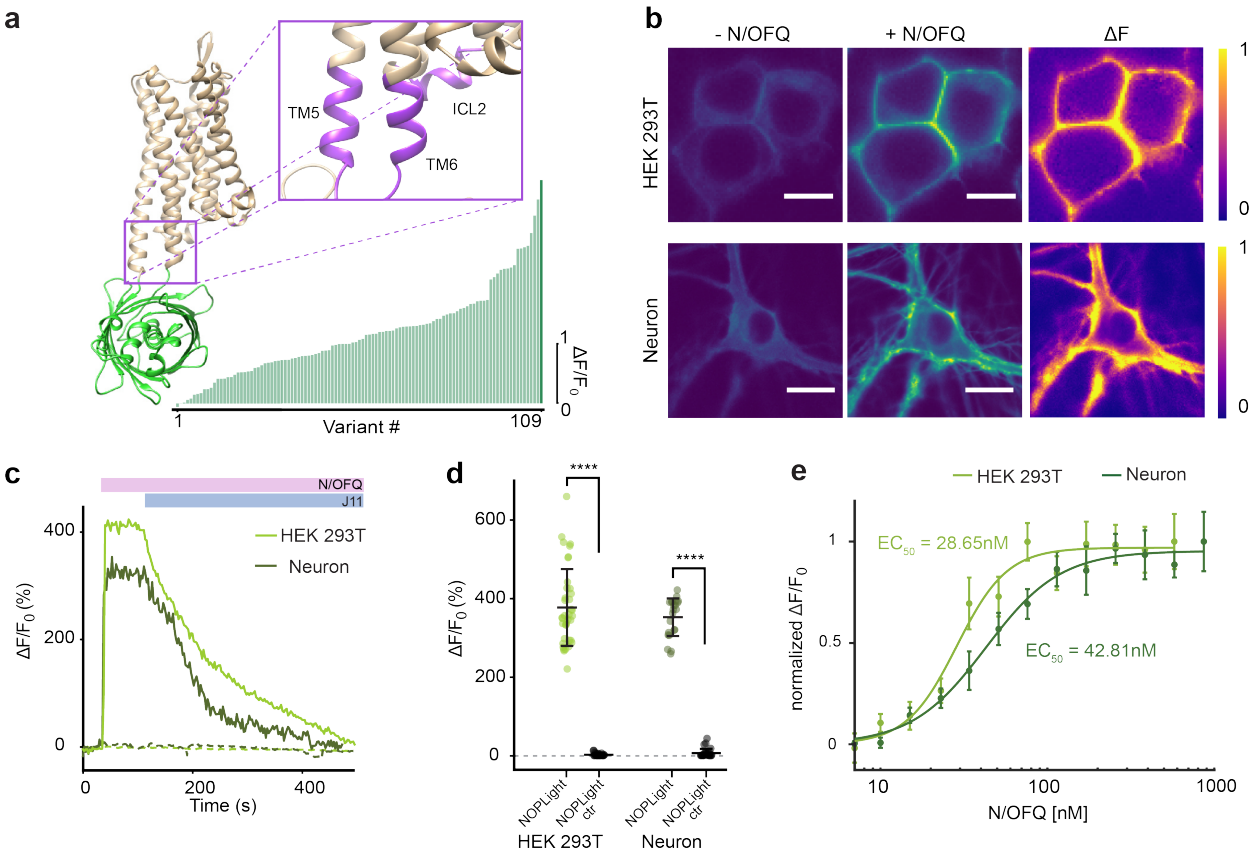

Figure 3.1: Development of NOPLight, a genetically encoded N/OFQ sensor.

(a) Structural model of NOPLight and screening summary. $n \geq 3$ cells per variant. **(b)** Representative images of HEK293T cells (top; scale bars, 10 µm) and neurons (bottom; scale bars, 20 µm) expressing NOPLight before and after application of 1 µM N/OFQ and ΔF heat map. **(c)** Responses of NOPLight or NOPLight-ctr in HEK293T cell and neurons to 1 µM N/OFQ, followed by competition with 10 µM J-113397. **(d)** Quantification of maximal responses from (**c**), N = 38, 30, 22, 27 cells from three independent experiments, respectively. Data shown as mean ± SD. (One-sided Mann–Whitney *U*-test, ****$P < 0.0001$, $P = 1.003 \times 10^{-12}$, and 1.262×10^{-9} for NOPLight versus NOPLight-ctr in HEK293T and neurons). **(e)** Normalized response of HEK293T cells and neurons expressing NOPLight to N/OFQ titrations (mean ± SD) fitted with three-parameter Hill equation. N = 3 independent experiments per concentration.

to modulate sensor response (Kagiampaki et al., 2023; Patriarchi et al., 2018). Thus, as a next step, we performed targeted mutagenesis focusing on the ICL2 of the sensor. Through these efforts we identified a beneficial mutation ($I156^{34.51}K$, **Figure S3.1e**) that was then carried forward onto the next rounds of screening, which focused on receptor and cpGFP residues around the insertion site of the fluorescent protein between transmembrane helixes 5/6 (TM5/TM6) (**Figure S3.1e**). The final variant, which we named NOPLight, had a $\Delta F/F_0$ of 388% in transfected HEK293T cells and a similar performance in transduced neuron culture ($\Delta F/F_0$ = 378%) upon activation by the high affinity, full agonist N/OFQ (**Figure 3.1b**). Furthermore, the evoked fluorescent signal could be reversed to baseline levels using the selective and competitive small molecule NOPR antagonist J-113397 (**Figure 3.1c**).

To aid in subsequent characterization experiments we also developed a control sensor, NOPLight-ctr, by mutating into alanine two key residues ($D110^{2.63}$, $D130^{3.32}$) located in the binding pocket of NOPR (Thompson et al., 2012) (**Figure S3.2a**). The control sensor was well expressed on the surface of HEK293T cells and neurons but showed negligible fluorescent response to N/OFQ (**Figures 3.1c, d, and S3.2a**) and a panel of other endogenous opioids and fast neurotransmitters, including dopamine, acetylcholine and GABA. (**Figure S3.2b**).

We characterized the apparent ligand affinity of NOPLight *in vitro* using NOPLight-expressing HEK293T cells and cultured neurons. In HEK293T cells, the endogenous ligand N/OFQ elicited a fluorescent response of NOPLight at a half maximal effective concentration (EC_{50}) of 28.65 ± 5.1 nM (pEC_{50} = 7.54), whereas in cultured neurons it showed an EC_{50} of 42.81 ± 5.4 nM (pEC_{50} = 7.37) (Fig. 1e), approximately one order of magnitude lower than the reported potency of N/OFQ to the wild type NOPR in the central nervous system (Malfacini et al., 2015).

3.2.2 *In vitro* characterization of NOPLight

We next sought to better examine the pharmacological and kinetic properties of the sensor. To determine the activation kinetics of NOPLight, we measured activation of NOPLight upon direct

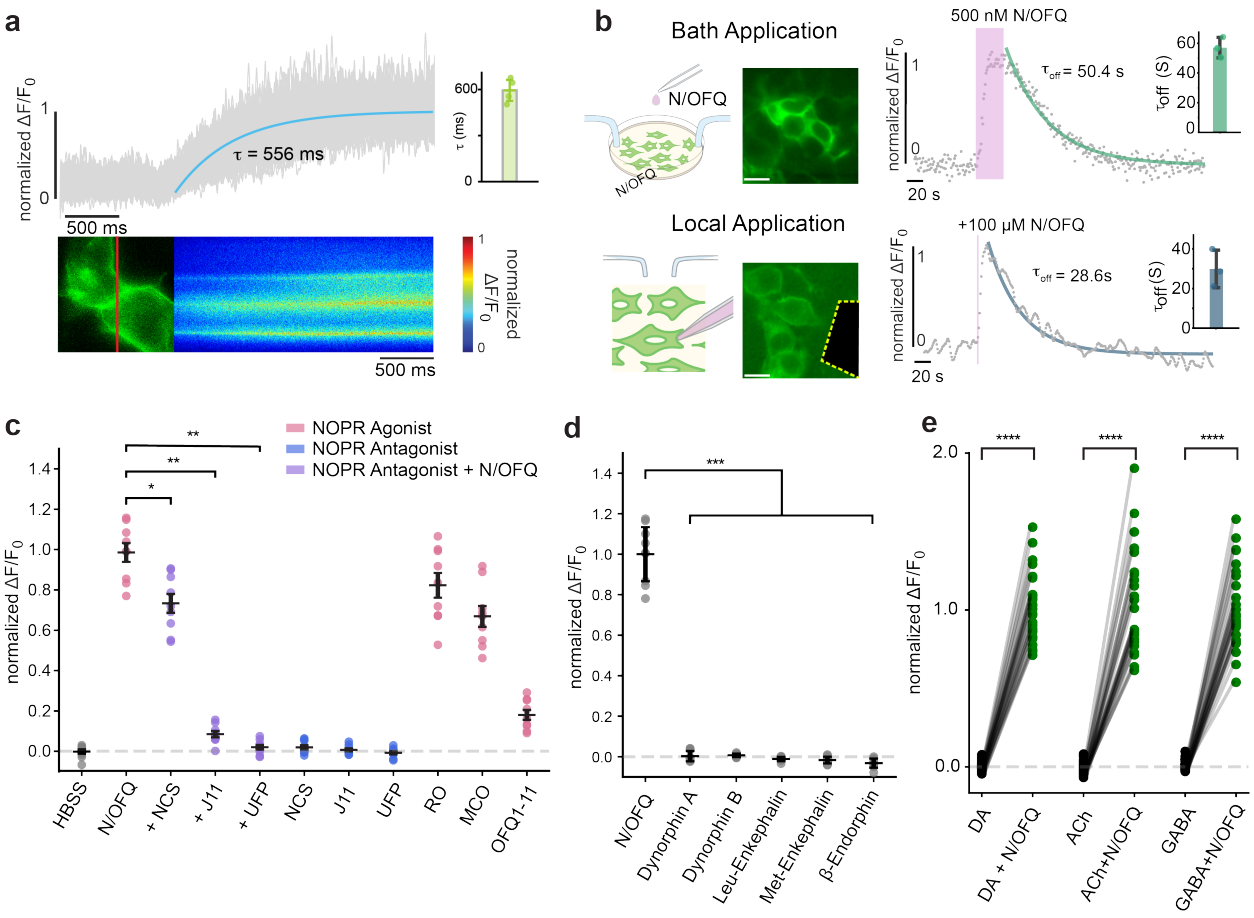

Figure 3.2: *In vitro* characterization of NOPLight.

(a) Line-scan time plot of NOPLight $\Delta F/F_0$ (gray) from membrane-pixels shown in bottom. Right, quantification of time constant (τ) from four independent experiments. Data represented as mean ± SD. **(b)** Left: experimental schematics and images (scale bars, 20 μm), right: time plot of normalized $\Delta F/F_0$ from a representative experiment (gray) with quantified time constant (τ_{off}). Data represented as mean ± SD. **(c)** Maximal NOPLight response to: NCS, Nocistatin; J11, J-113397; UFP, UFP-101; RO, RO 64-6198; MCO, MCOPPB; OFQ1-11, Orphanin-FQ (1–11)). $^*P < 0.05$, $^{**}P < 0.01$, $P = 0.024$, Nocistatin; 0.0012, J-113397; 0.0012, UFP-101. $n = 9$ cells except MCO (N = 8) from three independent experiments. **(d)** Maximal NOPLight response to endogenous opioid ligands (1 μM). $^{**}P < 0.01$, $P = 0.003$, Dynorphin A; $P = 0.003$, Dynorphin-B; $P = 0.003$, Leu-Enkephalin; $P = 0.003$, Met-Enkephalin; $P = 0.003$, β-endorphin. N = 9 from three independent experiments. Statistical comparisons in (**c**, **d**) by one-sided pairwise Mann–Whitney rank test with post hoc Bonferroni correction, data represented as mean ± SEM. **(e)** NOPLight response to neurotransmitters (DA dopamine, ACh acetylcholine, GABA gamma-Aminobutyric, all 1 mM). $n = 29$ (DA) or 30 (ACh, GABA) cells from three independent experiments (two-sided paired *t*-test, $^{****}P < 0.0001$, $P = 2.45 \times 10^{-22}$, 7.46×10^{-19}, and 7.82×10^{-21}, respectively).

bath-application of N/OFQ using high-speed line-scan confocal imaging. Mono-exponential fitting of NOPLight fluorescent response indicated a subsecond time constant of signal activation at the sensor (τ_{ON} = 595 ± 69 ms; **Figure 3.2a**). To determine the off kinetics of the sensor, we performed experiments on cells under constant bath-perfusion. Depending on the experimental set-up, the fluorescence response of NOPLight elicited by N/OFQ application returned to baseline with a τ_{off} of 57.1 ± 6.9 s for bath application and 29.9 ± 9.5 s for localized puff application of the ligand (**Figure 3.2b**).

We also characterized the pharmacological profile of NOPLight *in vitro*. We tested the response of NOPLight-expressing HEK293T cells to a panel of small-molecule and peptide ligands that are known NOPR agonists or antagonists (**Figure 3.2c–e**). Of the antagonist compounds tested, the antagonist peptide UFP-101 and the small molecule compound J-113397 produced robust competitive antagonism, fully reversing the activation of NOPLight at the concentrations used (1 μM), while nocistatin elicited a smaller decrease of the signal induced by N/OFQ. Importantly, none of the antagonistic ligands elicited a noticeable fluorescent response when applied alone to sensor-expressing cells. On the other hand, we could clearly detect positive fluorescent responses of NOPLight to several types of selective NOPR agonist compounds. In particular, the full agonist RO 64-6198 (RO) elicited the largest fluorescent response in this assay ($\Delta F/F_0$ = 323%) and produced a response of similarly large magnitude in NOPLight-expressing primary neuronal cultures ($\Delta F/F_0$ = 221%) (**Figure S3.2c–f**). Interestingly, all of the agonist compounds tested induced an overall smaller fluorescence response than N/OFQ itself, when applied at the same concentration (**Figure 3.2c**).

We then characterized the spectral properties of NOPLight and NOPLight-ctr. Under both one-photon and two-photon illumination, NOPLight exhibited similar spectral characteristics as other GPCR-based sensors (Duffet et al., 2022; Patriarchi et al., 2018). The sensor had an isosbestic point at around 440 nm, and peak performance, measured as the ratio between N/OFQ bound versus unbound state, at 472 nm and 920/990 nm, respectively (**Figure S3.3a, b**). When

tested with the NOPR agonist RO 64-6198, the sensor exhibited similar one-photon spectral properties, whereas the control sensor showed little difference in excitation and emission in the presence or absence of the ligands (**Figure S3.3a**).

The wild-type receptor of NOPLight, NOPR, is known to respond highly selectively to N/OFQ, as compared to all other endogenous opioid peptides (Donica et al., 2013; Wang et al., 2023). To ensure that NOPLight retained a similar degree of ligand-selectivity, we tested its response to a series of opioid peptides applied to NOPLight-expressing cells at a high concentration (1 μM). NOPLight showed negligible response to dynorphins, enkephalins and β-endorphin (**Figure 3.2d**). Similarly, the sensor showed minimal response to a panel of fast neurotransmitters (**Figure 3.2e**), indicating high N/OFQ ligand selectivity at NOPLight.

3.2.3 Pharmacological characterization of NOPLight *in vivo*

Our results *in vitro* (**Figure 3.2c**) showed potent and efficacious NOPLight responses to the small molecule NOPR agonist RO 64-6198 (RO). Thus, we determined whether we could use fiber photometry to record NOPLight fluorescence *in vivo* and track the target engagement of this NOPR agonist action in real-time within the brain (**Figure 3.3**). To do so, we injected WT mice with AAV-DJ-hSyn-NOPLight in the VTA and implanted optic fibers above the injection sites for fiber photometry recordings (**Figure 3.3a, b**). At 3-4 weeks post-viral injection, we detected robust, dose-dependent increases in NOPLight fluorescence in the VTA following systemic (i.p.) injection of increasing doses of RO (**Figure 3.3c**). To determine if the observed increase in NOPLight fluorescence in the VTA was produced by the sensor binding to the NOPR agonist, we pre-treated animals with two different selective NOPR antagonists, LY2940094 (LY, 10 mg/kg o.g.) or J-113397 (J11, 10 mg/kg i.p.) 30 min prior to injection of RO. Both NOPR-selective antagonists fully inhibited the agonist-induced fluorescent signal (**Figure 3.3d, e**).

Next, we injected additional cohorts of OPRL1-Cre (line characterized in the VTA in **Figure S3.4a–h**) or WT mice in the VTA with AAVs containing either a Cre-dependent variant of NOPLight

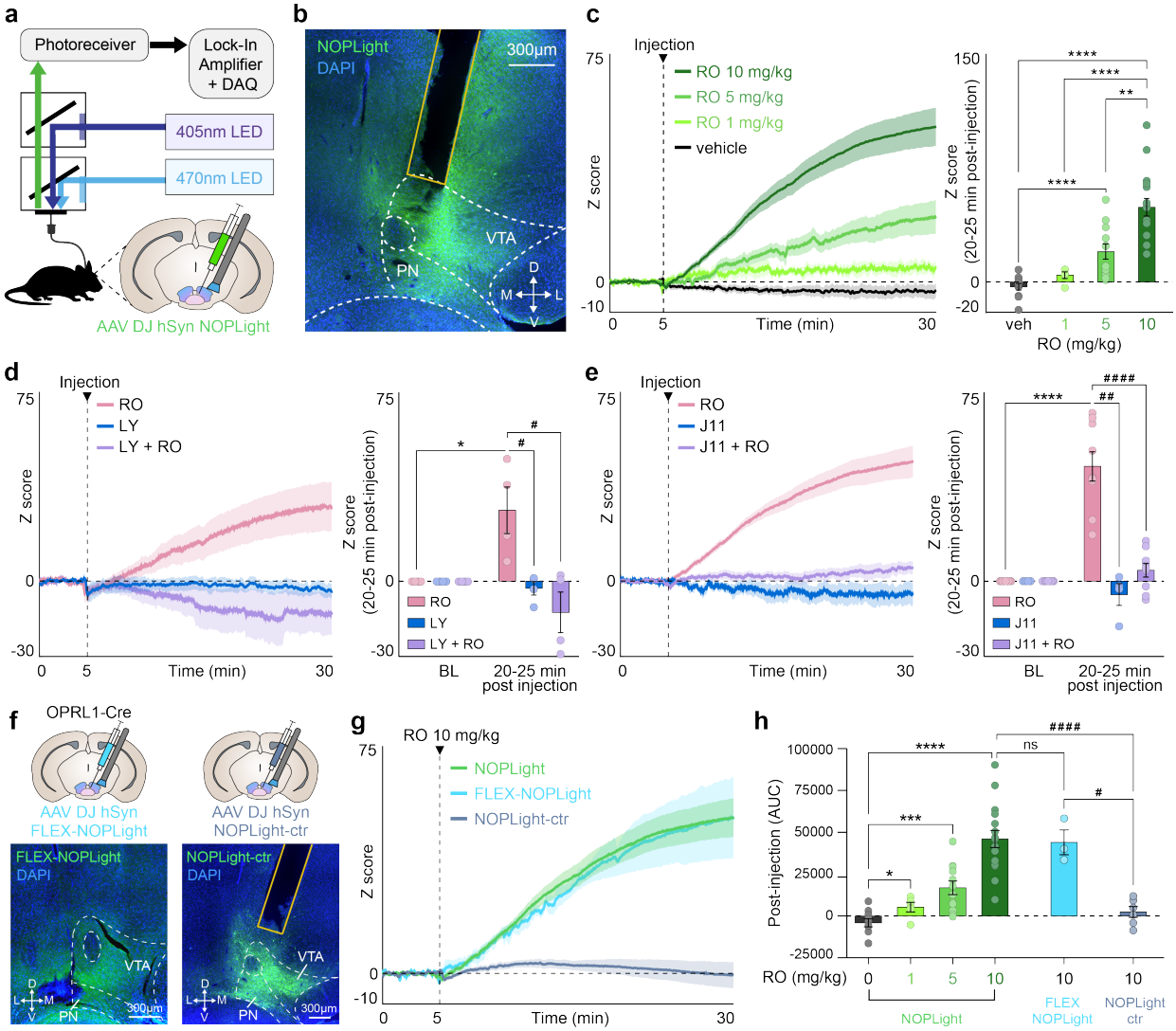

Figure 3.3: Pharmacological characterization of NOPLight *in vivo*.

(a) Fiber photometry schematic. Cartoon of NOPLight viral injection and fiber implant in the VTA. **(b)** Representative image showing DAPI (blue) and NOPLight (green) expression with fiber placement. **(c)** Left: Averaged traces of NOPLight fluorescence after systemic (i.p.) injection of vehicle (veh, black; N = 11 mice) or 1, 5, or 10 mg/kg of selective NOPR agonist RO 64-6198 (RO, green; N = 5, 12, or 16 mice/group, respectively). Right: Mean NOPLight fluorescence 20–25 min after RO injection increases dose-dependently (two-tailed Mann–Whitney test, $^{**}p = 0.0012$, $^{****}p < 0.0001$). **(d)** Left: Averaged traces of NOPLight fluorescence after 10 mg/kg RO (pink), 10 mg/kg selective NOPR antagonist LY2940094 (LY, o.g., blue), or both (purple) (N = 4 mice). Right: Increase in signal 20–25 min after RO is blocked by LY pretreatment (two-tailed Mann–Whitney test, $^{*}p = 0.0286$, $^{\#}p = 0.0286$, N = 4 mice). **(e)** Same as **d** for NOPR antagonist J-113397 (J11, i.p.) (two-tailed Mann–Whitney test, $^{\#\#}p = 0.0028$, $^{\#\#\#\#}p < 0.0001$, $^{****}p < 0.0001$, N = 9 mice, RO; 4 mice, J11; 9 mice, J11 + RO). **(f)** Top: Cartoon of FLEX-NOPLight or NOPLight-ctr viral injection and fiber implant in the VTA. Bottom: Representative image showing expression of DAPI (blue) and FLEX-NOPLight (left, green) or NOPLight-ctr (right, green), with fiber placement in VTA. **(g)** Averaged traces of NOPLight (green), FLEX-NOPLight (blue), or NOPLight-ctr (gray) fluorescence (N = 16, 3, 6 mice, respectively) after systemic (i.p.) injection of 10 mg/kg RO. **(h)** Area under the curve (AUC) of each NOPLight variant after RO injection (two-tailed Mann–Whitney test, $^{*}p = 0.0275$, $^{***}p = 0.0001$, $^{****}p < 0.0001$, ns not significant ($p = 0.9577$), $^{\#}p = 0.0238$, $^{\#\#\#\#}p < 0.0001$. Group sizes left to right: N = 11, 5, 12, 16, 3, and 6 mice). All data represented as mean ± SEM. PN = paranigral VTA, veh = vehicle, BL = baseline.

(AAV-DJ-hSyn-FLEX-NOPLight), or the control sensor (AAV-DJ-hSyn-NOPLight-ctr) respectively, with optic fibers implanted above the injection site (**Figure 3.3f**). We found that systemic injection of 10 mg/kg RO produced a robust increase in FLEX-NOPLight signal that was not significantly different from the agonist-induced signal we recorded from non-conditionally expressed NOPLight (**Figure 3.3g, h**). In contrast, the control sensor showed no fluorescent response to a 10 mg/kg RO injection (**Figure 3.3g, h**). These results indicate that NOPLight expressed in freely moving animals reliably provides dose-dependent and antagonist-sensitive detection of exogenous NOPR agonists in real time.

3.2.4 NOPLight detection of chemogenetically-evoked endogenous N/OFQ release

A primary goal motivating our development of the NOPLight sensor was to ultimately achieve real-time detection of local N/OFQ release in behaving animals. Thus, we set out to determine whether NOPLight reliably detects endogenous release of N/OFQ. To accomplish this, we evoked endogenous N/OFQ release in a local paranigral VTA (pnVTA) circuit we previously identified (Parker et al., 2019) by using a chemogenetic approach to selectively activate pnVTA^{PNOC} neurons while simultaneously recording changes in VTA-NOPLight fluorescence (**Figure 3.4**).

To achieve this, PNOC-Cre mice were co-injected in the VTA with two Cre-dependent AAVs containing i) AAV-DH-hSyn-NOPLight and ii) an mScarlet-tagged stimulatory hM3Dq DREADD (AAV5-EF1a-DIO-HA-hM3D(Gq)-mScarlet), with optic fibers implanted above the injection site (**Figure 3.4a**). Control animals received an mCherry (AAV5-EF1a-DIO-mCherry) injection in place of the red fluorophore-tagged DREADD. Based on our earlier spectral characterization which showed that the isosbestic point of NOPLight is closer to 440 nm (**Figure S3.3**), we tested and characterized an alternative set of LED wavelengths in this group of experiments, using 435 nm and 490 nm as the isosbestic and signal wavelengths, respectively.

Activation of the hM3Dq DREADD via systemic injection with 5 mg/kg of clozapine-N-oxide (CNO) produced a significant increase in NOPLight fluorescence that was not observed in

the control animals expressing mCherry in place of the DREADD (**Figure 3.4b**). To confirm that this increase was truly the result of chemogenetically evoked endogenous N/OFQ release and thus acting via a NOPR-dependent mechanism, pretreatment with the selective NOPR antagonist LY2940094 (Post et al., 2016) (LY, 10 mg/kg, o.g.) 30 min prior to CNO injection prevented the CNO-induced increase in NOPLight fluorescence (**Figure 3.4c**). Together, these results provide strong evidence that NOPLight can detect evoked endogenous release of N/OFQ in freely moving animals.

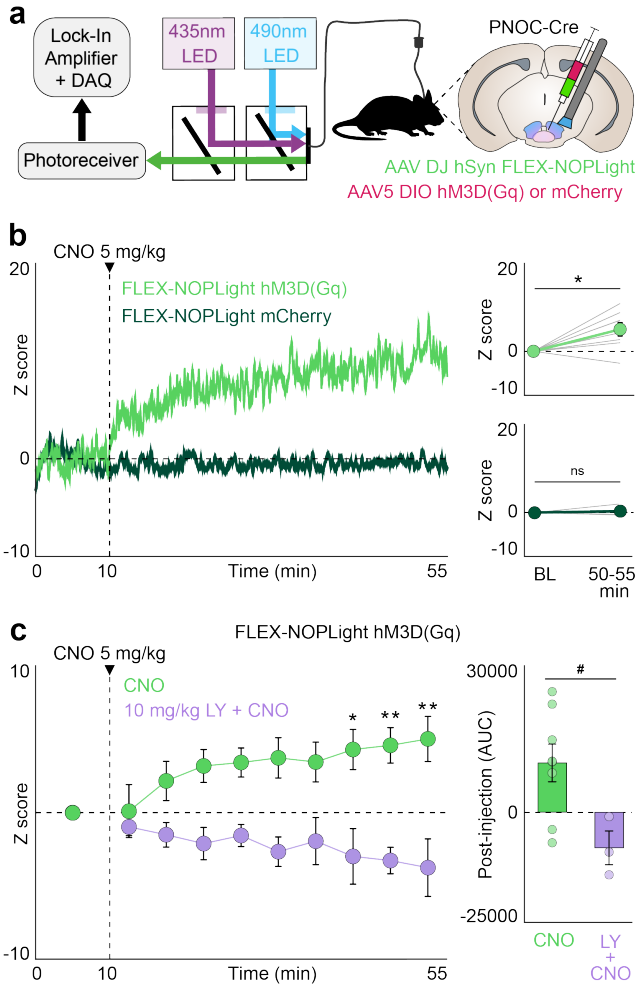

Figure 3.4: NOPLight *in vivo* detects chemogenetically-evoked N/OFQ release.

(a) Schematic of fiber photometry setup. Coronal brain cartoon of fiber implant and viral co-injection of FLEX-NOPLight with either DIO-hM3D(Gq) or mCherry in the VTA of PNOC-Cre mice. **(b)** Left: Representative traces of FLEX-NOPLight fluorescence after systemic (i.p.) injection of 5 mg/kg clozapine-N-oxide (CNO) in hM3D(Gq) (light green) or mCherry control (dark green) animals. Right: Mean FLEX-NOPLight fluorescence 40–45 min after CNO injection is significantly elevated relative to pre-injection baseline period (BL) in hM3D(Gq) (two-tailed Wilcoxon test, $*p = 0.0391$, N = 8 mice) but not control animals (two-tailed Wilcoxon test, $p > 0.9999$, N = 3 mice). Z-scores for each individual animal averaged at baseline and 50–55 min are shown (gray lines). **(c)** Left: FLEX-NOPLight fluorescence (green) averaged before injection of 5 mg/kg CNO (0–10 min), and in 5 min bins following injection. 10 mg/kg of selective NOPR antagonist LY2940094 (LY) was administered (o.g.) to the LY + CNO (purple) group 30 min prior to photometry recording (two-way repeated-measures ANOVA with Bonferroni's post hoc test, $*p = 0.0207$ (40–45 min), $**p = 0.0094$ (45–50 min) or 0.0024 (50–55 min), N = 8 mice, CNO; three mice, LY + CNO). All data represented as mean ± SEM.

3.2.5 Endogenous N/OFQ tone in VTA during consummatory behavior

We also examined NOPLight's ability to report transient, endogenous N/OFQ release evoked by different naturalistic behavioral states. N/OFQ and its receptor NOPR have been implicated in neuromodulation of a wide variety of essential behavioral processes including stress, aversion, motivation, reward seeking, and feeding (Ciccocioppo et al., 2014; Devine et al., 2003; Green and Devine, 2009; Hardaway et al., 2019; Jais et al., 2020; Morairty et al., 2023; Parker et al., 2019; Rodriguez-Romaguera et al., 2020; Witkin et al., 2014). We have previously identified a role for VTA N/OFQ signaling in reward-related and aversive behavior, and using GCaMP found that pnVTA^{PNOC} neurons activity is suppressed during sucrose consumption (Parker et al., 2019). Therefore, we injected WT mice with AAV-DJ-hSyn-NOPLight in the VTA, implanted optical fibers above the injection site, and secured stainless steel rings to allow for head-fixed fiber photometry recording of NOPLight during sucrose consumption (**Figure 3.5a**). Mice were food-restricted (85-90% of starting body weight) and then NOPLight signal was recorded during cued access to 10% sucrose solution (15 trials, 5s sucrose access/trial) (**Figure 3.5b**). Sucrose trials were cued by a 5-second auditory tone (4 kHz, 80 dB) that preceded the 5 seconds of sucrose access to determine if NOPLight would respond to any salient stimulus rather than specifically to sucrose consumption.

We found that NOPLight fluorescence remained unchanged during the 5-second tone but significantly decreased during sucrose consumption (**Figure 3.5c–f**). In contrast, animals that were pre-treated with the selective NOPR antagonist J-113397 (J11, 20 mg/kg, i.p.) 30 minutes prior to cued sucrose recordings had no change in NOPLight signal during sucrose consumption (**Figure 3.5c, f**). Mice made a similar number of licks on the sucrose spout during J-113397 and vehicle sessions (**Figure 3.5d**), suggesting that the lack of signal change during sucrose consumption following J-113397 treatment was a result of the NOPR antagonist blocking NOPLight's detection of endogenous N/OFQ levels. This finding is consistent with our previous

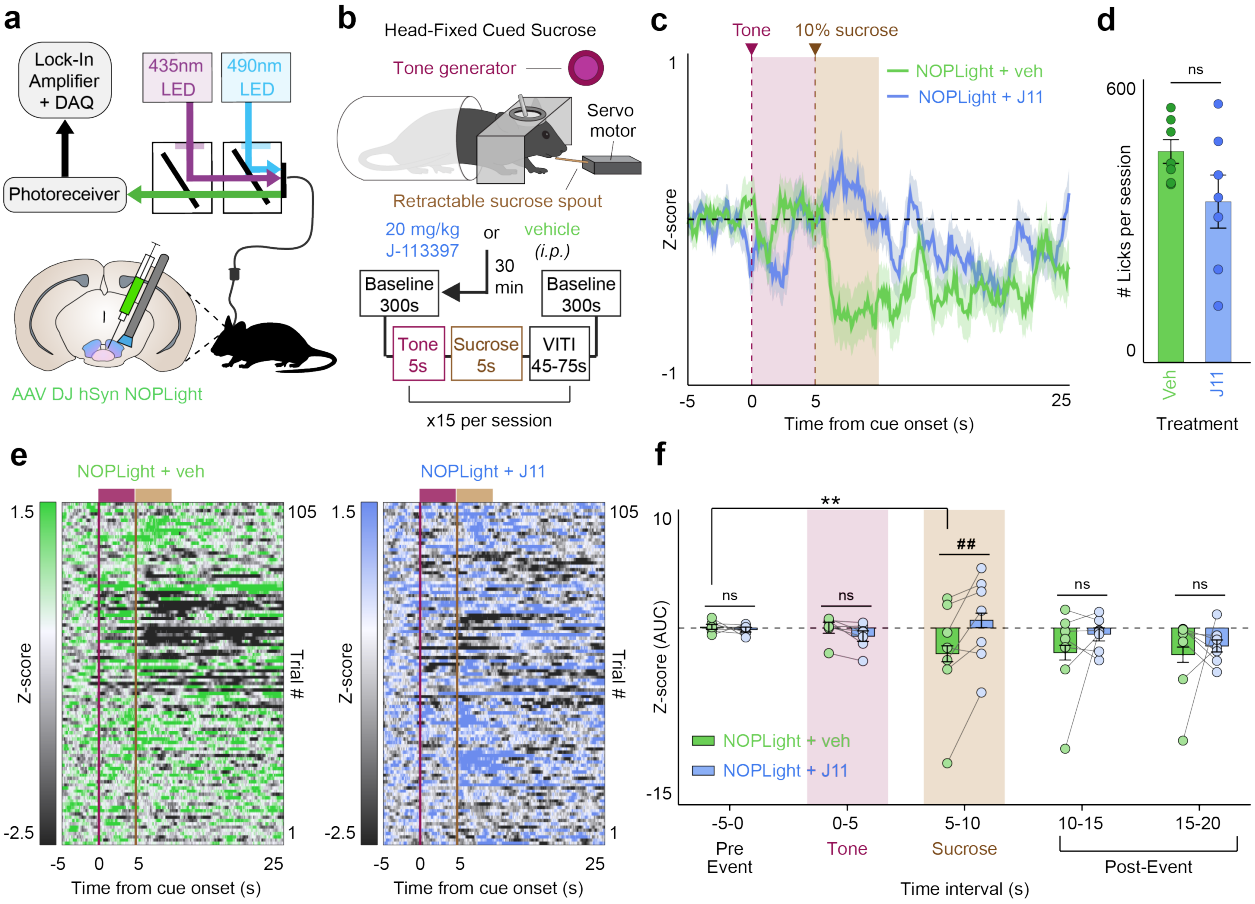

Figure 3.5: NOPLight *in vivo* reports antagonist sensitive decreases in N/OFQ signal during consummatory behaviors.

(a) Fiber photometry schematic. Cartoon of viral injection of NOPLight and fiber implant in VTA of wild-type mice (N = 7 mice). **(b)** Cartoon depicting head-fixed cued-sucrose setup and trial structure. **(c)** Averaged traces of NOPLight fluorescence following pretreatment with vehicle (veh, green) or 20 mg/kg NOPR antagonist J-113397 (J11, blue), aligned to tone onset (magenta, shaded). **(d)** Average licks made during vehicle or J-113397 sessions (two-tailed Wilcoxon test, p = 0.1649, ns not significant, N = 7 mice). **(e)** Heat maps of NOPLight fluorescence, rows correspond to trials averaged in **c** for vehicle (left) and J11 (right) sessions. **(f)** Area under the curve (AUC) for averaged traces from **c**, calculated over 5-s intervals surrounding cued-sucrose events. Decrease in NOPLight fluorescence during 10% sucrose access (two-tailed Wilcoxon test, **p = 0.0034, N = 7 mice) is blocked by J11 pretreatment (two-tailed Mann–Whitney test, ##p = 0.0022, N = 7 mice). All data represented as mean ± SEM.

study, which showed that nociceptin-containing neurons have lower activity during reward consumption. These results demonstrate that NOPLight is sensitive to changes in the endogenous N/OFQ tone *in vivo* within the VTA, in behaviorally relevant appetitive contexts.

3.2.6 NOPLight detects natural endogenous N/OFQ release following aversive stimuli

In addition to having a well-established role in reward processing, the VTA is known to mediate aversive states. Given that N/OFQ and NOPR are also widely implicated in stress and aversive responses, we evaluated whether NOPLight could detect endogenous N/OFQ release in the VTA during an aversive behavior in freely moving animals. Our previous findings indicated that stimulating pnVTA^{PNOC} neurons drives aversive responses (Parker et al., 2019), so we predicted that the VTA N/OFQ system would be engaged by an aversive stimulus. To test this, we used fiber photometry to record pnVTA^{PNOC} activity in response to tail suspension (**Figure 3.6a**). PNOC-Cre mice injected with AAV-DJ-EF1a-DIO-GCaMP6m and implanted with optic fibers in the VTA underwent four trials of a 10-second tail suspension, resulting in a robust increase in GCaMP6m fluorescence lasting for the duration of the suspension (**Figure 3.6b**). To determine if the increase in pnVTA^{PNOC} calcium activity was reflected by NOPLight as an increase in N/OFQ release in the VTA, we repeated the tail suspension test in OPRL1-Cre mice injected with AAV-DJ-hSyn-FLEX-NOPLight and WT mice injected with AAV-DJ-hSyn-NOPLight-ctr (**Figure 3.6c**). Fiber photometry recordings of FLEX-NOPLight showed an increase in fluorescence during tail suspension that was significantly elevated in comparison to NOPLight-ctr (**Figure 3.6c**). These data indicate that NOPLight can reliably reports the endogenous release of N/OFQ during aversive behavioral events within the VTA.

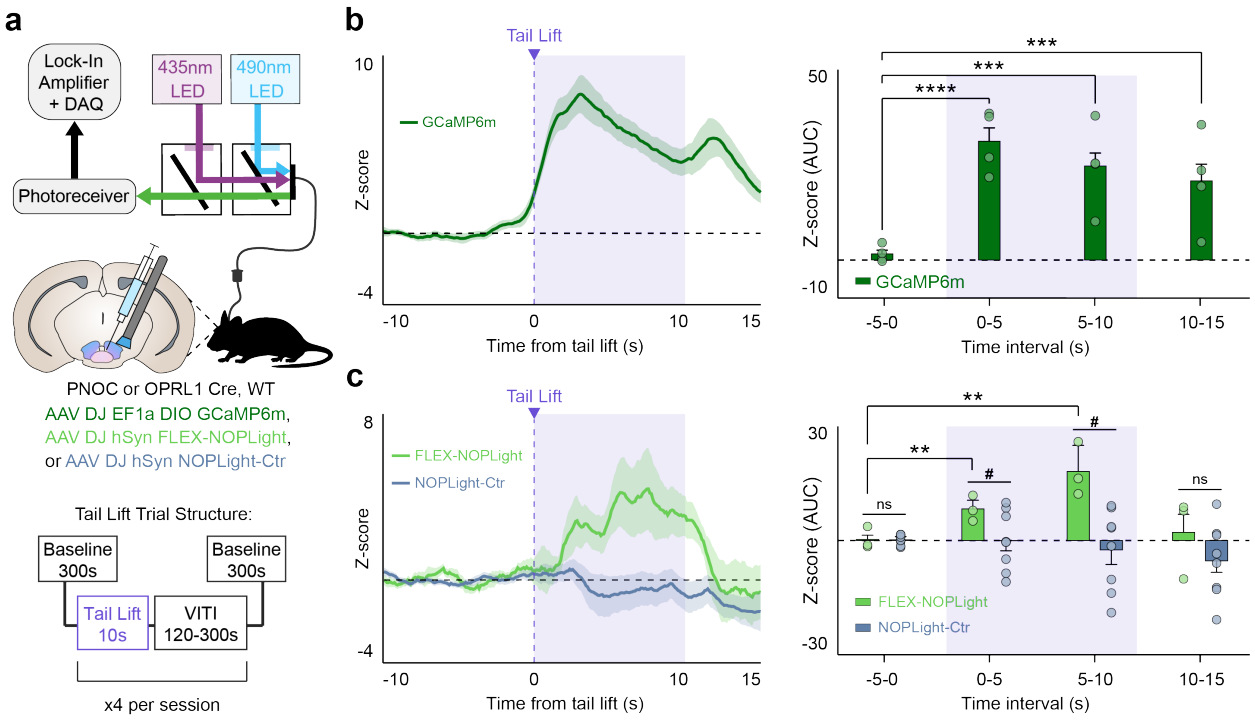

Figure 3.6: NOPLight *in vivo* detects natural N/OFQ release following aversive stimuli.

(a) Top: Fiber photometry schematic. Middle: Cartoon depicting fiber implant and viral injection of DIO-GCaMP6m, FLEX-NOPLight, or NOPLight-ctr into the VTA of PNOC-Cre, OPRL1-Cre, or WT mice, respectively. Bottom: Session trial structure. **(b)** Left: Averaged trace of pnVTA^{PNOC} GCaMP6m activity during tail lift. Right: AUC for photometry trace calculated over 5-s intervals surrounding tail lift (two-tailed Wilcoxon test, ***$p = 0.0002$ (5–10 s) or 0.0003 (10–15 s); ****$p < 0.0001$, $n = 4$ mice). **(c)** Left: Averaged traces of FLEX-NOPLight (green) and NOPLight-ctr (gray) fluorescence during the tail lift. Right: AUC for photometry traces calculated over 5-s intervals surrounding tail lift. FLEX-NOPLight fluorescence increases during tail lift (two-tailed Wilcoxon test, **$p = 0.0034$ (0–5 s) or 0.0093 (5–10 s); $n = 3$ mice), NOPLight-ctr fluorescence remains unchanged (two-tailed Mann–Whitney test, $^{\#}p = 0.0264$ (0–5 s) or 0.0326 (5–10 s); $n = 8$ mice, NOPLight-ctr; 3 mice, FLEX-NOPLight). All data represented as mean ± SEM. VITI = variable inter-trial interval.

3.2.7 Monitoring endogenous N/OFQ dynamics in reward-seeking operant behavior

Our prior work extensively characterized the calcium activity of pnVTA^{PNOC} neurons during operant responding for reward and identified a role for VTA N/OFQ signaling in constraining motivation to obtain a reward. Therefore, we sought to determine whether our sensor could report the dynamics of endogenous N/OFQ release in the VTA during operant reward-seeking behavior. WT mice injected with AAV-DJ-hSyn-NOPLight and implanted with optic fibers in the VTA were food-restricted (~85-90% of their starting body weight) and then trained on a Pavlovian and operant conditioning schedule (**Figures 3.7 and 3.8**). Mice were first trained in Pavlovian conditioning sessions to associate a 5-second house light cue (CS) with delivery of a sucrose pellet (US) (**Figure 3.7a**). Next, they were trained on a fixed ratio (FR) operant schedule, learning first to perform one (FR1) and later three (FR3) nose pokes into an active port to trigger the light cue and sucrose reward. Mice successfully learned that only nose pokes in the active port would result in reward delivery (**Figure 3.7b**). Tracking of pellet consumption across the training paradigm also confirmed that mice consumed the majority of rewards they obtained across sessions (**Figure 3.7c**).

NOPLight fluorescent signals recorded during early Pavlovian conditioning sharply increased in response to onset of the light cue (**Figure 3.7d**), which is consistent with fiber photometry recordings of the calcium activity (GCaMP6s) of a posterior population of pnVTA^{PNOC} neurons known to project locally within the VTA (Parker et al., 2019). Across all Pavlovian and operant conditioning schedules, we observed a robust decrease in NOPLight fluorescence that persisted throughout the reward consumption period, and was immediately followed by a transient increase in signal upon the end of a feeding bout (**Figure 3.7d–h**). This decrease in signal during reward consumption and subsequent increase at the end of the feeding period is consistent with previously reported calcium activity patterns of posterior pnVTA^{PNOC} neurons recorded during both Pavlovian and operant conditioning. Importantly, during FR3 recordings when mice performed an

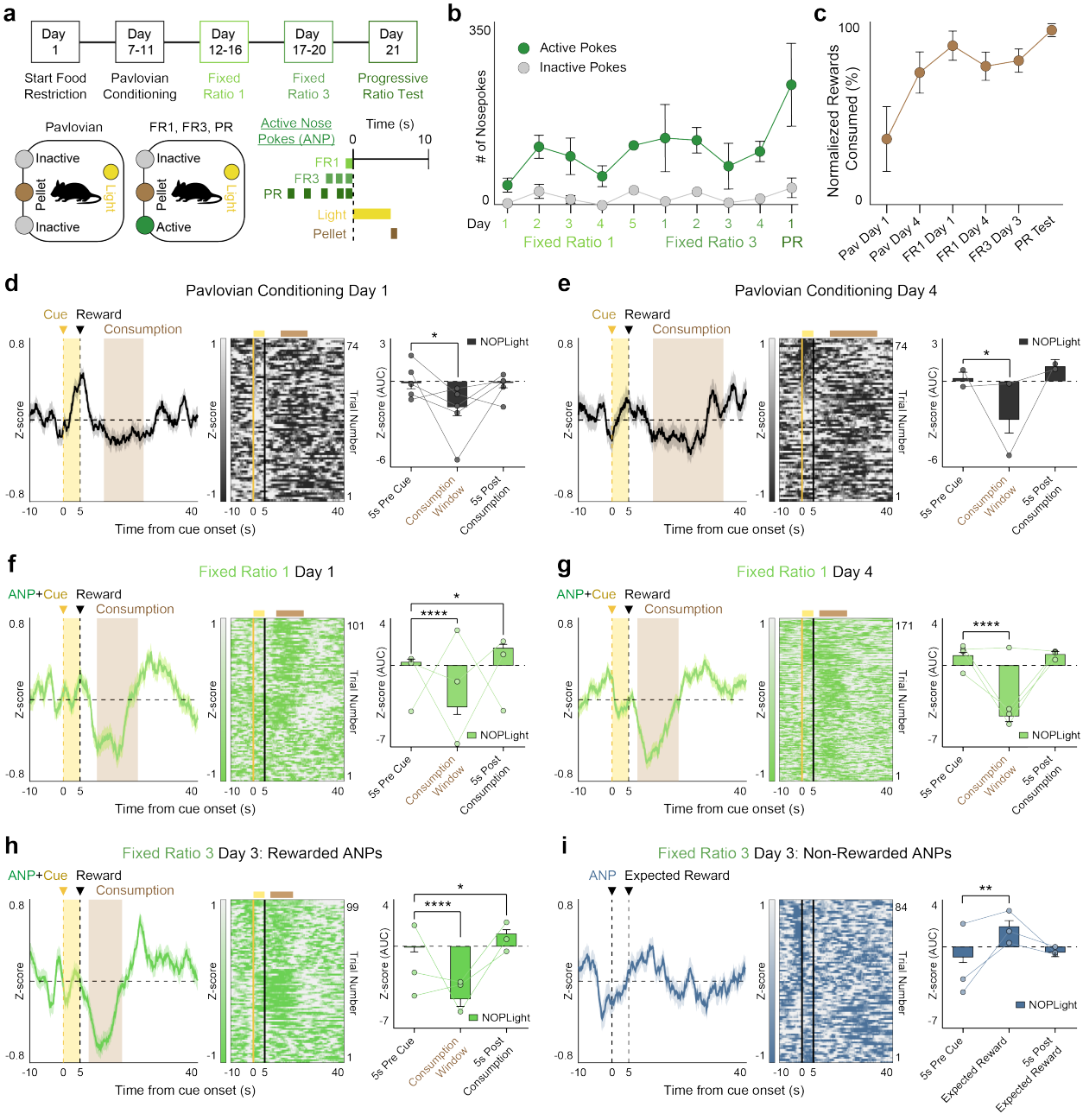

Figure 3.7: NOPLight detection of endogenous VTA N/OFQ release during Pavlovian and operant conditioning.

(a) Mice expressing NOPLight in the VTA were trained on Pavlovian and fixed ratio schedules prior to progressive ratio test (N = 5 mice). Top: Training regimen for conditioning. Bottom: Cartoon of operant box setup and trial structure. **(b)** Total number of nosepokes made in active (green) or inactive (gray) nose-poke ports across training days. **(c)** Proportion of delivered rewards that animals consumed on photometry recording days. **(d–e)** Left: Trace of mean NOPLight signal in the first (**d**) and fourth (**e**) Pavlovian conditioning sessions, aligned to light cue onset (yellow, shaded). Time to pellet retrieval and duration of consumption averaged across trials (brown, shaded). Middle: Corresponding heat map. Right: Area under the curve (AUC) for photometry traces from **d** and **e** respectively, calculated over the averaged reward consumption window and 5-second intervals surrounding the consumption period (two-tailed Wilcoxon test, d: *p=0.0364, N = 5 mice; e: *p=0.0152, N = 2 mice). **(f–g)** Same as **d–e** but

for the first (**f**) and fourth (**g**) fixed ratio 1 (FR1) sessions (two-tailed Wilcoxon test, *p=0.0105, ****p<0.0001, N = 3 mice). **(h)** Left: Trace of mean NOPLight signal during fixed ratio 3 (FR3) training, aligned to reinforced active nose-pokes. Shown with averaged time to pellet retrieval and duration of consumption (brown, shaded). Middle: Corresponding heat map. Right: AUC of photometry trace calculated over the averaged consumption window and in 5- second intervals surrounding the consumption period (two-tailed Wilcoxon test, *p=0.0477, ****p<0.0001, N = 3 mice). **(i)** Left: Trace of mean NOPLight signal during the same FR3 session as **h**, aligned to non-rewarded active nosepokes. Middle: Corresponding heat map. Right: AUC of photometry trace calculated over the expected reward period and in 5-second intervals surrounding expected reward (two-tailed Wilcoxon test, **p=0.0017, N = 3 mice). All data represented as mean ± SEM.

active nose poke that did not yet meet the threshold for a reward delivery, we observed an increase in NOPLight fluorescence following the nose poke instead of a decrease, indicating that the decrease is related to reward consumption and not the operant action (**Figure 3.7i**). Taken together, NOPLight signal in the VTA closely resembles known patterns of pnVTA^{PNOC} neuron GCaMP activity during Pavlovian and operant reward-related behaviors.

After completing FR3 operant training, mice were placed in a progressive ratio (PR) test where the required nose poke criterion increases exponentially with each subsequent reward until the animal reaches a motivational breakpoint where they are unwilling to exert any further effort to obtain a reward (**Figure 3.8b**). We extracted fiber photometry epochs surrounding active nose pokes that were reinforced with delivery of a sucrose pellet reward, finding that NOPLight fluorescence decreases during reward consumption in the PR test and transiently increases immediately upon completion of a consumption bout (**Figure 3.8c, f**). In contrast, NOPLight signal remained stable during epochs where animals performed an unsuccessful active nose poke that did not result in reward delivery (**Figure 3.8d, g**). NOPLight signal during reward consumption is significantly suppressed in comparison to time periods where animals expected but did not obtain a reward (**Figure 3.8e**). Notably, our detection of negative changes to NOPLight fluorescence relative to baseline suggests the presence of N/OFQ tone in the VTA, which is consistent with our previous findings regarding this circuit. Collectively, these results indicate that NOPLight faithfully

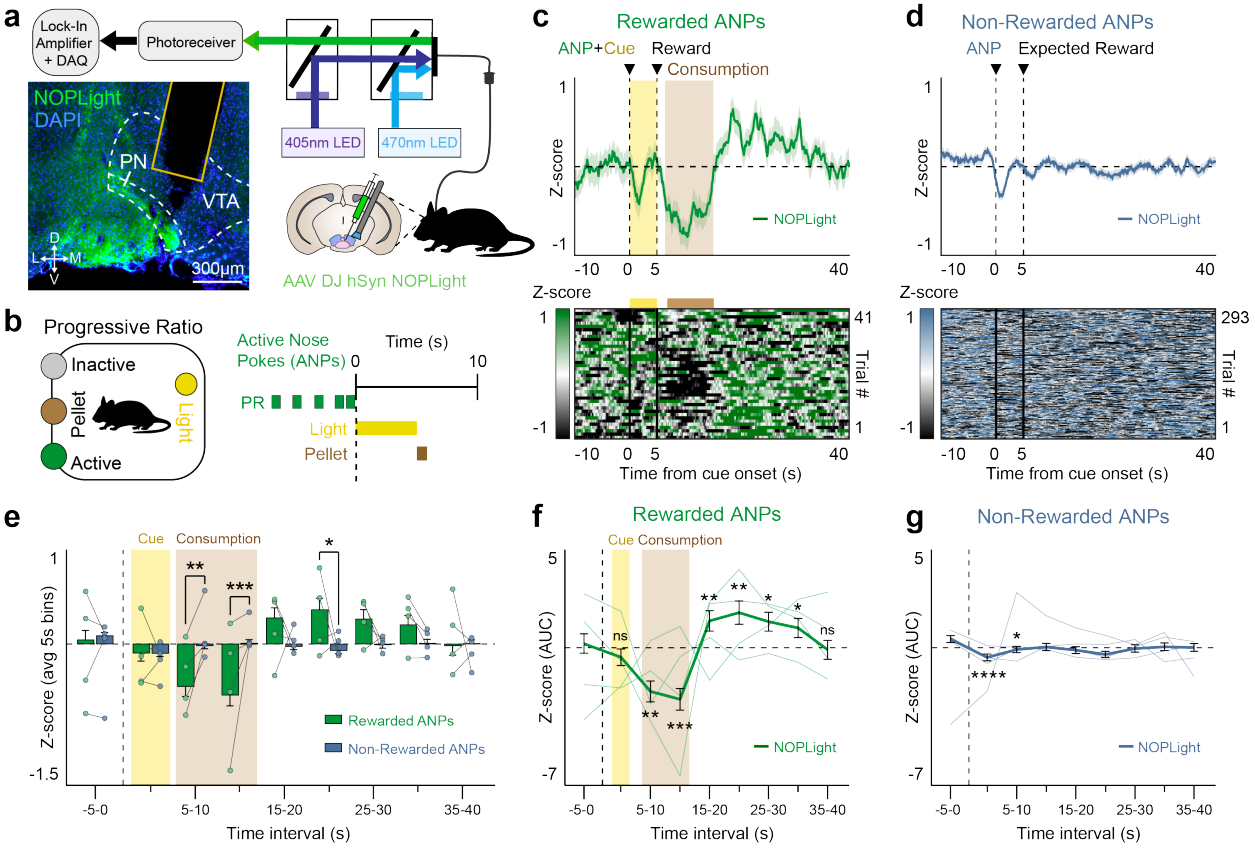

Figure 3.8: NOPLight detection of endogenous VTA N/OFQ release during high effort reward-seeking.

(a) Fiber photometry schematic. Cartoon of NOPLight viral injection and fiber implant in the VTA of WT mice (N = 4 mice). Representative image showing expression of DAPI (blue) and NOPLight (green) with fiber placement in VTA. **(b)** Left: Cartoon depicting operant box setup for the progressive ratio (PR) test. Right: Trial structure for reward delivery during the paradigm. **(c)** Top: Averaged trace of NOPLight signal for all mice (N = 4), aligned to rewarded active nose pokes (ANPs) made during the PR test. Epoch includes the 5 s light cue (yellow, shaded) that precedes reward delivery. Time to pellet retrieval and duration of consumption period averaged across all trials (brown, shaded). Bottom: Heat map, each row corresponds to a single, rewarded ANP epoch. **(d)** Top: Averaged trace of NOPLight signal for all mice (N = 4), aligned to non-rewarded ANPs made during the PR test. Bottom: Heat map, each row corresponds to a single, non-rewarded ANP epoch. **(e)** NOPLight fluorescence averaged over 5-s intervals for rewarded (green) and non-rewarded (blue) ANP epochs. Time to pellet retrieval and duration of consumption period averaged across all rewarded trials (brown, shaded). Across rewarded ANP trials, NOPLight signal decreases during reward consumption then immediately increases post-consumption relative to NOPLight signal measured during non-rewarded ANP epochs (two-way repeated-measures ANOVA with Bonferroni's post hoc test, *p = 0.0122, **p = 0.0033, ***p = 0.0003, N = 4 mice). **(f–g)** Area under the curve (AUC) for photometry traces from **c** and **d**, respectively, calculated over 5-s intervals surrounding (**f**) rewarded ANPs (two-tailed Wilcoxon test, *p = 0.0125 (25–30 s) or 0.031 (30–35 s); **p = 0.007 (5–10 s) or 0.0042 (15–20 s); ***p = 0.0008 (10–15 s); N = 4 mice) and (**g**) non-rewarded ANPs (two-tailed Wilcoxon test, *p = 0.0128 (5–10 s), ****p < 0.0001 (0–5 s), N = 4 mice). All data represented as mean ± SEM.

reports bidirectional changes in N/OFQ release in the VTA during freely moving behaviors. Our findings demonstrate NOPLight's utility in detecting endogenous N/OFQ release during discrete behavioral epochs within the VTA and potentially other N/OFQ brain regions.

3.3 Discussion

Here we describe the engineering, characterization, and application of a genetically encoded sensor (NOPLight) for monitoring the opioid neuropeptide N/OFQ *in vitro* and *in vivo*. Endogenous opioid peptides represent one of the largest classes of neuropeptide families, yet detecting their release, dynamics, and properties *in vitro* and *in vivo* has been a challenge for over 60 years since their discovery (Conway et al., 2022; Girven et al., 2022; Sandberg and Weber, 2003). We sought to develop a sensor which could detect: 1) evoked release, 2) endogenous release during naturalistic behavior, and 3) exogenous ligands *in vivo* to inform brain localization of pharmacological agents. These properties have been long sought after to better understand neuropeptide transmission generally, and more specifically opioid peptides and their actions.

The neuropeptide biosensor we developed exhibits a large dynamic range both in HEK293T cells and in neurons, sub-second activation kinetics, very high ligand selectivity, a similar pharmacological profile to that of NOPR, and no detectable interference with endogenous signaling pathways. We demonstrated that NOPLight dose-dependently responds to systemic administration of a NOPR agonist, with sensitivity to blockade by selective NOPR antagonists. NOPLight is also capable of detecting endogenous release of N/OFQ evoked by either chemogenetic stimulation (hM3Dq DREADD) of PNOC neurons or natural behaviors.

N/OFQ and NOPR are widely implicated in diverse behavioral states, which was reflected by our fiber photometry recordings of NOPLight during varied behaviors. Our recordings of NOPLight signal during head-fixed behavior revealed a NOPR antagonist sensitive decrease in N/OFQ signaling time-locked with access to a 10% sucrose solution. We also identified an increase in N/OFQ release in response to an aversive tail suspension using NOPLight, which was

not present in recordings of our control variant of the sensor. While it has been suggested that N/OFQ is released in response to aversive or stressful stimuli, our findings are the first to our knowledge to directly detect endogenous N/OFQ release during an aversive response.

Previous GCaMP recordings of PNOC neurons with local input in the VTA during operant conditioning tasks revealed dynamic engagement of pnVTA^{PNOC} neurons during reward-seeking and consumption behavior (Parker et al., 2019). While in many cases calcium mobilization is required for dense core vesicle fusion (van den Pol, 2012), calcium activity is not a direct correlate for peptide release and as such the dynamics of released N/OFQ could not be established in this prior study. Here we report NOPLight activity in the VTA in reward-seeking behavior during fixed ratio-1, -3, and progressive ratio paradigms, which identified a rapid and sustained decrease during reward consumption, and a transient increase after consumption had ended (**Figures 3.7 and 3.8**). This pattern of NOPLight signal closely resembles the expected dynamics of N/OFQ release based on the prior study's GCaMP recordings (Parker et al., 2019).

Notably, we observed both dynamic increases and decreases in NOPLight fluorescence during behavioral epochs, suggesting that the NOPLight can be used to detect changes in peptide tone over behaviorally relevant timescales. These data also provide the ability to align neuronal activity measured either by calcium dynamics or electrophysiology with neuropeptide release during freely-moving behavioral epochs. Given the recent discoveries that PNOC and NOPR are important for motivation, feeding, and sleep induction (Hardaway et al., 2019; Jais et al., 2020; Morairty et al., 2023; Parker et al., 2019; Rodriguez-Romaguera et al., 2020; Witkin et al., 2014), understanding the dynamic properties of this opioid peptide system is now of even greater importance as this receptor is now considered a major target for insomnia, addiction, and depression (Journigan et al., 2014; Kallupi et al., 2017; Post et al., 2016).

The endogenous activity of PNOC neurons in the VTA is thought to provide inhibitory tone onto VTA dopamine neurons, constraining motivation to seek rewards (Driscoll et al., 2019; Flau et al., 2002; Khan et al., 2018; Norton et al., 2002; Olianas et al., 2008; Parker et al., 2019).

Consistent with this concept, here we observed a decrease in NOPLight fluorescence when animals engaged in reward consumption. Additionally, we measured an increase in NOPLight signal immediately upon completion of a reward consumption bout, suggesting that N/OFQ is released in the VTA after animals have consumed an obtained reward. Since NOPR is largely expressed on dopamine neurons in the VTA and exerts inhibitory influence over their activity (Driscoll et al., 2019; Norton et al., 2002), it is possible that this increase in endogenous N/OFQ release after consumption reflects a temporarily satiated state where N/OFQ signaling transiently increases to suppress tonic dopamine neuron activity, thus reducing motivation to seek out additional rewards. These findings provide insight into the dynamics of N/OFQ signaling in the VTA which acts to coordinate motivated behavior through dopaminergic interactions. Future studies will be able to employ NOPLight in concert with the recently developed red-shifted dopamine sensors (Patriarchi et al., 2020) and other N/OFQ-selective tools like the new OPRL1-Cre line (**Figure S3.4**) to improve our understanding of N/OFQ modulation of dopamine circuitry during reward-seeking.

We tested the performance of the sensor *in vivo* using different wavelength pairs. Following the development of GCaMPs, sensor excitation has conventionally employed a 405 nm wavelength light as a read-out for non-ligand sensitive signals (known as the isosbestic channel), that typically acts as an internal control for fiber photometry experiments, particularly in freely moving animals (Gunaydin et al., 2014; Lerner et al., 2015). As a result, most commercially-available photometry setups are tailored to accommodate this wavelength. In this work we noted that, based on the results from our spectral characterization of NOPLight, excitation at a wavelength of 435 nm is better suited as a control ‘isosbestic’ channel. It is particularly worth noting that many recently-developed intensiometric GPCR-based biosensors exhibit a similar spectral property with a right-shifted isosbestic point (i.e. > 420 nm) (Duffet et al., 2023, 2022; Jing et al., 2020; Qian et al., 2023; Wu et al., 2022). In these cases, use of 405 nm as the isosbestic channel for these sensors may lead to confounding results or difficulty in interpretation

in some contexts, such as regions where N/OFQ release in response to a given behavior is relatively low, or during behaviors that are highly subject to motion artefact. Since it can be cost and time prohibitive for research groups to add an alternative recording parameter to existing photometry setups, we demonstrated that we were still able to detect meaningful changes in NOPLight fluorescence when using the 405 nm wavelength in some of our fiber photometry recordings. Furthermore, head-fixation and red fluorophore-based motion controls are commonly used as alternatives to isosbestic controls that could easily be implemented with NOPLight (Lerner et al., 2015; Meng et al., 2018). Our careful evaluation of NOPLight's performance when recorded with different isosbestic and excitation wavelengths provides valuable insight into its photophysical properties that will help inform successful application of NOPLight and other neuropeptide sensors in future studies. Our work here lays critical groundwork that will need to be built upon through continued use of NOPLight and its control variant in similar reward-related behaviors, different brain regions, and with additional controls, which will be important for optimizing their implementation and developing general best practices amidst the rapidly expanding use of fluorescent peptide sensors.

Our findings present NOPLight as an approach to improve investigations of endogenous opioid peptide dynamics with high spatiotemporal resolution. We characterized NOPLight expression, selectivity, and sensitivity to endogenous N/OFQ release both *in vivo* and *in vitro*. Future optimization of the sensor should seek to improve quantum yield (fluorescent readout) at lower peptide concentrations and to develop red-shifted variants to provide more flexibility in multiplexing NOPLight with other optical tools and sensors. This sensor directly helps to address a longstanding limitation in understanding the real-time dynamics of endogenous peptide release during behavioral epochs. Future applications of neuropeptide sensors such as NOPLight will advance our understanding of the underlying mechanisms by which endogenous opioid peptides control, stabilize and modulate neural circuits to regulate behavior.

3.4 Methods

Ethical statement

Animal procedures were performed in accordance with the guidelines of the European Community Council Directive or the Animal Welfare Ordinance (TSchV 455.1) of the Swiss Federal Food Safety and Veterinary Office and were approved by the Zürich Cantonal Veterinary Office, and the other respective local government authorities (Bezirksregierung Köln, Animal Care and Use Committee of University of Washington).

Molecular cloning and structural modelling

The prototype sensor was designed in silico by sequence alignment (Clustal Omega2) and ordered as a geneblock (Thermo Fisher) flanked by HindIII and NotI restriction sites to be subsequently cloned into pCMV vector (Addgene #111053). For sensor optimization, site directed mutagenesis and Circular Polymerase Extension Cloning was performed by polymerase chain reaction with custom designed primers (Thermo Fisher) using a Pfu-Ultra II fusion High Fidelity DNA Polymerase (Agilent). Sanger sequencing (Microsynth) was performed for all constructs reported in the manuscript. The structural prediction of the NOPLight was generated by a deep learning-based modelling method, RoseTTAFold (Baek et al., 2021).

Cell culture, confocal imaging, and quantification

HEK293T cells (ATCC CRL-3216) were authenticated by the vendor. They were seeded in glass bottom 35-mm (MatTek, P35G-1.4-14-C) or 24-well plates (Cellvis, P24-0-N) and cultured in Dulbecco's modified Eagle's medium (Gibco) with 10% Fetal Bovine Serum (Gibco) and antibiotic-antimycotic (1:100 from 10,000 units/ml penicillin; 10,000 µg/ml streptomycin, 25 µg/ml amphotericin B, Gibco) mix at 37°C and 5% CO2. Cells were transduced at 70% confluency using Effectene transfection kit (QIAGEN) and imaged after 24 – 48 hours.

Primary neuronal cultures were prepared as the following: the cerebral cortex of 18 days old rat embryos was carefully dissected and washed with 5 ml sterile-filtered PBGA buffer (PBS containing 10 mM glucose, 1 mg/ml bovine serum albumin and antibiotic-antimycotic 1:100 (10,000 units/ml penicillin; 10,000 µg/ml streptomycin; 25 µg/ml amphotericin B)). The cortices were cut into small pieces with a sterile scalpel and digested in 5 ml sterile filtered papain solution for 15 min at 37°C. The supernatant was removed, and tissue washed twice with complete DMEM/FCS medium (Dulbecco's Modified Eagle's Medium containing 10% Fetal Calf Serum and penicillin/streptomycin, 1:100). Fresh DMEM/FCS was then added, and the tissue gently triturated and subsequently filtered through a 40-µm cell-strainer. Finally, the neurons were plated at a concentration of 40,000-50,000 cells per well onto the poly-L-lysine (50 µg/ml in PBS) coated 24-well culture plate and incubated overnight at 37°C and 5% CO_2. After 24 hours of incubation, the DMEM medium was replaced with freshly prepared NU-medium (Minimum Essential Medium (MEM) with 15% NU serum, 2% B27 supplement, 15 mM HEPES, 0.45% glucose, 1 mM sodium pyruvate, 2 mM GlutaMAX). Cultured neurons were transduced at 4 days *in vitro* (DIV4) with AAV-DJ-hSynapsin1-NOPLight, AAV1-hSyn1-NES-jRCaMP1b, or AAV-DJ-hSynapsin1-NOPLight-ctr viruses in culture media using a final titer for each virus between $4x10^9$ and $4x10^{10}$ GC/ml and were imaged between DIV19–21. All reagents used are from Gibco.

Confocal images were acquired on an inverted Zeiss LSM 800 microscope with a 488-nm laser for NOPLight and NOPLight-ctr, and a 564-nm laser for Red-Dextran dye and JRCaMP1b. For characterization of the dynamic range, expression level and pharmacological properties, HEK293T cells and/or neurons expressing the construct were first rinsed with HBSS (Gibco) and imaged at a final volume of 100 µL HBSS under a 40x objective. For pharmacological characterizations, the following compounds were used: Nocistatin (Abbiotec); J-113397 (Sigma-Aldrich); UFP-101 (Sigma-Aldrich); RO 64-6198 (Sigma-Aldrich); MCOPPB (Cayman); Orphanin FQ (1-11) (Tocris); Leu-Enkephalin (Cayman); Met-Enkephalin (Cayman); Dynorphin A (Cayman); Dynorphin B (Cayman); β-Endorphin (Sigma-Aldrich); γ-Aminobutyric acid (Sigma-Aldrich);

Dopamine hydrochloride (Sigma-Aldrich), Acetylcholine bromide (Sigma-Aldrich), Glutamate (Sigma-Aldrich). All compounds are diluted to the desired final concentration in HBSS before experiment except RO 64-6198 and J-113397, which were diluted in <0.02% DMSO. All ligands were carefully pipetted into the imaging buffer during experiment. To determine the apparent affinity of the sensor, HEK293T cells and neurons cultured in glass bottom 24-well plates were rinsed with HBSS and imaged under a 20x objective with a final buffer volume of 500 µL HBSS. Ligands were manually applied on the cells during imaging to reach the desired final concentration.

$\Delta F/F_0$ was determined as the ratio of change in fluorescence signal change upon ligand activation and the baseline fluorescence level

$$\frac{F_t - F_0}{F_0} \quad (1)$$

where F_0 is determined as the mean intensity value over the baseline imaging period.

$$F_0 = \frac{1}{n}\sum_{t=0}^{t=n} F_t \quad (2)$$

Unless stated otherwise, only pixels corresponding to cell membrane were considered as regions of interest (ROIs) and thus included in the analysis. ROIs were selected by auto-thresholding function of ImageJ and confirmed by visual inspection.

Kinetic measurements and analysis

To obtain the time constant for sensor activation, red fluorescent dye Antonia Red-Dextran (3000 M.W., Sigma-Aldrich) and N/OFQ (MedChem Express) were simultaneously applied in bolus to sensor-expressing HEK293T cells at 37°C with a stage-top incubator (Tokai Hit). Fluorescent signals were excited at 488 nm (NOPLight) and 561 nm (Red-Dextran dye) and recorded using the high-speed line-scan function (Zeiss LSM 800) at 800Hz. The onset latency of each

experiment was first determined by calculating the time for the red-dextran fluorescent signal to reach 85% percent of maximal value at the plateau. Only experiments with an onset latency smaller than 50 ms were considered in subsequent analysis to minimize the contribution of N/OFQ peptide diffusion to the temporal profile of sensor response. Membrane-corresponding pixels were first selected by thresholding pixel-wise $\Delta F/F_0$ at 65% criteria. Fluorescent signal change of each membrane pixel was then normalized and fitted by a mono-exponential association model using custom-written MATLAB script to derive the time constant τ_{on}.

To obtain the time constant for ligand wash-off, HEK293T cells were cultured on Poly-D-Lysine (Gibco) coated 18-mm coverslips in Dulbecco's modified Eagle's medium (Gibco) with 10% Fetal Bovine Serum (Gibco) and antibiotic-antimycotic (1:100 from 10,000 units/ml penicillin; 10,000 µg/ml streptomycin, 25 µg/ml amphotericin B, Gibco) mix at 37°C and 5% CO2. Cells were transduced at 70% confluency using Effectene transfection kit (QIAGEN) and imaged after 24 – 48 hours. On the day of recording, coverslips with NOPLight expressing HEK293T cells were transferred to the imaging chamber perfused with 37°C HBSS (Gibco). Fluorescence response was obtained with a blue (469 nm) LED (Colibri 7, Zeiss) on an upright Axio Examiner A1 microscope (Zeiss) using an N-Achroplan 10x/0.3 M27 objective (Zeiss). Images were collected at a sampling rate of 1 Hz (Live Acquisition, Thermo Fisher Scientific). For wash-off experiments, N/OFQ was added into the imaging chamber to a final concentration of 500 nM with the perfusion flow turned off. The perfusion system was turned on after 30 s of ligand application to allow equilibrium of sensor response. For puffed application experiments, a glass pipette mounted on a microinjector (Nanoject II™ Drummond) filled with N/OFQ was place near the imaged field of view. 50 nL of 100 µM N/OFQ was puffed onto the cells at a rate of 50 nL/s. Regions of interest for quantification of the fluorescence response was selected in Fiji (Image J). All cell membranes in the field of view were selected for analysis for wash-off experiments, whereas in puffed application experiments, only cell membranes within the radius of ½ of the glass pipette diameter

were selected. A mono-exponential decay model was fitted to the data using Curve Fitting Toolbox (MATLAB) to deduce the time constant τ_{off}.

One-photon spectral characterization

One-photon fluorescence excitation (l_{em} = 560 nm) and emission (l_{exc} = 470 nm) spectra were determined using a Tecan M200 Pro plate reader at 37°C. HEK293T cells were transfected with Effectene transfection kit (QIAGEN). 24 hours after transfection cells were dissociated with Versene (Thermo Fisher) and thoroughly washed with PBS. Next, cells were resuspended in PBS to a final concentration of 3.3 x 10^6 cells/mL and aliquoted into two individual wells of a 96-well microplate with or without ligand (N/OFQ or RO 64-6198, 1 µM), together with two wells containing the same amount of non-transfected cells to account for autofluorescence and a single well containing PBS to determine the Raman bands of the solvent. To determine the excitation and emission spectra of NOPLight at various pH, PBS was adjusted to the desired pH using 10 M HCl or 10 M NaOH.

Two-photon brightness characterization

Two-photon brightness profiles of NOPLight were obtained from HEK293T cells before and after addition of N/OFQ (1 µM). Cells were transfected with Lipofectamine 3000 and were imaged 24 hours post transfection. The medium was replaced with PBS prior to imaging in order to avoid DMEM autofluorescence. The two-photon spectra were acquired as described previously (Duffet et al., 2022).

Virus production

The adeno associated virus (AAV) encoding NOPLight was produced by the Viral Vector Facility at the University of Zurich (VVF). The AAVs encoding the NOPLight-ctr sensor and the Cre-dependent NOPLight were produced by Vigene Biosciences. All other viruses used in this study

were obtained either from the VVF or Addgene. The viruses used in this study were: AAVDJ-hSyn-NOPLight, $4.1x10^{13}$ GC/ml; AAVDJ-hSyn-NOPLight-ctr, $2.9x10^{13}$ GC/ml; AAVDJ-hSyn-FLEX-NOPLight, $2.5x10^{13}$ GC/ml; AAV5-EF1a-DIO-HA-hM3D(Gq)-mScarlet, $1.7x10^{13}$ GC/ml; AAV5-DIO-hSyn-mCherry, $2.4x10^{12}$ GC/ml; AAV8-hSyn-DIO-hM3Dq.mcherry, $1x10^{13}$ GC/ml; AAV-DJ-EF1a_DIO-GCaMP6m $1.2x10^{13}$ GC/ml; AAV1-hSyn1-NES-jRCaMP1b, $6.9x10^{12}$ GC/ml.

Animals

Ten- to 24-week-old, wild-type C57BL/6 mice, PNOC-Cre (as described previously, (Jais et al., 2020; Parker et al., 2019)) and OPRL1-Cre mice were used in this study. Animal procedures were performed in accordance with the guidelines of the European Community Council Directive or the Animal Welfare Ordinance (TSchV 455.1) of the Swiss Federal Food Safety and Veterinary Office and were approved by the Zürich Cantonal Veterinary Office, and the other respective local government authorities (Bezirksregierung Köln; Animal Care and Use Committee of University of Washington). Mice were housed in the animal facility at 22–24 °C on a 12h/12h reverse light/dark cycle (7:00AM lights off) in ventilated cages receiving standard chow and water access ad libitum. Animals placed in the Pavlovian and operant conditioning paradigms were food restricted down to ~90% of their ad libitum body weight beginning one-week prior to conditioning for the entire duration of the paradigm.

Stereotaxic surgery, viral vector injection, and optic fiber implantation in the VTA

Following a minimum of seven days of acclimation to the holding facility, mice were initially anesthetized in an induction chamber (1-4% isoflurane) and placed into a stereotaxic frame (Kopf Instruments, Model 1900) where anesthesia was maintained at 1-2% isoflurane. Depending on the specific experimental paradigm, mice received viral injections either unilaterally or bilaterally using a blunt neural syringe (86200, Hamilton Company) at a rate of 100nL/min. For exogenous pharmacology experiments, wild-type (WT) mice were injected with AAV-DJ-hSyn-NOPLight

(200-500 nL, viral titer 2-4 x 10^{12} vg/mL) or AAV-DJ-hSyn-NOPLight-ctr (300 nL, viral titer 2.9 x 10^{13} vg/mL) and OPRL1-Cre mice were injected with AAV-DJ-hSyn-FLEX-NOPLight (300 nL, viral titer 2.5 x 10^{13} vg/mL). For chemogenetic experiments, PNOC-Cre mice were co-injected with a 1:1 mix of AAV-DJ-hSyn-FLEX-NOPLight (300 nL, viral titer 2.5 x 10^{12} vg/mL) and either AAV5-EF1a-DIO-HA-hM3D(Gq)-mScarlet (300 nL, viral titer 1.7 x 10^{13} vg/mL) or AAV5-DIO-hSyn-mCherry (300 nL, viral titer 2.4 x 10^{12} vg/mL).

For head-fixed behavioral experiments, WT mice were injected with AAV-DJ-hSyn-NOPLight (300 nL, viral titer 4.1 x 10^{12} vg/mL). For freely moving tail lift experiments, PNOC-Cre mice were injected with AAV-DJ-EF1a-DIO-GCaMP6m (300nL, viral titer 1.2 x 10^{13} vg/mL); OPRL1-Cre mice were injected with AAV-DJ-hSyn-FLEX-NOPLight (300nL, viral titer 2.5 x 10^{12} vg/mL); WT mice were injected with AAV-DJ-hSyn-NOPLight-ctr (300nL, viral titer 2.9 x 10^{12} vg/mL). For freely moving reward seeking experiments (Pavlovian conditioning, operant conditioning, progressive ratio test), WT mice were injected with AAV-DJ-hSyn-NOPLight (300 nL, viral titer 4.1 x 10^{13} vg/mL).

All viruses were injected into the VTA (stereotaxic coordinates from Bregma: -3.3 to -3.4 AP, +1.6 ML, -4.75 to -4.3 DV) at a 15° angle, with an optic fiber (4.5 mm fiber length, 400 µm core, 2.5 mm diameter ferrule, Doric) implanted above the injection site. For animals undergoing head-fixed behaviors, a stainless-steel head-ring was also secured to allow for head fixation. All implants were secured using Metabond (C & B Metabond). Animals were allowed to recover from surgery for a minimum of 3 weeks before any behavioral testing, permitting optimal viral expression.

Tissue preparation and immunohistochemistry (IHC)

Animals were transcardially perfused with 0.1 M phosphate-buffered saline (PBS) followed by 40 mL 4% paraformaldehyde (PFA). Brains were extracted and post-fixed in 4% PFA overnight and then transferred to 30% sucrose in PBS for cryoprotection. Brains were sectioned at 30 µm on a

microtome and stored in a 0.1 M phosphate buffer at 4°C prior to immunohistochemistry. For behavioral cohorts, viral expression and optical-fiber placements were confirmed before inclusion in the presented datasets. Immunohistochemistry was performed as previously described (Al-Hasani et al., 2013; Kim et al., 2013). In brief, free-floating sections were washed in 0.1 M PBS for 3 x 10 min intervals. Sections were then placed in blocking buffer (0.5% Triton X-100 and 5% natural goat serum in 0.1 M PBS) for 1 hour at room temperature. After blocking buffer, sections were placed in primary antibody (chicken anti-GFP, 1:2000, Abcam) overnight at 4°C. After 3 x 10 min 0.1 M PBS washes, sections were incubated in secondary antibody (AlexaFluor 488 goat anti-chicken, Abcam) for 2 hours at room temperature, followed by another round of washes (3 x 10 min in 0.1 M PBS, 3 x 10 min in 0.1 M PBS). After immunostaining, sections were mounted and coverslipped with Vectashield HardSet mounting medium containing DAPI (Vector Laboratories) and imaged on a Leica DM6 B microscope.

Generation of OPRL1-Cre mouse line and reporter crosses

OPRL1$^{iresCre:GFP}$ knock-in mice were generated at the University of Washington. A cassette encoding IRES-mnCre:GFP was inserted just 3' of the termination codon in the last coding exon of the *Oprl1* gene. The 5′ arm (12 kb with *Pac*I and *Sal*I sites at 5' and 3'ends, respectively) and 3′ arm (3.5 kb with *Xho*I and *Not*I sites at 5'and 3' ends, respectively) of the OPRL1 gene were amplified from a C57BL/6 BAC clone by PCR using Q5 Polymerase (New England Biolabs) and cloned into polylinkers of a targeting construct that contained IRES-mnCre:GFP, a frt-flanked Sv40Neo gene for positive selection, and HSV thymidine kinase and *Pgk*-diphtheria toxin A chain genes for negative selection. The IRES-mnCre:GFP cassette has an internal ribosome entry sequence (IRES), a myc-tag and nuclear localization signals at the N-terminus of Cre recombinase, which is fused to green fluorescent protein followed by a SV40

polyadenylation sequence (Cre:GFP). The construct was electroporated into G4 ES cells (C57Bl/6 × 129 Sv hybrid) and correct targeting was determined by Southern blot of DNA digested with *BamHI* using a 32P-labeled probe downstream of the 3′ arm of the targeting construct. Five of 77 clones analyzed were correctly targeted. One clone that was injected into blastocysts resulted in good chimeras that transmitted the targeted allele through the germline. Progeny were bred with *Gt(Rosa)26Sor*-FLP recombinase mice to remove the frt-flanked SV-Neo gene. Mice were then continuously backcrossed to C57Bl/6 mice.

To visualize OPRL1-Cre expression in the VTA, OPRL1-Cre mice were crossed to the Ai3 EYFP flox-stop reporter line (Jackson Lab, #007903). Adult OPRL1-Cre x Ai3 mice were transcardially perfused with 0.1 M phosphate-buffered saline (PBS) followed by 40 mL of 4% paraformaldehyde (PFA). Brains were extracted and post-fixed in 4% PFA overnight and then transferred to 30% sucrose in PBS for cryoprotection. Brains were sectioned at 30 µm on a microtome and stored in a 0.1 M phosphate buffer at 4°C. Midbrain sections were mounted on Super Frost Plus slides (ThermoFisher) and coverslipped with Vectashield HardSet mounting medium containing DAPI (Vector Laboratories) and imaged on a Leica DM6 B microscope.

RNAscope fluorescent in situ hybridization (FISH)

Immediately after rapid decapitation of OPRL1-Cre mice (n = 2), brains were extracted, flash frozen in -50°C 2-methylbutane, and then stored at -80°C. Brains were sectioned coronally into 15 µm slices on a cryostat at -20°C, mounted onto Super Frost Plus slides (Fisher), and then stored at -80°C prior to RNAScope FISH. FISH was performed according to the RNAScope Fluorescent Multiplex Assay for use with fixed frozen tissues (Advanced Cell Diagnostics, Inc.). Slides with 2-4 brain sections each that contained the VTA were post-fixed in prechilled 10% neutral-buffered formalin for 15 minutes at 4°C, dehydrated in ethanol, and then treated with a

protease IV solution for 30 minutes at 40°C. The sections were then incubated for 2 hours at 40°C with target probes (Advance Cell Diagnostics, Inc.) for mouse *Oprl1* (accession number NM_011012.5, target region 988 – 1937), *Th* (accession number NM_009377.1, target region 483 – 1603), and Cre (target region 2 – 972).

Next, sections underwent a series of probe amplifications (AMP1-4) at 40°C, including a final incubation with fluorescently labelled probes (Alex 488, Atto 550, Atto 647) targeted to the specified channels (C1-C3) that were associated with each of the probes. Finally, sections were stained with DAPI, and slides were coverslipped with Vectashield HardSet mounting medium (Vector Laboratories). Slides were imaged on a Leica TCS SPE confocal microscope (Leica) at 60x magnification, and Fiji and HALO software were used to process images and quantify expression. Images were obtained under consistent threshold and exposure time standards. Leica images were opened and converted to TIFs for compatibility with HALO software. In HALO, cell ROIs were first made using the DAPI channel, and then *Oprl1*+ and Cre+ cells were identified if a fluorescent threshold for each channel was met within the cell ROI. 2-3 separate slices were quantified for each animal.

Fiber photometry recordings

For fiber-photometry studies in the pnVTA, recordings were made continuously throughout the entirety of the pharmacology (30 min), chemogenetic (55 min), head-fixed sucrose (25 min), tail lift (20 min), and conditioned reward-seeking (60 min) sessions. Prior to recording, an optic fiber was attached to the implanted fiber using a ferrule sleeve (Doric, ZR_2.5). In pharmacology and conditioned reward-seeking experiments, a 531-Hz sinusoidal LED light (Thorlabs, LED light: M470F3; LED driver: DC4104) was bandpass filtered (470 ± 20 nm, Doric, FMC4) to excite NOPLight and evoke NOPR-agonist dependent emission while a 211-Hz sinusoidal LED light

(Thorlabs, M405FP1; LED driver: DC4104) was bandpass filtered (405 ± 10 nm, Doric, FMC4) to excite NOPLight and evoke NOPR-agonist independent isosbestic control emission.

In chemogenetics, head-fixed sucrose, and tail lift experiments, a 531-Hz sinusoidal LED light (Thorlabs, LED light: M490F3; LED driver: DC4104) was bandpass filtered (490 ± 20 nm, Doric, FMC6) to excite NOPLight and evoke NOPR-agonist dependent emission while a 211-Hz sinusoidal LED light (Doric, CLED_435; Thorlabs, LED driver: DC4104) was bandpass filtered (435 ± 10 nm, Doric, FMC6) to excite NOPLight and evoke NOPR-agonist independent isosbestic control emission. Prior to recording, a minimum 120s period of NOPLight excitation with either 470-nm and 405-nm or 490-nm and 435-nm light was used to remove the majority of baseline drift. Power output for each LED was measured at the tip of the optic fiber and adjusted to ~ 30 µW before each day of recording. NOPLight fluorescence traveled back through the same optic fiber before being bandpass filtered (525 ± 25 nm, Doric, FMC4 or FMC6), detected with a photodetector system (Doric, DFD_FOA_FC), and recorded by a real-time processor (TDT, RZ5P). The 531-Hz and 211-Hz signals were extracted in real time by the TDT program Synapse at a sampling rate of 1017.25 Hz.

In vivo animal experiments

All animal behaviors were performed within a sound-attenuated room maintained at 23°C at least one week after habituation to the holding room. Animals were handled for a minimum of three days prior to experimentation, as well as habituated to the attachment of a fiber photometry patch cord to their fiber implants. For all experiments, mice were brought into the experimental room and allowed to acclimate to the space for at least 30 min prior to beginning any testing. All experiments were conducted in red light to accommodate the reverse light cycle schedule, unless otherwise stated. All pharmacological interventions were administered in a counterbalanced manner. All sessions were video recorded.

In vivo pharmacology experiments

WT mice injected with either AAV-DJ-hSyn-NOPLight (N = 16) or AAV-DJ-hSyn-NOPLight-ctr (N = 6) and OPRL1-Cre mice injected with AAV-DJ-hSyn-FLEX-NOPLight (N = 3) were allowed to recover a minimum of 3 weeks after surgery (adult male and female, 4-6 months old). Three days before testing they were habituated to handling, fiber photometry cable attachment, and to the behavioral test box. On test day, animals were placed into a 10” x 10” clear acrylic box with a layer of bedding on the floor illuminated by a dim, diffuse white light (~30 lux). Fiber photometry recordings were made using a 405 nm LED as the isosbestic channel and a 470 nm LED as the signal channel. After starting the photometry recording, the mice were free to move around the box with no intervention for 5 min to establish a baseline photometry signal. At 5 min into the recording, NOPLight mice (N = 16) were scruffed and received an intraperitoneal (i.p.) injection of vehicle or 1, 5, or 10 mg/kg of the selective NOPR agonist RO 64-6198 (RO) and were recorded for an additional 25 min. NOPLight-ctr and FLEX-NOPLight mice received an i.p. injection of 10 mg/kg RO 64-6198 5 min into the recording.

Two subsets of the NOPLight animals were recorded on three separate, counterbalanced days (at least 24 hours apart). The first subset (N = 4) received either i) an i.p. injection of 10 mg/kg RO 64-6198 5 min into the recording (RO), ii) an oral gavage (o.g.) treatment with 10 mg/kg of selective NOPR antagonist LY2940094 5 min into the recording (LY), or iii) an o.g. treatment with 10 mg/kg LY2940094 30 min prior to the recording followed by an i.p. injection with 10 mg/kg RO 64-6198 5 min into the recording (LY pretreatment + RO). The second subset (N = 4-9) received either i) an i.p. injection of 10 mg/kg RO 64-6198 5 min into the recording (RO), ii) an i.p. injection of 10 mg/kg of selective NOPR antagonist J-113397 5 min into the recording (J11), or iii) an i.p. injection of 10 mg/kg J-113397 30 min prior to the recording followed by an i.p. injection with 10 mg/kg RO 64-6198 5 min into the recording (J11 pretreatment + RO). For all cohorts, animals were recorded for an additional 25 minutes following RO injection.

In vivo chemogenetics (DREADD) experiments

PNOC-Cre mice co-injected with AAVDJ-hSyn-FLEX-NOPLight and either AAV5-EF1a-DIO-HA-hM3D(Gq)-mScarlet (N = 8) or AAV5-DIO-hSyn-mCherry (N = 3) were allowed to recover a minimum of 3 weeks after surgery (adult male, 4-6 months old). Three days before testing they were habituated to handling, fiber photometry cable attachment, and to the behavioral test box. On test day, animals were placed into the behavioral test box, which was a 10" x 10" clear acrylic box with a layer of bedding on the floor illuminated by a dim, diffuse white light (~30 lux). Fiber photometry recordings were made using a 435 nm LED as the isosbestic channel and a 490 nm LED as the signal channel. After starting the photometry recording, the mice were free to move around the box with no intervention for 10 min to establish a baseline photometry signal. At 10 min into the recording, mice were scruffed and received an intraperitoneal (i.p.) injection of 5 mg/kg clozapine-N-oxide (CNO) and were recorded for an additional 45 min. A subset of the DIO hM3D(Gq) animals (N = 3) were recorded on two separate, counterbalanced days (at least 24 hours apart). On one recording day, they received the CNO treatment and recording timeline described above. On the other recording day, they were administered an oral gavage (o.g.) treatment with 10 mg/kg of the selective NOPR antagonist LY2940094 30 min prior to the photometry recording. The LY-pretreatment group then underwent the same recording timeline and CNO injection (5 mg/kg i.p., after a 10 min baseline) as the CNO only day.

Head-fixed cued sucrose access paradigm

WT mice injected with AAV-DJ-hSyn-NOPLight (N = 7) and implanted with an optic fiber and stainless-steel head-ring to allow for head-fixation during fiber photometry recording were allowed to recover a minimum of 3 weeks after surgery (adult male, 4-6 months old). One week prior to behavioral testing, mice were food restricted down to ~85-90% of their free feeding body weight. For the four days prior to testing, animals were habituated to handling, fiber photometry cable attachment, and head-fixation. Animals were head-fixed to minimize motion-related artefacts in

the fiber photometry signal, and all head-fixed testing was completed using the open-source OHRBETS platform (Gordon-Fennell et al., 2023).

Fiber photometry recordings of NOPLight signal during tone-cued access to 10% sucrose solution were made over two counterbalanced sessions where animals received an i.p. injection 30 min prior to the recording of either i) 20 mg/kg NOPR antagonist J-113397 or ii) vehicle. Each session consisted of a 5-minute baseline period where animals were head-fixed with no stimuli delivery, 15 tone-cued sucrose trials, and then a 5-minute baseline period at the end of the session (25 minutes total). Each cued sucrose trial consisted of a 5-second auditory tone (4kHz, 80dB) immediately followed by a 5-second extension of a retractable lick spout and delivery of five pulses of 10% sucrose solution (~1.5 µL/pulse, 200ms inter-pulse interval) where mice could lick the spout to consume the solution. Cued sucrose trials were separated by a variable inter-trial interval of 45 to 75 seconds.

All behavioral hardware was controlled using an Arduino Mega 2560 REV3 (Arduino) and custom Arduino programs. Individual licks were detected using a capacitive touch sensor (Adafruit MPR121) that was attached to the retractable lick spout. The pulsed sucrose delivery was controlled by a solenoid (Parker 003-0257-900). The timing of solenoid openings and lick events were recorded and synchronized with the photometry signal via TTL communication from the Arduino Mega to the fiber photometry system. Fiber photometry recordings were made using a 435 nm LED as the isosbestic channel and a 490 nm LED as the signal channel.

Tail lift behavioral experiments

PNOC-Cre mice injected with AAV-DJ-EF1a-DIO-GCaMP6m (N = 4), OPRL1-Cre mice injected with AAV-DJ-hSyn-FLEX-NOPLight (N = 3), and WT mice injected with AAV-DJ-hSyn-NOPLight-ctr (n = 3) were allowed to recover a minimum of 3 weeks after surgery (adult male, 10-14 weeks old). Three days before testing they were habituated to handling, fiber photometry cable attachment, and to the behavioral test box. On test day, animals were placed into the behavioral

test box, which was a 10” x 10” clear acrylic box illuminated by a dim, diffuse white light (~30 lux). Fiber photometry recordings were made using a 435-nm LED as the isosbestic channel and a 490-nm LED as the signal channel. After starting the photometry recording, mice were free to move around the box with no intervention for 5 minutes to establish a baseline photometry signal. After the 5-minute baseline, mice underwent four tail lift trials where they were suspended by the tail for 10 seconds and then gently returned to the behavioral test box. Tail lift trials were separated by a variable inter-trial interval of 120-300 seconds. All suspensions were made to the same height. After the final trial, photometry recording continued for an additional 5 minutes to establish a post-test signal baseline.

Reward-seeking (Pavlovian, operant) conditioning paradigms

One week prior to Pavlovian conditioning and 3 weeks after surgery, WT fiber photometry mice expressing AAV-DJ-hSyn-NOPLight in the VTA (N = 4) were food restricted down to ~85-90% of their free feeding body weight (adult male, 4 months old). All reward-seeking training was completed in Med-Associates operant conditioning boxes (ENV-307A). Fiber photometry recordings were made using a 405nm LED as the isosbestic channel and a 470 nm LED as the signal channel. Mice were first trained to associate illumination of a house light (CS, 5 s) with delivery of a single sucrose pellet (US) occurring immediately after the house light turned off. A randomized intertrial interval of between 30-120 s separated consecutive trials. Pavlovian conditioning sessions lasted for 60 min, during which between 36-38 rewards were presented. Pavlovian conditioning was repeated over 5 days a total of 5 times, with simultaneous fiber photometry recordings made during session 1 and session 4.

Animals were then moved onto a fixed ratio 1 (FR1) schedule for 5 days (60 min/session), where they were required to perform a nose-poke in the active nosepoke port one time to receive the 5 s house light cue and subsequent pellet delivery. Pokes made into the inactive port had no effect. Simultaneous fiber photometry recordings were made during FR1 sessions 1 and 4.

Following FR1 training, the ratio was increased to an FR3 schedule for 4 days (60 min/session) requiring the mice to perform 3 active port nosepokes to receive the house light cue and a sucrose pellet, with simultaneous photometry recording during session 3. Last, mice were placed in a single, 120 min session on a progressive ratio schedule (PR) where the nose-poke criteria for each subsequent reward delivery followed the geometric progression $n_i = 5e^{i/5} - 5$ (1, 2, 4, 6, 9, 12…), increasing in an exponential manner.

Data analysis for photometry recordings

Custom MATLAB scripts were developed for analyzing fiber-photometry data in the context of mouse behavior. A linear least squares (LLS) fit was applied to the control signal (405 or 435 nm) to align and fit it to the excitation signal (470 or 490 nm). For pharmacology and chemogenetics experiments where the entire length of the recording was analyzed to evaluate long-term changes in NOPLight fluorescence following drug injection, LLS fit was calculated using the recording's 'baseline' period that preceded the injection (first 5 or 10 min) and the fitted isosbestic signal was subtracted from the excitation signal to detrend bleaching and remove movement artefacts. To reduce high-frequency noise, data were down-sampled by a factor of 300. The processed fiber photometry trace was then smoothed across a rolling 10 s window, and z-scored relative to the mean and standard deviation of the baseline period preceding drug injection (first 5 or 10 min of the recording for pharmacology and chemogenetics experiments, respectively).

For all behavioral experiments (head-fixed sucrose, tail lift, conditioned reward seeking) where short epochs were evaluated, decay from bleaching was first detrended by fitting a 4th degree polynomial function to the raw signal and isosbestic traces, then dividing by the resulting curve. Next, the LLS fit of the isosbestic signal to the excitation signal was calculated over the entire session and the excitation signal was normalized by dividing the resulting fitted isosbestic signal. To reduce high-frequency noise, data were down-sampled by a factor of 100. The processed traces were then smoothed across a rolling 1 s window, extracted in windows

surrounding the onset of relevant behavioral events (e.g., nose poke, cue onset, reward delivery, tail lift), z-scored relative to the mean and standard deviation of each event window, and then averaged. The post-processed fiber photometry signal was analyzed in the context of animal behavior during Pavlovian conditioning and operant task performance.

Statistics and reproducibility

All data were averaged and expressed as mean ± SEM unless specified otherwise. Statistical significance was taken as *p < 0.05, ** p < 0.01, ***p < 0.001, and ****p < 0.0001, as determined by Mann-Whitney test, Wilcoxon test, two-way repeated-measures ANOVA followed by Bonferroni post hoc tests as appropriate. All N values for each experimental group are described in the corresponding figure legend. All *in vitro* and *ex vivo* experiments were performed at least three times independently with similar results. For behavioral experiments, group size ranged from N = 3 to N = 16. Statistical analyses were performed in GraphPad Prism 9 (GraphPad, La Jolla, CA) and MATLAB 9.9 (The MathWorks, Natick, MA). No data were excluded from the analyses. Group allocations used in this study were randomly assigned to animals and/or cultured cells. The Investigators were not blinded to allocation during experiments and outcome assessment.

3.5 Acknowledgements

These results are part of a project that has received funding from the European Research Council (ERC) under the European Union's Horizon 2020 research and innovation program (Grant agreement No.s 891959 and 101016787 to TP; 742106 to JCB). We also acknowledge funding from the University of Zürich Forschungskredit (FK-20-042, XZ), the Swiss National Science Foundation (Grant No. 310030_196455, TP; PCEFP3_181282, MS), the NIMH P50MH119467 (MRB), the NIH/NIDA F31 F31DA059438-01A1 (CS), and the Deutsche Forschungsgemeinschaft (401832153, 431549029, EXC 2030-390661388, P.K). We would like to thank Jean-Charles

Paterna and the Viral Vector Facility of the Neuroscience Center Zürich (ZNZ) for the kind help with virus production.

3.6 Author Contributions

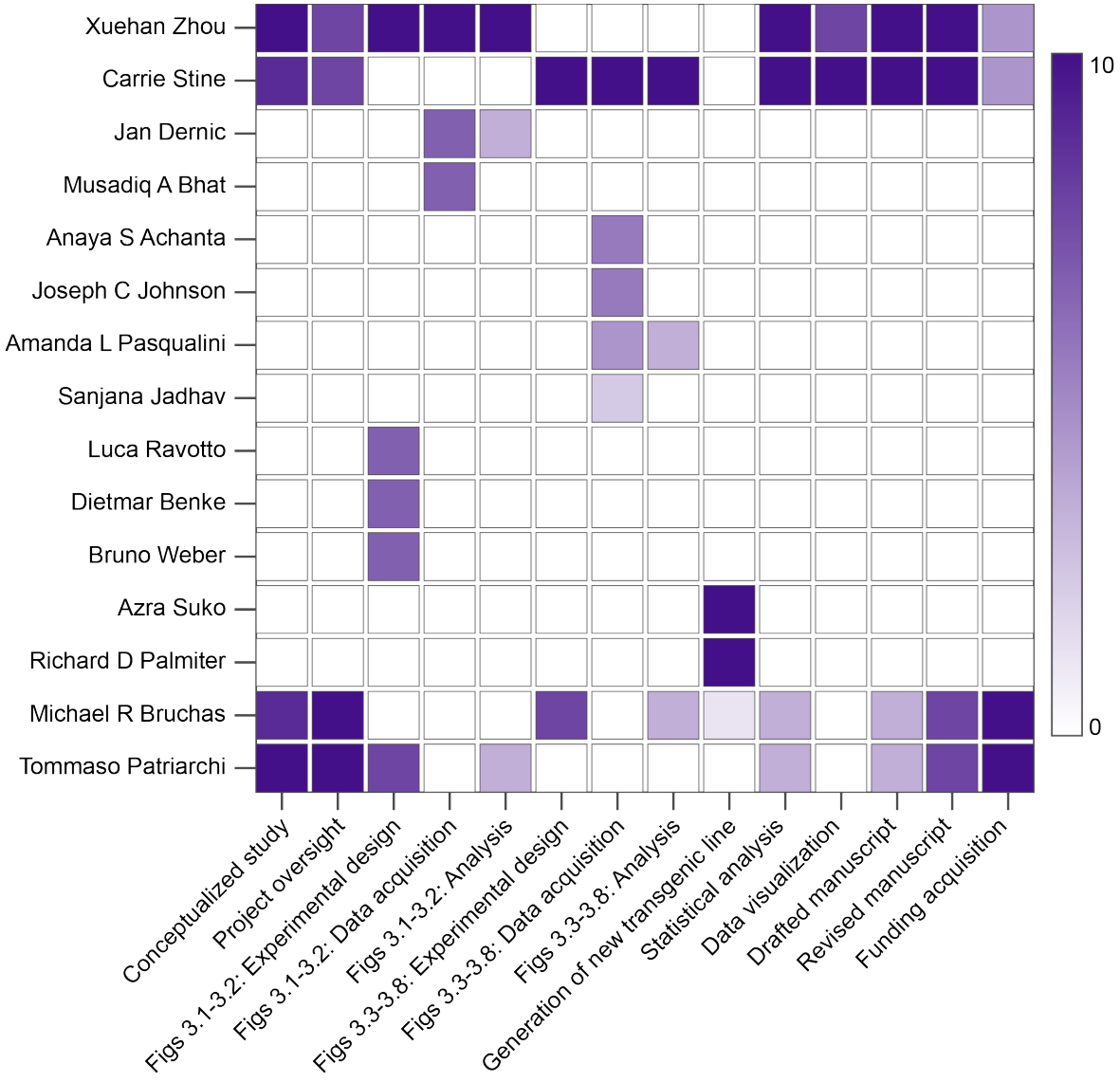

CHAPTER 4: Stress-dependent modulation of nociceptin opioid peptide neurons in the ventral tegmental area.

This chapter includes results and figures adapted from the following preprint:

> **Stine C*,** Marcus DJ, Pasqualini AL, Achanta AS, Johnson JC, Jadhav S, Bruchas MR. Identification of a stress-sensitive endogenous opioid-containing neuronal population in the paranigral ventral tegmental area. *bioRxiv,* 2025.

4.1 Introduction

Recent studies have expanded on the molecular complexity of the ventral tegmental area (VTA) by revealing diverse neuropeptide subpopulations, released both by the VTA itself and by upstream inputs such as the lateral hypothalamus (LH), that have significant influence over critical mesolimbic reward circuitry (Anderegg et al., 2015; Morales and Margolis, 2017; Perez-Bonilla et al., 2020; Poulin et al., 2018). Among these subpopulations, neurons in the paranigral nucleus of the VTA (pnVTA) enriched with the endogenous opioid peptide nociceptin/orphanin FQ (N/OFQ) have recently emerged as key regulators of motivated behavior (Parker et al., 2019). Our group previously reported that activation of these N/OFQ-expressing pnVTA neurons ($pnVTA^{PNOC}$ neurons) suppresses motivated reward-seeking behavior and drives aversive responses. Notably, N/OFQ signaling through its cognate G-protein coupled receptor NOPR, which is largely expressed on VTA dopamine neurons (Norton et al., 2002), negatively regulates dopamine tone (Zheng et al., 2002), paralleling the effects of stress (Bouarab et al., 2019; Lowes and Harris, 2022). Despite widespread implications of N/OFQ in stress responses (Gavioli et al., 2021), whether stress impacts this particular $pnVTA^{PNOC}$ population which is critically situated to regulate motivation and reward-related behaviors remains unexplored.

Here we employed *in vivo* calcium imaging to monitor $pnVTA^{PNOC}$ neuronal dynamics during exposure to various acute stressors including foot shock, tail suspension, and predator-related stimuli. We also examined their engagement during risk avoidance, or anxiety-like

exploratory behaviors. To further isolate the putative upstream circuitry underlying pnVTA^{PNOC} activation, we investigated synaptic inputs from the lateral hypothalamus (LH), a key region implicated in stress and motivation with known influence in the VTA on the expression of motivated behaviors (Kempadoo et al., 2013; Nieh et al., 2016). By combining optogenetics, electrophysiology, and behavioral assays, we aimed to uncover the connectivity and functional relevance of LH projections to pnVTA^{PNOC} neurons during stress exposure.

This study identifies the selective sensitivity of pnVTA^{PNOC} neurons to physical, environmental, and predatory forms of stress. Moreover, we identify the LH as a significant afferent input to pnVTA^{PNOC} neurons, offering a mechanistic basis for their engagement during stress. These findings contribute to a growing understanding of VTA circuitry in stress processing and identify pnVTA N/OFQ neurons as a tenable bridge between stress and motivated behavior.

4.2 Results

4.2.1 pnVTA^{PNOC} neurons exhibit sustained activity during acute stress exposure across varied stress conditions.

N/OFQ-containing neurons in the pnVTA (pnVTA^{PNOC} neurons) act to suppress motivated behaviors. Stress is also known to disrupt motivation, but despite evidence linking N/OFQ with stress, the impact of stress on the activity of this population remains unknown. Importantly, the effects of stress exposure on motivation can vary depending on the form and duration of the stressor. To evaluate the effects of diverse stress conditions on pnVTA^{PNOC} activity, we injected PNOC-Cre mice with a Cre-dependent GCaMP6s (AAV-DJ-Ef1a-DIO-GCaMP6s) and implanted optic fibers in the paranigral ventral tegmental area (pnVTA) to record the calcium activity of pnVTA N/OFQ neurons (pnVTA^{PNOC}) during exposure to a variety of stressful stimuli (**Figure 4.1a, b**). At 3-4 weeks post injection we detected robust, transient activation of pnVTA^{PNOC} neurons in response to a mild foot shock (**Figure 4.1c–f**, 1-way ANOVA $F_{3,24}$=14.26, p<0.0001), the onset and offset of a 20-second tail lift (**Figure 4.1g–i**, 1-way ANOVA $F_{4,44}$=10.94, p<0.0001), and a brief

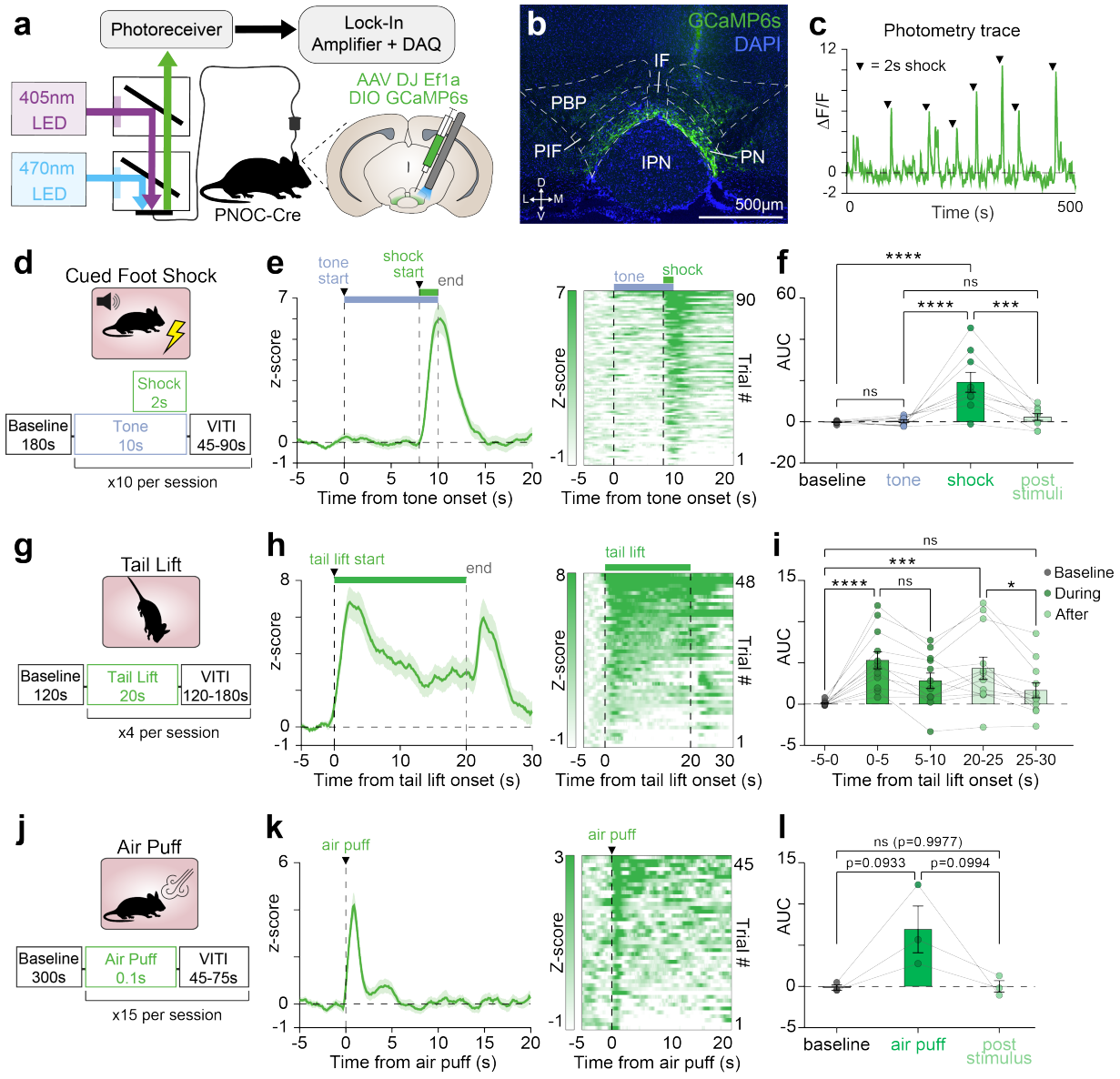

Figure 4.1: pnVTA^{PNOC} neuron activity during exposure to acute stressors.

(a) Fiber photometry schematic and cartoon of DIO-GCaMP6s (GCaMP6s) viral injection and fiber implant in the pnVTA of PNOC-Cre mice. **(b)** Representative image showing DAPI (blue) and GCaMP6s (green) expression in pnVTA. **(c)** Representative trace of GCaMP6s ΔF/F fluorescence throughout a cued foot shock session. Black arrows are aligned with foot shock onset. **(d)** Trial structure for a cued foot shock session (10s tone co-terminating with 2s 0.5 mA shock). **(e)** Left: Averaged trace of pnVTA^{PNOC} GCaMP6s activity during epoch surrounding tone-cued foot shock, aligned to tone onset. Right: Heat map of GCaMP6s fluorescence during same epoch, each row correspond to a trial in the averaged trace (left). (N = 9 mice). **(f)** Area under the curve (AUC) for averaged traces from **e**, calculated over 8-second intervals surrounding cued-foot shock events. GCaMP6s signal increases in response to shock but not tone (1-way ANOVA with Tukey's test, ****p < 0.0001, ***p < 0.001, N = 9 mice). **(g–i)** Same as **d–f** but for pnVTA^{PNOC} GCaMP6s activity during 20s tail lift. Activity averaged in 5-second intervals surrounding each tail lift shows increases first during tail lift and again when animal is lowered to the ground (1-way ANOVA with Tukey's test, ****p < 0.0001, ***p < 0.001, *p < 0.05, N = 12 mice). **(j–l)** Same as **d–f** but for pnVTA^{PNOC} GCaMP6s activity during acute air puff (0.1s, 20 PSI). Activity averaged in 5-second intervals surrounding each air puff (1-way ANOVA with Tukey's test, N = 3 mice). All data represented as mean ± SEM.

0.1s air puff delivered to the whiskers (**Figure 4.1j–l**, 1-way ANOVA $F_{2,4}$=5.417, p=0.0727). Interestingly, pnVTA^{PNOC} activity was time-locked with the duration of the stressor, returning quickly to baseline levels following the 0.1s air puff or 2s foot shock, but remaining elevated throughout the 20s tail suspension (**Figure 4.1e, h, k**). Across these stressors we observed similar activity in both male and female mice, although foot shock elicited a larger response in females (**Figure S4.1a, b**). Notably, pnVTA^{PNOC} neurons were not activated in response to the 10s tone preceding each foot shock (**Figure 4.1e, f**, Tukey's test baseline vs. tone p=0.9993), suggesting that pnVTA^{PNOC} neurons have selective sensitivity to stress rather than simply responding indiscriminately to any salient stimuli.

We next evaluated pnVTA^{PNOC} dynamics during innately anxiogenic exploratory behaviors (**Figure 4.2a**). In the open field test (OFT), we detected a significant increase in calcium activity as animals transitioned from the 'safe' edge of the arena to the open, 'risky' center (**Figure 4.2b, d**, 1-way ANOVA $F_{2,30}$=16.18, p<0.0001). We observed a similar increase in the elevated zero maze (EZM) as animals entered the unprotected open arms of the maze (**Figure 4.2c, e**, 1-way ANOVA $F_{2,30}$=6.305, p=0.0052). No sex-dependent effects were identified in either OFT or EZM (**Figure S4.1c, d**) These findings demonstrate that pnVTA^{PNOC} neurons are also engaged by innately stressful environmental stimuli.

4.2.2 Predator odor stress engages pnVTA^{PNOC} neurons in both sexes, while predator looming stress elicits a response only in males.

We further characterized the stress sensitivity of pnVTA^{PNOC} neurons by recording calcium activity following different predatory stressors (**Figure 4.3a**). When exposed to a looming stimulus that mimics the threat of an overhead predator, male mice displayed a significant increase in pnVTA^{PNOC} calcium activity while females did not (**Figure 4.3b, c,** 2-way ANOVA males vs. females $F_{1,10}$=11.14, p=0.0075). We also assessed pnVTA^{PNOC} calcium activity dynamics in response to an aversive predator odor (2% 2MT, a predator urine derivative (Isosaka et al., 2015))

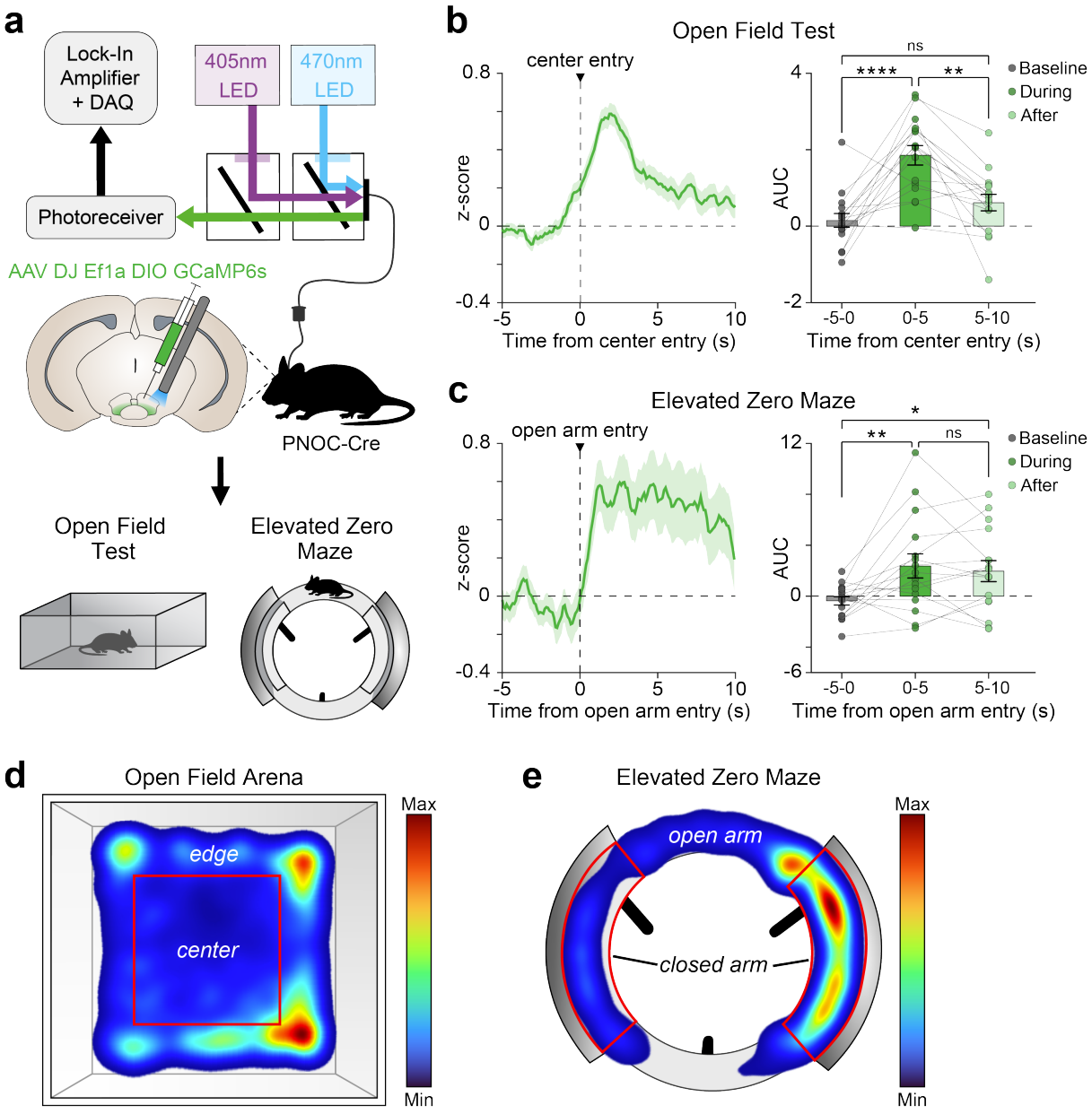

Figure 4.2: Anxiogenic exploratory behaviors drive pnVTA^{PNOC} activity.

(a) Cartoon of DIO-GCaMP6s (GCaMP6s) injection and fiber implant into pnVTA of PNOC-Cre mice. GCaMP6s activity was recorded during open field test (OFT) and elevated zero maze (EZM). **(b)** Left: Averaged traces of pnVTA^{PNOC} GCaMP6s activity during high-anxiety epochs of the OFT, aligned to entries into the center zone of the open field arena. Right: Area under the curve (AUC) for averaged traces (left) calculated over 5-second intervals surrounding center zone entry. GCaMP6s activity increases during and immediately after center entry (1-way ANOVA with Tukey's multiple comparisons test, ****$p < 0.0001$, **$p < 0.01$, N = 16 mice). **(c)** Same as **b** but for pnVTA^{PNOC} GCaMP6s activity during high-anxiety epochs of the EZM, aligned to entries into either open arm of the maze (1-way ANOVA with Tukey's multiple comparisons test, **$p < 0.01$, *$p < 0.05$, N = 16 mice). **(d)** Heat map from a representative animal showing proportion of time spent in each area of the open field arena. Heat map shows more time spent around the edge than in the center. **(e)** Same as **d** but showing proportion of time spent in each area of the elevated zero maze. Heat map shows more time spent in the closed arms than in the open arms. All data represented as mean ± SEM.

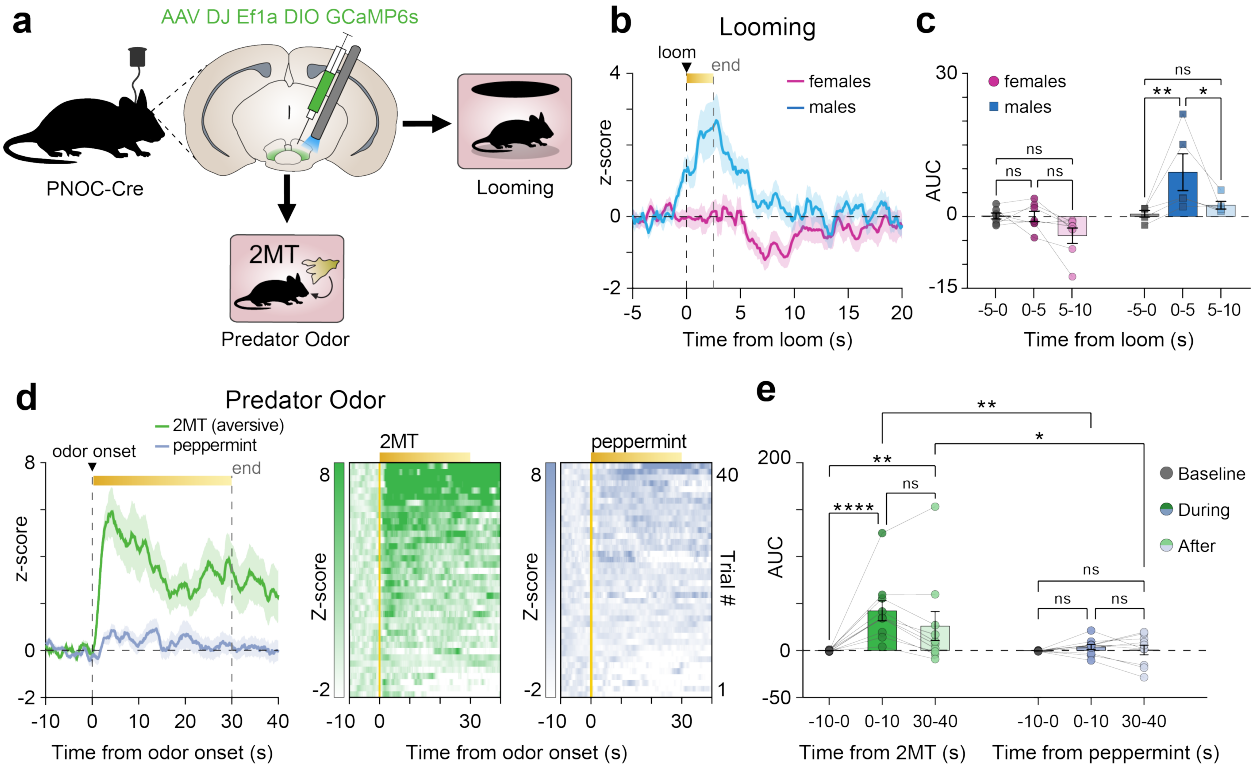

Figure 4.3: pnVTA^{PNOC} neuron activation in response to predatory threat.

(a) Cartoon of DIO-GCaMP6s (GCaMP6s) injection and fiber implant into pnVTA of PNOC-Cre mice. GCaMP6s activity was recorded during looming or exposure to predator odor. **(b)** Averaged traces of pnVTA^{PNOC} GCaMP6s activity for males (blue, N = 5 mice) and females (magenta, N = 7 mice) aligned to looming onset. **(c)** Area under the curve (AUC) for averaged traces from **b** for females (left, magenta) and males (right, blue), calculated over 5-second intervals. GCaMP6s activity increases during and immediately after looming in males, but not females (2-way ANOVA with Tukey's multiple comparisons test, **p < 0.01, *p < 0.05, N = 5 males, 7 females). **(d)** Left: Averaged traces of pnVTA^{PNOC} GCaMP6s activity surrounding 30-second exposure to either predator odor (2% 2MT, green) or a control non-predator odor (2% peppermint oil, blue). Right: Heat map of GCaMP6s fluorescence during same epoch, each row correspond to a trial in the averaged trace (left). (N = 10 mice). **(e)** AUC for averaged traces from **d** calculated over 10-second intervals surrounding exposure to either the 2MT predator odor (left, green) or the peppermint oil (right, blue). pnVTA^{PNOC} GCaMP6s activity increases during 2MT but not peppermint oil exposure (2-way ANOVA with Tukey's multiple comparisons test, ****p < 0.0001, **p < 0.01, *p < 0.05, N = 10 mice). All data represented as mean ± SEM.

and a non-aversive novel odor (2% peppermint oil), which served as a control for salience (**Figure 4.3d**). The aversive 2MT predator odor evoked a robust, sustained increase in calcium activity, whereas the non-aversive peppermint odor elicited no response (**Figure 4.3e**, 2MT: 2-way ANOVA $F_{4,32}$=5.713, p=0.0014; peppermint oil: 2-way ANOVA $F_{4,32}$=0.3368, p=0.8511). These data are consistent with our initial findings that pnVTA^{PNOC} neurons are selectively activated by stressful stimuli, while also revealing a sex-dependent effect in response to certain predatory stressors.

4.2.3 Lateral hypothalamic connectivity onto pnVTA^{PNOC} neurons

The VTA receives heterogeneous inputs from stress-related regions throughout the brain, so we next investigated which afferent pathways modulate this stress-sensitive pnVTA^{PNOC} subpopulation. The lateral hypothalamus (LH) sends dense and diverse projections to the VTA (Soden et al., 2020; Watabe-Uchida et al., 2012), and is broadly involved in motivation, aversion, and the stress response (Gomes-de-Souza et al., 2021; Jong et al., 2019; Lazaridis et al., 2019; Marino et al., 2020; Nieh et al., 2016; Schiffino et al., 2019; Weera et al., 2021). In line with prior tracing studies (Soden et al., 2020), our injection of AAV2-retro-Ef1a-DIO-eYFP into the pnVTA of VGAT-Cre or VGLUT2-Cre mice effectively labeled GABAergic and glutamatergic neurons in the LH that project to the pnVTA (**Figure S4.2**).

We next determined if these LH GABA and glutamate (LH$^{GABA/Glut}$) inputs have synaptic connectivity onto pnVTA^{PNOC} neurons (**Figure 4.4**). Using PNOC-Cre mice, we injected AAV5-CaMKII-ChR2-eYFP bilaterally into the LH to allow for optogenetic control of LH$^{GABA/Glut}$ neurons and then injected AAV5-Ef1a-DIO-mCherry bilaterally into the pnVTA to label PNOC neurons for voltage clamp recordings (**Figure 4.4a, b**). At 4-6 weeks post injection, mice were sacrificed and coronal brain slices were prepared for *ex vivo* electrophysiological studies.

To assess both glutamatergic and GABAergic input from the LH within the same PNOC neurons, we used a Cesium based internal solution to record optically-evoked inhibitory and excitatory postsynaptic currents (oIPSCs and oEPSCs) at +10mV and -70mV, respectively (see

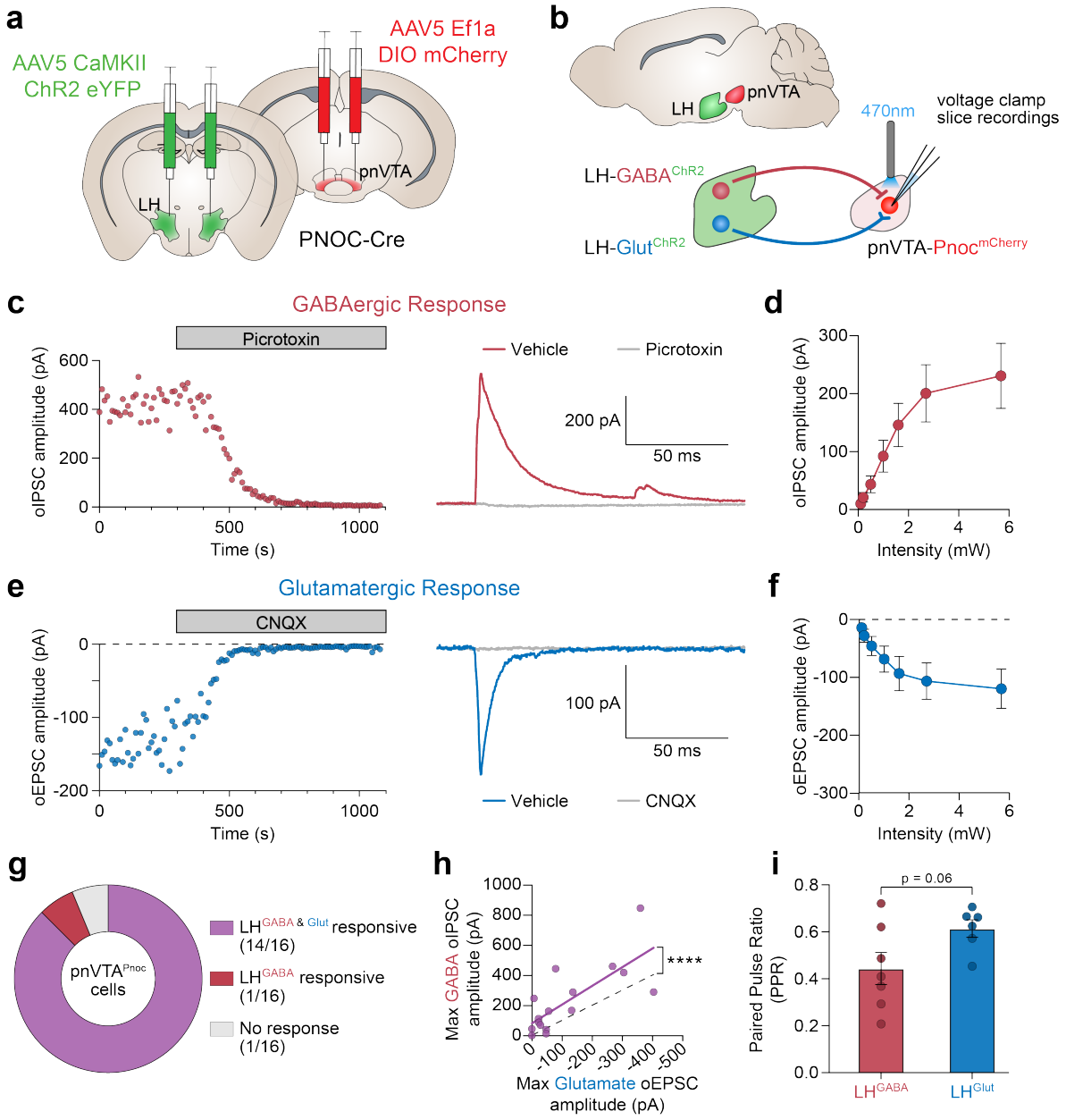

Figure 4.4: Lateral hypothalamic GABA and glutamatergic connectivity onto pnVTA^{PNOC} neurons.

(a) Cartoon of bilateral CaMKII-ChR2-eYFP injection into lateral hypothalamus (LH) and DIO-mCherry injection into pnVTA of PNOC-Cre mice. **(b)** Schematic for voltage-clamp recordings of oIPSCs or oEPSCs from LH^{GABA} and LH^{Glut} terminals in the pnVTA. **(c)** Example trace and effect of 50 μM picrotoxin on oIPSC amplitude recorded from pnVTA^{PNOC} neurons (n = 16, N = 3). **(d)** Optically-evoked input/output curve of oIPSCs recorded from pnVTA^{PNOC} neurons at increasing LED stimulation intensities (n = 16, N = 3). Data represented as mean ± SEM. **(e)** Example trace and effect of 10 μM CNQX on oEPSC amplitude recorded from pnVTA^{PNOC} neurons (n = 16, N = 3). **(f)** Optically-evoked input/output curve of oEPSCs recorded from pnVTA^{PNOC} neurons at increasing LED stimulation intensities (n = 16, N = 3). Data represented as mean ± SEM. **(g)** Summary of excitatory and inhibitory responses to LH terminal stimulation from all recorded pnVTA^{PNOC} neurons. **(h)** Maximum oIPSC vs maximum oEPSC amplitude recorded from pnVTA^{PNOC} neurons. Nonlinear regression using a least squares fit (purple line) and null hypothesis (no GABA or glutamate amplitude bias, dashed line) are shown. (n = 16 cells per group, ****p < 0.0001). **(i)** Paired pulse ratio (PPR) of oIPSCs from LH^{GABA} inputs (red) and oEPSCs from LH^{Glut} inputs (blue) (n = 6-7 cells per group; two-tailed t-test, p = 0.0607). Data represented as mean ± SEM.

Supplementary Methods). Optogenetic stimulation of LH terminals in the pnVTA reliably evoked oIPSCs in mCherry-labeled pnVTA^{PNOC} neurons held at +10mV that could be blocked by the $GABA_A$ receptor antagonist picrotoxin (**Figure 4.4c, d**). Similarly, we recorded oEPSCs in pnVTA^{PNOC} neurons held at -70mV following LH terminal stimulation, which were blocked by the competitive AMPA receptor antagonist CNQX (**Figure 4.4e, f**). While the majority of pnVTA^{PNOC} neurons recorded responded to both LH^{GABA} and LH^{Glut} stimulation (**Figure 4.4g**), we found that the magnitude of the inhibitory response was significantly greater than the excitatory response (**Figure 4.4h**). This was accompanied by a trend toward a lower paired pulse ratio (PPR) for the inhibitory responses, suggesting higher release probability and stronger synaptic input (**Figure 4.4i**). Ultimately, these data indicate that pnVTA^{PNOC} neurons receive significant GABAergic and glutamatergic input from the lateral hypothalamus.

4.2.4 Lateral hypothalamic function in the pnVTA during stress exposure

After identifying synaptic connectivity between the LH and pnVTA^{PNOC} neurons, we investigated the functional activity of these LH terminals in the pnVTA during stress exposure (**Figure 4.5**). We injected VGAT-Cre mice with AAV-DJ-DIO-GCaMP6s bilaterally in the LH and implanted optic fibers above the pnVTA in order to record the calcium activity of LH^{GABA} terminals during exposure to predator odor (**Figure 4.5a, b**). While our earlier findings showed an increase in pnVTA^{PNOC} activity in response to predator odor, when recording from LH^{GABA} terminals we instead observed a decrease in calcium activity (**Figure 4.5c, d**, 1-way ANOVA, $F_{4,8}$=4.593, p=0.0321). These results suggest that in contrast to pnVTA^{PNOC} activity, LH^{GABA} terminals in the pnVTA may be suppressed during stress exposure.

To evaluate LH glutamatergic function at pnVTA terminals during stress, we used an optogenetic approach to stimulate LH^{Glut} terminal activity during the tail suspension test (TST) (Can et al., 2012). We injected a Flp-dependent AAV-CAG-FLP-ChrimsonR-tdTomato bilaterally into the LH and then implanted an optic fiber above the pnVTA in VGLUT2-FLP x PNOC-Cre mice

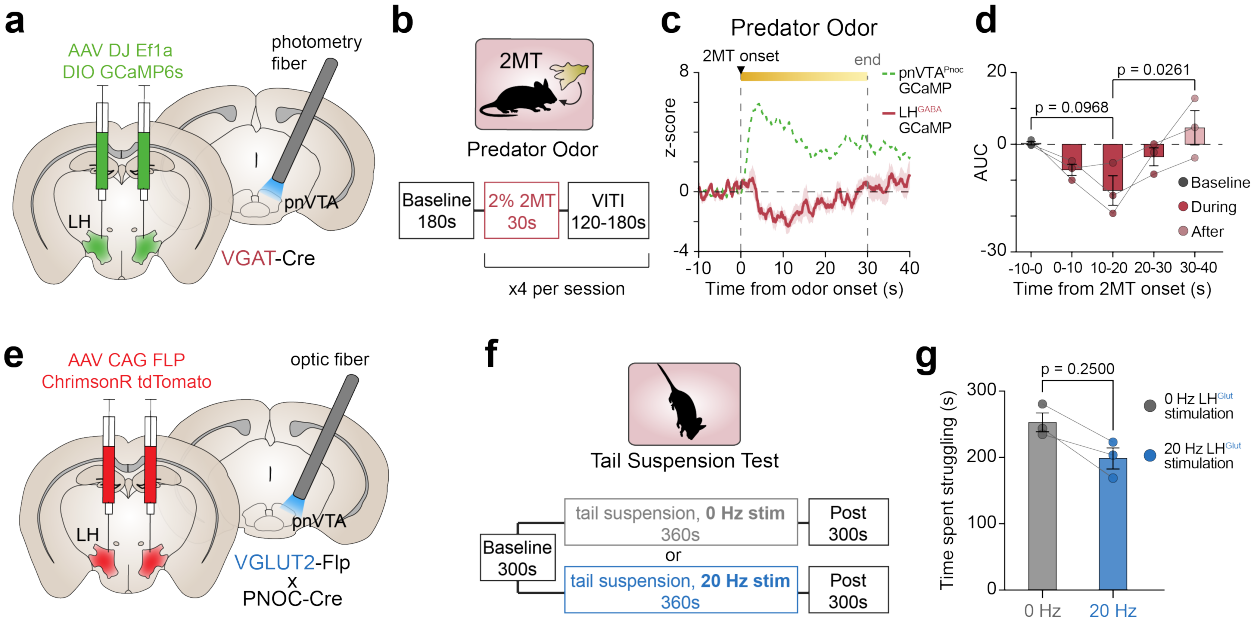

Figure 4.5: Functional evaluation of lateral hypothalamic input to the pnVTA during stress exposure.

(a) Cartoon of bilateral DIO-GCaMP6s injection into lateral hypothalamus (LH) with fiber implant above the pnVTA in VGAT-Cre mice. **(b)** LH^{GABA} terminals in the pnVTA were recorded during exposure to predator odor (2% 2MT, same trial structure as in Figure 2). **(c)** Averaged trace of LH^{GABA} terminal activity in the pnVTA during predator odor exposure (red). Averaged $pnVTA^{PNOC}$ GCaMP6s trace from Figure 4.2 is shown in the green dotted line for comparison. **(d)** Area under the curve (AUC) for averaged traces from **c** for $pnVTA^{PNOC}$ neurons (green) and LH^{GABA} terminals in the pnVTA (red). LH^{GABA} terminals are suppressed during 2MT exposure while $pnVTA^{PNOC}$ neurons become activated (2-way ANOVA with Tukey's multiple comparisons test, $^{**}p < 0.01$, N = 10 mice, $pnVTA^{PNOC}$; N = 3 mice, LH^{GABA}). **(e)** Cartoon of bilateral FLP-ChrimsonR-tdTomato injection in the LH with fiber implant above the pnVTA in VGLUT2-Flp x PNOC-Cre mice. **(f)** Trial structure for the tail suspension test (TST). Mice were suspended for 6 minutes and received either 0 or 20 Hz ChrimsonR stimulation (1mW power, cycling ON for 5s and OFF for 15s throughout the 6-minute suspension) in counterbalanced sessions. **(g)** Total time spent struggling during the TST for mice receiving 0 Hz (gray) or 20 Hz (blue) stimulation of LH^{Glut} terminals in the pnVTA (two-tailed Wilcoxon test, p = 0.25, N = 3 mice). All data represented as mean ± SEM.

(**Figure 4.5e**). At 3-4 weeks post injection, mice were suspended by the tail for 6 minutes while receiving either 20Hz or 0Hz control stimulation (cycling 5s ON 15s OFF throughout suspension) on counterbalanced days, and the total time the mice spent struggling was quantified (**Figure 4.5f**). We observed a general trend toward less time spent struggling during the TST when mice received continuous 20Hz stimulation of LH^{Glut} terminals compared to control days, indicative of increased anhedonia (**Figure 4.5g**). These results suggest that LH^{Glut} activity in the pnVTA may enhance stress-induced anhedonia.

4.3 Discussion

Our findings reveal new insights into a pathway by which stress interfaces with a neuropeptide subpopulation known to direct motivated reward-seeking behaviors through its influence on mesolimbic circuitry. We demonstrate that $pnVTA^{PNOC}$ neurons are selectively activated in response to stress rather than salience in a primarily non-sex-dependent manner, except during looming predator stress where activity increased in males only. Our findings also indicate that $pnVTA^{PNOC}$ neurons have varying sensitivity to different stressors, with physical and predator-based stimuli seeming to produce a larger dynamic response than the innately stressful environmental cues experienced during exploratory behaviors. Whether these differences in dynamics are related to the perceived valence of the stressful stimulus will need to be evaluated in further studies.

N/OFQ signaling has been widely implicated in the stress response, but the observed effects of stress on the N/OFQ-NOPR system vary widely both across the brain and depending on the form and duration of stress exposure (Gavioli et al., 2021; Witkin et al., 2014). Prior studies have also reported notable sex differences in rats, where stress-induced changes to N/OFQ signaling were more prominent in males (Randesi et al., 2018; Zhang et al., 2019). While most of the stressors we evaluated in this study evoked similar $pnVTA^{PNOC}$ responses in males and females, the activity during looming that occurred exclusively in male mice mirrors these prior

findings where a stress-evoked change in N/OFQ signaling was only seen in males. On the contrary, we observed a potentiation of pnVTA^{PNOC} activation during foot shock in females relative to males (**Figure S4.1**), suggesting sex-dependent effects in N/OFQ's response to stress can also extend to females. Beyond sex-based differences, future studies should also explore whether individual heterogeneity in terms of an animal's resilience or vulnerability to stress further shapes how pnVTA^{PNOC} neurons respond during stress exposure.

The upstream circuitry that engages the pnVTA^{PNOC} subpopulation has previously been unknown. The lateral hypothalamus (LH) is a critical hub with roles in stress and reward-seeking that innervates the pnVTA with both excitatory and inhibitory inputs (Soden et al., 2020), making it promising candidate for pnVTA^{PNOC} afferent modulation. Our results identify synaptic connectivity from both GABAergic and glutamatergic inputs onto pnVTA^{PNOC} neurons (**Figures 4.4, S4.2**) and indicate a functional role of LH glutamatergic activity at the pnVTA in driving anhedonic behavior (**Figure 4.5**). These findings align with other studies of LH function in the VTA, where LH glutamatergic activity has been shown to drive avoidance behaviors and LH GABAergic activity to promote positive reinforcement (Jong et al., 2019; Nieh et al., 2016). Our recordings of LH^{GABA} terminal activity during predator odor stress could indicate that suppression of LH^{GABA} activity may serve as a disinhibitory mechanism that allows for heightened activation of pnVTA^{PNOC} neurons in response to stress, however we only observed a trend toward LH^{GABA} suppression, and a larger cohort size will need to be recorded from to determine the statistical significance of this result.

It is also important to note that our electrophysiological studies used a CaMKII-driven channelrhodopsin to target both GABA and glutamate LH populations simultaneously, and separation of oEPSCs and oIPSCs was achieved through a voltage-clamp approach. Follow-up work should isolate the synaptic input from GABAergic and glutamatergic LH inputs separately. Furthermore, given the evidence of LH peptidergic neuromodulation of motivated behaviors within the VTA, future studies should evaluate the effect of LH neuropeptide release, particularly the

peptides orexin, hypocretin, and neurotensin, on pnVTA^{PNOC} activity (Borgland et al., 2006; Harris et al., 2005; Kempadoo et al., 2013; Opland et al., 2013).

In conclusion, our findings provide important insights into how stress modulates N/OFQ signaling in the VTA and reveal the involvement of LH inputs in driving these responses. These results advance our understanding of how the N/OFQ system interfaces with both stress and motivational deficits within a single circuit, laying the groundwork for further studies to explore stress-related mechanisms for anhedonic behavior in the context of this neuropeptidergic pathway. Future research should examine the long-term effects of chronic stress on pnVTA^{PNOC} activity and evaluate the therapeutic potential of NOPR antagonism within this circuit during motivation in models of stress-induced anhedonia.

4.4 Methods

Animals

Adult (18–35 g) male and female *Pnoc*-IRES-Cre (PNOC-Cre), *Slc32a1*-IRES-Cre (VGAT-Cre), *Slc17a6*-IRES-Cre (VGLUT2-Cre), and VGLUT2-Flp x PNOC-Cre mice were group housed in the animal facility at 22–24 °C on a 12h/12h reverse light/dark cycle (9:00AM lights off) in ventilated cages with ad libitum access to standard chow and water. All animals were monitored for health status daily and before experimentation for the entirety of the study. Animal procedures were approved by the Animal Care and Use Committee of the University of Washington and conformed to US National Institutes of Health guidelines. All resources are listed in **Table 4.1**.

Stereotaxic surgery

All coordinates, viruses, and volumes for experiments are listed in **Table 4.2**. After acclimating to the holding facility for at least seven days, mice were anaesthetized in an induction chamber (1%-4% isoflurane) and placed into a stereotaxic frame (Kopf Instruments, model 1900) where they were maintained at 1%-2% isoflurane. A blunt needle syringe (86200, Hamilton Company) was

used to deliver virus at a rate of 100nL/min either in the LH or pnVTA. For mice receiving intracranial fiber photometry implants, an optic fiber (400µm core, 2.5mm ferrule, Doric) was slowly lowered to 0.05mm above the injection site and secured using MetaBond (C & B Metabond). A stainless-steel head-ring was also secured on animals undergoing air puff to allow for head-fixation. Animals were allowed to recover from surgery for a minimum of 3 weeks before any behavioral testing, permitting optimal viral expression.

Fiber photometry recordings

Fiber photometry studies were completed as described previously (Zhou and Stine et al., 2024). In brief, 531-Hz sinusoidal LED light (Thorlabs, LED light: M470F3; LED driver: DC4104) was bandpass filtered (470 ± 20nm, Doric, FMC4) to excite GCaMP6s, a 211-Hz sinusoidal LED light (Thorlabs, M405FP1; LED driver: DC4104) was bandpass filtered (405 ± 10nm, Doric, FMC4) to evoke Ca^{2+}-independent isosbestic control emission. LED intensities were measured at the tip of the optic fiber and adjusted to 30µW before each recording. GCaMP6s emission traveled back through the same optic fiber then was bandpass filtered, (525 ± 25nm, Doric, FMC4), detected by a photoreceiver (Doric, DFD_FOA_FC), and recorded by a real-time processor (TDT, RZ5P). For the ChrimsonR stimulation experiments, a 635nm laser was passed through the filter cube at 1mW intensity to deliver red light at the tip of the optic fiber (Al-Hasani et al., 2021).

In vivo animal experiments

All animal behaviors were performed within a sound-attenuated room maintained at 23°C at least one week after habituation to the holding room. Animals were handled for a minimum of three days prior to experimentation and were habituated to fiber photometry patch cord attachment to their fiber implants. For all experiments, mice were brought into the experimental room and allowed to acclimate to the space for at least 30 minutes prior to any testing. All experiments were conducted in red light to accommodate the reverse light cycle schedule, unless otherwise stated.

Behaviors

Cued foot shock: Mice were placed in Med Associates Fear Conditioning Chambers (NIR-022MD) which consisted of a 29.5 x 23.5 x 21 cm chamber with a conductive grid floor lit by infrared light and contained within a soundproof box. Mice were exposed to ten 10s tones co-terminating with a 2s 0.5 mA shock with a variable inter-trial interval (VITI) of 45s-90s.

Tail lift: Mice were placed in a 10" x 10" clear acrylic box illuminated by a dim, diffuse white light (~30 lux). Mice were suspended by the tail four times for 20s with a VITI of 120s-180s. All suspensions were made to the same height.

Air puff: Four days before testing, mice were habituated to head-fixation on the OHRBETS platform (Gordon-Fennell et al., 2023) as described previously (Zhou and Stine et al., 2024). A fixed, solenoid-controlled O_2 valve was positioned above the animal's left whiskers. Mice were exposed to fifteen 0.1s 20 PSI air puffs with a VITI of 45s-75s. Solenoid opening (Parker, 003-0257-900) was controlled using an Arduino Mega 2560 REV3 (Arduino) and custom Arduino programs.

Looming: Mice were placed in a white-walled plexiglass arena (50 x 50 cm) illuminated by a diffuse white light (~80 lux) and allowed to roam freely. Looming was simulated four times via a posterboard blocking the arena's overhead lighting (arena illumination reduced to ~25 lux) for 1s-2s, with a VITI of 120s.

Odor delivery: Mice were placed in a polyethylene chamber approximately 12 x 12 x 24 cm where air was continuously vacuumed out at a rate of 2L/min (Luskin et al., 2024). To minimize odor release into the room, the chamber was placed in a fume hood and vacuumed air was passed through a carbon filter. Odors (2% 2MT or 2% peppermint oil, in separate sessions) were delivered four times per session for 30s periods with a VITI of 120s-180s.

Tail suspension test (TST): TST was completed as described previously (Can et al., 2012). Following a 5-minute baseline in a 10" x 10" clear acrylic box, mice were suspended by the tail

continuously for 6 minutes. On counterbalanced test days, mice received either 0 or 20 Hz (5ms pulse width, 1mW laser power) cycling ON for 5s and OFF for 15s throughout the suspension.

Open field test (OFT): OFT was completed as described previously (Luskin et al., 2024; McCall et al., 2017) in a white-walled plexiglass arena (50 x 50 cm) illuminated by a white light (~200 lux). Center zone was defined as the middle 50% of the arena size. Mice were allowed to roam the arena freely for 30 minutes.

Elevated zero maze (EZM): EZM was completed as described previously (Luskin et al., 2024; McCall et al., 2017) in a circular maze (Harvard Apparatus) with a 200 cm circumference comprise of four 50 cm sections (two open and two closed 'arms'), elevated 50 cm above the floor illuminated by a white light (~25 lux). The maze path was 4 cm wide with a 0.5 cm lip on each open arm and 17 cm walls on each closed arm. Mice were positioned head-first into a closed arm and allowed to roam the maze freely for 7 minutes.

Electrophysiology and ex-vivo optogenetics

Coronal brain slices for electrophysiology recordings were prepared as previously described (Marcus et al., 2020) at 250 μM on a vibrating Leica VT1000S microtome. Mice were anesthetized with Isoflurane, and transcardially perfused with an ice-cold, oxygenated cutting solution consisting of (in mM): 93 N-Methyl-D-glucamine (NMDG), 2.5 KCL, 20 HEPES, 30 NaHCO3, NaH2PO4, 10 MgSO4·7H20, 0.5 CaCl2·2H20, 25 glucose, 3 Na^+-pyruvate, 5 Na^+-ascorbate, and 5 N-acetylcysteine. Following collection of coronal sections, the brain slices were transferred to a 34°C chamber containing oxygenated cutting solution for a 10-minute recovery period. Slices were then transferred to a holding chamber consisting of (in mM) 92 NaCl, 2.5 KCl, 20 HEPES, 2 MgSO4·7H20, 1.2 NaH2PO4, 30NaHCO3, 2 CaCl2·2H20, 25 glucose, 3 Na-pyruvate, 5 Na-ascorbate, 5 N-acetylcysteine and were allowed to recover for ≥ 30 min. For recording, slices were perfused with oxygenated artificial cerebrospinal fluid (ACSF; 31-33°C; 300-303 milliosmoles) consisting of (in mM): 113 NaCl, 2.5 KCl, 1.2 MgSO4·7H20, 2.5 CaCl2·6H20, 1

NaH2PO4, 26 NaHCO3, 20 glucose, 3 Na^+-pyruvate, 1 Na^+-ascorbate, at a flow rate of 2-3ml/min. For recordings of inhibitory currents, 10 μM CNQX was added to the external solution.

mCherry-labeled $pnVTA^{Pnoc}$ neurons were initially voltage clamped in whole-cell configuration using borosilicate glass pipettes (2-4MΩ). For recordings of excitatory currents, pipettes were filled with internal solution containing (in mM): 125 K^+-gluconate, 4 NaCl, 10 HEPES, 4 MgATP, 0.3 Na-GTP, and 10 Na-phosphocreatine (pH 7.30-7.35). The patch pipette also included 50 μM picrotoxin to block $GABA_A$ currents. For recordings of inhibitory currents, pipettes were filled with 115 CsCl2, 5 NaCl, 10 HEPES, 5 QX-314, 4 Mg-ATP, 0.3 Na-GTP, and 10 Glucose (pH 7.30-7.35). After break-in to the cell, we waited ≥ 3 minutes to allow for exchange of internal solution and stabilization of membrane properties. Neurons with an access resistance of > 30MΩ or that exhibited greater than a 20% change in access resistance during the recording were excluded from results. For all voltage clamp experiments, neurons were held at -70mV.

Ex vivo optogenetics

PNOC-Cre mice were injected with 300 nL of AAV5-CaMKII-ChR2(H134R)-eYFP bilaterally into the LH, and 300 nL of AAV5-EF1a-DIO-mCherry was injected bilaterally into the pnVTA to allow us to record from $PNOC^+$ neurons in the pnVTA. 3-5 weeks of viral expression was allowed prior to sacrificing the mice. For optogenetic recordings of input/output curves, we used a Thorlabs LEDD1B T-Cube driver and obtained separate recordings of 470nm wavelength oEPSCs / oIPSCs at 7 output levels corresponding to 5.7, 2.7, 1.6, 1, 0.5, 0.2, and 0.1 mW of LED intensity. Paired pulse ratio (PPR) recordings of oEPSCs / oIPSCs were obtained in voltage-clamp with an inter-stimulus interval of 50ms. PPR is reported as a ratio between the amplitude of the second oEPSC / oIPSC divided by the first. All optogenetic experiments used 2ms of light exposure time.

Tissue preparation and immunohistochemistry (IHC)

Unless otherwise stated, animals were transcardially perfused with 0.1M phosphate-buffered saline (PBS) followed by 40mL 4% paraformaldehyde. Brains were dissected and post-fixed in 4% paraformaldehyde overnight and then transferred to 30% sucrose solution for cryoprotection. Brains were sectioned at 30µm on a microtome and stored in 0.1M phosphate buffer at 4°C prior to immunohistochemistry and tracing experiments. Immunohistochemistry was completed as described previously (Al-Hasani et al., 2013; Kim et al., 2013; Zhou and Stine et al., 2024). In brief, free-floating brain sections were washed in 0.1 M PBS for 3 x 10 min intervals. Sections were then placed in blocking buffer (0.5% Triton X-100 and 5% natural goat serum in 0.1 M PBS) for 1 hour at room temperature. After blocking buffer, sections were placed in primary antibody (chicken anti-GFP, 1:2000, Abcam) overnight at 4°C. After 3 x 10 min 0.1 M PBS washes, sections were incubated in secondary antibody (AlexaFluor 488 goat anti-chicken, Abcam) for 2 hours at room temperature, followed by another round of washes (3 x 10 min in 0.1 M PBS, 3 x 10 min in 0.1 M PBS). After immunostaining, sections were mounted and coverslipped with Vectashield HardSet mounting medium containing DAPI (Vector Laboratories) and imaged on a Leica DM6 B microscope. For behavioral cohorts, viral expression and optic fiber placements were evaluated before inclusion in the presented datasets.

Fiber photometry analysis

Fiber photometry data were analyzed as described previously (Zhou and Stine et al., 2024). In brief, custom MATLAB scripts were used to detrend decay from bleaching by fitting a 4^{th} degree polynomial function to the raw signal (470nm) and isosbestic (405nm) traces, then dividing by the resulting curve. Then signal was normalized by dividing an LLS fit of the isosbestic trace scaled to the signal. The processed traces were then down-sampled by a factor of 100, smoothed across a rolling 1s window, extracted in windows surrounding the onset of relevant behavioral events (tail

lift, odor, shock, air puff, looming, open arm entry, center entry), z-scored relative to the mean and standard deviation of each event window, and then averaged.

Statistical analyses

Statistical analyses were performed as indicated in GraphPad Prism 9 and MATLAB 9.9 (MathWorks). All data are expressed as mean ± SEM unless specified otherwise.

4.5 Acknowledgments

This research was supported by NIH/NIMH P50 MH119467 (MRB), NIH/NIDA F31 F31DA059438-01A1 (CS), and the Mallinckrodt Foundation (MRB). We would like to thank Drs. Azra Suko and Larry Zweifel for their help with virus production, and Drs. Diego Pizzagalli and Raaj Gowrishankar for providing feedback on the manuscript.

4.6 Author Contributions

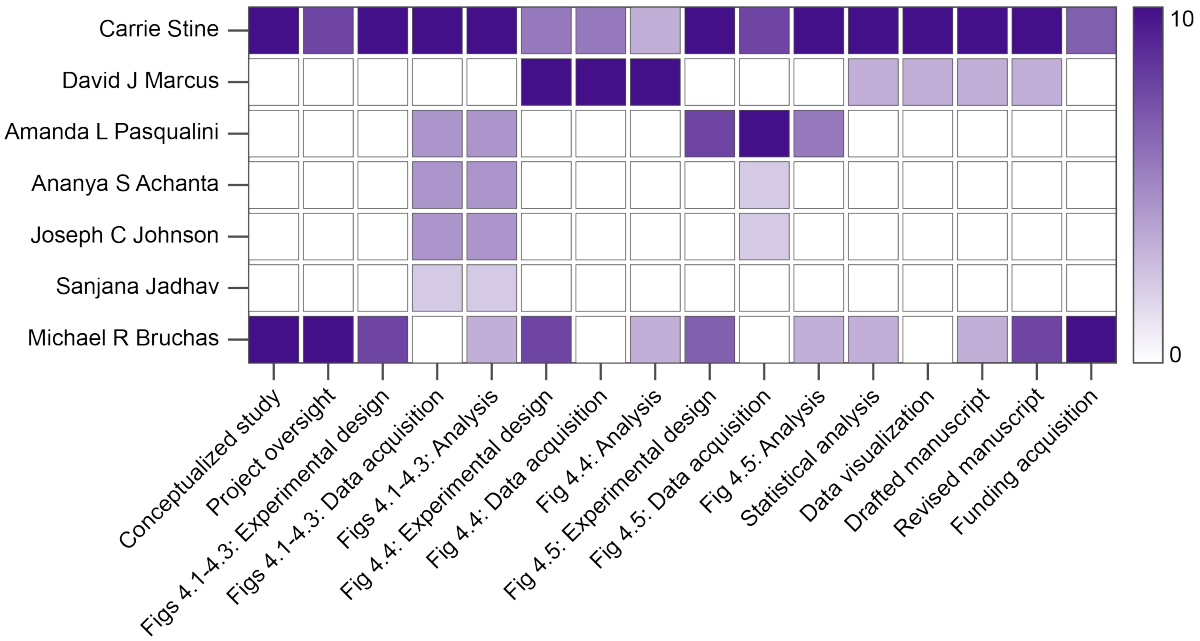

4.7 Tables

Table 4.1: Resources used in Chapter 4

REAGENT OR RESOURCE	SOURCE	IDENTIFIER
Antibodies		
Chicken-anti-GFP 1:2000	Abcam	Ab13970
Goat anti-chicken IgY, Alexa Fluor 488	Abcam	Ab150169
Bacterial and Virus Strains		
AAV-DJ-Ef1a-DIO-GCaMP6s	Stanford University Gene Vector and Viral Core	N/A
AAV2-retro-Ef1a-DIO-eYFP	The Hope Center Viral Core Washington University at St. Louis	N/A
AAV5-CaMKII-hChR2-eYFP	UNC Vector Core	N/A
AAV5-Ef1a-DIO-mCherry	UNC Vector Core	N/A
AAV-CAG-FLP-ChrimsonR-tdTomato	Addgene	#130909
Experimental Models: Organisms/Strains		
Pnoc-IRES-Cre (PNOC-Cre)	The Jackson Laboratory	#034278
Slc32a1-IRES-Cre (VGAT-Cre)	The Jackson Laboratory	#016962
Slc17a6-IRES-Cre (VGLUT2-Cre)	The Jackson Laboratory	#016963
Slc17a6-IRES2-FlpO x *Pnoc*-IRES-Cre (VGLUT2-Flp x PNOC-Cre)	Bred in house	N/A
Reagents		
2-Methylthiazoline (2MT)	Tokyo Chemical Industry Co	M0285
Peppermint oil	Sigma Aldrich	77411

Table 4.2: Viruses and injection coordinates used in Chapter 4

Experiment	Mouse Line	Virus	Amount	Coordinates
pnVTA-PNOC stress response (Figures 1–3)	PNOC-Cre	AAV-DJ-Ef1a-DIO-GCaMP6s	300nL	AP -3.25, ML 1.6, DV -4.65 (15° angle)
pnVTA retrograde tracing (Supplementary Figure 2)	VGAT-Cre, VGLUT2-Cre	AAV2-retro-Ef1a-DIO-eYFP	300nL	AP -3.25, ML 0.4, DV -4.65

LH-GABA/Glut to pnVTA-PNOC electrophysiology (Figure 4)	PNOC-Cre	AAV5-CaMKII-hChR2-eYFP	300nL	AP -1.25, ML ±1.0, DV - 5.35
		AAV5-Ef1a-DIO-mCherry	300nL	AP -3.25, ML ±0.4, DV -4.65
LH-GABA odor response (Figure 5)	VGAT-Cre	AAVDJ-Ef1a-DIO-GCaMP6s	300nL	AP -1.25, ML ±1.0, DV - 5.35
LH-Glut TST optogenetics (Figure 5)	VGLUT2-Flp x PNOC-Cre	AAV-CAG-FLP-ChrimsonR-tdTom	300nL	AP -1.25, ML ±1.0, DV - 5.35

CHAPTER 5: Discussion

The opioid peptide N/OFQ is clearly involved in mood, stress, and motivation. However, the innate neurocircuitry and specific mechanisms by which the N/OFQ-NOPR system influences stress and reward responses remain poorly understood. My dissertation work extends our knowledge in this area by investigating N/OFQ expression, connectivity, and function during stress and reward behaviors in key mesolimbic circuitry.

5.1 Molecular and spatial architecture of striatal N/OFQ expression

First, we mapped *Pnoc* expression across the dorsal and ventral striatum in different neuronal subtypes (**Chapter 2**). We found that *Pnoc* neurons are primarily D1 MSNs, clustered within striosomes in the dorsal striatum and localized to the dorsomedial area of the NAc core and shell in the ventral striatum (**Figures 2.1–2.3**). Using a Cre-dependent approach to induce lifetime tdTomato labeling of $PNOC^+$ neurons for visualization, our initial findings suggested that a substantial population of *Pnoc*-expressing neurons exist in the striatum. However, examining *Pnoc* mRNA expression in adult mice revealed a much smaller population of active *Pnoc* expression at this stage (**Figure 2.4**). This suggested that our initial results reflected *Pnoc* expression that had occurred at any point in the neurons' lifespan, either transiently in adulthood or at an earlier stage of development. Indeed, we discovered that striatal *Pnoc* mRNA expression is high during early development but dramatically decreases by adulthood (**Figure 2.5**). This suggests striatal N/OFQ signaling has a more prominent role during development, similar to many other genes that are developmentally expressed in the striatum (Enard, 2011; Fong et al., 2018; Kelly et al., 2018). Future studies should investigate whether disrupting developmental striatal N/OFQ expression affects striatal architecture, such as neural sensitivity to reward and stress, and/or affects behavioral function, such as stress vulnerability and motivation.

Our anterograde tracing results in neonates and adults show that striosomal $PNOC^+$ D1 MSNs project to the SNc, suggesting that N/OFQ signaling during development may help shape

formation of the striosome-dendron bouquet (**Figure 2.6**). It is unclear from our results whether these neurons also release N/OFQ locally in the striatum during early development, which warrants further investigation. Furthermore, a lack of striatal *Pnoc* expression in adult mice does not indicate that N/OFQ signaling within the striatum is entirely absent in adulthood, as other afferent inputs may release N/OFQ in the striatum and we did not investigate the prevalence of striatal NOPR (*Oprl1*) expression. *Oprl1* mRNA expression patterns should therefore be examined to determine if striatal NOPR undergoes similar developmental regulation, or if it is constitutively expressed, suggesting other afferent sources of N/OFQ input to the striatum.

5.2 Real-time detection of endogenous N/OFQ release in the VTA

Neuroanatomical and behavioral studies of N/OFQ since its discovery 30 years ago have separately provided some insight into its relevance in these states, but only a few studies have combined these approaches to investigate real-time N/OFQ function within specific brain circuits during active behavior (Hardaway et al., 2019; Parker et al., 2019). This is in large part because until recently, the molecular tools necessary to access this neuropeptide system *in vivo* did not exist. Our research group has made a substantial effort to address this limitation over the past several years by working alongside collaborators to develop i) *Pnoc*-Cre (Parker et al., 2019) and *Oprl1*-Cre (Zhou and Stine et al., 2024) transgenic mouse lines to selectively target N/OFQ and NOPR expressing neurons, respectively; ii) NOPLight (Zhou and Stine et al., 2024), a genetically encoded fluorescent sensor that reports real-time N/OFQ release in discrete circuitry; iii) *Pnoc* and *Oprl1* conditional knockout mouse lines (*Pnoc*-cKO and *Oprl1*-cKO) for genetic removal of N/OFQ or NOPR expression; and iv) a CRISPR guide for Cre-dependent knockdown of *Pnoc* using a recently published single-guide viral CRISPR SaCas9 conditional knockout system (Hunker et al., 2020).

In my dissertation work I characterized and published two of these toolsets, the NOPLight sensor and the *Oprl1*-Cre transgenic line (**Chapter 3**) (Zhou and Stine et al., 2024). I combined

the use of these tools in a single approach to record real-time N/OFQ release in the VTA during stress exposure for the first time (**Figure 3.6**). Interestingly, we also observed a decrease in VTA N/OFQ levels during reward consumption, suggesting the presence of tonic N/OFQ release that is negatively regulated by reward (**Figures 3.7–3.8**). The premise of tonic N/OFQ activity is also supported by our prior work in this circuit, where we reported that inhibition of N/OFQ neurons in the VTA can enhance motivation relative to baseline levels. Together, these findings suggest that N/OFQ activity acts to limit motivation and is suppressed upon successful receipt of reward.

These findings are significant both for advancing our understanding of N/OFQ signaling and for addressing a broader challenge within the neuropeptide field, which has historically lacked the tools necessary to investigate mechanisms of neuropeptide release, signaling, range, and dynamics at this level of spatiotemporal resolution. While neuropeptide sensors hold immense promise, they are not without limitations. NOPLight is a first-generation tool, and like other early versions of sensors, it presents with certain challenges related to isosbestic wavelength, pH sensitivity, and low dynamic range *in vivo* that will likely require further iterations of the sensor to resolve. Still, with the advent of our N/OFQ sensor and other novel neuropeptide biosensors, the neuropeptide field is poised for a significant leap forward. These tools and their future iterations will enable countless researchers to explore previously inaccessible questions regarding the mechanisms by which neuropeptides shape circuit activity to regulate behavior.

5.3 Stress sensitivity of N/OFQ neurons known to modulate motivation

Finally, we used fiber photometry to record N/OFQ neuron activity in the paranigral VTA (pnVTA) during exposure to a variety of different stressors. (**Chapter 4**). pnVTA^{PNOC} neurons became transiently activated in response to a wide array of acutely stressful stimuli including physical, predator, and innate environmental stressors. Importantly, these neurons did not respond to matched controls for salience, indicating they are selectively engaged during stress exposure rather than by salient stimuli (**Figures 4.1–4.3**).

The N/OFQ-NOPR system has emerged as a promising therapeutic target for anhedonia. Preclinical studies with NOPR antagonists have repeatedly shown them to exhibit an antidepressant-like profile, and one antagonist evaluated in a clinical trial was found to improve depression scores, although it did not reach the predefined efficacy criteria (required >88% efficacy relative to placebo; achieved 82.9%) (Post et al., 2016). Despite the large body of evidence demonstrating that NOPR inhibition induces an antidepressant-like phenotype (for a summary see (Gavioli and Calo', 2013)), the specific circuit-level mechanisms by which blockade of N/OFQ signaling improves anhedonic symptoms are less understood.

Previous work from our lab showed that inhibition of pnVTA^{PNOC} activity enhances effort-based reward seeking in mice (Parker et al., 2019), suggesting a mechanism by which N/OFQ signaling may regulate anhedonic behaviors. Given that stress is a prominent factor in the pathophysiology and development of anhedonic-like behaviors (Kirshenbaum et al., 2024), our findings in this study identify a pathway through which stress could suppress motivation by driving excessive activation of N/OFQ signaling in the pnVTA (**Figure 5.1**). We propose that under normal conditions, tonic N/OFQ signaling in the VTA acts as a brake on motivation that becomes downregulated when animals successfully obtain a reward, facilitating continued reward-seeking behavior. Stress exposure, however, leads to elevated N/OFQ activity in this circuit, which based on our prior research could suppress reward seeking and drive anhedonic behaviors. We hypothesize that this is mediated by N/OFQ activation of NOPR on dopamine neurons, which have an inhibitory effect and could lead to reduced dopamine release in downstream targets such as the NAc. Further work is needed to test this hypothesis however, particularly in evaluating the effects of chronic stress on pnVTA^{PNOC} activity and subsequent dopamine release in the NAc, as well as functional studies that determine if manipulating pnVTA^{PNOC} activity can restore stress-induced motivation deficits.

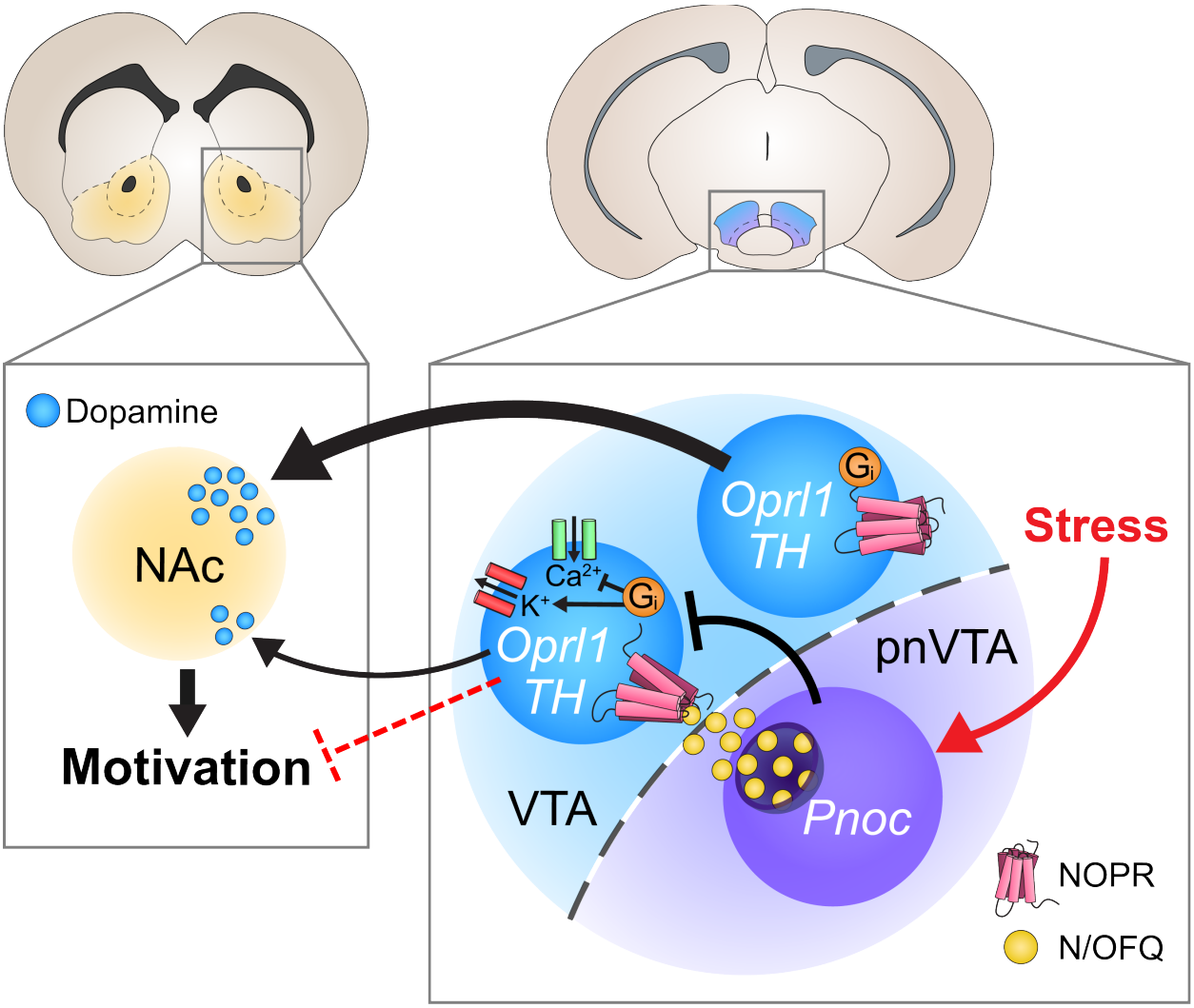

Figure 5.1: Proposed mechanism for N/OFQ integration of stress exposure with motivation.

Model depicting how stress exposure could activate pnVTA N/OFQ neuron activity, driving N/OFQ (yellow) release onto NOPR-expressing VTA dopamine neurons. As a G_i-coupled GPCR, NOPR activation would suppress dopamine neuron excitability, potentially lowering dopamine release at downstream sites such as the NAc, where dopamine is known to regulate motivated behaviors.

Clinical studies have found increased plasma levels of N/OFQ in patients with major depressive disorder (MDD), post-partum depression, and bipolar depression, all of which are commonly associated with anhedonic behaviors and reduced motivation (Gu et al., 2003; Wang et al., 2009). Interestingly, plasma N/OFQ levels are suppressed relative to healthy controls in patients with bipolar mania (Wang et al., 2009), which is more often associated with increased impulsivity and higher reward-seeking drive. This suggests that N/OFQ signaling may be critical for fine-tuning reward-related behavior, and imbalances in either direction of standard expression levels could drive opposing effects on motivation. Our prior findings also support this idea, as we saw that over-activation of pnVTA^{PNOC} neurons suppressed reward-seeking behavior while pnVTA^{PNOC} inhibition enhanced motivation (Parker et al., 2019).

Our findings here broadly showed pnVTA^{PNOC} activation in response to stress, thus we would predict that stress-induced activation of this population would contribute to an overall anhedonic phenotype. However, it is important to note that our findings are limited by the selection of stressors used in this study. Given that stress exposure does not always induce an anhedonic phenotype and can instead exacerbate impulsive behaviors such as drug self-administration (Han et al., 2017; Leonard et al., 2017; Ostroumov et al., 2016; Polter et al., 2017; Tovar-Díaz et al., 2018), further work should investigate if other forms or extended durations of stress beyond the parameters we selected to evaluate here have a suppressive effect on pnVTA^{PNOC} activity.

SUPPLEMENTARY FIGURES

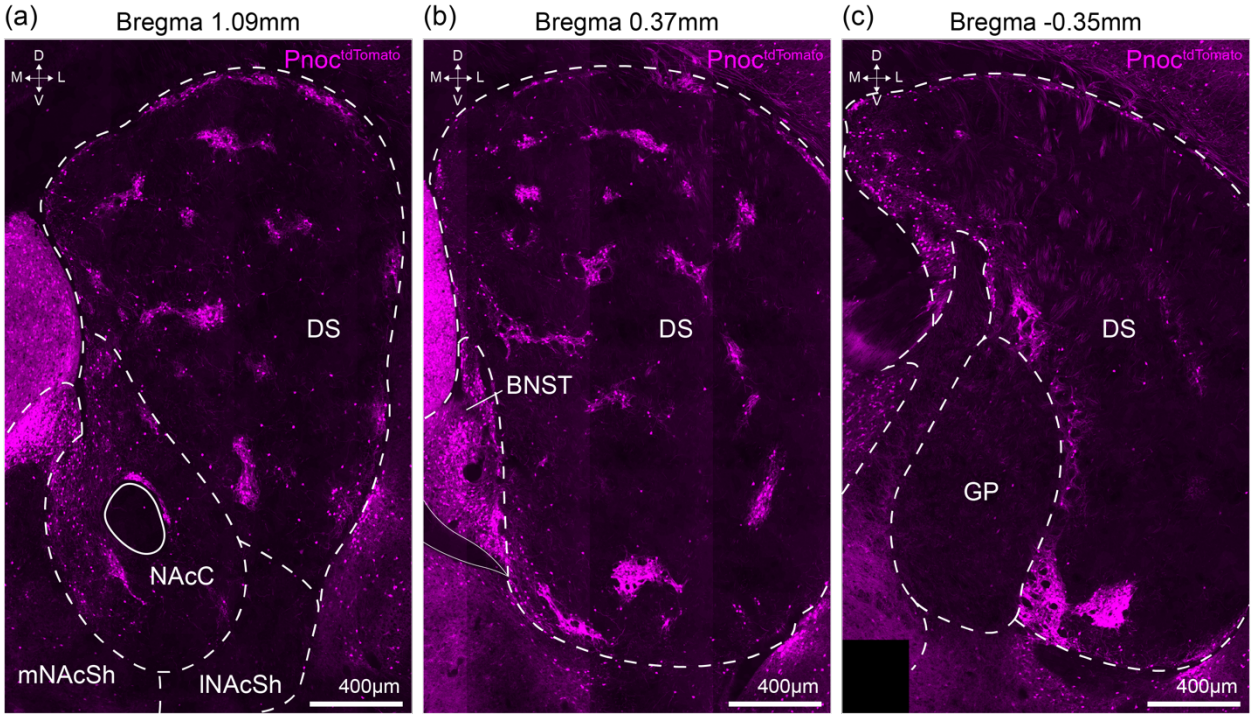

Figure S2.1: Pnoc^{tdTomato} striatal expression across the anterior to posterior axis.

(a–c) Striatal Pnoc^{tdTomato} reporter expression (magenta) across the anterior (a, bregma = 1.09mm) medial (b, bregma = 0.37mm), and posterior (c, bregma = -0.35mm) striatum. DS = dorsal striatum, NAcC = nucleus accumbens core; mNAcSh = medial accumbens shell; lNAcSh = lateral accumbens shell; BNST = bed nucleus of the stria terminalis; GP = globus pallidus.

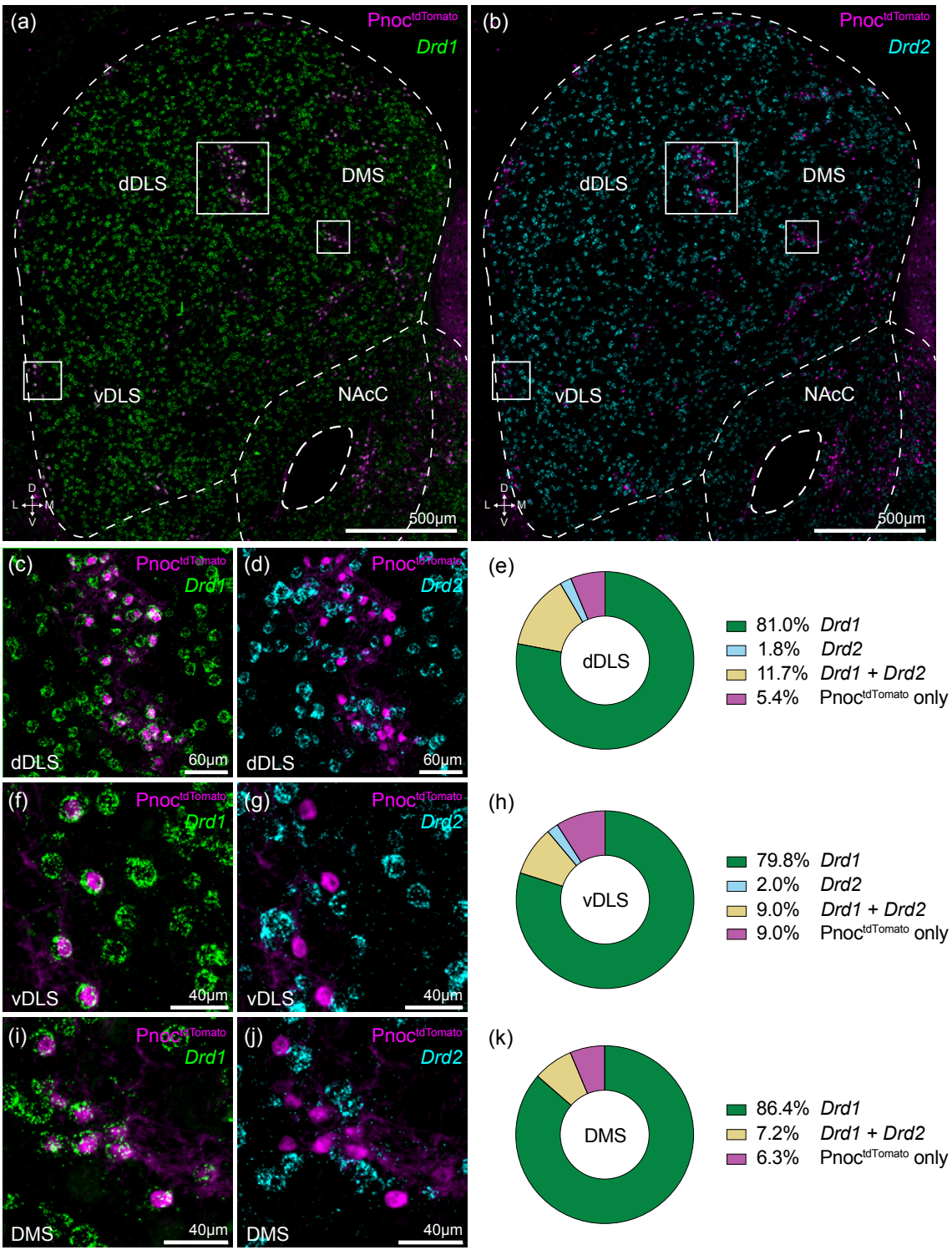

Figure S2.2: Pnoc^{tdTomato} expression across dorsal striatal subregions marks *Drd1* neurons.

Pnoc^{tdTomato} cells (magenta, IHC) co-labeled by ISH with **(a)** *Drd1* expression (green, ISH) or **(b)** *Drd2* expression (cyan, ISH) in the dorsal striatum. Higher magnification of insets from (a) and (b) in dorsal DLS **(c,d)**, ventral DLS **(f,g)**, and DMS **(i,j)**. Summary of quantified Pnoc^{tdTomato} cells co-labeled by ISH with SPNs in dDLS **(e)**, vDLS **(h)**, and DMS **(k)**. dDLS = dorsal aspect of dorsolateral striatum; vDLS = ventral aspect of dorsolateral striatum; DMS = dorsomedial striatum.

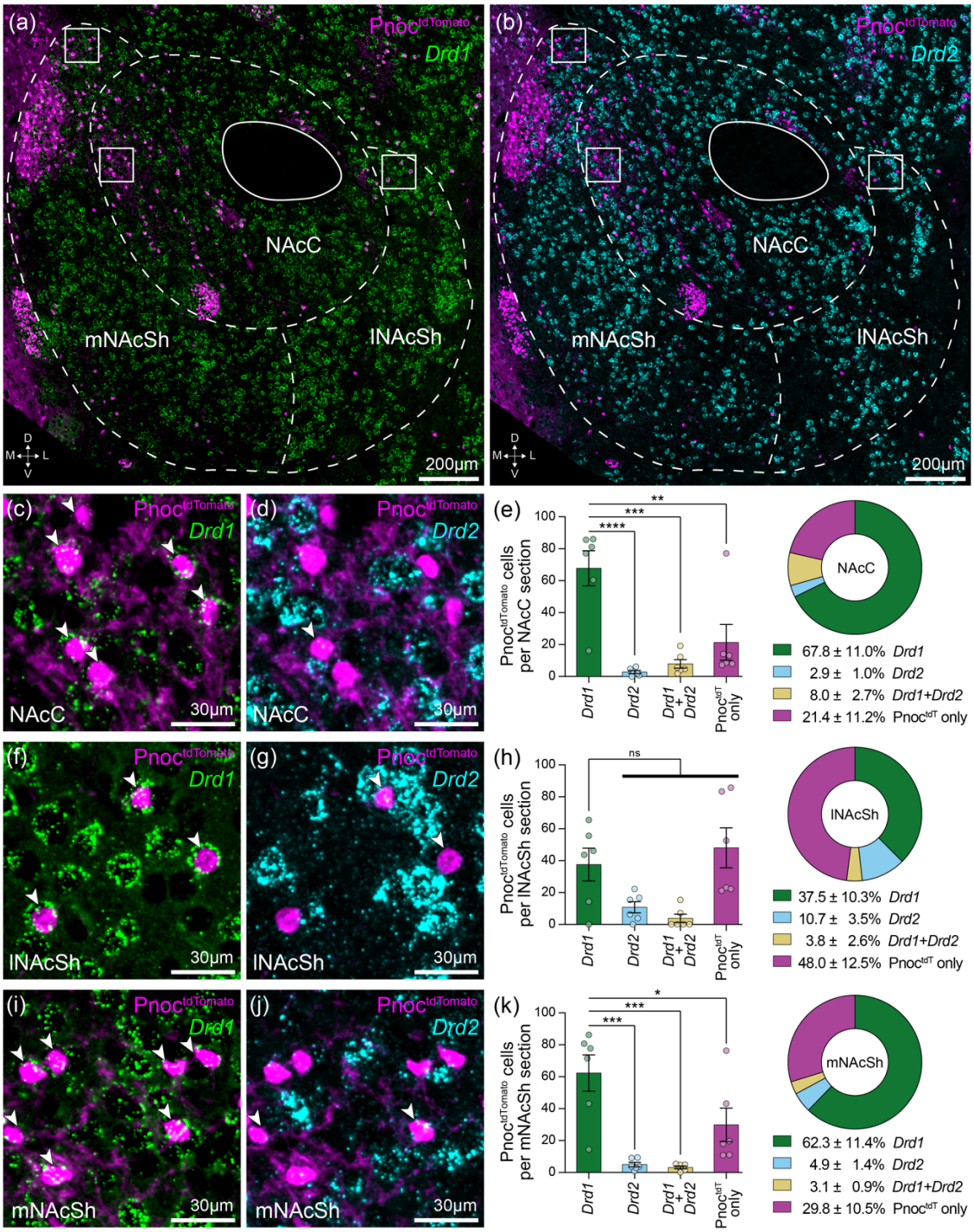

Figure S2.3: Pnoc^{tdTomato} expression in *Drd1* and *Drd2* striatal neurons varies across subregions of the nucleus accumbens.
Pnoc^{tdTomato} cells (magenta, IHC) co-labeled by ISH with **(a)** *Drd1* expression (green, ISH) or **(b)** *Drd2* expression (cyan, ISH) in the nucleus accumbens. Higher magnification of insets from **a** and **b** in nucleus accumbens core **(c,d)**, lateral shell **(f,g)**, and medial shell **(i,j)**. Summary of quantified Pnoc^{tdTomato} cells co-labeled by ISH with *Drd1* and/or *Drd2*-type SPNs in nucleus accumbens core **(e)**, lateral shell **(h)**, and medial shell **(k)**. NAcC = nucleus accumbens core; lNAcSh = lateral accumbens shell; mNAcSh = medial accumbens shell.

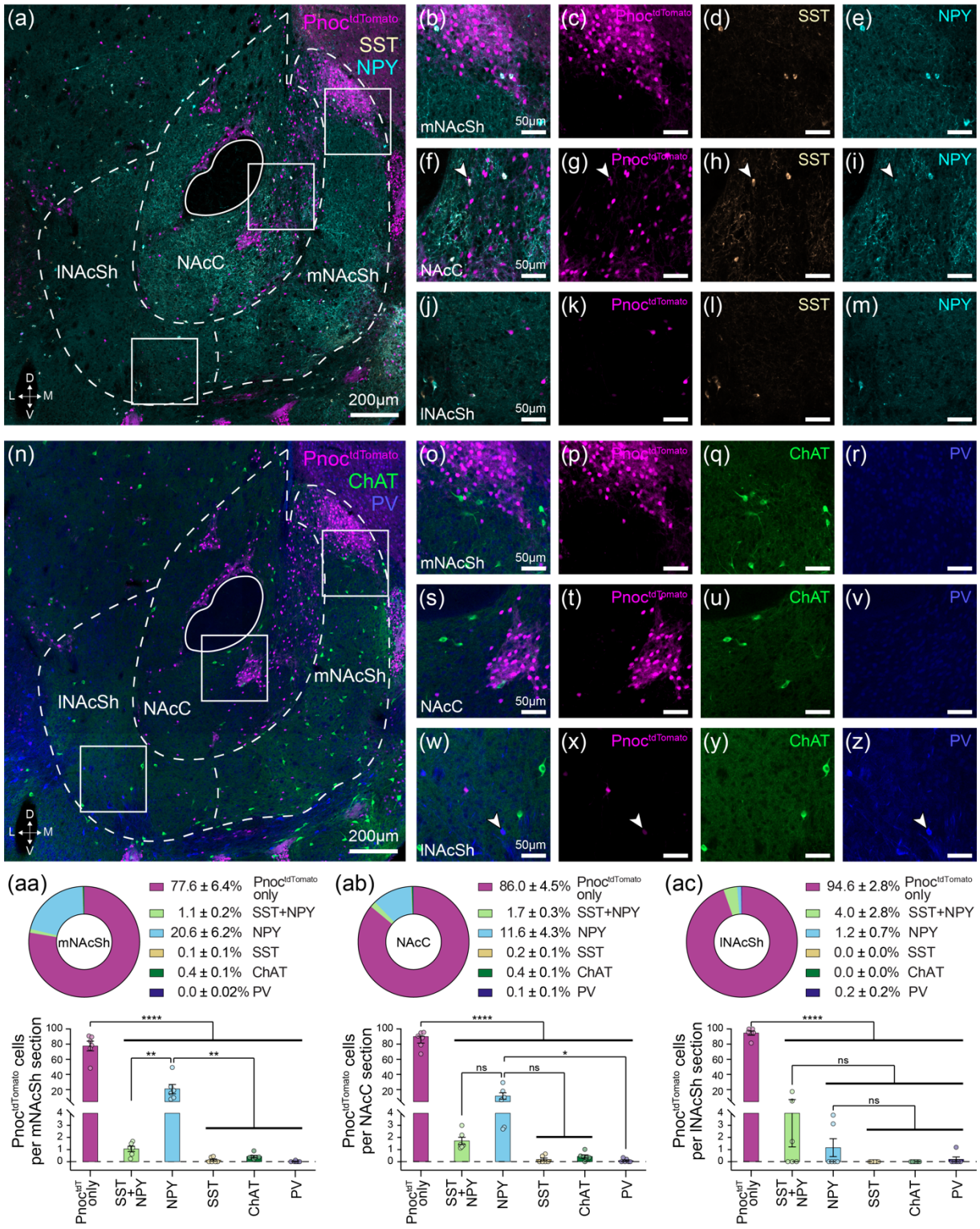

Figure S2.4: **Pnoc^{tdTomato} NPY-labeled interneurons are enriched in the nucleus accumbens core and medial shell.**

(a) Pnoc^{tdTomato} cells (magenta, IHC) imaged with interneuron markers somatostatin (yellow, SST) and neuropeptide Y (cyan, NPY) in the nucleus accumbens. Higher magnification of insets from (a) in **(b-e)** medial accumbens shell, **(f–i)** accumbens core, and **(j–m)** lateral accumbens shell. **(n–z)** Same as (a-m)

but for Pnoc^{tdTomato} cell colocalization with the interneuron markers choline acetyltransferase (green, ChAT) and parvalbumin (dark blue, PV) in the nucleus accumbens. **(aa–ac)** Summary of Pnoc^{tdTomato} colocalization with different interneuron markers in nucleus accumbens medial shell **(aa)**, core **(ab)**, and lateral shell **(ac)**. NAcC = nucleus accumbens core; lNAcSh = lateral accumbens shell; mNAcSh = medial accumbens shell.

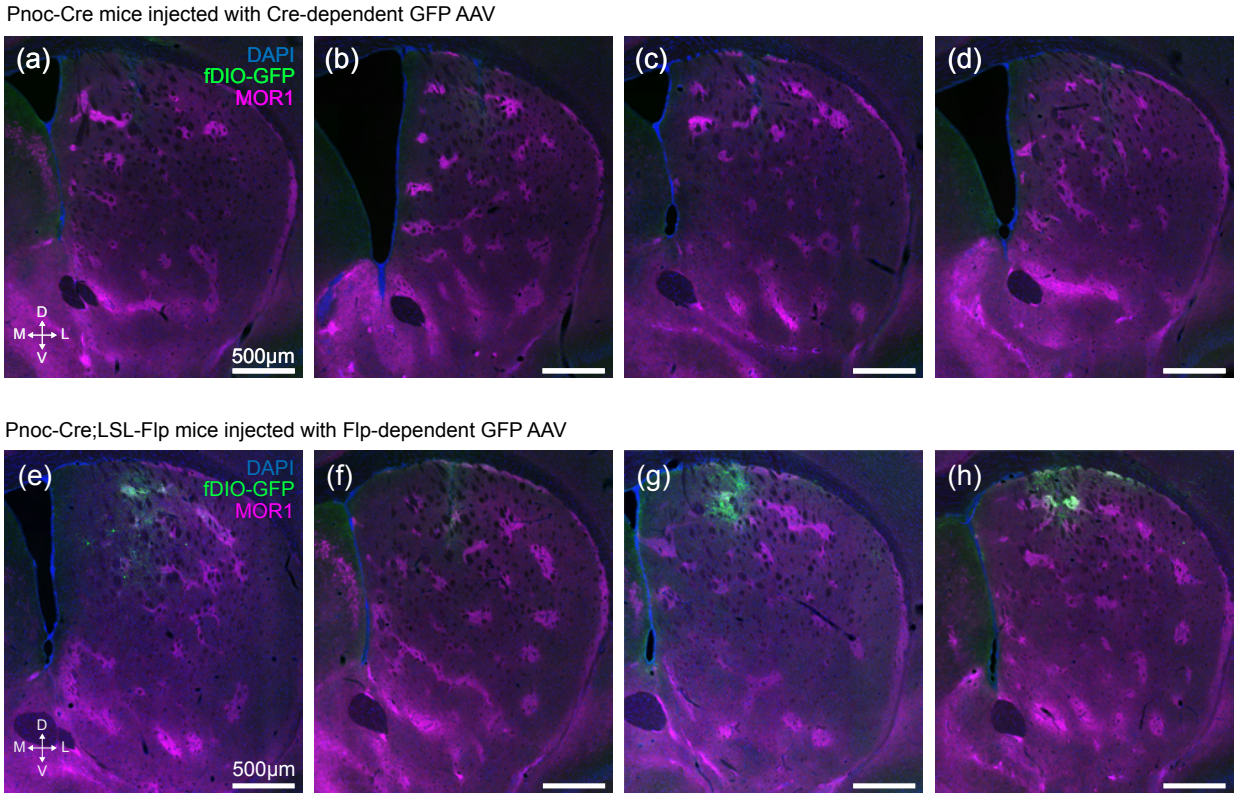

Figure S2.5: ***Pnoc* promoter-driven Cre-expression is insufficient in adult mice to recombine virally delivered Cre-dependent reporter.**

(a–d) Sections from four adult PNOC-Cre mice injected in dorsal striatum with Cre-dependent AAV expressing membrane-GFP (mGFP) showing a lack of Cre-dependent mGFP expression. **(e–h)** Sections from four adult *PNOC*-Cre*; LSL-Flp* mice to confer persisting Flp expression. Injection with a Flp-dependent version of the mGFP construct shows successful Flp-dependent mGFP expression.

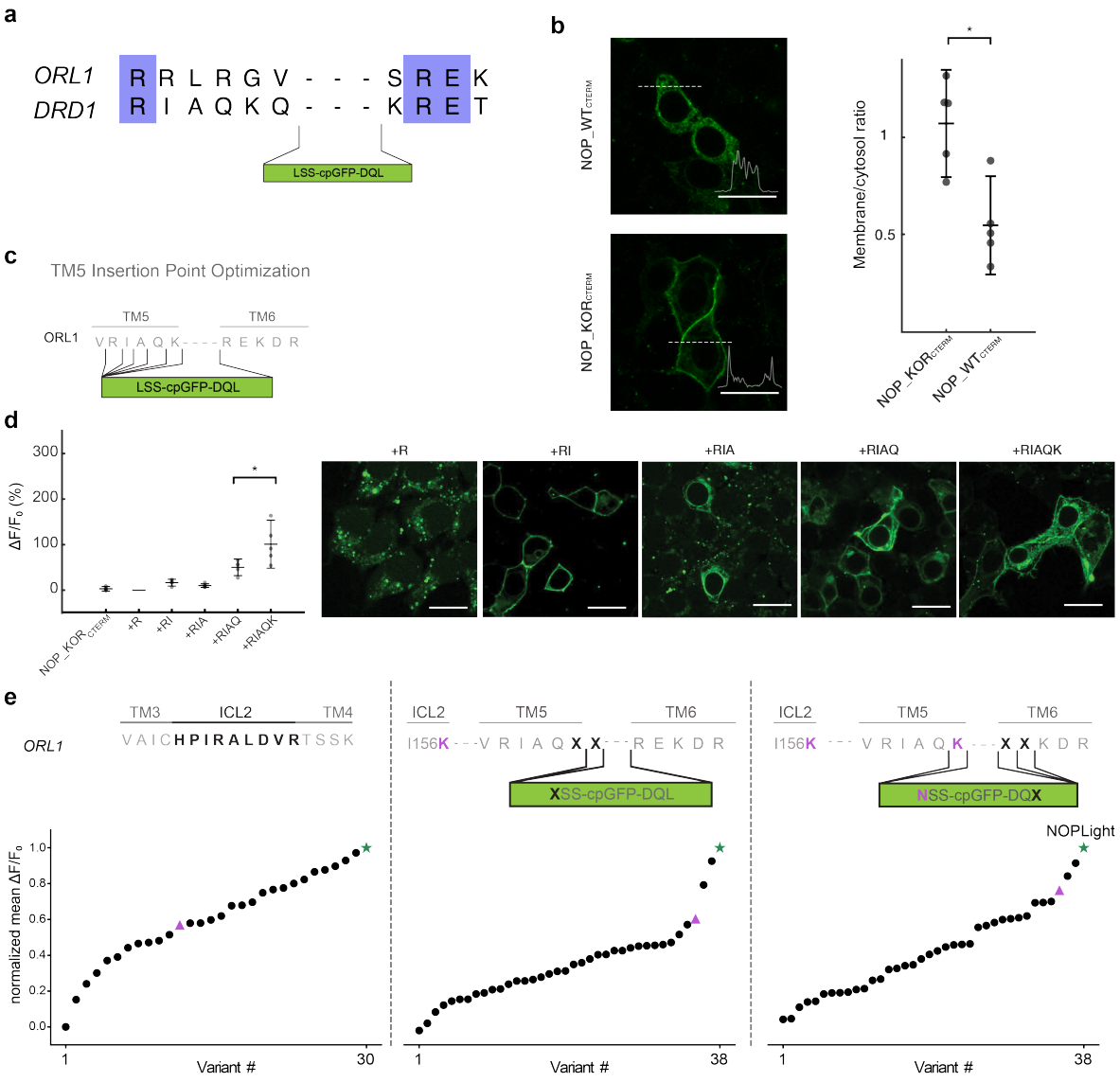

Figure S3.1: **Development and optimization of NOPLight.**

(a) Sequence alignment of transmembrane domains (TM) 5 and 6 from OPRL1 and DRD1 to determine the insertion site for the cpGFP module from dLight1.3. Color code indicates percent identity between the human NOPR and DRD1. **(b)** Left: Representative images of membrane expression profile of HEK293T cells expressing *in silico* designed sensor prototype with a wild-type NOPR C-terminus (NOP_WT$_{CTERM}$) and a chimeric sensor with the C-terminus of kappa opioid receptor (NOP_KOR$_{CTERM}$). Insets: fluorescent intensity of all pixels along the dotted line of each image. Scale bars, 10 μm. Right: Quantification of the ratio between pixel-averaged fluorescent intensity of cell membrane and that of the cytosol. N = 5 cells. (p = 0.011, one-sided Mann Whitney U test) **(c)** Schematic representation of the optimization of the insertion site at TM5 linker region. **(d)** Left: Maximal $\Delta F/F_0$ response to 10 μM N/OFQ of all sensor prototypes shown in **c**. Right: representative image of HEK293T cells expressing sensor prototypes. **(e)** Top: Schematic representation of three rounds of directed mutagenesis to improve sensor dynamic range. Amino acids that were mutated into a subset of different amino acids in the screening process are labelled in bold. Selected mutation from previous round of screening labelled in magenta. Bottom: Normalized $\Delta F/F_0$ response of HEK293T cells expressing each variant to 10 μM N/OFQ. Each data point represents averaged $\Delta F/F_0$ response from > 3 cells in 3 independent experiments normalized to the maximal $\Delta F/F_0$ response of the best variant in the current round of screening. Magenta: Selected variant from previous round of screening. Green: Best variant in current round of screening.

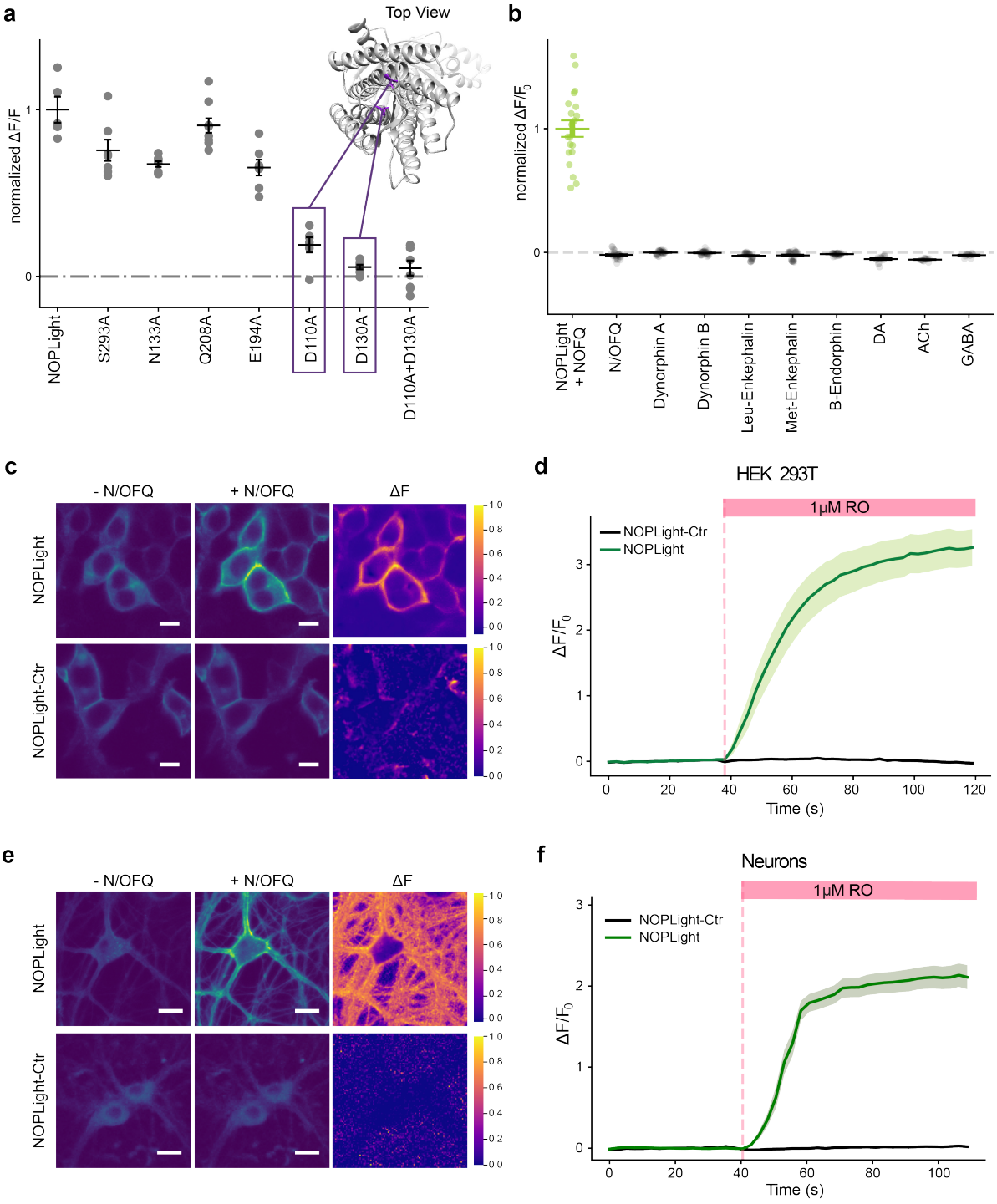

Figure S3.2: **Development and characterization of NOPLight-ctr.**

(a) Quantification of maximal $\Delta F/F_0$ in response to 10 μM N/OFQ in HEK 293T cells expressing NOPLight mutants. Mutated residues indicated by their absolute residue numbering in reference to human NOPR. Structural model of NOPLight-ctr is predicted by RoseTTAfold78. The two mutations selected for NOPLight-ctr are highlighted in purple. **(b)** Normalized maximal $\Delta F/F_0$ of NOPLight-ctr-expressing HEK 293T cells in response to endogenous opioid peptides (1 μM) and fast neurotransmitters (DA: dopamine, Ach: acetylcholine, GABA: gamma-Aminobutyric acid (1 mM)). All data normalized to NOPLight-expressing

HEK293T cells (green). **(c)** Representative images of HEK 293T cells expressing NOPLight (top; scale bars, 10 μm) and NOPLight-ctr (bottom; scale bars, 10 μm) before and after application of 1 μM RO 64-6198. Corresponding normalized pixelwise ΔF shown on the right. **(d)** Average fluorescent fold-change ($\Delta F/F_0$) of HEK 293T cell expressing NOPLight (light green trace) or NOPLight-ctr (black trace) in response to 1 μM RO 64-6198 (3 experiments, data shown as mean ± SEM). **(e)** Representative images of neurons expressing NOPLight (top; scale bars, 20 μm) and NOPLight-ctr (bottom; scale bars, 20 μm) before and after application of 1 μM RO 64-6198. The corresponding normalized pixelwise ΔF is shown on the right. **(f)** Average fluorescent fold-change ($\Delta F/F_0$) of neurons expressing NOPLight (light green trace) or NOPLight-ctr (black trace) in response to 1 μM RO 64-6198 (3 experiments, data shown as mean ± SEM).

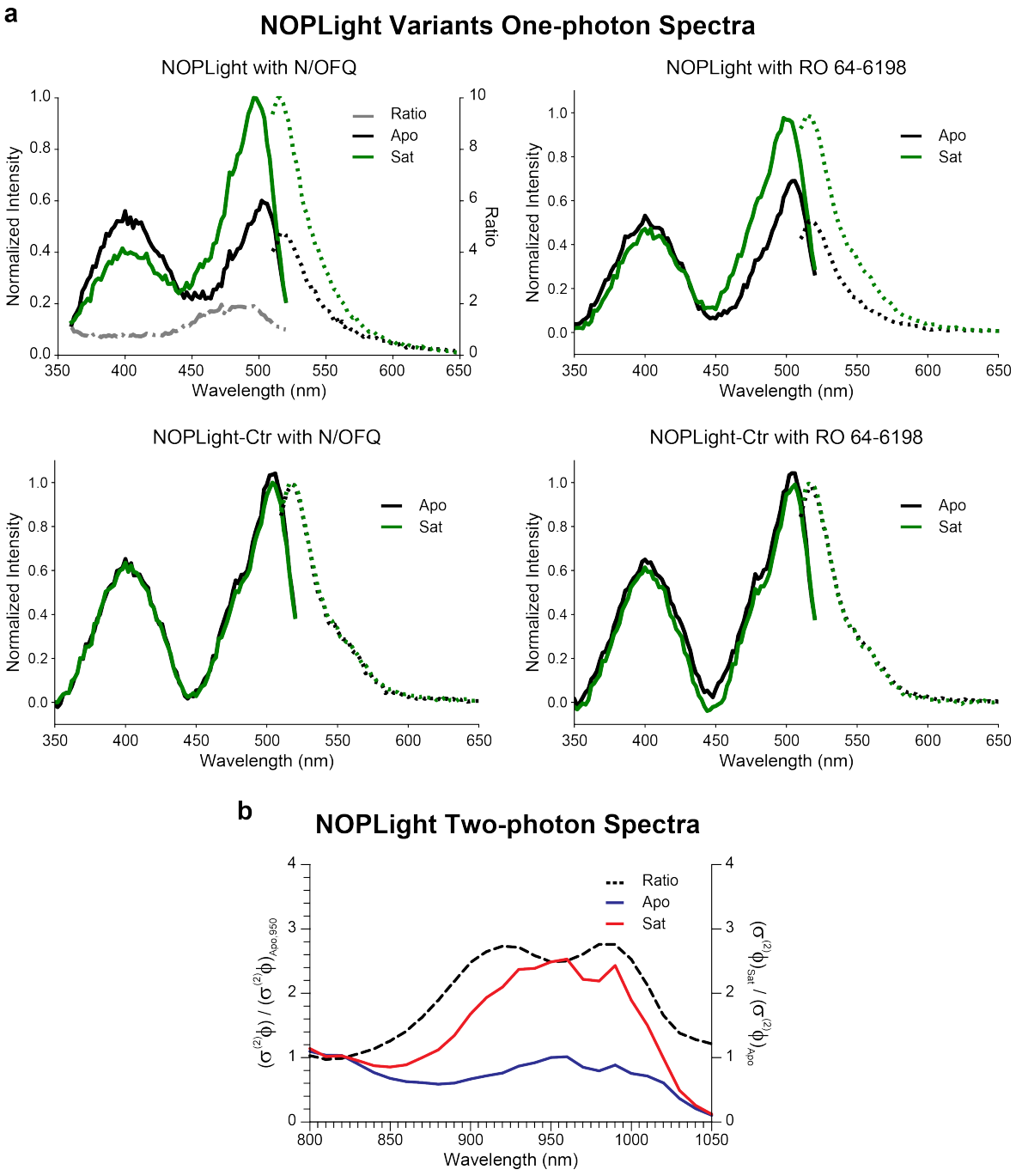

Figure S3.3: **Spectral properties of NOPLight and NOPLight-ctr.**

(a) Top, normalized one-photon fluorescence excitation (solid lines, $\lambda_{excitation}$ = 360 – 520 nm, $\lambda_{emission}$ = 560 nm) and emission (dotted lines, $\lambda_{excitation}$ = 470 nm, $\lambda_{emission}$ = 510 – 650 nm) spectra of NOPLight-expressing HEK293T cells in the absence and presence of either N/OFQ (1 μM) or RO 64-6198 (1 μM). Traces shown are averaged from 3 independent experiments. Intensity measured at each wavelength is normalized to the maximum intensities measured for both the excitation and emission spectra. Bottom, same as on top with NOPLight-Ctr expressing HEK293T cells in the absence and presence of N/OFQ (1 μM) or RO 64-6198 (1 μM). **(b)** Relative two-photon brightness of NOPLight imaged in transfected HEK cells grown attached to a glass coverslip in the presence (Sat) or absence (Apo) of N/OFQ (1 μM). Ratio between Sat and Apo shown in dashed line. Each trace is the average of 3 independent experiments.

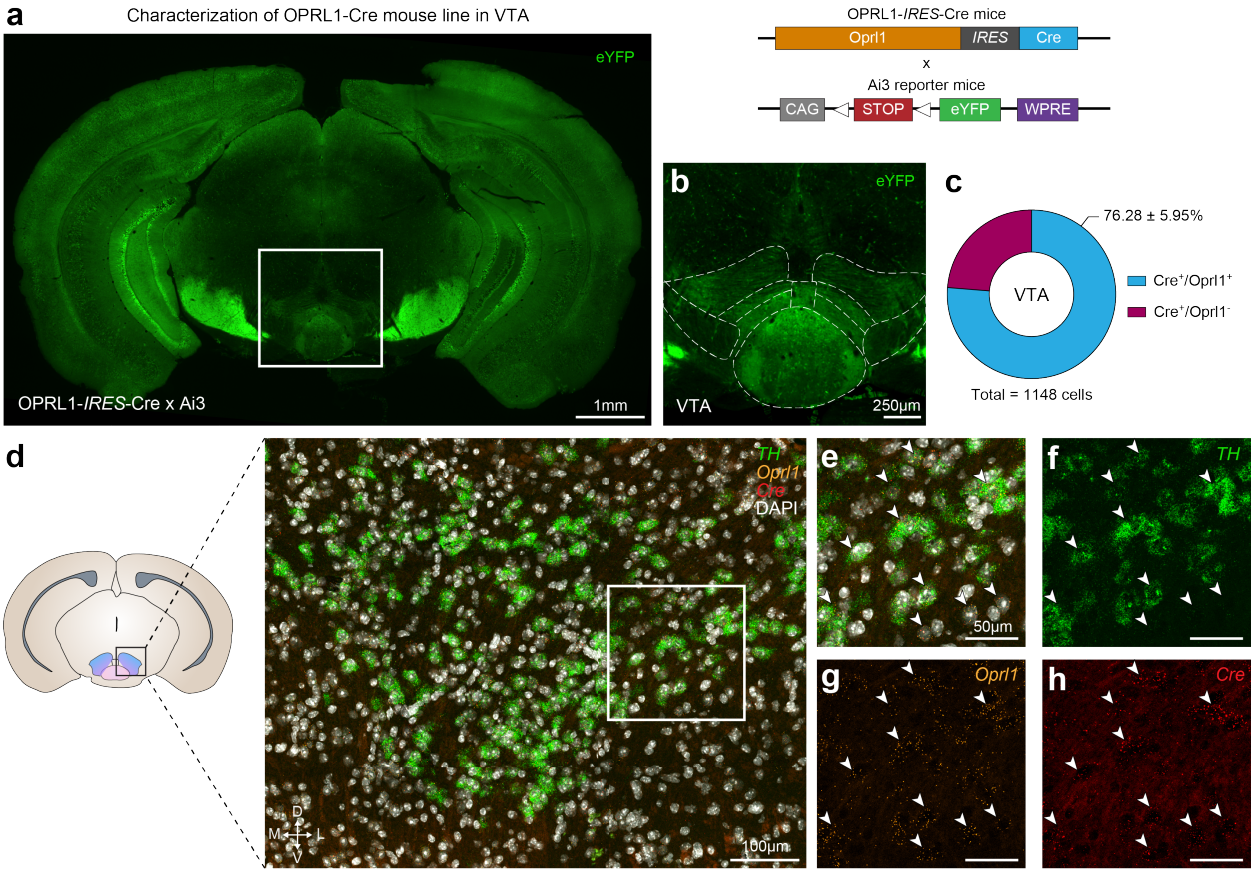

Figure S3.4: **Anatomical characterization of the OPRL1-Cre mouse line in the ventral tegmental area.**

(a) An OPRL1-Cre mouse line was generated and crossed with an Ai3 reporter line. Coronal image at bregma -3.28 mm showing Ai3-eYFP expression driven by OPRL1-Cre. **(b)** Higher magnification of inset from a showing eYFP reporter expression in the ventral tegmental area (VTA). **(c)** Quantification of *Oprl1* expression within Cre-expressing cells detected by *in situ* hybridization in the VTA (N = 2; 2 mice, 2 and 3 slices/mouse). Data represented as mean ± SEM. **(d)** Representative image showing *Oprl1* and Cre expression patterns in OPRL1-Cre mice via *in situ* hybridization of *Oprl1* (orange), Cre (red), *Th* (tyrosine hydroxylase, green), and DAPI (white) in the VTA. **(e–h)**. Higher magnification of inset from **d** showing combined **(e)** and individual **(f–h)** channels for *Th*, *Oprl1*, Cre, and DAPI. Scale bars, 50 µm.

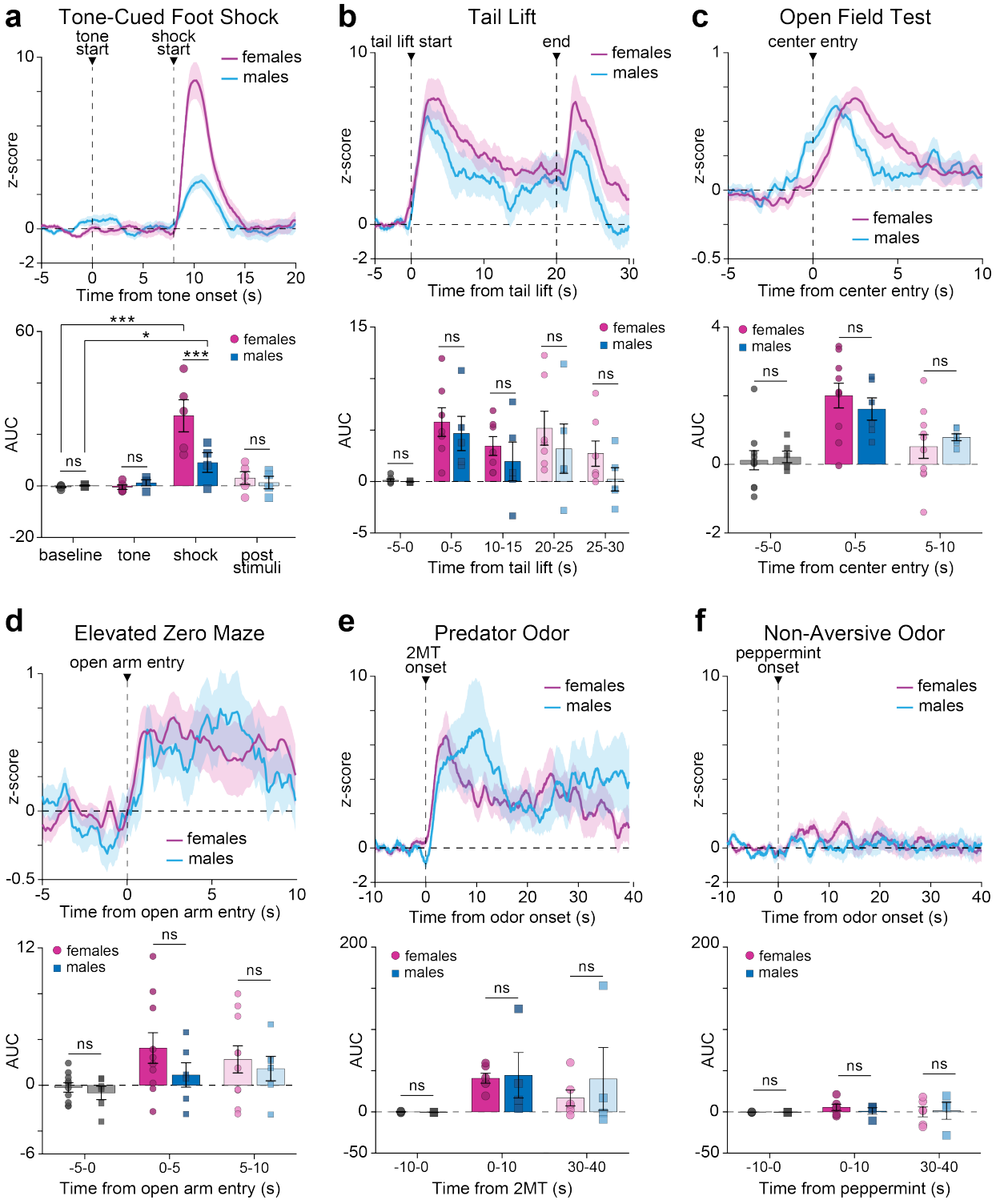

Figure S4.1: **Stress engages pnVTA^{PNOC} neurons in both female and male mice.**

(a) Top: Averaged trace of pnVTA^{PNOC} GCaMP6s activity during epoch surrounding tone-cued foot shock, aligned to tone onset in male (blue) and female (magenta) mice. Bottom: Area under the curve (AUC) for averaged traces, calculated over 8-second intervals surrounding cued-foot shock events for males (blue) and females (magenta). GCaMP6s signal increases in response to shock but not tone for both sexes (1-way ANOVA with Tukey's multiple comparison test, ***$p < 0.001$ *$p < 0.05$, N = 4 males, 5 females), although

the magnitude of the increase is larger in females (2-way ANOVA with Tukey's multiple comparisons test, ***p < 0.001, N = 4 males, 5 females). **(b–f)** Same as **a** for **(b)** 20s tail lift (2-way ANOVA p=0.3767, N = 5 males, 7 females), **(c)** open field test center entry (2-way ANOVA p=0.9794, N = 6 males, 10 females), **(d)** elevated zero maze open arm entry (2-way ANOVA p=0.3212, N = 6 males, 10 females), **(e)** predator (2% 2MT) odor (2-way ANOVA p=0.7345, N = 4 males, 6 females), and **(f)** non-aversive (2% peppermint oil) odor (2-way ANOVA p=0.7633, N = 4 males, 6 females). All data represented as mean ± SEM.

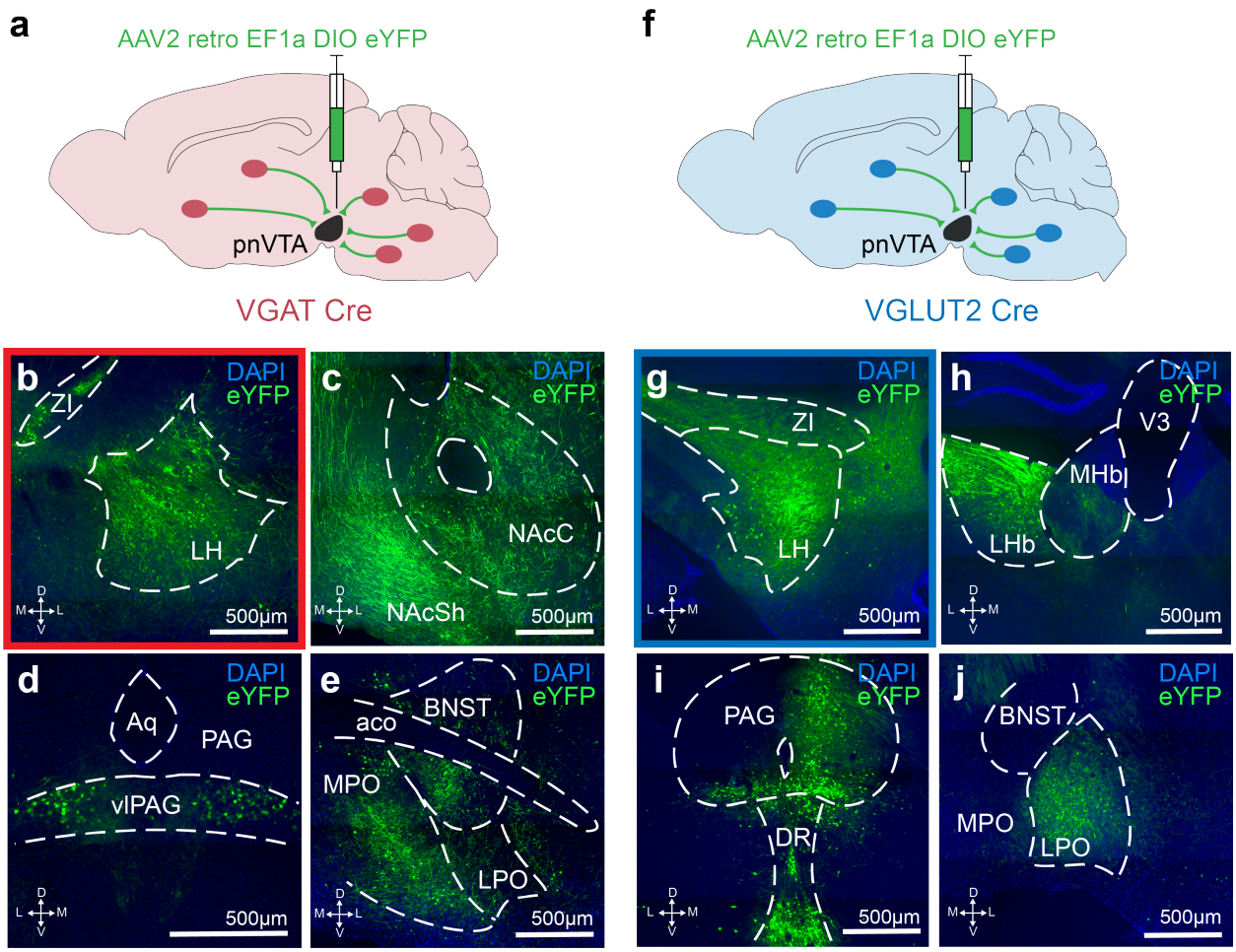

Figure S4.2: **Retrograde tracing identifies GABA and glutamatergic inputs from lateral hypothalamus to pnVTA.**

(a) Cartoon showing injection of a retrograde DIO-eYFP into the pnVTA of VGAT-Cre mice (N = 2). Slices across the entire brain were imaged to identify sources of GABAergic input to the pnVTA. **(b–e)** Representative images from brain regions with relatively high expression of retrograde eYFP (eYFP, green; DAPI, blue). **(f–j)** Same as **a–e** but in VGLUT2-Cre mice (N = 2) to identify sources of glutamatergic input to the pnVTA. LH = lateral hypothalamus, ZI = zona incerta, NAcC = nucleus accumbens core, NAcSh = nucleus accumbens shell, (vl)PAG = (ventro-lateral) periaqueductal gray, Aq = cerebral aqueduct, BNST = bed nuclei of the stria terminalis, MPO = medial preoptic area, LPO = lateral preoptic area, aco = anterior commissure, LHb = lateral habenula, MHb = medial habenula, V3 = third ventricle, DR = dorsal raphe.

REFERENCES

Al-Hasani, R., Gowrishankar, R., Schmitz, G.P., Pedersen, C.E., Marcus, D.J., Shirley, S.E., Hobbs, T.E., Elerding, A.J., Renaud, S.J., Jing, M., Li, Y., Alvarez, V.A., Lemos, J.C., Bruchas, M.R., 2021. Ventral tegmental area GABAergic inhibition of cholinergic interneurons in the ventral nucleus accumbens shell promotes reward reinforcement. Nat. Neurosci. 24, 1414–1428. https://doi.org/10.1038/s41593-021-00898-2

Al-Hasani, R., McCall, J.G., Foshage, A.M., Bruchas, M.R., 2013. Locus coeruleus kappa-opioid receptors modulate reinstatement of cocaine place preference through a noradrenergic mechanism. Neuropsychopharmacol. Off. Publ. Am. Coll. Neuropsychopharmacol. 38, 2484–2497. https://doi.org/10.1038/npp.2013.151

Al-Hasani, R., McCall, J.G., Shin, G., Gomez, A.M., Schmitz, G.P., Bernardi, J.M., Pyo, C.-O., Park, S.I., Marcinkiewcz, C.M., Crowley, N.A., Krashes, M.J., Lowell, B.B., Kash, T.L., Rogers, J.A., Bruchas, M.R., 2015. Distinct Subpopulations of Nucleus Accumbens Dynorphin Neurons Drive Aversion and Reward. Neuron 87, 1063–1077. https://doi.org/10.1016/j.neuron.2015.08.019

Al-Hasani, R., Wong, J.-M.T., Mabrouk, O.S., McCall, J.G., Schmitz, G.P., Porter-Stransky, K.A., Aragona, B.J., Kennedy, R.T., Bruchas, M.R., 2018. In vivo detection of optically-evoked opioid peptide release. eLife 7, e36520. https://doi.org/10.7554/eLife.36520

Allen, R.G., Peng, B., Pellegrino, M.J., Miller, E.D., Grandy, D.K., Lundblad, J.R., Washburn, C.L., Pintar, J.E., 2001. Altered Processing of Pro-Orphanin FQ/Nociceptin and Pro-Opiomelanocortin-Derived Peptides in the Brains of Mice Expressing Defective Prohormone Convertase 2. J. Neurosci. 21, 5864–5870. https://doi.org/10.1523/JNEUROSCI.21-16-05864.2001

Amemori, K., Graybiel, A.M., 2012. Localized microstimulation of primate pregenual cingulate cortex induces negative decision-making. Nat. Neurosci. 15, 776–785. https://doi.org/10.1038/nn.3088

Amemori, K.-I., Amemori, S., Gibson, D.J., Graybiel, A.M., 2018. Striatal Microstimulation Induces Persistent and Repetitive Negative Decision-Making Predicted by Striatal Beta-Band Oscillation. Neuron 99, 829-841.e6. https://doi.org/10.1016/j.neuron.2018.07.022

Amemori, S., Amemori, K.-I., Yoshida, T., Papageorgiou, G.K., Xu, R., Shimazu, H., Desimone, R., Graybiel, A.M., 2020. Microstimulation of primate neocortex targeting striosomes induces negative decision-making. Eur. J. Neurosci. 51, 731–741. https://doi.org/10.1111/ejn.14555

Amemori, S., Graybiel, A.M., Amemori, K.-I., 2021. Causal Evidence for Induction of Pessimistic Decision-Making in Primates by the Network of Frontal Cortex and Striosomes. Front. Neurosci. 15, 649167. https://doi.org/10.3389/fnins.2021.649167

Anderegg, A., Poulin, J.-F., Awatramani, R., 2015. Molecular Heterogeneity of Midbrain Dopaminergic Neurons – Moving Toward Single Cell Resolution. FEBS Lett. 589, 3714–3726. https://doi.org/10.1016/j.febslet.2015.10.022

Andero, R., 2015. Nociceptin and the nociceptin receptor in learning and memory. Prog. Neuropsychopharmacol. Biol. Psychiatry 62, 45–50. https://doi.org/10.1016/j.pnpbp.2015.02.007

Baek, M., DiMaio, F., Anishchenko, I., Dauparas, J., Ovchinnikov, S., Lee, G.R., Wang, J., Cong, Q., Kinch, L.N., Schaeffer, R.D., Millán, C., Park, H., Adams, C., Glassman, C.R., DeGiovanni, A., Pereira, J.H., Rodrigues, A.V., van Dijk, A.A., Ebrecht, A.C., Opperman, D.J., Sagmeister, T., Buhlheller, C., Pavkov-Keller, T., Rathinaswamy, M.K., Dalwadi, U., Yip, C.K., Burke, J.E., Garcia, K.C., Grishin, N.V., Adams, P.D., Read, R.J., Baker, D., 2021. Accurate prediction of protein structures and interactions using a three-track neural network. Science 373, 871–876. https://doi.org/10.1126/science.abj8754

Baik, J.-H., 2013. Dopamine Signaling in reward-related behaviors. Front. Neural Circuits 7, 152. https://doi.org/10.3389/fncir.2013.00152

Banghart, M.R., Neufeld, S.Q., Wong, N.C., Sabatini, B.L., 2015. Enkephalin Disinhibits Mu Opioid Receptor-Rich Striatal Patches via Delta Opioid Receptors. Neuron 88, 1227–1239. https://doi.org/10.1016/j.neuron.2015.11.010

Bankhead, P., Loughrey, M.B., Fernández, J.A., Dombrowski, Y., McArt, D.G., Dunne, P.D., McQuaid, S., Gray, R.T., Murray, L.J., Coleman, H.G., James, J.A., Salto-Tellez, M., Hamilton, P.W., 2017. QuPath: Open source software for digital pathology image analysis. Sci. Rep. 7, 16878. https://doi.org/10.1038/s41598-017-17204-5

Beaulieu, J.-M., Gainetdinov, R.R., 2011. The Physiology, Signaling, and Pharmacology of Dopamine Receptors. Pharmacol. Rev. 63, 182–217. https://doi.org/10.1124/pr.110.002642

Bebawy, D., Marquez, P., Samboul, S., Parikh, D., Hamid, A., Lutfy, K., 2010. Orphanin FQ/nociceptin not only blocks but also reverses behavioral adaptive changes induced by repeated cocaine in mice. Biol. Psychiatry 68, 223–230. https://doi.org/10.1016/j.biopsych.2010.02.010

Berghorst, L.H., Bogdan, R., Frank, M.J., Pizzagalli, D.A., 2013. Acute stress selectively reduces reward sensitivity. Front. Hum. Neurosci. 7. https://doi.org/10.3389/fnhum.2013.00133

Bernard, C., 1957. An Introduction to the Study of Experimental Medicine. Courier Corporation.

Berridge, K.C., 2007. The debate over dopamine's role in reward: the case for incentive salience. Psychopharmacology (Berl.) 191, 391–431. https://doi.org/10.1007/s00213-006-0578-x

Berthele, A., Platzer, S., Dworzak, D., Schadrack, J., Mahal, B., Büttner, A., Assmus, H.P., Wurster, K., Zieglgänsberger, W., Conrad, B., Tölle, T.R., 2003. [3H]-nociceptin ligand-binding and nociceptin opioid receptor mrna expression in the human brain. Neuroscience 121, 629–640. https://doi.org/10.1016/s0306-4522(03)00484-6

Bloem, B., Huda, R., Amemori, K., Abate, A.S., Krishna, G., Wilson, A.L., Carter, C.W., Sur, M., Graybiel, A.M., 2022. Multiplexed action-outcome representation by striatal striosome-matrix compartments detected with a mouse cost-benefit foraging task. Nat. Commun. 13, 1541. https://doi.org/10.1038/s41467-022-28983-5

Bloem, B., Huda, R., Sur, M., Graybiel, A.M., 2017. Two-photon imaging in mice shows striosomes and matrix have overlapping but differential reinforcement-related responses. eLife 6, e32353. https://doi.org/10.7554/eLife.32353

Bockaert, J., Marin, P., Dumuis, A., Fagni, L., 2003. The “magic tail” of G protein-coupled receptors: an anchorage for functional protein networks. FEBS Lett. 546, 65–72. https://doi.org/10.1016/s0014-5793(03)00453-8

Bodnar, R.J., Glass, M.J., Ragnauth, A., Cooper, M.L., 1995. General, mu and kappa opioid antagonists in the nucleus accumbens alter food intake under deprivation, glucoprivic and palatable conditions. Brain Res. 700, 205–212. https://doi.org/10.1016/0006-8993(95)00957-r

Bogdan, R., Pizzagalli, D.A., 2006. Acute Stress Reduces Reward Responsiveness: Implications for Depression. Biol. Psychiatry 60, 1147–1154. https://doi.org/10.1016/j.biopsych.2006.03.037

Borgland, S.L., Taha, S.A., Sarti, F., Fields, H.L., Bonci, A., 2006. Orexin A in the VTA Is Critical for the Induction of Synaptic Plasticity and Behavioral Sensitization to Cocaine. Neuron 49, 589–601. https://doi.org/10.1016/j.neuron.2006.01.016

Bouarab, C., Thompson, B., Polter, A.M., 2019. VTA GABA Neurons at the Interface of Stress and Reward. Front. Neural Circuits 13, 78. https://doi.org/10.3389/fncir.2019.00078

Boulanger, L.M., 2009. Immune proteins in brain development and synaptic plasticity. Neuron 64, 93–109. https://doi.org/10.1016/j.neuron.2009.09.001

Brake, W.G., Zhang, T.Y., Diorio, J., Meaney, M.J., Gratton, A., 2004. Influence of early postnatal rearing conditions on mesocorticolimbic dopamine and behavioural responses to psychostimulants and stressors in adult rats. Eur. J. Neurosci. 19, 1863–1874. https://doi.org/10.1111/j.1460-9568.2004.03286.x

Brimblecombe, K.R., Cragg, S.J., 2017. The Striosome and Matrix Compartments of the Striatum: A Path through the Labyrinth from Neurochemistry toward Function. ACS Chem. Neurosci. 8, 235–242. https://doi.org/10.1021/acschemneuro.6b00333

Brown, G.W., Harris, T. (Eds.), 1978. Social Origins of Depression: A study of psychiatric disorder in women. Routledge, London. https://doi.org/10.4324/9780203714911

Brown, S.A., Vik, P.W., Patterson, T.L., Grant, I., Schuckit, M.A., 1995. Stress, vulnerability and adult alcohol relapse. J. Stud. Alcohol 56, 538–545. https://doi.org/10.15288/jsa.1995.56.538

Burbach, J.P.H., 2011. What Are Neuropeptides?, in: Merighi, A. (Ed.), Neuropeptides: Methods and Protocols. Humana Press, Totowa, NJ, pp. 1–36. https://doi.org/10.1007/978-1-61779-310-3_1

Cabib, S., Puglisi-Allegra, S., 2012. The mesoaccumbens dopamine in coping with stress. Neurosci. Biobehav. Rev. 36, 79–89. https://doi.org/10.1016/j.neubiorev.2011.04.012

Can, A., Dao, D.T., Terrillion, C.E., Piantadosi, S.C., Bhat, S., Gould, T.D., 2012. The Tail Suspension Test. J. Vis. Exp. JoVE 3769. https://doi.org/10.3791/3769

Canales, J.J., Graybiel, A.M., 2000. A measure of striatal function predicts motor stereotypy. Nat. Neurosci. 3, 377–383. https://doi.org/10.1038/73949

Caputi, F.F., Di Benedetto, M., Carretta, D., Bastias del Carmen Candia, S., D'Addario, C., Cavina, C., Candeletti, S., Romualdi, P., 2014. Dynorphin/KOP and nociceptin/NOP gene expression and epigenetic changes by cocaine in rat striatum and nucleus accumbens. Prog. Neuropsychopharmacol. Biol. Psychiatry 49, 36–46. https://doi.org/10.1016/j.pnpbp.2013.10.016

Castro, D.C., Berridge, K.C., 2014. Opioid Hedonic Hotspot in Nucleus Accumbens Shell: Mu, Delta, and Kappa Maps for Enhancement of Sweetness "Liking" and "Wanting." J. Neurosci. 34, 4239–4250. https://doi.org/10.1523/JNEUROSCI.4458-13.2014

Castro, D.C., Bruchas, M.R., 2019. A Motivational and Neuropeptidergic Hub: Anatomical and Functional Diversity within the Nucleus Accumbens Shell. Neuron 102, 529–552. https://doi.org/10.1016/j.neuron.2019.03.003

Castro, D.C., Oswell, C.S., Zhang, E.T., Pedersen, C.E., Piantadosi, S.C., Rossi, M.A., Hunker, A.C., Guglin, A., Morón, J.A., Zweifel, L.S., Stuber, G.D., Bruchas, M.R., 2021. An endogenous opioid circuit determines state-dependent reward consumption. Nature 598, 646–651. https://doi.org/10.1038/s41586-021-04013-0

Chiou, L.-C., Liao, Y.-Y., Fan, P.-C., Kuo, P.-H., Wang, C.-H., Riemer, C., Prinssen, E.P., 2007. Nociceptin/orphanin FQ peptide receptors: pharmacology and clinical implications. Curr. Drug Targets 8, 117–135. https://doi.org/10.2174/138945007779315605

Ciccocioppo, R., Angeletti, S., Panocka, I., Massi, M., 2000. Nociceptin/orphanin FQ and drugs of abuse. Peptides 21, 1071–1080. https://doi.org/10.1016/s0196-9781(00)00245-x

Ciccocioppo, R., Borruto, A.M., Domi, A., Teshima, K., Cannella, N., Weiss, F., 2019. NOP-Related Mechanisms in Substance Use Disorders. Handb. Exp. Pharmacol. 254, 187–212. https://doi.org/10.1007/164_2019_209

Ciccocioppo, R., de Guglielmo, G., Hansson, A.C., Ubaldi, M., Kallupi, M., Cruz, M.T., Oleata, C.S., Heilig, M., Roberto, M., 2014. Restraint stress alters nociceptin/orphanin FQ and CRF systems in the rat central amygdala: significance for anxiety-like behaviors. J. Neurosci. Off. J. Soc. Neurosci. 34, 363–372. https://doi.org/10.1523/JNEUROSCI.2400-13.2014

Civelli, O., 2008. The orphanin FQ/nociceptin (OFQ/N) system. Results Probl. Cell Differ. 46, 1–25. https://doi.org/10.1007/400_2007_057

Clark, S.D., Abi-Dargham, A., 2019. The Role of Dynorphin and the Kappa Opioid Receptor in the Symptomatology of Schizophrenia: A Review of the Evidence. Biol. Psychiatry 86, 502–511. https://doi.org/10.1016/j.biopsych.2019.05.012

Conway, S.M., Mikati, M.O., Al-Hasani, R., 2022. Challenges and new opportunities for detecting endogenous opioid peptides in reward. Addict. Neurosci. 2, 100016. https://doi.org/10.1016/j.addicn.2022.100016

Crittenden, J.R., Graybiel, A.M., 2011. Basal Ganglia disorders associated with imbalances in the striatal striosome and matrix compartments. Front. Neuroanat. 5, 59. https://doi.org/10.3389/fnana.2011.00059

Crittenden, J.R., Tillberg, P.W., Riad, M.H., Shima, Y., Gerfen, C.R., Curry, J., Housman, D.E., Nelson, S.B., Boyden, E.S., Graybiel, A.M., 2016. Striosome-dendron bouquets highlight a unique striatonigral circuit targeting dopamine-containing neurons. Proc. Natl. Acad. Sci. U. S. A. 113, 11318–11323. https://doi.org/10.1073/pnas.1613337113

Cui, Y., Ostlund, S.B., James, A.S., Park, C.S., Ge, W., Roberts, K.W., Mittal, N., Murphy, N.P., Cepeda, C., Kieffer, B.L., Levine, M.S., Jentsch, J.D., Walwyn, W.M., Sun, Y.E., Evans, C.J., Maidment, N.T., Yang, X.W., 2014. Targeted expression of μ-opioid receptors in a subset of striatal direct-pathway neurons restores opiate reward. Nat. Neurosci. 17, 254–261. https://doi.org/10.1038/nn.3622

da Silva, J.A., Tecuapetla, F., Paixão, V., Costa, R.M., 2018. Dopamine neuron activity before action initiation gates and invigorates future movements. Nature 554, 244–248. https://doi.org/10.1038/nature25457

Damier, P., Hirsch, E.C., Agid, Y., Graybiel, A.M., 1999. The substantia nigra of the human brain. I. Nigrosomes and the nigral matrix, a compartmental organization based on calbindin D(28K) immunohistochemistry. Brain J. Neurol. 122 (Pt 8), 1421–1436. https://doi.org/10.1093/brain/122.8.1421

Der-Avakian, A., D'Souza, M.S., Potter, D.N., Chartoff, E.H., Carlezon, W.A., Pizzagalli, D.A., Markou, A., 2017. Social defeat disrupts reward learning and potentiates striatal nociceptin/orphanin FQ mRNA in rats. Psychopharmacology (Berl.) 234, 1603–1614. https://doi.org/10.1007/s00213-017-4584-y

Der-Avakian, A., Markou, A., 2012. The neurobiology of anhedonia and other reward-related deficits. Trends Neurosci., Special Issue: Neuropsychiatric Disorders 35, 68–77. https://doi.org/10.1016/j.tins.2011.11.005

Devine, D.P., Hoversten, M.T., Ueda, Y., Akil, H., 2003. Nociceptin/Orphanin FQ Content is Decreased in Forebrain Neurones During Acute Stress. J. Neuroendocrinol. 15, 69–74. https://doi.org/10.1046/j.1365-2826.2003.00868.x

Devine, D.P., Watson, S.J., Akil, H., 2001. Nociceptin/orphanin FQ regulates neuroendocrine function of the limbic–hypothalamic–pituitary–adrenal axis. Neuroscience 102, 541–553. https://doi.org/10.1016/S0306-4522(00)00517-0

Di Giannuario, A., Pieretti, S., 2000. Nociceptin differentially affects morphine-induced dopamine release from the nucleus accumbens and nucleus caudate in rats. Peptides 21, 1125–1130. https://doi.org/10.1016/s0196-9781(00)00250-3

D'Oliveira da Silva, F., Zaveri, N.T., Moulédous, L., 2023. Acute single non-sedative doses of NOP receptor agonists affect acquisition of object location memory but repeated high doses do

not induce long-lasting deficits. Neurobiol. Learn. Mem. 205, 107841. https://doi.org/10.1016/j.nlm.2023.107841

Donica, C.L., Awwad, H.O., Thakker, D.R., Standifer, K.M., 2013. Cellular mechanisms of nociceptin/orphanin FQ (N/OFQ) peptide (NOP) receptor regulation and heterologous regulation by N/OFQ. Mol. Pharmacol. 83, 907–918. https://doi.org/10.1124/mol.112.084632

Donica, C.L., Ramirez, V.I., Awwad, H.O., Zaveri, N.T., Toll, L., Standifer, K.M., 2011. Orphanin FQ/nociceptin activates nuclear factor kappa B. J. Neuroimmune Pharmacol. Off. J. Soc. NeuroImmune Pharmacol. 6, 617–625. https://doi.org/10.1007/s11481-011-9279-2

Driscoll, J.R., Wallace, T.L., Martin, W.J., Margolis, E.B., 2019. Differential modulation of ventral tegmental area circuits by the nociceptin/orphanin FQ system (preprint). Neuroscience. https://doi.org/10.1101/776484

Duffet, L., Kosar, S., Panniello, M., Viberti, B., Bracey, E., Zych, A.D., Radoux-Mergault, A., Zhou, X., Dernic, J., Ravotto, L., Tsai, Y.-C., Figueiredo, M., Tyagarajan, S.K., Weber, B., Stoeber, M., Gogolla, N., Schmidt, M.H., Adamantidis, A.R., Fellin, T., Burdakov, D., Patriarchi, T., 2022. A genetically encoded sensor for in vivo imaging of orexin neuropeptides. Nat. Methods 19, 231–241. https://doi.org/10.1038/s41592-021-01390-2

Duffet, L., Williams, E.T., Gresch, A., Chen, S., Bhat, M.A., Benke, D., Hartrampf, N., Patriarchi, T., 2023. Optical tools for visualizing and controlling human GLP-1 receptor activation with high spatiotemporal resolution. eLife 12, RP86628. https://doi.org/10.7554/eLife.86628

Eblen, F., Graybiel, A.M., 1995. Highly restricted origin of prefrontal cortical inputs to striosomes in the macaque monkey. J. Neurosci. Off. J. Soc. Neurosci. 15, 5999–6013. https://doi.org/10.1523/JNEUROSCI.15-09-05999.1995

Enard, W., 2011. FOXP2 and the role of cortico-basal ganglia circuits in speech and language evolution. Curr. Opin. Neurobiol. 21, 415–424. https://doi.org/10.1016/j.conb.2011.04.008

Evans, R.C., Twedell, E.L., Zhu, M., Ascencio, J., Zhang, R., Khaliq, Z.M., 2020. Functional Dissection of Basal Ganglia Inhibitory Inputs onto Substantia Nigra Dopaminergic Neurons. Cell Rep. 32, 108156. https://doi.org/10.1016/j.celrep.2020.108156

Fields, H.L., Margolis, E.B., 2015. Understanding opioid reward. Trends Neurosci. 38, 217–225. https://doi.org/10.1016/j.tins.2015.01.002

Flau, K., Redmer, A., Liedtke, S., Kathmann, M., Schlicker, E., 2002. Inhibition of striatal and retinal dopamine release via nociceptin/orphanin FQ receptors. Br. J. Pharmacol. 137, 1355–1361. https://doi.org/10.1038/sj.bjp.0704998

Fong, W.L., Kuo, H.-Y., Wu, H.-L., Chen, S.-Y., Liu, F.-C., 2018. Differential and Overlapping Pattern of Foxp1 and Foxp2 Expression in the Striatum of Adult Mouse Brain. Neuroscience 388, 214–223. https://doi.org/10.1016/j.neuroscience.2018.07.017

Fouriezos, G., Wise, R.A., 1976. Pimozide-induced extinction of intracranial self-stimulation: Response patterns rule out motor or performance deficits. Brain Res. 103, 377–380. https://doi.org/10.1016/0006-8993(76)90809-X

Friedman, A., Homma, D., Bloem, B., Gibb, L.G., Amemori, K.-I., Hu, D., Delcasso, S., Truong, T.F., Yang, J., Hood, A.S., Mikofalvy, K.A., Beck, D.W., Nguyen, N., Nelson, E.D., Toro Arana, S.E., Vorder Bruegge, R.H., Goosens, K.A., Graybiel, A.M., 2017. Chronic Stress Alters Striosome-Circuit Dynamics, Leading to Aberrant Decision-Making. Cell 171, 1191-1205.e28. https://doi.org/10.1016/j.cell.2017.10.017

Friedman, A., Homma, D., Gibb, L.G., Amemori, K.-I., Rubin, S.J., Hood, A.S., Riad, M.H., Graybiel, A.M., 2015. A Corticostriatal Path Targeting Striosomes Controls Decision-Making under Conflict. Cell 161, 1320–1333. https://doi.org/10.1016/j.cell.2015.04.049

Friedman, A., Hueske, E., Drammis, S.M., Toro Arana, S.E., Nelson, E.D., Carter, C.W., Delcasso, S., Rodriguez, R.X., Lutwak, H., DiMarco, K.S., Zhang, Q., Rakocevic, L.I., Hu, D., Xiong, J.K., Zhao, J., Gibb, L.G., Yoshida, T., Siciliano, C.A., Diefenbach, T.J., Ramakrishnan, C., Deisseroth, K., Graybiel, A.M., 2020. Striosomes Mediate Value-Based Learning Vulnerable in Age and a Huntington's Disease Model. Cell 183, 918-934.e49. https://doi.org/10.1016/j.cell.2020.09.060

Fu, X., Zhu, Z.-H., Wang, Y.-Q., Wu, G.-C., 2007. Regulation of proinflammatory cytokines gene expression by nociceptin/orphanin FQ in the spinal cord and the cultured astrocytes. Neuroscience 144, 275–285. https://doi.org/10.1016/j.neuroscience.2006.09.016

Gavioli, E.C., Calo', G., 2013. Nociceptin/orphanin FQ receptor antagonists as innovative antidepressant drugs. Pharmacol. Ther. 140, 10–25. https://doi.org/10.1016/j.pharmthera.2013.05.008

Gavioli, E.C., Holanda, V.A.D., Calo, G., Ruzza, C., 2021. Nociceptin/orphanin FQ receptor system blockade as an innovative strategy for increasing resilience to stress. Peptides 141, 170548. https://doi.org/10.1016/j.peptides.2021.170548

Gavioli, E.C., Marzola, G., Guerrini, R., Bertorelli, R., Zucchini, S., De Lima, T.C.M., Rae, G.A., Salvadori, S., Regoli, D., Calo, G., 2003. Blockade of nociceptin/orphanin FQ–NOP receptor signalling produces antidepressant-like effects: pharmacological and genetic evidences from the mouse forced swimming test. Eur. J. Neurosci. 17, 1987–1990. https://doi.org/10.1046/j.1460-9568.2003.02603.x

Gavioli, E.C., Rae, G.A., Calo', G., Guerrini, R., De Lima, T.C.M., 2002. Central injections of nocistatin or its C-terminal hexapeptide exert anxiogenic-like effect on behaviour of mice in the plus-maze test. Br. J. Pharmacol. 136, 764–772. https://doi.org/10.1038/sj.bjp.0704739

Gavioli, E.C., Vaughan, C.W., Marzola, G., Guerrini, R., Mitchell, V.A., Zucchini, S., De Lima, T.C.M., Rae, G.A., Salvadori, S., Regoli, D., Calo', G., 2004. Antidepressant-like effects of the nociceptin/orphanin FQ receptor antagonist UFP-101: new evidence from rats and mice. Naunyn. Schmiedebergs Arch. Pharmacol. 369, 547–553. https://doi.org/10.1007/s00210-004-0939-0

Giguère, N., Burke Nanni, S., Trudeau, L.-E., 2018. On Cell Loss and Selective Vulnerability of Neuronal Populations in Parkinson's Disease. Front. Neurol. 9, 455. https://doi.org/10.3389/fneur.2018.00455

Girven, K.S., Mangieri, L., Bruchas, M.R., 2022. Emerging approaches for decoding neuropeptide transmission. Trends Neurosci. 45, 899–912. https://doi.org/10.1016/j.tins.2022.09.005

Goeldner, C., Reiss, D., Kieffer, B.L., Ouagazzal, A.-M., 2010. Endogenous nociceptin/orphanin-fq in the dorsal hippocampus facilitates despair-related behavior. Hippocampus 20, 911–916. https://doi.org/10.1002/hipo.20760

Gokce, O., Stanley, G.M., Treutlein, B., Neff, N.F., Camp, J.G., Malenka, R.C., Rothwell, P.E., Fuccillo, M.V., Südhof, T.C., Quake, S.R., 2016. Cellular Taxonomy of the Mouse Striatum as Revealed by Single-Cell RNA-Seq. Cell Rep. 16, 1126–1137. https://doi.org/10.1016/j.celrep.2016.06.059

Gomes-de-Souza, L., Benini, R., Costa-Ferreira, W., Crestani, C.C., 2019. GABAA but not GABAB receptors in the lateral hypothalamus modulate the tachycardic response to emotional stress in rats. Eur. Neuropsychopharmacol. J. Eur. Coll. Neuropsychopharmacol. 29, 672–680. https://doi.org/10.1016/j.euroneuro.2019.03.001

Gomes-de-Souza, L., Costa-Ferreira, W., Mendonça, M.M., Xavier, C.H., Crestani, C.C., 2021. Lateral hypothalamus involvement in control of stress response by bed nucleus of the stria terminalis endocannabinoid neurotransmission in male rats. Sci. Rep. 11, 16133. https://doi.org/10.1038/s41598-021-95401-z

Gordon-Fennell, A., Barbakh, J.M., Utley, M.T., Singh, S., Bazzino, P., Gowrishankar, R., Bruchas, M.R., Roitman, M.F., Stuber, G.D., 2023. An open-source platform for head-fixed operant and consummatory behavior. eLife 12, e86183. https://doi.org/10.7554/eLife.86183

Gorwood, P., 2008. Neurobiological mechanisms of anhedonia. Dialogues Clin. Neurosci. 10, 291–299.

Goto, Y., Grace, A.A., 2005. Dopaminergic modulation of limbic and cortical drive of nucleus accumbens in goal-directed behavior. Nat. Neurosci. 8, 805–812. https://doi.org/10.1038/nn1471

Goto, Y., Otani, S., Grace, A.A., 2007. The Yin and Yang of dopamine release: a new perspective. Neuropharmacology 53, 583–587. https://doi.org/10.1016/j.neuropharm.2007.07.007

Grace, A.A., Floresco, S.B., Goto, Y., Lodge, D.J., 2007. Regulation of firing of dopaminergic neurons and control of goal-directed behaviors. Trends Neurosci. 30, 220–227. https://doi.org/10.1016/j.tins.2007.03.003

Graybiel, A.M., 1990. Neurotransmitters and neuromodulators in the basal ganglia. Trends Neurosci. 13, 244–254. https://doi.org/10.1016/0166-2236(90)90104-i

Graybiel, A.M., Hickey, T.L., 1982. Chemospecificity of ontogenetic units in the striatum: demonstration by combining [3H]thymidine neuronography and histochemical staining. Proc. Natl. Acad. Sci. U. S. A. 79, 198–202. https://doi.org/10.1073/pnas.79.1.198

Graybiel, A.M., Matsushima, A., 2023. Striosomes and Matrisomes: Scaffolds for Dynamic Coupling of Volition and Action. Annu. Rev. Neurosci. 46, 359–380. https://doi.org/10.1146/annurev-neuro-121522-025740

Green, M.K., Barbieri, E.V., Brown, B.D., Chen, K.-W., Devine, D.P., 2007. Roles of the bed nucleus of stria terminalis and of the amygdala in N/OFQ-mediated anxiety and HPA axis activation. Neuropeptides 41, 399–410. https://doi.org/10.1016/j.npep.2007.09.002

Green, M.K., Devine, D.P., 2009. Nociceptin/Orphanin FQ and NOP receptor gene regulation after acute or repeated social defeat stress. Neuropeptides 43, 507–514. https://doi.org/10.1016/j.npep.2009.08.003

Gu, H., Hu, D., Hong, X., Mao, J., Cui, Y., Hui, N., Sha, J., 2003. [Changes and significance of orphanin and serotonin in patients with postpartum depression]. Zhonghua Fu Chan Ke Za Zhi 38, 727–728.

Gunaydin, L.A., Grosenick, L., Finkelstein, J.C., Kauvar, I.V., Fenno, L.E., Adhikari, A., Lammel, S., Mirzabekov, J.J., Airan, R.D., Zalocusky, K.A., Tye, K.M., Anikeeva, P., Malenka, R.C., Deisseroth, K., 2014. Natural Neural Projection Dynamics Underlying Social Behavior. Cell 157, 1535–1551. https://doi.org/10.1016/j.cell.2014.05.017

Halbout, B., Marshall, A.T., Azimi, A., Liljeholm, M., Mahler, S.V., Wassum, K.M., Ostlund, S.B., 2019. Mesolimbic dopamine projections mediate cue-motivated reward seeking but not reward retrieval in rats. eLife 8, e43551. https://doi.org/10.7554/eLife.43551

Han, X., DeBold, J.F., Miczek, K.A., 2017. Prevention and reversal of social stress-escalated cocaine self-administration in mice by intra-VTA CRFR1 antagonism. Psychopharmacology (Berl.) 234, 2813–2821. https://doi.org/10.1007/s00213-017-4676-8

Hanson, J.L., Hariri, A.R., Williamson, D.E., 2015. Blunted Ventral Striatum Development in Adolescence Reflects Emotional Neglect and Predicts Depressive Symptoms. Biol. Psychiatry 78, 598–605. https://doi.org/10.1016/j.biopsych.2015.05.010

Hardaway, J.A., Halladay, L.R., Mazzone, C.M., Pati, D., Bloodgood, D.W., Kim, M., Jensen, J., DiBerto, J.F., Boyt, K.M., Shiddapur, A., Erfani, A., Hon, O.J., Neira, S., Stanhope, C.M., Sugam, J.A., Saddoris, M.P., Tipton, G., McElligott, Z., Jhou, T.C., Stuber, G.D., Bruchas, M.R., Bulik, C.M., Holmes, A., Kash, T.L., 2019. Central Amygdala Prepronociceptin-Expressing Neurons Mediate Palatable Food Consumption and Reward. Neuron 102, 1037-1052.e7. https://doi.org/10.1016/j.neuron.2019.03.037

Harris, G.C., Wimmer, M., Aston-Jones, G., 2005. A role for lateral hypothalamic orexin neurons in reward seeking. Nature 437, 556–559. https://doi.org/10.1038/nature04071

He, M., Tucciarone, J., Lee, S., Nigro, M.J., Kim, Y., Levine, J.M., Kelly, S.M., Krugikov, I., Wu, P., Chen, Y., Gong, L., Hou, Y., Osten, P., Rudy, B., Huang, Z.J., 2016. Strategies and Tools for Combinatorial Targeting of GABAergic Neurons in Mouse Cerebral Cortex. Neuron 92, 555. https://doi.org/10.1016/j.neuron.2016.10.009

Henn, F.A., Vollmayr, B., 2005. Stress models of depression: Forming genetically vulnerable strains. Neurosci. Biobehav. Rev., Animal Models of Depression and Antidepressant Activity 29, 799–804. https://doi.org/10.1016/j.neubiorev.2005.03.019

Henny, P., Brown, M.T.C., Northrop, A., Faunes, M., Ungless, M.A., Magill, P.J., Bolam, J.P., 2012. Structural correlates of heterogeneous in vivo activity of midbrain dopaminergic neurons. Nat. Neurosci. 15, 613–619. https://doi.org/10.1038/nn.3048

Hikosaka, O., Kim, H.F., Yasuda, M., Yamamoto, S., 2014. Basal ganglia circuits for reward value-guided behavior. Annu. Rev. Neurosci. 37, 289–306. https://doi.org/10.1146/annurev-neuro-071013-013924

Holanda, V.A.D., Pacifico, S., Azevedo Neto, J., Finetti, L., Lobão-Soares, B., Calo, G., Gavioli, E.C., Ruzza, C., 2019. Modulation of the NOP receptor signaling affects resilience to acute stress. J. Psychopharmacol. Oxf. Engl. 33, 1540–1549. https://doi.org/10.1177/0269881119864942

Howe, M.W., Dombeck, D.A., 2016. Rapid signalling in distinct dopaminergic axons during locomotion and reward. Nature 535, 505–510. https://doi.org/10.1038/nature18942

Hsu, R., Taylor, J.R., Newton, S.S., Alvaro, J.D., Haile, C., Han, G., Hruby, V.J., Nestler, E.J., Duman, R.S., 2005. Blockade of melanocortin transmission inhibits cocaine reward. Eur. J. Neurosci. 21, 2233–2242. https://doi.org/10.1111/j.1460-9568.2005.04038.x

Hunker, A.C., Soden, M.E., Krayushkina, D., Heymann, G., Awatramani, R., Zweifel, L.S., 2020. Conditional Single Vector CRISPR/SaCas9 Viruses for Efficient Mutagenesis in the Adult Mouse Nervous System. Cell Rep. 30, 4303-4316.e6. https://doi.org/10.1016/j.celrep.2020.02.092

Iglesias, A.G., Chiu, A.S., Wong, J., Campus, P., Li, F., Liu, Z. (Nemo), Bhatti, J.K., Patel, S.A., Deisseroth, K., Akil, H., Burgess, C.R., Flagel, S.B., 2023. Inhibition of Dopamine Neurons Prevents Incentive Value Encoding of a Reward Cue: With Revelations from Deep Phenotyping. J. Neurosci. 43, 7376–7392. https://doi.org/10.1523/JNEUROSCI.0848-23.2023

Ironside, M., Amemori, K.-I., McGrath, C.L., Pedersen, M.L., Kang, M.S., Amemori, S., Frank, M.J., Graybiel, A.M., Pizzagalli, D.A., 2020. Approach-Avoidance Conflict in Major Depressive Disorder: Congruent Neural Findings in Humans and Nonhuman Primates. Biol. Psychiatry 87, 399–408. https://doi.org/10.1016/j.biopsych.2019.08.022

Isosaka, T., Matsuo, T., Yamaguchi, T., Funabiki, K., Nakanishi, S., Kobayakawa, R., Kobayakawa, K., 2015. Htr2a-Expressing Cells in the Central Amygdala Control the Hierarchy between Innate and Learned Fear. Cell 163, 1153–1164. https://doi.org/10.1016/j.cell.2015.10.047

Jais, A., Paeger, L., Sotelo-Hitschfeld, T., Bremser, S., Prinzensteiner, M., Klemm, P., Mykytiuk, V., Widdershooven, P.J.M., Vesting, A.J., Grzelka, K., Minère, M., Cremer, A.L., Xu, J., Korotkova, T., Lowell, B.B., Zeilhofer, H.U., Backes, H., Fenselau, H., Wunderlich, F.T., Kloppenburg, P., Brüning, J.C., 2020. PNOCARC Neurons Promote Hyperphagia and Obesity upon High-Fat-Diet Feeding. Neuron 106, 1009-1025.e10. https://doi.org/10.1016/j.neuron.2020.03.022

Jaquins-Gerstl, A., Michael, A.C., 2015. A review of the effects of FSCV and microdialysis measurements on dopamine release in the surrounding tissue. The Analyst 140, 3696–3708. https://doi.org/10.1039/c4an02065k

Jenck, F., Moreau, J.L., Martin, J.R., Kilpatrick, G.J., Reinscheid, R.K., Monsma, F.J., Nothacker, H.P., Civelli, O., 1997. Orphanin FQ acts as an anxiolytic to attenuate behavioral responses to stress. Proc. Natl. Acad. Sci. U. S. A. 94, 14854–14858. https://doi.org/10.1073/pnas.94.26.14854

Jennings, J.H., Ung, R.L., Resendez, S.L., Stamatakis, A.M., Taylor, J.G., Huang, J., Veleta, K., Kantak, P.A., Aita, M., Shilling-Scrivo, K., Ramakrishnan, C., Deisseroth, K., Otte, S., Stuber, G.D., 2015. Visualizing Hypothalamic Network Dynamics for Appetitive and Consummatory Behaviors. Cell 160, 516–527. https://doi.org/10.1016/j.cell.2014.12.026

Jing, M., Li, Yuexuan, Zeng, J., Huang, P., Skirzewski, M., Kljakic, O., Peng, W., Qian, T., Tan, K., Zou, J., Trinh, S., Wu, R., Zhang, S., Pan, S., Hires, S.A., Xu, M., Li, H., Saksida, L.M., Prado, V.F., Bussey, T.J., Prado, M.A.M., Chen, L., Cheng, H., Li, Yulong, 2020. An optimized acetylcholine sensor for monitoring in vivo cholinergic activity. Nat. Methods 17, 1139–1146. https://doi.org/10.1038/s41592-020-0953-2

Jong, J.W. de, Afjei, S.A., Dorocic, I.P., Peck, J.R., Liu, C., Kim, C.K., Tian, L., Deisseroth, K., Lammel, S., 2019. A Neural Circuit Mechanism for Encoding Aversive Stimuli in the Mesolimbic Dopamine System. Neuron 101, 133-151.e7. https://doi.org/10.1016/j.neuron.2018.11.005

Journigan, V.B., Polgar, W.E., Khroyan, T.V., Zaveri, N.T., 2014. Designing bifunctional NOP receptor-mu opioid receptor ligands from NOP-receptor selective scaffolds. Part II. Bioorg. Med. Chem. 22, 2508–2516. https://doi.org/10.1016/j.bmc.2014.02.047

Kagiampaki, Z., Rohner, V., Kiss, C., Curreli, S., Dieter, A., Wilhelm, M., Harada, M., Duss, S.N., Dernic, J., Bhat, M.A., Zhou, X., Ravotto, L., Ziebarth, T., Wasielewski, L.M., Sönmez, L., Benke, D., Weber, B., Bohacek, J., Reiner, A., Wiegert, J.S., Fellin, T., Patriarchi, T., 2023. Sensitive multicolor indicators for monitoring norepinephrine in vivo. Nat. Methods 20, 1426–1436. https://doi.org/10.1038/s41592-023-01959-z

Kallupi, M., Scuppa, G., de Guglielmo, G., Calò, G., Weiss, F., Statnick, M.A., Rorick-Kehn, L.M., Ciccocioppo, R., 2017. Genetic Deletion of the Nociceptin/Orphanin FQ Receptor in the Rat Confers Resilience to the Development of Drug Addiction. Neuropsychopharmacology 42, 695–706. https://doi.org/10.1038/npp.2016.171

Kash, T.L., Pleil, K.E., Marcinkiewcz, C.A., Lowery-Gionta, E.G., Crowley, N., Mazzone, C., Sugam, J., Hardaway, J.A., McElligott, Z.A., 2015. Neuropeptide regulation of signaling and behavior in the BNST. Mol. Cells 38, 1–13. https://doi.org/10.14348/molcells.2015.2261

Kelly, S.M., Raudales, R., He, M., Lee, J.H., Kim, Y., Gibb, L.G., Wu, P., Matho, K., Osten, P., Graybiel, A.M., Huang, Z.J., 2018. Radial Glial Lineage Progression and Differential Intermediate Progenitor Amplification Underlie Striatal Compartments and Circuit Organization. Neuron 99, 345-361.e4. https://doi.org/10.1016/j.neuron.2018.06.021

Kempadoo, K.A., Tourino, C., Cho, S.L., Magnani, F., Leinninger, G.-M., Stuber, G.D., Zhang, F., Myers, M.G., Deisseroth, K., de Lecea, L., Bonci, A., 2013. Hypothalamic neurotensin projections promote reward by enhancing glutamate transmission in the VTA. J. Neurosci. Off. J. Soc. Neurosci. 33, 7618–7626. https://doi.org/10.1523/JNEUROSCI.2588-12.2013

Kennedy, S.E., Koeppe, R.A., Young, E.A., Zubieta, J.-K., 2006. Dysregulation of endogenous opioid emotion regulation circuitry in major depression in women. Arch. Gen. Psychiatry 63, 1199–1208. https://doi.org/10.1001/archpsyc.63.11.1199

Khan, M.S., Boileau, I., Kolla, N., Mizrahi, R., 2018. A systematic review of the role of the nociceptin receptor system in stress, cognition, and reward: relevance to schizophrenia. Transl. Psychiatry 8, 38. https://doi.org/10.1038/s41398-017-0080-8

Kim, T., McCall, J.G., Jung, Y.H., Huang, X., Siuda, E.R., Li, Y., Song, J., Song, Y.M., Pao, H.A., Kim, R.-H., Lu, C., Lee, S.D., Song, I.-S., Shin, G., Al-Hasani, R., Kim, S., Tan, M.P., Huang, Y., Omenetto, F.G., Rogers, J.A., Bruchas, M.R., 2013. Injectable, cellular-scale optoelectronics with applications for wireless optogenetics. Science 340, 211–216. https://doi.org/10.1126/science.1232437

Kirshenbaum, J.S., Pagliaccio, D., Pizzagalli, D.A., Auerbach, R.P., 2024. Neural sensitivity following stress predicts anhedonia symptoms: a 2-year multi-wave, longitudinal study. Transl. Psychiatry 14, 1–9. https://doi.org/10.1038/s41398-024-02818-x

Koizumi, M., Midorikawa, N., Takeshima, H., Murphy, N.P., 2004. Exogenous, but not endogenous nociceptin modulates mesolimbic dopamine release in mice. J. Neurochem. 89, 257–263. https://doi.org/10.1111/j.1471-4159.2003.02322.x

Koob, G.F., 2008. A Role for Brain Stress Systems in Addiction. Neuron 59, 11–34. https://doi.org/10.1016/j.neuron.2008.06.012

Koob, G.F., Nestler, E.J., 1997. The neurobiology of drug addiction. J. Neuropsychiatry Clin. Neurosci. 9, 482–497. https://doi.org/10.1176/jnp.9.3.482

Kordower, J.H., Olanow, C.W., Dodiya, H.B., Chu, Y., Beach, T.G., Adler, C.H., Halliday, G.M., Bartus, R.T., 2013. Disease duration and the integrity of the nigrostriatal system in Parkinson's disease. Brain J. Neurol. 136, 2419–2431. https://doi.org/10.1093/brain/awt192

Korotkova, T.M., Sergeeva, O.A., Eriksson, K.S., Haas, H.L., Brown, R.E., 2003. Excitation of ventral tegmental area dopaminergic and nondopaminergic neurons by orexins/hypocretins. J. Neurosci. Off. J. Soc. Neurosci. 23, 7–11. https://doi.org/10.1523/JNEUROSCI.23-01-00007.2003

Kosten, T.R., Gawin, F.H., Rounsaville, B.J., Kleber, H.D., 1986. Cocaine abuse among opioid addicts: demographic and diagnostic factors in treatment. Am. J. Drug Alcohol Abuse 12, 1–16. https://doi.org/10.3109/00952998609083739

Kunisato, Y., Okamoto, Y., Ueda, K., Onoda, K., Okada, G., Yoshimura, S., Suzuki, S., Samejima, K., Yamawaki, S., 2012. Effects of depression on reward-based decision making and variability of action in probabilistic learning. J. Behav. Ther. Exp. Psychiatry 43, 1088–1094. https://doi.org/10.1016/j.jbtep.2012.05.007

Kuzmin, A., Kreek, M.J., Bakalkin, G., Liljequist, S., 2007. The nociceptin/orphanin FQ receptor agonist Ro 64-6198 reduces alcohol self-administration and prevents relapse-like alcohol drinking. Neuropsychopharmacol. Off. Publ. Am. Coll. Neuropsychopharmacol. 32, 902–910. https://doi.org/10.1038/sj.npp.1301169

Labouesse, M.A., Patriarchi, T., 2021. A versatile GPCR toolkit to track in vivo neuromodulation: not a one-size-fits-all sensor. Neuropsychopharmacol. Off. Publ. Am. Coll. Neuropsychopharmacol. 46, 2043–2047. https://doi.org/10.1038/s41386-021-00982-y

Lambert, D.G., 2008. The nociceptin/orphanin FQ receptor: a target with broad therapeutic potential. Nat. Rev. Drug Discov. 7, 694–710. https://doi.org/10.1038/nrd2572

Lança, A.J., Boyd, S., Kolb, B.E., van der Kooy, D., 1986. The development of a patchy organization of the rat striatum. Brain Res. 392, 1–10. https://doi.org/10.1016/0165-3806(86)90226-9

Lazaridis, I., Crittenden, J.R., Ahn, G., Hirokane, K., Yoshida, T., Wickersham, I.R., Mahar, A., Skara, V., Loftus, J.H., Parvataneni, K., Meletis, K., Ting, J.T., Hueske, E., Matsushima, A., Graybiel, A.M., 2024. Striosomes Target Nigral Dopamine-Containing Neurons via Direct-D1 and Indirect-D2 Pathways Paralleling Classic Direct-Indirect Basal Ganglia Systems. BioRxiv Prepr. Serv. Biol. 2024.06.01.596922. https://doi.org/10.1101/2024.06.01.596922

Lazaridis, I., Tzortzi, O., Weglage, M., Märtin, A., Xuan, Y., Parent, M., Johansson, Y., Fuzik, J., Fürth, D., Fenno, L.E., Ramakrishnan, C., Silberberg, G., Deisseroth, K., Carlén, M., Meletis, K., 2019. A hypothalamus-habenula circuit controls aversion. Mol. Psychiatry 24, 1351–1368. https://doi.org/10.1038/s41380-019-0369-5

Lee, I.B., Lee, E., Han, N.-E., Slavuj, M., Hwang, J.W., Lee, A., Sun, T., Jeong, Y., Baik, J.-H., Park, J.-Y., Choi, S.-Y., Kwag, J., Yoon, B.-J., 2024. Persistent enhancement of basolateral amygdala-dorsomedial striatum synapses causes compulsive-like behaviors in mice. Nat. Commun. 15, 219. https://doi.org/10.1038/s41467-023-44322-8

Leonard, M.Z., DeBold, J.F., Miczek, K.A., 2017. Escalated cocaine “binges” in rats: enduring effects of social defeat stress or intra-VTA CRF. Psychopharmacology (Berl.) 234, 2823–2836. https://doi.org/10.1007/s00213-017-4677-7

Lerner, T.N., Shilyansky, C., Davidson, T.J., Evans, K.E., Beier, K.T., Zalocusky, K.A., Crow, A.K., Malenka, R.C., Luo, L., Tomer, R., Deisseroth, K., 2015. Intact-Brain Analyses Reveal Distinct Information Carried by SNc Dopamine Subcircuits. Cell 162, 635–647. https://doi.org/10.1016/j.cell.2015.07.014

Levenson, J., Pizzi, M., Sweatt, J., 2006. NF-KB/Rel Transcription Factor Family. Austin: Landes Bioscience.

Li, S.-B., Borniger, J.C., Yamaguchi, H., Hédou, J., Gaudilliere, B., de Lecea, L., 2020. Hypothalamic circuitry underlying stress-induced insomnia and peripheral immunosuppression. Sci. Adv. 6, eabc2590. https://doi.org/10.1126/sciadv.abc2590

Lincoln, S.H., Pisoni, A., Bondy, E., Kumar, P., Singleton, P., Hajcak, G., Pizzagalli, D.A., Auerbach, R.P., 2019. Altered reward processing following an acute social stressor in adolescents. PLOS ONE 14, e0209361. https://doi.org/10.1371/journal.pone.0209361

Liu, B., Kwok, R.P., Fernstrom, J.D., 1991. Colchicine-induced increases in immunoreactive neuropeptide levels in hypothalamus: use as an index of biosynthesis. Life Sci. 49, 345–352. https://doi.org/10.1016/0024-3205(91)90441-d

Lowes, D.C., Harris, A.Z., 2022. Stressed and wired: The effects of stress on the VTA circuits underlying motivated behavior. Curr. Opin. Endocr. Metab. Res. 26, 100388. https://doi.org/10.1016/j.coemr.2022.100388

Luskin, A.T., Li, L., Fu, X., Martin, M.M., Barcomb, K., Girven, K.S., Blackburn, T., Wells, B.A., Thai, S.T., Li, E.M., Rana, A.N., Simon, R.C., Sun, L., Gao, L., Murry, A.D., Golden, S.A., Stuber, G.D., Ford, C.P., Gu, L., Bruchas, M.R., 2024. A diverse population of pericoerulear neurons controls arousal and exploratory behaviors. https://doi.org/10.1101/2022.06.30.498327

Lutfy, K., Do, T., Maidment, N.T., 2001. Orphanin FQ/nociceptin attenuates motor stimulation and changes in nucleus accumbens extracellular dopamine induced by cocaine in rats. Psychopharmacology (Berl.) 154, 1–7. https://doi.org/10.1007/s002130000609

Lutfy, K., Khaliq, I., Carroll, F.I., Maidment, N.T., 2002. Orphanin FQ/nociceptin blocks cocaine-induced behavioral sensitization in rats. Psychopharmacology (Berl.) 164, 168–176. https://doi.org/10.1007/s00213-002-1192-1

Madisen, L., Zwingman, T.A., Sunkin, S.M., Oh, S.W., Zariwala, H.A., Gu, H., Ng, L.L., Palmiter, R.D., Hawrylycz, M.J., Jones, A.R., Lein, E.S., Zeng, H., 2010. A robust and high-throughput Cre reporting and characterization system for the whole mouse brain. Nat. Neurosci. 13, 133–140. https://doi.org/10.1038/nn.2467

Malfacini, D., Ambrosio, C., Gro', M.C., Sbraccia, M., Trapella, C., Guerrini, R., Bonora, M., Pinton, P., Costa, T., Calo', G., 2015. Pharmacological Profile of Nociceptin/Orphanin FQ Receptors Interacting with G-Proteins and β-Arrestins 2. PloS One 10, e0132865. https://doi.org/10.1371/journal.pone.0132865

Marcus, D.J., Bedse, G., Gaulden, A.D., Ryan, J.D., Kondev, V., Winters, N.D., Rosas-Vidal, L.E., Altemus, M., Mackie, K., Lee, F.S., Delpire, E., Patel, S., 2020. Endocannabinoid Signaling Collapse Mediates Stress-Induced Amygdalo-Cortical Strengthening. Neuron 105, 1062-1076.e6. https://doi.org/10.1016/j.neuron.2019.12.024

Margolis, E.B., Moulton, M.G., Lambeth, P.S., O'Meara, M.J., 2023. The life and times of endogenous opioid peptides: Updated understanding of synthesis, spatiotemporal dynamics, and the clinical impact in alcohol use disorder. Neuropharmacology 225, 109376. https://doi.org/10.1016/j.neuropharm.2022.109376

Marino, R.A.M., McDevitt, R.A., Gantz, S.C., Shen, H., Pignatelli, M., Xin, W., Wise, R.A., Bonci, A., 2020. Control of food approach and eating by a GABAergic projection from lateral hypothalamus to dorsal pons. Proc. Natl. Acad. Sci. U. S. A. 117, 8611–8615. https://doi.org/10.1073/pnas.1909340117

Marquez, P., Nguyen, A.T., Hamid, A., Lutfy, K., 2008. The endogenous OFQ/N/ORL-1 receptor system regulates the rewarding effects of acute cocaine. Neuropharmacology 54, 564–568. https://doi.org/10.1016/j.neuropharm.2007.11.003

Marti, M., Mela, F., Veronesi, C., Guerrini, R., Salvadori, S., Federici, M., Mercuri, N.B., Rizzi, A., Franchi, G., Beani, L., Bianchi, C., Morari, M., 2004. Blockade of nociceptin/orphanin FQ receptor signaling in rat substantia nigra pars reticulata stimulates nigrostriatal

dopaminergic transmission and motor behavior. J. Neurosci. Off. J. Soc. Neurosci. 24, 6659–6666. https://doi.org/10.1523/JNEUROSCI.0987-04.2004

Märtin, A., Calvigioni, D., Tzortzi, O., Fuzik, J., Wärnberg, E., Meletis, K., 2019. A Spatiomolecular Map of the Striatum. Cell Rep. 29, 4320-4333.e5. https://doi.org/10.1016/j.celrep.2019.11.096

Matsushima, A., Graybiel, A.M., 2020. Combinatorial Developmental Controls on Striatonigral Circuits. Cell Rep. 31, 107778. https://doi.org/10.1016/j.celrep.2020.107778

Mazure, C.M., 1998. Life stressors as risk factors in depression. Clin. Psychol. Sci. Pract. 5, 291–313. https://doi.org/10.1111/j.1468-2850.1998.tb00151.x

McCall, J.G., Siuda, E.R., Bhatti, D.L., Lawson, L.A., McElligott, Z.A., Stuber, G.D., Bruchas, M.R., 2017. Locus coeruleus to basolateral amygdala noradrenergic projections promote anxiety-like behavior. eLife 6, e18247. https://doi.org/10.7554/eLife.18247

Mccutcheon, J., Ebner, S., Loriaux, A., Roitman, M., 2012. Encoding of Aversion by Dopamine and the Nucleus Accumbens. Front. Neurosci. 6, 137. https://doi.org/10.3389/fnins.2012.00137

McMakin, D.L., Olino, T.M., Porta, G., Dietz, L.J., Emslie, G., Clarke, G., Wagner, K.D., Asarnow, J.R., Ryan, N.D., Birmaher, B., Shamseddeen, W., Mayes, T., Kennard, B., Spirito, A., Keller, M., Lynch, F.L., Dickerson, J.F., Brent, D.A., 2012. Anhedonia Predicts Poorer Recovery Among Youth With Selective Serotonin Reuptake Inhibitor Treatment–Resistant Depression. J. Am. Acad. Child Adolesc. Psychiatry 51, 404–411. https://doi.org/10.1016/j.jaac.2012.01.011

Medeiros, I.U., Ruzza, C., Asth, L., Guerrini, R., Romão, P.R.T., Gavioli, E.C., Calo, G., 2015. Blockade of nociceptin/orphanin FQ receptor signaling reverses LPS-induced depressive-like behavior in mice. Peptides 72, 95–103. https://doi.org/10.1016/j.peptides.2015.05.006

Menalled, L., Brunner, D., 2014. Animal models of Huntington's disease for translation to the clinic: best practices. Mov. Disord. Off. J. Mov. Disord. Soc. 29, 1375–1390. https://doi.org/10.1002/mds.26006

MÉNARD, C., HODES, G.E., RUSSO, S.J., 2016. Pathogenesis of depression: insights from human and rodent studies. Neuroscience 321, 138–162. https://doi.org/10.1016/j.neuroscience.2015.05.053

Mendez, I., Sanchez-Pernaute, R., Cooper, O., Viñuela, A., Ferrari, D., Björklund, L., Dagher, A., Isacson, O., 2005. Cell type analysis of functional fetal dopamine cell suspension transplants in the striatum and substantia nigra of patients with Parkinson's disease. Brain J. Neurol. 128, 1498–1510. https://doi.org/10.1093/brain/awh510

Meng, C., Zhou, J., Papaneri, A., Peddada, T., Xu, K., Cui, G., 2018. Spectrally resolved fiber photometry for multi-component analysis of brain circuits. Neuron 98, 707-717.e4. https://doi.org/10.1016/j.neuron.2018.04.012

Meunier, J.-C., Mollereau, C., Toll, L., Suaudeau, C., Moisand, C., Alvinerie, P., Butour, J.-L., Guillemot, J.-C., Ferrara, P., Monsarrat, B., Mazarguil, H., Vassart, G., Parmentier, M.,

Costentin, J., 1995. Isolation and structure of the endogenous agonist of opioid receptor-like ORL1 receptor. Nature 377, 532–535. https://doi.org/10.1038/377532a0

Moffett, M.C., Vicentic, A., Kozel, M., Plotsky, P., Francis, D.D., Kuhar, M.J., 2007. Maternal separation alters drug intake patterns in adulthood in rats. Biochem. Pharmacol. 73, 321–330. https://doi.org/10.1016/j.bcp.2006.08.003

Mogil, J.S., Grisel, J.E., Reinscheid, R.K., Civelli, O., Belknap, J.K., Grandy, D.K., 1996. Orphanin FQ is a functional anti-opioid peptide. Neuroscience 75, 333–337. https://doi.org/10.1016/0306-4522(96)00338-7

Mollereau, C., Mouledous, L., 2000. Tissue distribution of the opioid receptor-like (ORL1) receptor. Peptides 21, 907–917. https://doi.org/10.1016/s0196-9781(00)00227-8

Montalban, E., Giralt, A., Taing, L., Schut, E.H.S., Supiot, L.F., Castell, L., Nakamura, Y., de Pins, B., Pelosi, A., Goutebroze, L., Tuduri, P., Wang, W., Neiburga, K.D., Vestito, L., Castel, J., Luquet, S., Nairn, A.C., Hervé, D., Heintz, N., Martin, C., Greengard, P., Valjent, E., Meye, F.J., Gambardella, N., Roussarie, J.-P., Girault, J.-A., 2022. Translational profiling of mouse dopaminoceptive neurons reveals region-specific gene expression, exon usage, and striatal prostaglandin E2 modulatory effects. Mol. Psychiatry 27, 2068–2079. https://doi.org/10.1038/s41380-022-01439-4

Moore, H., Rose, H.J., Grace, A.A., 2001. Chronic Cold Stress Reduces the Spontaneous Activity of Ventral Tegmental Dopamine Neurons. Neuropsychopharmacology 24, 410–419. https://doi.org/10.1016/S0893-133X(00)00188-3

Morairty, S.R., Sun, Y., Toll, L., Bruchas, M.R., Kilduff, T.S., 2023. Activation of the nociceptin/orphanin-FQ receptor promotes NREM sleep and EEG slow wave activity. Proc. Natl. Acad. Sci. 120, e2214171120. https://doi.org/10.1073/pnas.2214171120

Morales, M., Margolis, E.B., 2017. Ventral tegmental area: cellular heterogeneity, connectivity and behaviour. Nat. Rev. Neurosci. 18, 73–85. https://doi.org/10.1038/nrn.2016.165

Morigaki, R., Lee, J.H., Yoshida, T., Wüthrich, C., Hu, D., Crittenden, J.R., Friedman, A., Kubota, Y., Graybiel, A.M., 2020. Spatiotemporal Up-Regulation of Mu Opioid Receptor 1 in Striatum of Mouse Model of Huntington's Disease Differentially Affecting Caudal and Striosomal Regions. Front. Neuroanat. 14, 608060. https://doi.org/10.3389/fnana.2020.608060

Moulédous, L., 2019. The Nociceptin/Orphanin FQ System and the Regulation of Memory. Handb. Exp. Pharmacol. 254, 259–278. https://doi.org/10.1007/164_2018_185

Murphy, N.P., Ly, H.T., Maidment, N.T., 1996. Intracerebroventricular orphanin FQ/Nociceptin supresses dopamine release in the nucleus accumbens of anaesthetized rats. Neuroscience 75, 1–4. https://doi.org/10.1016/0306-4522(96)00322-3

Murphy, N.P., Maidment, N.T., 1999. Orphanin FQ/nociceptin modulation of mesolimbic dopamine transmission determined by microdialysis. J. Neurochem. 73, 179–186. https://doi.org/10.1046/j.1471-4159.1999.0730179.x

Nakamura, T., Uramura, K., Nambu, T., Yada, T., Goto, K., Yanagisawa, M., Sakurai, T., 2000. Orexin-induced hyperlocomotion and stereotypy are mediated by the dopaminergic system. Brain Res. 873, 181–187. https://doi.org/10.1016/s0006-8993(00)02555-5

Neal, C.R., Mansour, A., Reinscheid, R., Nothacker, H.P., Civelli, O., Watson, S.J., 1999. Localization of orphanin FQ (nociceptin) peptide and messenger RNA in the central nervous system of the rat. J. Comp. Neurol. 406, 503–547.

Nestler, E.J., Carlezon, W.A., 2006. The Mesolimbic Dopamine Reward Circuit in Depression. Biol. Psychiatry 59, 1151–1159. https://doi.org/10.1016/j.biopsych.2005.09.018

Nieh, E.H., Matthews, G.A., Allsop, S.A., Presbrey, K.N., Leppla, C.A., Wichmann, R., Neve, R., Wildes, C.P., Tye, K.M., 2015. Decoding Neural Circuits that Control Compulsive Sucrose Seeking. Cell 160, 528–541. https://doi.org/10.1016/j.cell.2015.01.003

Nieh, E.H., Vander Weele, C.M., Matthews, G.A., Presbrey, K.N., Wichmann, R., Leppla, C.A., Izadmehr, E.M., Tye, K.M., 2016. Inhibitory Input from the Lateral Hypothalamus to the Ventral Tegmental Area Disinhibits Dopamine Neurons and Promotes Behavioral Activation. Neuron 90, 1286–1298. https://doi.org/10.1016/j.neuron.2016.04.035

Nikolova, Y., Bogdan, R., Pizzagalli, D.A., 2011. Perception of a Naturalistic Stressor Interacts with 5-HTTLPR/rs25531 Genotype and Gender to Impact Reward Responsiveness. Neuropsychobiology 65, 45–54. https://doi.org/10.1159/000329105

Norton, C.S., Neal, C.R., Kumar, S., Akil, H., Watson, S.J., 2002. Nociceptin/orphanin FQ and opioid receptor-like receptor mRNA expression in dopamine systems. J. Comp. Neurol. 444, 358–368. https://doi.org/10.1002/cne.10154

Olianas, M.C., Dedoni, S., Boi, M., Onali, P., 2008. Activation of nociceptin/orphanin FQ-NOP receptor system inhibits tyrosine hydroxylase phosphorylation, dopamine synthesis, and dopamine D1 receptor signaling in rat nucleus accumbens and dorsal striatum. J. Neurochem. 107, 544–556. https://doi.org/10.1111/j.1471-4159.2008.05629.x

Opland, D., Sutton, A., Woodworth, H., Brown, J., Bugescu, R., Garcia, A., Christensen, L., Rhodes, C., Myers, M., Leinninger, G., 2013. Loss of neurotensin receptor-1 disrupts the control of the mesolimbic dopamine system by leptin and promotes hedonic feeding and obesity. Mol. Metab. 2, 423–434. https://doi.org/10.1016/j.molmet.2013.07.008

Ostroumov, A., Thomas, A.M., Kimmey, B.A., Karsch, J.S., Doyon, W.M., Dani, J.A., 2016. Stress Increases Ethanol Self-Administration via a Shift toward Excitatory GABA Signaling in the Ventral Tegmental Area. Neuron 92, 493–504. https://doi.org/10.1016/j.neuron.2016.09.029

Paladini, C.A., Roeper, J., 2014. Generating bursts (and pauses) in the dopamine midbrain neurons. Neuroscience, The Ventral Tegmentum and Dopamine: A New Wave of Diversity 282, 109–121. https://doi.org/10.1016/j.neuroscience.2014.07.032

Parker, K.E., Pedersen, C.E., Gomez, A.M., Spangler, S.M., Walicki, M.C., Feng, S.Y., Stewart, S.L., Otis, J.M., Al-Hasani, R., McCall, J.G., Sakers, K., Bhatti, D.L., Copits, B.A., Gereau, R.W., Jhou, T., Kash, T.J., Dougherty, J.D., Stuber, G.D., Bruchas, M.R., 2019. A

Paranigral VTA Nociceptin Circuit that Constrains Motivation for Reward. Cell 178, 653-671.e19. https://doi.org/10.1016/j.cell.2019.06.034

Patchev, V.K., Patchev, A.V., 2006. Experimental models of stress. Dialogues Clin. Neurosci. 8, 417–432.

Patriarchi, T., Cho, J.R., Merten, K., Howe, M.W., Marley, A., Xiong, W.-H., Folk, R.W., Broussard, G.J., Liang, R., Jang, M.J., Zhong, H., Dombeck, D., von Zastrow, M., Nimmerjahn, A., Gradinaru, V., Williams, J.T., Tian, L., 2018. Ultrafast neuronal imaging of dopamine dynamics with designed genetically encoded sensors. Science 360, eaat4422. https://doi.org/10.1126/science.aat4422

Patriarchi, T., Mohebi, A., Sun, J., Marley, A., Liang, R., Dong, C., Puhger, K., Mizuno, G.O., Davis, C.M., Wiltgen, B., von Zastrow, M., Berke, J.D., Tian, L., 2020. An expanded palette of dopamine sensors for multiplex imaging in vivo. Nat. Methods 17, 1147–1155. https://doi.org/10.1038/s41592-020-0936-3

Pedersen, M.L., Ironside, M., Amemori, K., McGrath, C.L., Kang, M.S., Graybiel, A.M., Pizzagalli, D.A., Frank, M.J., 2021. Computational phenotyping of brain-behavior dynamics underlying approach-avoidance conflict in major depressive disorder. PLOS Comput. Biol. 17, e1008955. https://doi.org/10.1371/journal.pcbi.1008955

Pereira Luppi, M., Azcorra, M., Caronia-Brown, G., Poulin, J.-F., Gaertner, Z., Gatica, S., Moreno-Ramos, O.A., Nouri, N., Dubois, M., Ma, Y.C., Ramakrishnan, C., Fenno, L., Kim, Y.S., Deisseroth, K., Cicchetti, F., Dombeck, D.A., Awatramani, R., 2021. Sox6 expression distinguishes dorsally and ventrally biased dopamine neurons in the substantia nigra with distinctive properties and embryonic origins. Cell Rep. 37, 109975. https://doi.org/10.1016/j.celrep.2021.109975

Perez-Bonilla, P., Santiago-Colon, K., Leinninger, G.M., 2020. Lateral Hypothalamic Area Neuropeptides Modulate Ventral Tegmental Area Dopamine Neurons and Feeding. Physiol. Behav. 223, 112986. https://doi.org/10.1016/j.physbeh.2020.112986

Persad, S.M., Polivy, J., 1993. Differences between depressed and nondepressed individuals in the recognition of and response to facial emotional cues. J. Abnorm. Psychol. 102, 358–368. https://doi.org/10.1037/0021-843X.102.3.358

Phillips, R.A., Tuscher, J.J., Black, S.L., Andraka, E., Fitzgerald, N.D., Ianov, L., Day, J.J., 2022. An atlas of transcriptionally defined cell populations in the rat ventral tegmental area. Cell Rep. 39. https://doi.org/10.1016/j.celrep.2022.110616

Pittenger, C., Duman, R.S., 2008. Stress, Depression, and Neuroplasticity: A Convergence of Mechanisms. Neuropsychopharmacology 33, 88–109. https://doi.org/10.1038/sj.npp.1301574

Pizzagalli, D.A., Iosifescu, D., Hallett, L.A., Ratner, K.G., Fava, M., 2008. Reduced hedonic capacity in major depressive disorder: Evidence from a probabilistic reward task. J. Psychiatr. Res. 43, 76–87. https://doi.org/10.1016/j.jpsychires.2008.03.001

Polter, A.M., Barcomb, K., Chen, R.W., Dingess, P.M., Graziane, N.M., Brown, T.E., Kauer, J.A., 2017. Constitutive activation of kappa opioid receptors at ventral tegmental area inhibitory synapses following acute stress. eLife 6, e23785. https://doi.org/10.7554/eLife.23785

Post, A., Smart, T.S., Krikke-Workel, J., Dawson, G.R., Harmer, C.J., Browning, M., Jackson, K., Kakar, R., Mohs, R., Statnick, M., Wafford, K., McCarthy, A., Barth, V., Witkin, J.M., 2016. A Selective Nociceptin Receptor Antagonist to Treat Depression: Evidence from Preclinical and Clinical Studies. Neuropsychopharmacology 41, 1803–1812. https://doi.org/10.1038/npp.2015.348

Poulin, J.-F., Caronia, G., Hofer, C., Cui, Q., Helm, B., Ramakrishnan, C., Chan, C.S., Dombeck, D.A., Deisseroth, K., Awatramani, R., 2018. Mapping projections of molecularly defined dopamine neuron subtypes using intersectional genetic approaches. Nat. Neurosci. 21, 1260–1271. https://doi.org/10.1038/s41593-018-0203-4

Qian, T., Wang, H., Wang, P., Geng, L., Mei, L., Osakada, T., Wang, L., Tang, Y., Kania, A., Grinevich, V., Stoop, R., Lin, D., Luo, M., Li, Y., 2023. A genetically encoded sensor measures temporal oxytocin release from different neuronal compartments. Nat. Biotechnol. 41, 944–957. https://doi.org/10.1038/s41587-022-01561-2

Ragnauth, A., Moroz, M., Bodnar, R.J., 2000. Multiple opioid receptors mediate feeding elicited by mu and delta opioid receptor subtype agonists in the nucleus accumbens shell in rats. Brain Res. 876, 76–87. https://doi.org/10.1016/s0006-8993(00)02631-7

Ragsdale, C.W., Graybiel, A.M., 1988. Fibers from the basolateral nucleus of the amygdala selectively innervate striosomes in the caudate nucleus of the cat. J. Comp. Neurol. 269, 506–522. https://doi.org/10.1002/cne.902690404

Randesi, M., Zhou, Y., Mazid, S., Odell, S.C., Gray, J.D., Correa da Rosa, J., McEwen, B.S., Milner, T.A., Kreek, M.J., 2018. Sex differences after chronic stress in the expression of opioid-, stress- and neuroplasticity-related genes in the rat hippocampus. Neurobiol. Stress 8, 33–41. https://doi.org/10.1016/j.ynstr.2018.01.001

Ravotto, L., Duffet, L., Zhou, X., Weber, B., Patriarchi, T., 2020. A Bright and Colorful Future for G-Protein Coupled Receptor Sensors. Front. Cell. Neurosci. 14, 67. https://doi.org/10.3389/fncel.2020.00067

Reinscheid, R.K., Nothacker, H.P., Bourson, A., Ardati, A., Henningsen, R.A., Bunzow, J.R., Grandy, D.K., Langen, H., Monsma, F.J., Civelli, O., 1995. Orphanin FQ: a neuropeptide that activates an opioidlike G protein-coupled receptor. Science 270, 792–794. https://doi.org/10.1126/science.270.5237.792

Resendez, S.L., Dome, M., Gormley, G., Franco, D., Nevárez, N., Hamid, A.A., Aragona, B.J., 2013. μ-Opioid receptors within subregions of the striatum mediate pair bond formation through parallel yet distinct reward mechanisms. J. Neurosci. Off. J. Soc. Neurosci. 33, 9140–9149. https://doi.org/10.1523/JNEUROSCI.4123-12.2013

Rodriguez-Romaguera, J., Ung, R.L., Nomura, H., Otis, J.M., Basiri, M.L., Namboodiri, V.M.K., Zhu, X., Robinson, J.E., van den Munkhof, H.E., McHenry, J.A., Eckman, L.E.H., Kosyk, O., Jhou, T.C., Kash, T.L., Bruchas, M.R., Stuber, G.D., 2020. Prepronociceptin-Expressing Neurons in the Extended Amygdala Encode and Promote Rapid Arousal

Responses to Motivationally Salient Stimuli. Cell Rep. 33, 108362. https://doi.org/10.1016/j.celrep.2020.108362

Rolle, C.E., Pedersen, M.L., Johnson, N., Amemori, K., Ironside, M., Graybiel, A.M., Pizzagalli, D.A., Etkin, A., 2021. The Role of the Dorsal–Lateral Prefrontal Cortex in Reward Sensitivity During Approach–Avoidance Conflict. Cereb. Cortex. https://doi.org/10.1093/cercor/bhab292

Romualdi, P., Di Benedetto, M., D'Addario, C., Collins, S.L., Wade, D., Candeletti, S., Izenwasser, S., 2007. Chronic cocaine produces decreases in N/OFQ peptide levels in select rat brain regions. J. Mol. Neurosci. MN 31, 159–164. https://doi.org/10.1385/jmn/31:02:159

Rorick-Kehn, L.M., Ciccocioppo, R., Wong, C.J., Witkin, J.M., Martinez-Grau, M.A., Stopponi, S., Adams, B.L., Katner, J.S., Perry, K.W., Toledo, M.A., Diaz, N., Lafuente, C., Jiménez, A., Benito, A., Pedregal, C., Weiss, F., Statnick, M.A., 2016. A Novel, Orally Bioavailable Nociceptin Receptor Antagonist, LY2940094, Reduces Ethanol Self-Administration and Ethanol Seeking in Animal Models. Alcohol. Clin. Exp. Res. 40, 945–954. https://doi.org/10.1111/acer.13052

Russo, S.J., Nestler, E.J., 2013. The brain reward circuitry in mood disorders. Nat. Rev. Neurosci. 14, 609–625. https://doi.org/10.1038/nrn3381

Ryan, M.M., Lockstone, H.E., Huffaker, S.J., Wayland, M.T., Webster, M.J., Bahn, S., 2006. Gene expression analysis of bipolar disorder reveals downregulation of the ubiquitin cycle and alterations in synaptic genes. Mol. Psychiatry 11, 965–978. https://doi.org/10.1038/sj.mp.4001875

Sabatini, B.L., Tian, L., 2020. Imaging Neurotransmitter and Neuromodulator Dynamics In Vivo with Genetically Encoded Indicators. Neuron 108, 17–32. https://doi.org/10.1016/j.neuron.2020.09.036

Saito, Y., Maruyama, K., Kawano, H., Hagino-Yamagishi, K., Kawamura, K., Saido, T.C., Kawashima, S., 1996. Molecular cloning and characterization of a novel form of neuropeptide gene as a developmentally regulated molecule. J. Biol. Chem. 271, 15615–15622. https://doi.org/10.1074/jbc.271.26.15615

Saito, Y., Maruyama, K., Saido, T.C., Kawashima, S., 1997. Overexpression of a neuropeptide nociceptin/orphanin FQ precursor gene, N23K/N27K, induces neurite outgrowth in mouse NS20Y cells. J. Neurosci. Res. 48, 397–406. https://doi.org/10.1002/(sici)1097-4547(19970601)48:5<397::aid-jnr2>3.0.co;2-9

Saito, Y., Maruyama, K., Saido, T.C., Kawashima, S., 1995. N23K, a gene transiently up-regulated during neural differentiation, encodes a precursor protein for a newly identified neuropeptide nociceptin. Biochem. Biophys. Res. Commun. 217, 539–545. https://doi.org/10.1006/bbrc.1995.2809

Saito, Y., Nothacker, H.P., Wang, Z., Lin, S.H., Leslie, F., Civelli, O., 1999. Molecular characterization of the melanin-concentrating-hormone receptor. Nature 400, 265–269. https://doi.org/10.1038/22321

Sakoori, K., Murphy, N.P., 2008. Endogenous nociceptin (orphanin FQ) suppresses basal hedonic state and acute reward responses to methamphetamine and ethanol but facilitates chronic responses. Neuropsychopharmacol. Off. Publ. Am. Coll. Neuropsychopharmacol. 33, 877–891. https://doi.org/10.1038/sj.npp.1301459

Sakoori, K., Murphy, N.P., 2004. Central administration of nociceptin/orphanin FQ blocks the acquisition of conditioned place preference to morphine and cocaine, but not conditioned place aversion to naloxone in mice. Psychopharmacology (Berl.) 172, 129–136. https://doi.org/10.1007/s00213-003-1643-3

Sandberg, M., Weber, S.G., 2003. Techniques for neuropeptide determination. Trends Anal. Chem. TRAC 22, 522–527. https://doi.org/10.1016/S0165-9936(03)00910-5

Saunders, A., Macosko, E.Z., Wysoker, A., Goldman, M., Krienen, F.M., de Rivera, H., Bien, E., Baum, M., Bortolin, L., Wang, S., Goeva, A., Nemesh, J., Kamitaki, N., Brumbaugh, S., Kulp, D., McCarroll, S.A., 2018. Molecular Diversity and Specializations among the Cells of the Adult Mouse Brain. Cell 174, 1015-1030.e16. https://doi.org/10.1016/j.cell.2018.07.028

Schiffino, F.L., Siemian, J.N., Petrella, M., Laing, B.T., Sarsfield, S., Borja, C.B., Gajendiran, A., Zuccoli, M.L., Aponte, Y., 2019. Activation of a lateral hypothalamic-ventral tegmental circuit gates motivation. PloS One 14, e0219522. https://doi.org/10.1371/journal.pone.0219522

Schneiderman, N., Ironson, G., Siegel, S.D., 2005. STRESS AND HEALTH: Psychological, Behavioral, and Biological Determinants. Annu. Rev. Clin. Psychol. 1, 607–628. https://doi.org/10.1146/annurev.clinpsy.1.102803.144141

Schultz, W., 2016. Dopamine reward prediction-error signalling: a two-component response. Nat. Rev. Neurosci. 17, 183–195. https://doi.org/10.1038/nrn.2015.26

Schultz, W., 1997. Dopamine neurons and their role in reward mechanisms. Curr. Opin. Neurobiol. 7, 191–197. https://doi.org/10.1016/S0959-4388(97)80007-4

Selye, H., 1978. The stress of life, Rev. ed, The stress of life, Rev. ed. Mcgraw Hill, Oxford, England.

Sgroi, S., Tonini, R., 2018. Opioidergic Modulation of Striatal Circuits, Implications in Parkinson's Disease and Levodopa Induced Dyskinesia. Front. Neurol. 9, 524. https://doi.org/10.3389/fneur.2018.00524

Smith, J.B., Klug, J.R., Ross, D.L., Howard, C.D., Hollon, N.G., Ko, V.I., Hoffman, H., Callaway, E.M., Gerfen, C.R., Jin, X., 2016. Genetic-Based Dissection Unveils the Inputs and Outputs of Striatal Patch and Matrix Compartments. Neuron 91, 1069–1084. https://doi.org/10.1016/j.neuron.2016.07.046

Soares, J.M., Sampaio, A., Ferreira, L.M., Santos, N.C., Marques, F., Palha, J.A., Cerqueira, J.J., Sousa, N., 2012. Stress-induced changes in human decision-making are reversible. Transl. Psychiatry 2, e131–e131. https://doi.org/10.1038/tp.2012.59

Soden, M.E., Chung, A.S., Cuevas, B., Resnick, J.M., Awatramani, R., Zweifel, L.S., 2020. Anatomic resolution of neurotransmitter-specific projections to the VTA reveals diversity of GABAergic inputs. Nat. Neurosci. 23, 968–980. https://doi.org/10.1038/s41593-020-0657-z

Soden, M.E., Yee, J.X., Zweifel, L.S., 2023. Circuit coordination of opposing neuropeptide and neurotransmitter signals. Nature 619, 332–337. https://doi.org/10.1038/s41586-023-06246-7

Spijker, J., Bijl, R.V., De Graaf, R., Nolen, W.A., 2001. Determinants of poor 1-year outcome of DSM-III-R major depression in the general population: results of the Netherlands Mental Health Survey and Incidence Study (NEMESIS). Acta Psychiatr. Scand. 103, 122–130. https://doi.org/10.1034/j.1600-0447.2001.103002122.x

Sun, F., Zeng, J., Jing, M., Zhou, J., Feng, J., Owen, S.F., Luo, Y., Li, F., Wang, H., Yamaguchi, T., Yong, Z., Gao, Y., Peng, W., Wang, L., Zhang, S., Du, J., Lin, D., Xu, M., Kreitzer, A.C., Cui, G., Li, Y., 2018. A Genetically Encoded Fluorescent Sensor Enables Rapid and Specific Detection of Dopamine in Flies, Fish, and Mice. Cell 174, 481-496.e19. https://doi.org/10.1016/j.cell.2018.06.042

Suslow, T., Dannlowski, U., Lalee-Mentzel, J., Donges, U.-S., Arolt, V., Kersting, A., 2004. Spatial processing of facial emotion in patients with unipolar depression: a longitudinal study. J. Affect. Disord. 83, 59–63. https://doi.org/10.1016/j.jad.2004.03.003

Tajima, K., Fukuda, T., 2013. Region-specific diversity of striosomes in the mouse striatum revealed by the differential immunoreactivities for mu-opioid receptor, substance P, and enkephalin. Neuroscience 241, 215–228. https://doi.org/10.1016/j.neuroscience.2013.03.012

Tejeda, H.A., Wu, J., Kornspun, A.R., Pignatelli, M., Kashtelyan, V., Krashes, M.J., Lowell, B.B., Carlezon, W.A., Bonci, A., 2017. Pathway- and Cell-Specific Kappa-Opioid Receptor Modulation of Excitation-Inhibition Balance Differentially Gates D1 and D2 Accumbens Neuron Activity. Neuron 93, 147–163. https://doi.org/10.1016/j.neuron.2016.12.005

Thompson, A.A., Liu, W., Chun, E., Katritch, V., Wu, H., Vardy, E., Huang, X.-P., Trapella, C., Guerrini, R., Calo, G., Roth, B.L., Cherezov, V., Stevens, R.C., 2012. Structure of the nociceptin/orphanin FQ receptor in complex with a peptide mimetic. Nature 485, 395–399. https://doi.org/10.1038/nature11085

Toll, L., Bruchas, M.R., Calo', G., Cox, B.M., Zaveri, N.T., 2016. Nociceptin/Orphanin FQ Receptor Structure, Signaling, Ligands, Functions, and Interactions with Opioid Systems. Pharmacol. Rev. 68, 419–457. https://doi.org/10.1124/pr.114.009209

Tovar-Díaz, J., Pomrenze, M.B., Kan, R., Pahlavan, B., Morikawa, H., 2018. Cooperative CRF and α1 Adrenergic Signaling in the VTA Promotes NMDA Plasticity and Drives Social Stress Enhancement of Cocaine Conditioning. Cell Rep. 22, 2756–2766. https://doi.org/10.1016/j.celrep.2018.02.039

Tritsch, N.X., Sabatini, B.L., 2012. Dopaminergic modulation of synaptic transmission in cortex and striatum. Neuron 76, 33–50. https://doi.org/10.1016/j.neuron.2012.09.023

Ubaldi, M., Cannella, N., Borruto, A.M., Petrella, M., Micioni Di Bonaventura, M.V., Soverchia, L., Stopponi, S., Weiss, F., Cifani, C., Ciccocioppo, R., 2021. Role of Nociceptin/Orphanin FQ-NOP Receptor System in the Regulation of Stress-Related Disorders. Int. J. Mol. Sci. 22, 12956. https://doi.org/10.3390/ijms222312956

van den Pol, A.N., 2012. Neuropeptide transmission in brain circuits. Neuron 76, 98–115. https://doi.org/10.1016/j.neuron.2012.09.014

Varty, G.B., Lu, S.X., Morgan, C.A., Cohen-Williams, M.E., Hodgson, R.A., Smith-Torhan, A., Zhang, H., Fawzi, A.B., Graziano, M.P., Ho, G.D., Matasi, J., Tulshian, D., Coffin, V.L., Carey, G.J., 2008. The anxiolytic-like effects of the novel, orally active nociceptin opioid receptor agonist 8-[bis(2-methylphenyl)methyl]-3-phenyl-8-azabicyclo[3.2.1]octan-3-ol (SCH 221510). J. Pharmacol. Exp. Ther. 326, 672–682. https://doi.org/10.1124/jpet.108.136937

Vazquez-DeRose, J., Stauber, G., Khroyan, T.V., Xie, X.S., Zaveri, N.T., Toll, L., 2013. Retrodialysis of N/OFQ into the nucleus accumbens shell blocks cocaine-induced increases in extracellular dopamine and locomotor activity. Eur. J. Pharmacol. 699, 200–206. https://doi.org/10.1016/j.ejphar.2012.11.050

Verharen, J.P.H., Adan, R.A.H., Vanderschuren, L.J.M.J., 2019. Differential contributions of striatal dopamine D1 and D2 receptors to component processes of value-based decision making. Neuropsychopharmacology 44, 2195–2204. https://doi.org/10.1038/s41386-019-0454-0

Vidal-Ribas, P., Benson, B., Vitale, A.D., Keren, H., Harrewijn, A., Fox, N.A., Pine, D.S., Stringaris, A., 2019. Bidirectional Associations Between Stress and Reward Processing in Children and Adolescents: A Longitudinal Neuroimaging Study. Biol. Psychiatry Cogn. Neurosci. Neuroimaging 4, 893–901. https://doi.org/10.1016/j.bpsc.2019.05.012

Vitale, G., Ruggieri, V., Filaferro, M., Frigeri, C., Alboni, S., Tascedda, F., Brunello, N., Guerrini, R., Cifani, C., Massi, M., 2009. Chronic treatment with the selective NOP receptor antagonist [Nphe1,Arg14,Lys15]N/OFQ-NH2 (UFP-101) reverses the behavioural and biochemical effects of unpredictable chronic mild stress in rats. Psychopharmacology (Berl.) 207, 173–189. https://doi.org/10.1007/s00213-009-1646-9

Walker, J.R., Terenius, L., Koob, G.F., 2002. Conditioned opioid withdrawal decreases nociceptin/orphanin FQ levels in the frontal cortex and olfactory tubercle. Neuropsychopharmacol. Off. Publ. Am. Coll. Neuropsychopharmacol. 27, 203–211. https://doi.org/10.1016/S0893-133X(02)00292-0

Wang, D., Li, A., Dong, K., Li, Huihui, Guo, Y., Zhang, X., Cai, M., Li, Huiming, Zhao, G., Yang, Q., 2021. Lateral hypothalamus orexinergic inputs to lateral habenula modulate maladaptation after social defeat stress. Neurobiol. Stress 14, 100298. https://doi.org/10.1016/j.ynstr.2021.100298

Wang, L., Liu, L., Zhang, J., Zhao, G., 2009. [Plasma levels of nociceptin/orphanin FQ in patients with bipolar disorders and health adults]. Zhonghua Yi Xue Za Zhi 89, 916–918.

Wang, Y., Zhuang, Y., DiBerto, J.F., Zhou, X.E., Schmitz, G.P., Yuan, Q., Jain, M.K., Liu, W., Melcher, K., Jiang, Y., Roth, B.L., Xu, H.E., 2023. Structures of the entire human opioid receptor family. Cell 186, 413-427.e17. https://doi.org/10.1016/j.cell.2022.12.026

Wardenaar, K.J., Giltay, E.J., van Veen, T., Zitman, F.G., Penninx, B.W.J.H., 2012. Symptom dimensions as predictors of the two-year course of depressive and anxiety disorders. J. Affect. Disord. 136, 1198–1203. https://doi.org/10.1016/j.jad.2011.11.037

Watabe-Uchida, M., Eshel, N., Uchida, N., 2017. Neural Circuitry of Reward Prediction Error. Annu. Rev. Neurosci. 40, 373–394. https://doi.org/10.1146/annurev-neuro-072116-031109

Watabe-Uchida, M., Zhu, L., Ogawa, S.K., Vamanrao, A., Uchida, N., 2012. Whole-brain mapping of direct inputs to midbrain dopamine neurons. Neuron 74, 858–873. https://doi.org/10.1016/j.neuron.2012.03.017

Weera, M.M., Shackett, R.S., Kramer, H.M., Middleton, J.W., Gilpin, N.W., 2021. Central Amygdala Projections to Lateral Hypothalamus Mediate Avoidance Behavior in Rats. J. Neurosci. Off. J. Soc. Neurosci. 41, 61–72. https://doi.org/10.1523/JNEUROSCI.0236-20.2020

Wise, R.A., 2004. Dopamine, learning and motivation. Nat. Rev. Neurosci. 5, 483–494. https://doi.org/10.1038/nrn1406

Witkin, J.M., Statnick, M.A., Rorick-Kehn, L.M., Pintar, J.E., Ansonoff, M., Chen, Y., Tucker, R.C., Ciccocioppo, R., 2014. The biology of Nociceptin/Orphanin FQ (N/OFQ) related to obesity, stress, anxiety, mood, and drug dependence. Pharmacol. Ther. 141, 283–299. https://doi.org/10.1016/j.pharmthera.2013.10.011

Witkin, J.M., Wallace, T.L., Martin, W.J., 2019. Therapeutic Approaches for NOP Receptor Antagonists in Neurobehavioral Disorders: Clinical Studies in Major Depressive Disorder and Alcohol Use Disorder with BTRX-246040 (LY2940094). Handb. Exp. Pharmacol. 254, 399–415. https://doi.org/10.1007/164_2018_186

Wu, Z., Cui, Y., Wang, H., Wu, H., Wan, Y., Li, B., Wang, L., Pan, S., Peng, W., Dong, A., Yuan, Z., Jing, M., Xu, M., Luo, M., Li, Y., 2023. Neuronal activity-induced, equilibrative nucleoside transporter-dependent, somatodendritic adenosine release revealed by a GRAB sensor. Proc. Natl. Acad. Sci. U. S. A. 120, e2212387120. https://doi.org/10.1073/pnas.2212387120

Wu, Z., Lin, D., Li, Y., 2022. Pushing the frontiers: tools for monitoring neurotransmitters and neuromodulators. Nat. Rev. Neurosci. 23, 257–274. https://doi.org/10.1038/s41583-022-00577-6

Yamada, T., McGeer, P.L., Baimbridge, K.G., McGeer, E.G., 1990. Relative sparing in Parkinson's disease of substantia nigra dopamine neurons containing calbindin-D28K. Brain Res. 526, 303–307. https://doi.org/10.1016/0006-8993(90)91236-a

Yang, H., de Jong, J.W., Tak, Y., Peck, J., Bateup, H., Lammel, S., 2018. Nucleus accumbens subnuclei regulate motivated behavior via direct inhibition and disinhibition of VTA

dopamine subpopulations. Neuron 97, 434-449.e4. https://doi.org/10.1016/j.neuron.2017.12.022

Yoshizawa, T., Ito, M., Doya, K., 2018. Reward-Predictive Neural Activities in Striatal Striosome Compartments. eNeuro 5, ENEURO.0367-17.2018. https://doi.org/10.1523/ENEURO.0367-17.2018

Zaveri, N.T., 2011. The Nociceptin/Orphanin FQ Receptor (NOP) as a Target for Drug Abuse Medications. Curr. Top. Med. Chem. 11, 1151–1156.

Zaveri, N.T., Waleh, N., Toll, L., 2006. Regulation of the prepronociceptin gene and its effect on neuronal differentiation. Gene 384, 27–36. https://doi.org/10.1016/j.gene.2006.07.007

Zhang, Y., Schalo, I., Durand, C., Standifer, K.M., 2019. Sex Differences in Nociceptin/Orphanin FQ Peptide Receptor-Mediated Pain and Anxiety Symptoms in a Preclinical Model of Post-traumatic Stress Disorder. Front. Psychiatry 9. https://doi.org/10.3389/fpsyt.2018.00731

Zheng, F., Grandy, D.K., Johnson, S.W., 2002. Actions of orphanin FQ/nociceptin on rat ventral tegmental area neurons in vitro. Br. J. Pharmacol. 136, 1065–1071. https://doi.org/10.1038/sj.bjp.0704806

Zhou, X., Stine, C., Prada, P.O., Fusca, D., Assoumou, K., Dernic, J., Bhat, M.A., Achanta, A.S., Johnson, J.C., Pasqualini, A.L., Jadhav, S., Bauder, C.A., Steuernagel, L., Ravotto, L., Benke, D., Weber, B., Suko, A., Palmiter, R.D., Stoeber, M., Kloppenburg, P., Brüning, J.C., Bruchas, M.R., Patriarchi, T., 2024. Development of a genetically encoded sensor for probing endogenous nociceptin opioid peptide release. Nat. Commun. 15, 5353. https://doi.org/10.1038/s41467-024-49712-0